# Texture based formability enhancement of Mg AZ31 using high speed friction stir processing

Vom Promotionsausschuss der
Technischen Universität Hamburg - Harburg
zur Erlangung des akademischen Grades
Doktor-Ingenieur (Dr.-Ing.)
genehmigte Dissertation

von
Leon Leander Hütsch

aus
Berlin

2014

**Gutachter:**

Prof. Dr. Norbert Huber

Prof. Dr. Swantje Bargmann

**Vorsitzender des Prüfungsausschusses:**

Prof. Dr. Otto von Estorff

**Tag der mündlichen Prüfung:**

4. November 2014

# Acknowledgements

I would like to express my deepest gratitude to the following people for their continuous support and contribution to this work:

- Prof. Dr. Norbert Huber for his support and guidance as well as for opening up numerous opportunities to extend my knowledge beyond the scope of this work.
- Prof. Dr. Swantje Bargmann for being the second reviewer of this work.
- Dr. Jorge F. dos Santos for his continuous encouragement and support in every aspect of this work, for giving me the scientific freedom to develop my research autonomously as well as for being a role model for the future.
- Petra Fischer, Dr. Jan Bohlen, Dr. Lennart Stutz, Manfred Horstmann and Gert Wiese for their support with the experimental work.
- Stephanie Koch and Dagmar Koschek for their administrative and personal support.
- My students Klaas Herzberg, Gustavo Trindade Valio, Tayron Zilli and Clement Gayton for their support.
- All members of WMP for creating an enjoyable work environment and the fun we had together.
- My wife Julia for her uninterrupted support, experimentally and personally, for challenging and continuously scrutinizing my conclusions as well as for her patience during the long nights and weekends.
- My son Jasper for always understanding when I needed to go to work.
- My parents Hilli and Heiner as well as my sister Candan for never giving up on me.

# Contents

# Abbreviations

## Analysis

| | |
|---|---|
| E | Young's Modulus |
| EBSD | Electron Backscatter Diffraction |
| FLC | Forming Limit Curve |
| FLD | Forming Limit Diagram |
| HAB | High Angle Boundary |
| IPF | Inverse Pole Figure |
| IPFM | Inverse Pole Figure Map |
| LAB | Low Angle Boundary |
| m.rd. | Multiple Times Random |
| MA | Misorientation Angle |
| n | Strain Hardening Exponent |
| OM | Optical Microscope / Microscopy |
| PF | Pole Figure |
| SEM | Scanning Electron Microscope / Microscopy |

## Material

| | |
|---|---|
| $\tau_{CRSS}$ | Critical Resolved Shear Stress |
| 45° | 45° to Rolling Direction |
| A | Elongation at Fracture |
| BM | Base Material |
| CDRX | Continuous Dynamic Recrystallization |
| DDRX | Discontinuous Dynamic Recrystallization |
| DRX | Dynamic Recrystallization |
| HCP | Hexagonal Closed Packed |
| m | Schmid Factor |
| Mg | Magnesium |
| ND | Normal Direction |
| $R_m$ | Ultimate Tensile Strength |
| $R_{p0.2}$ | Yield Strength |

RD ..... Rolling Direction

RSS ..... Resolved Shear Stress

TD ..... Transverse Rolling Direction

## Process

$\varphi_x$ ..... Tool Tilt Around x

$\varphi_y$ ..... Tool Tilt Around y

AS ..... Advancing Side

FSP ..... Friction Stir Processing

FSW ..... Friction Stir Welding

HAZ ..... Heat Affected Zone

HS-FSP ..... High Speed - Friction Stir Processing

PD ..... Processing Direction

PZ ..... Process Zone

RPM ..... Tool Rotational Speed

RS ..... Retreating Side

SZ ..... Stir Zone

TMAZ ..... Thermo Mechanically Affected Zone

# 1 Abstract

The widespread industrial use of magnesium alloys as a structural material is often limited by their poor room temperature formability, resulting from the low symmetry of readily available slip systems. Controlled microstructural and textural modifications, imposed by severe plastic deformation processes, have the ability to reduce the anisotropy and furthermore increase the ease of activating basal slip. Such modifications have been realized by friction stir processing (FSP), a derivative of friction stir welding, which can be used to impose the necessary amounts of massive local deformation without altering the shape of a structural component. In the present study, FSP has been conducted at industrially viable speeds of up to 20 m/min. A numerical thermal model, calibrated by thermo couple measurements, has been adapted to predict the thermal evolution in the center of the process zone in order to gain insight into the occurring recrystallization processes. The model predicts the resulting temperatures and corresponding cooling rates to be sufficiently high for dynamic recrystallization processes to take place as well as to prevent annealing after processing, respectively. In combination with metallurgical investigations, these results provided the foundation for a knowledge-based selection of suitable processing parameters within the investigated parameter range. Micromechanical and textural investigations revealed the stir zone to be particularly suited for enhanced formability. The effect of different processing conditions on the mechanical response of the stir zone has been evaluated by micro flat tensile tests showing an increase in ductility with rising processing speed, surpassing the base material values by over 80%. Additional texture investigations revealed that the observed increase can be ascribed to the continuous alignment of the basal planes with the macroscopic shear plane, represented by the shear layer, which is surrounding the tool. It has further been shown that the geometry of the shear layer can be controlled using suitable processing parameters resulting in the ability to tailor the texture of the material, and thus its ductility. Finally, this knowledge has been transferred to process larger areas out of which formability specimens have been prepared. The evaluation of the processed as well as base material specimens has been conducted at ambient temperature, in which information obtained from a digital image correlation system has been used to establish forming limit curves. The results show a significant improvement in formability and a decrease in anisotropy of the processed over the base material.

# 2 Introduction, Motivation and Objectives

In a globalized society, the need for rapid transportation becomes increasingly important. For decades, steels have been used to produce cars and trains due to their high abundance, low production cost as well as their wide range of adjustable properties. In recent years however, the utilization of steels in the transportation industry is decreasing [1]. Their high specific weight is a disadvantage in the aim for faster, lighter and more fuel efficient means of transportation, while at the same time structural safety and durability have to be maintained [2]. Additional restrictions are imposed by governmental regulations such as the corporate average fuel economy program of the US government which aims at fuel reduction, as well as lowering the $CO_2$ emissions by almost 50% from 2009 to 2020 [3].

The industry has adjusted to these demands by increasing the use of novel materials [4]. As a 10% reduction in total vehicle weight can decrease the fuel consumption by up to 8%, the use of lightweight metallic materials and polymer composites in automotive applications gains continuous importance [5]. Since the shift to lighter structural metals became a sustainable trend, a significant amount of research has been focused on the development of new high strength aluminum alloys [6], but it has not been until the 1990s that magnesium (Mg) and its alloys regained wider attention in the metal consuming industries [7, 8].

In comparison to the widely used aluminum alloys, Mg-alloys offer an even greater weight saving potential, as they are up to 37% lighter while portraying an excellent strength to weight ratio [9]. Due to a small chipping size, Mg-alloys can be machined easily at low cutting speeds [10, 11], are easy to cast [12, 13] and their recycling capabilities have improved [14,15]. While Mg-alloys have been used in the transportation industry for years, their application is limited mainly to castings and forgings [16], such as power trains and gear boxes [17–20], steering wheels [21], rims [22] and casings [23].

While the weight saving potential in the area of power trains and gear boxes for a vehicle of standard size adds up to 6%, a far greater potential can be realized in the bodywork [24]. In areas such as the car body, Mg-alloys have not yet been widely introduced, which is partly due to the custom of using wrought alloys for these applications. While wrought semi-finished products possess higher strength and ductility compared to their cast counterparts, rolled sheets usually need to undergo additional deformation processes in order to obtain their final shape. As these processes often involve deformations at low temperature, suitable materials have to accommodate large amounts of uniform plastic deformation [25]. In this context, Mg-alloys exhibit significant restrains. Even though Mg-alloys can easily be formed at elevated temperatures between 200°C and 250°C, the

formability at ambient temperature is limited [26]. These limitations arise mostly from the low symmetry of readily available slip systems to accommodate strains in the *c*-axis direction of the inherent hexagonal close-packed unit cell [27, 28]. In detail, with a total number of only four independent slip systems, Mg does not satisfy the von Mises criterion for homogeneous uniform deformation of a polycrystal [29].

A promising approach to overcome these limitations is texture modification, either by alloying or by thermo-mechanical processing. Considering the former, weak non-basal textures which are considered favorable for increasing the forming capabilities can be achieved by adding small quantities of rare earths such as cerium [30]. To alter the c/a axis ratio and thus create a higher rotational symmetry, low amounts of lithium can be used [31]. Adding high amounts of lithium ($> 30\%$) results in a two-phase structure of which the $\beta$ phase is highly ductile [32].

For texture modification of conventional Mg-alloys, an alternative route to enhanced ductility is given by the application of thermo-mechanical processes. While a randomization of the initial basal texture by hot deformation has shown to improve tensile ductility [33], a controlled tilt of the basal planes out of the sheet normal direction promises a possible tailoring of the deformation properties [34]. In both cases, the increased ductility is attributed to the easier activation of basal slip or by grain boundary sliding and grain rotation of small recrystallized grains, resulting in a reduction of the strain hardening rate [35].

The required amount of texture modification is usually obtained by severe plastic deformation processes like channel die compression [36]. As in such processes the entire sample is deformed, they are not applicable on structural parts. In order to make use of the resulting textural adjustments, the imposed changes need to be applied locally without altering the geometry of the part itself.

One possible way to achieve high amounts of plastic deformation on a local scale is given by friction stir processing (FSP) [37, 38]. FSP is based on friction stir welding (FSW) and has proven to be a suitable process for modifying the textures inherent to rolled sheet material [39, 40] which can also help to reduce the critical resolved shear stress ($\tau_{CRSS}$) [41–44], aiding the formability at ambient temperature. Additionally, FSP can be used to achieve grain refinement in Mg-alloys [45,46] which could allow for grain boundary sliding [47–49].

FSP can thus be applied as part of a joining operation during fabrication and at the same

time allows for local processing of regions which in further production steps will undergo large deformations at ambient temperatures.
The objectives of present study have thus been defined as follows:

- To develop process parameters and procedures leading to massive local deformation on the Mg-alloy AZ31 under consideration of high processing speeds for improved productivity.
- To understand the effect of thermo-mechanical phenomena imposed by FSP on the microstructural and textural evolution in the Mg-alloy AZ31 and the resulting local mechanical properties as well as to demonstrate the transferability of the knowledge on processing to larger scales.
- To analyze the formability of processed material at ambient temperatures and establish strategies addressing the applicability of the technology to industrial products.

In this section, a short introduction, the motivation as well as the resulting objectives for the present study have been presented. The state of the art in materials processing technology including techniques which alter and enhance the microstructure and texture as well as the formability of Mg and its alloys is reviewed in section 3. In section 4 the experimental approach, the employed equipment and investigative methods, as well as the base material characterization is presented. Results including thermal numerical analysis, microstructural and textural investigations, as well as mechanical testing will be presented and discussed in section 5. In section 6 the results are summarized and finally, conclusions are drawn in section 7.

# 3 State of the Art

## 3.1 Materials Processing

In the field of materials science, processing is used to generate microstructures which possess desired properties. Just as the alteration may range from small scale atomistic changes to large scale microstructural changes, the resulting properties range from basic physical enhancements, such as electrical or thermal conductivity, to macroscopic enhancements, such as strength and ductility. While the processing of materials from an engineering point of view can be regarded as a complementation of materials technology or materials engineering, the ever increasing field of applications has excelled it beyond these bounds. Today, materials processing can be viewed as a discipline of its own in the field of materials science and stretches from atomic and nanoscale alterations over microstructural changes to multi scale processes [50].

The demand for materials processing technologies is mainly derived from the need to tailor material properties to a certain application. In metals, the earliest application of materials processing reaches back as far as the bronze age (2200 - 800 B.C.). During this time, alloying copper with various other elements has been used to increase the casting abilities or enhance the materials fracture toughness [51].

Over the years, this knowledge has been further refined and led to one of the most well known and investigated materials processing technologies, the processing of steels. It has been found, that by applying small quantities of carbon, the otherwise easily deformable iron transforms into tough steel and that additional thermo mechanical treatments such as forging and quenching, can increase thought after mechanical properties even further [52]. Today, processing techniques as well as processed materials have evolved as their usage has found their way into everyones daily live from consumers [53] to professionals [54].

### 3.1.1 High Strain Thermo - Mechanical Processes

As a wide range of different processing techniques exist, the following discourse is mainly focused on processes including large amounts of deformation at elevated temperatures.

#### Metalworking

In general, metalworking is applied with the preset of introducing a shape as well as a metallurgical change to a given material. It is a thermo mechanical plastic forming process which can be divided into hot and cold forming. While the boundary between hot

and cold forming depends on the properties of the material, the applied processes remain fundamentally the same [55]. Tab. 3.1 lists an overview over the various traditional metalworking techniques.

Table 3.1: Summary of traditional metalworking techniques [55].

| **Process** | **Stress state** | **Comments** |
|---|---|---|
| Forging | Compression | Compression using an open or closed die. |
| Rolling | Compression between rolls | Shape can be given by the rolls. |
| Wire drawing | Tension | Shape can be given by the die. |
| Extrusion | Compression | Shape can be given by the die. |
| Sheet forming | Multiaxial | Similar processing techniques are deep drawing, ironing, sinking, bending, spinning etc. |

Each process is designed to alter a specific material property. While hot-forging can be applied to homogenize and recrystallize the microstructure, hot-rolling can be applied to break up an as cast microstructure and reduce gas inclusions. Extrusion or sheet forming on the other hand can be used to obtain near net shaped components. While all of these techniques may potentially invoke recrystallization and textural reorientation of the initial microstructure and texture, its magnitude strongly depends on the imposed strain, strain rate and temperature. Depending on the process, the microstructure and texture might be homogeneous (rolling) or vary within the produced geometry (sheet forming).
Recently, the traditional metalworking techniques are being supplemented by newly developed processes. These techniques are specifically designed to further refine the grain size and evoke substantial textural alterations. The necessary amounts of internal strains are usually introduced by applying plastic strains $> 5$ [56].
A summary of the most commonly used high strain metalworking techniques with detailing references to the respective processes for a variety of investigated materials is presented in Tab. 3.2. Due to the vast variety of investigated materials, the following review will be limited to possible formability enhancements of Mg-alloys.
Friction stir processing will be discussed in more detail in section 3.1.2. From the group of novel metalworking techniques, accumulative roll bonding and equal channel angular extrusion are in essence comparable to the traditional ones as they do not impose torsion

on the material as high pressure torsion or FSP do.

Table 3.2: Summary of novel metalworking techniques [56].

| **Process** | **Description** |
|---|---|
| Accumulative roll bonding [57–60] | A repetitive rolling and stacking of similar or dissimilar materials. |
| High pressure torsion [61–64] | A coin shaped specimen is rotated in a die under pressure. |
| Equal channel angular extrusion [65–68] | Material is repeatedly extruded around a bent within a die. |
| Friction stir processing | Material is stirred around a probe. |

### Accumulative Roll Bonding

Even though accumulative roll bonding has been conducted on a large variety of materials, the literature concerning the formability of processed Mg is scarce. A schematic of the process can be seen in Fig. 3.1. While multiple passes on pure Mg have shown to improve the strength to a certain level, the effects on ductility are described to be inhomogeneous [69]. This inhomogeneity has been correlated to the difficult bonding conditions between the two processed sheets.

Other investigations have shown that accumulative roll bonding of Mg-alloy AZ31 can develop a fine grain structure (1.3 $\mu$m) via dynamic recrystallization by transitioning from a low angle grain boundary to a high angle grain boundary dominated structure [70]. Similar investigations have shown superplastic forming capabilities at temperature above 300°C [71] which the authors argue to be correlated to the ultra fine grain structure. While superplastic forming capabilities at elevated temperatures have also been observed in conventionally rolled Mg AZ31 [72], accumulative roll bonding has the advantage, that previously rolled sheets can be combined, followed by additional rolling steps,

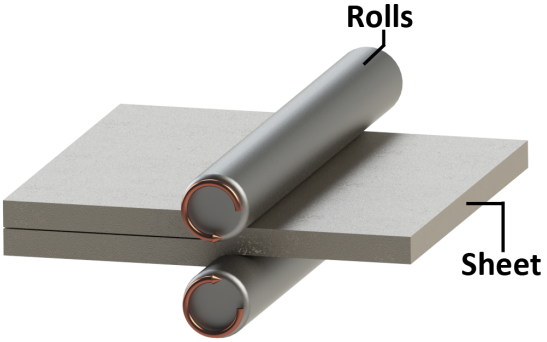


Figure 3.1: Schematic of the accumulative roll bonding process.

in order to further reduce the resulting grain size.

Conclusively it can be noted that accumulative roll bonding does indeed represent a tool for introducing severe plastic deformation into a given material. By varying the precursor material or adding particles, composites- or even tailored materials can be manufactured [60]. On the other hand, the process lacks the ability to alter the microstructure and texture locally. This bounds its applicability to the production of specimens with evenly distributed properties.

#### High Pressure Torsion

Similar to accumulative roll bonding, the available literature dealing with high pressure torsion of Mg is limited. Due to the setup of high pressure torsion (Fig. 3.2), the resulting strain imposed onto the material is higher towards the outer circumference of the specimen than in the center.

As a result, the grain refinement and consequently the mechanical properties are a function of specimen radius [73]. Through thickness variations in grain size have also been reported and are accredited to inhomogenious flow stresses in the setup [74]. Generally, grain refinement is reported in high pressure torsion material and is described to be a function of the atomic bond energy, the specific heat capacity and activation energy for self diffusion as well as the homologous temperature [75]. Grain refinement is reported to have a positive effect on ductility as superplastic effects have been demonstrated at temperature between 150°C to 200°C [76].

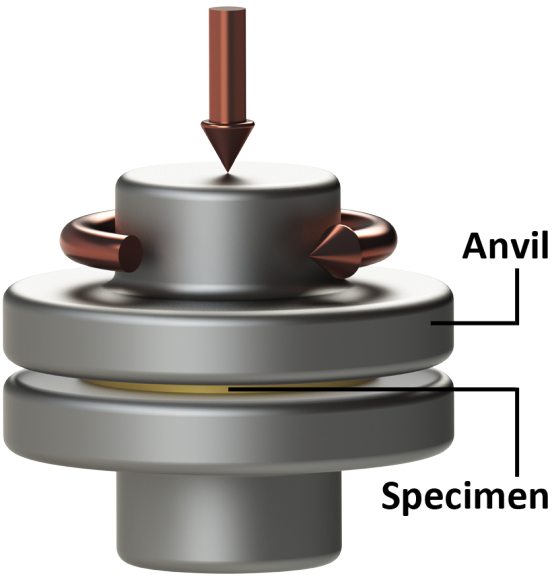


Figure 3.2: Schematic of the high pressure torsion process.

Compared to accumulative roll bonding, high pressure torsion deforms small scale material ($V \approx 62$ mm$^3$ ($r = 5$ mm, $h = 0.8$ mm) [74,76]) with the aim to impose a specific amount of strain at a predefined strain rate. While the results such as grain refinement and textural variations as a function of specimen radius is of great scientific relevance, it lacks the direct transferability to an industrial environment and must thus be regarded as purely scientific.

### Equal Channel Angular Extrusion/Pressing

Compared to accumulative roll bonding and high pressure torsion, the investigations on the microstructural and textural effects of equal channel angular extrusion and pressing (Fig. 3.3) regarding the formability of Mg and Mg-alloys are more extensive. Generally equal channel angular extrusion is conducted at elevated temperatures between 200°C and 400°C using various die geometries and processing routes. In pure Mg [48], Mg AZ31 [47] as well as Mg ZK60 [77] an initial reduction in grain size after the first pass has been observed.

Multiple equal channel angular extrusion passes of the same orientation, on the other hand, do not change the resulting grain size significantly. The resulting texture appears to be strongly influenced by the die geometry [78], the texture of the base material [79] and the billet orientation (common rotations are multiples of 90°) [66]. During the equal channel angular extrusion process the basal planes of the Mg unit cell align themselves to the macroscopic shear plane which in case of equal channel angular extrusion is the bent of the die. The degree of {0001} basal plane reorientation is a function of the die angle [80] and processing temperature, as some authors reported no observable basal tilt in specimen processed above 400°C [66].

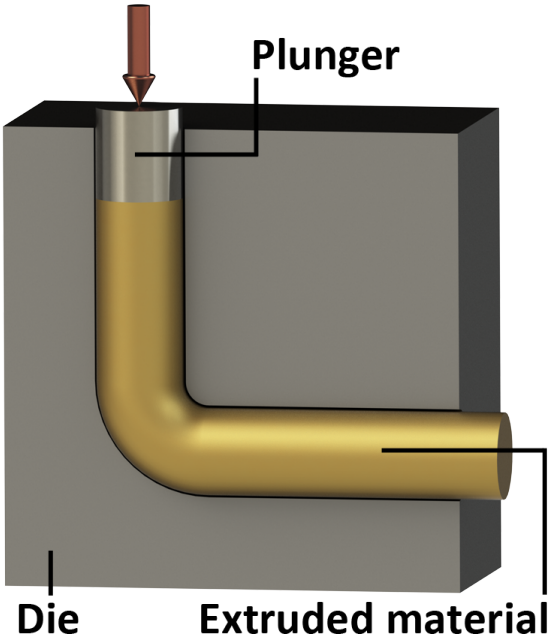


Figure 3.3: Schematic of the equal channel angular extrusion process.

On the other hand, the effects of grain size reduction and textural changes on the resulting mechanical properties are discussed controversially. While some authors attribute the observed increase in ductility to the homogenization of the grain boundary structure [35] or an overall reduction in grain size [48,77], others include textural modifications. In detail, slip on the tilted basal planes [66, 80, 81] and non basal planes [27] have been identified to be the main contributors to the observed increases in ductility.

While equal channel angular extrusion uses larger specimen ($V \approx 4.7$ cm$^3$ ($r = 5$ mm, $l = 60$ mm) [78]) compared to high pressure torsion, the microstructural and textural alterations

usually exhibit only minor variations within the specimen thickness. Even though the initial specimen is completely deformed during the process, a suited die configuration has the potential of expanding the use of the process towards technological applications [82].

Even though all of the above processes result in grain refinement and textural alterations, they are limited to a specific specimen geometry. While in the case of accumulative roll bonding, the initial shape is restored after rolling (depending on the thickness reduction), high pressure torsion and equal channel angular extrusion both deform the specimen such that the original morphology is lost. Thus, their applicability to semi-finished products is limited, and their usage often remain scientific in nature. FSP on the other hand can be applied locally on a semi-finished product or in a production line without destroying the general specimen geometry and can thus be applied industrially while remaining of high scientific relevance. In the following, a brief historical overview as well as an in-depth description of the process will be given.

### 3.1.2 Friction Stir Based Processes

Since FSP is a derivative of FSW, a brief overview over the basic principles of the process as well as some related applications will be discussed.

#### Friction Stir Welding

FSW belongs to the class of pressure welding processes which also includes the sub class of friction bonding. It has been developed in 1991 at TWI Ltd., Cambridge, UK as a solid state joining process with the aim to investigating the joining of aluminum alloys. TWI Ltd. holds the patent for FSW until December 2015 and remains the only licensor [83, 84]. Since then many advancements have been made in all fields of the process including tool design, handling system, metallurgical achievements as well as modeling [85–94].
In traditional fusion welding techniques, including arc welding, gas shield welding or even more sophisticated techniques like electron and laser beam welding, the material is heated up without external force until a local melt flow is created. Once the heat source is removed the molten material cools down and solidifies, creating the desired bond [95].
Pressure welding incorporates a local heating of the workpiece as well, but adds pressure to support the joining process. Friction based processes constitute a subgroup of pressure welding, as the local heating does not create bulk melting within the processed material

[96]. Thus the working temperature remains beneath the melting point of the joining partners, practically eliminating solidification problems such as pores due to gas inclusions or solidification cracking [97].

Due to the low thermal input, the residual stresses are low compared to fusion welding techniques, leading to a minimum of distortion which reduces the need for post weld straightening [98–101]. An adequate setup or clamping, e.g. vacuum clamping or pre-tensioning, can further reduce residual stresses. Compared to fusion welding processes, the mechanical properties, such as fatigue resistance and fracture strain, can also be improved [102, 103] and the tensile strength can even reach base material values [104]. On the other hand the welding speed in materials with a high plasticization temperature is limited [105]. In FSW no filling wire/material is needed, eliminating concerns about composition incompatibility often found in joining of aluminum alloys. The process is easy to use and has the prerequisites to be automated if desired [106]. Even though shielding gases are required for some alloys it is possible to weld in virtually any position (with an appropriate handling system), in different seam configurations and with a minimum of noise and fumes [107]. Due to these characteristics, alloys which have been deemed hard to weld using conventional welding processes, can now be joined effortlessly with FSW, including high strength aluminum alloys, magnesium, titanium, steel or copper [108–112] or even dissimilar material combinations such as Al & Ti, Al & Fe, Al & Mg, Mg & Ti, Mg & Fe [113–124].

A detailed description of the process, the involved tools as well as the resulting microstructural changes will be given in section 3.1.2. In-depth information on FSW and FSP as well as its versatile applicabilities can be found elsewhere in the literature [125–128].

#### Friction Stir Processing

FSP is a derivative of FSW and has been first reported in the literature by Mishra et al. [46]. It is a processing method to locally modify the microstructure and texture of a material. Using appropriate processing parameters, the resulting material properties can be tuned to fit a specific purpose i.e. homogenization and refinement of an as-cast microstructure, or alteration of the microstructure in such ways that enhanced ductility or formability can be achieved [129–134]. The microstructure of pre-rolled aluminum plates can be refined and ultra fine grains can be created by underwater FSP [135, 136]. Other authors used FSP to fabricate surface composites on aluminum substrates with SiC or

$Al_2Cu$ particles [37, 137]. FSP has also been used in powder metallurgical investigations with the aim of dispersing nano sized powders as well as in microstructural evolution investigations of pure iron [138–140].

### FSW / FSP Equipment

In FSP, identical tools, handling systems, welding tables and clamping utilities as in FSW can be used [141]. The handling system (section 4.2.1), which is holding the tool is used to apply the desired loads and conduct the translation motion. The tool (section 4.2.3), on the other hand, conducts the actual processing and must be designed to withstand the acting thermo-mechanical loads. As these loads strongly depend on processing parameters and on the material which is to be processed, several investigations focused on tool geometry and material have previously been conducted [142–146]. The process equipment can be divided into the backing bar which includes a sub structure as well as the employed clamping devices. While the backing bar, usually made of a hot working steel, is used to counteract the applied forces, its sub-structure is used to clamp the sheets and is usually fixed itself on a machine table.

### Processing Phases

The processing itself can be divided into four distinct phases which are illustrated in Fig. 3.4. Within the first phase (Fig. 3.4(a)) of the process, the handling system prepositions the tool at the location from which the processing initiates.

In the following phase (Fig. 3.4(b)) the prepositioned tool is brought to the desired rotational speed and plunges into the material for a defined distance and at a defined speed until the shoulder touches the top of the plate. Due to the rotation of the tool and the friction created by the shoulder, the material surrounding the tools is heated up and brought into a plasticized state. The introduced thermal energy is constantly conducted away from the process zone (PZ) into the backing bar, the surrounding plate material, the tool and the spindle. The processing parameters, in particular the rotational speed and axial force, must therefore be set with great care to avoid tool and machine damage.

Once the material surrounding the tool is sufficiently plasticized, the third phase (Fig. 3.4(c)) begins in which a predefined axial force is applied and the translational movement is initiated. During the translational motion the tool moves through the material, along a predefined path, while the rotational speed of the spindle as well as the axial force are

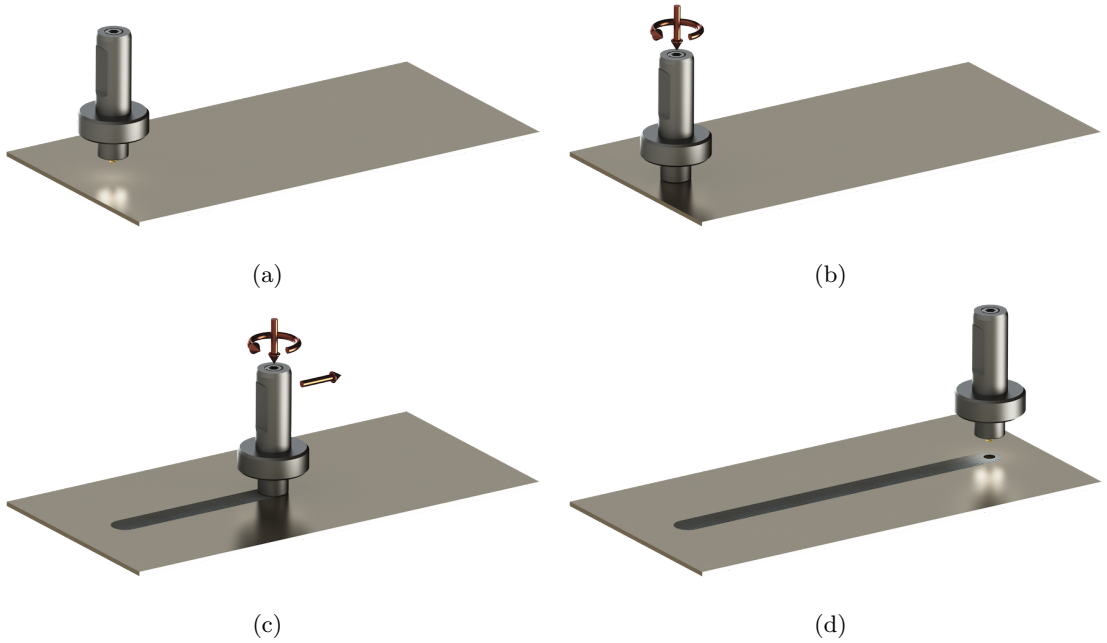


Figure 3.4: Schematic of the different steps in FSP. (a) Prepositioning of the tool. (b) Plunging into the material and plastification of the material underneath the tool. (c) Translational movement creating the process zone. (d) Extraction of the tool.

kept constant. The unprocessed material, which is continuously fed into the process zone, is picked up in front of the tool, transported around the probe and redeposited behind the tool [147]. To support the material transport in vertical direction as well as around the probe, additional features such as threads and flats can be employed at the tool [148]. While the shoulder is primarily used for heat generation, the use of additional features such as threads on the bottom of the shoulder can restrict plasticized material from exiting the process zone towards the sides [149].

In the final phase (Fig. 3.4(d)), the tool is lifted off the plate once the end of the path is reached. The end of the process zone is characterized by a remaining keyhole which has previously been occupied by the probe. While filling of the keyhole is usually not necessary, several techniques have been developed addressing this issue for the case in which it does pose a problem [150, 151].

### Microstructural Zones

Compared to the three metallurgical zones typically found in fusion processes like laser beam welding [152], the process zone created by FSP features four metallurgically distinct zones: The stir zone (SZ), the thermo mechanically affected zone (TMAZ), the heat affected zone (HAZ) and the base material as detailed in Fig. 3.5.

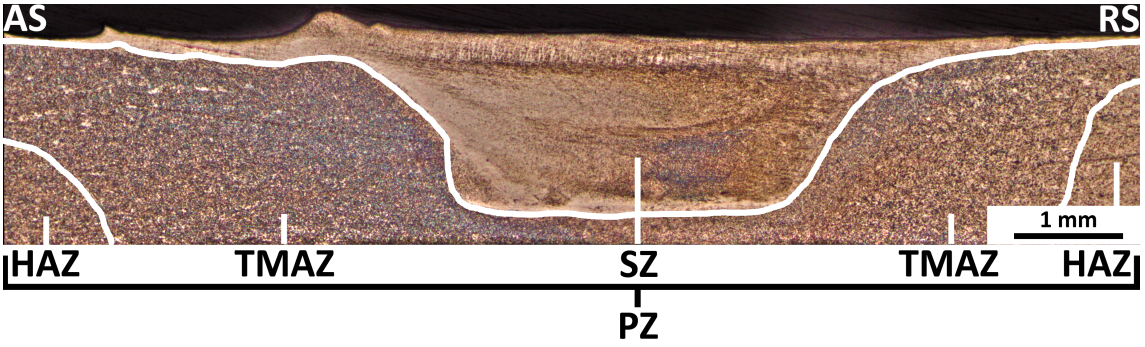


Figure 3.5: Commonly described zones which develop during FSP. In the center of the process zone is the stir zone which undergoes the highest thermo-mechanical loads. The adjacent thermo mechanically affected zone still exhibits thermo-mechanical loads while the heat affected zone exhibits thermal loads only.

The center of the process zone, which endures most of the thermal and mechanical loads, is denoted stir zone. As this region, which is located directly under the shoulder and surrounding the probe, experiences most of the strain, it features a significantly different microstructure than its surroundings. Its size and shape, on the other hand, is derived from the shear layer which can be regarded as the material volume of plasticized material surrounding the probe during processing. Due to the high strains and temperatures, the material in the stir zone usually undergoes recrystallization [153], while the grain shape and morphology in this region is strongly dependent on the material and the processing parameters. This is reflected by the literature as some authors note FSP induced grain size increases up to abnormal grain growth (due to thermally intensive processing parameters) [154], while others found significant grain refinement [155, 156] up to ultra fine grains in the range of 200 nm [136].

Adjacent to the stir zone resides the thermo mechanically affected zone, which is typical for friction welding processes. The material in the thermo mechanically affected zone still experiences large amounts of thermal energy as well as parts of the applied mechanical loads originating from the tool, even though the overall magnitude is not as high as in

the stir zone. While the size and shape of the thermo mechanically affected zone depends on the utilized tool, processing parameters and base material, the microstructure is often recrystallized or underwent recovery processes. Even though the thermo mechanically affected zone endures thermo-mechanical loads as well, it can clearly be distinguished from the stir zone either by grain size, grain morphology or textural differences [157].

Adjacent to the thermo mechanically affected zone is the heat affected zone. This zone experiences no mechanical loads and is solely affected by the imposed thermal cycle resulting in recovery processes, grain growth and other microstructural effects [158].

The base material, surrounding the process zone, is unaffected by the processing [159].

#### Asymmetry

In FSP the rotational movement of the tool is superimposed by an unidirectional translational movement. This results in an asymmetry in the process zone which is characteristic for FSP. In order to clarify which side of the weld is investigated, a terminology has been created in which the side of the process zone with the tangential vector of the rotational movement and the vector of the translational movement of the same sign is termed advancing side (AS) while the opposite side is termed retreating side (RS) [160].

#### FSW and FSP of Mg AZ31

In the following, previous investigations conducted on the Mg-alloy AZ31 are reviewed, with the focus on grain size evolution, mechanical properties, texture and formability. In order to broaden the spectrum of available literature, FSW and FSP will be discussed jointly as both processes are comparable in most aspects.

The effect of FSP on the resulting grain size has been thoroughly investigated. Even though some authors report an increase of grain size in the stir zone when using FSP parameters leading to high thermal inputs, [161–163] a vast majority of the available literature reports a grain size reduction in the stir zone through dynamic recrystallization [45, 145, 155, 164–171]. Notwithstanding the above, the authors agree that the final grain size is a function of thermal input, which in turn depends on FSP parameters such as the ratio of processing speed to rotational speed, known as processing pitch [161, 164]. With increasing thermal energy, the recrystallized material has a higher potential for grain growth. It has also been argued that an active external temperature regulation, such as cooling, can be a suitable tool to control the resulting grain size without the need

to significantly alter the processing parameters [45, 155, 165, 168].

In addition to the grain size, the hardness has been subjected to extensive investigations as well. The overall trend of the investigations shows a weak hardness dependence on grain size throughout the process zone, cumulating in a hardness decrease in the stir zone [145, 161, 162, 164, 167, 171, 172]. On the other hand, an increase in hardness has been reported for material incorporating a grain size in the sub-micron regime (100 nm to 1 $\mu$m) [45, 155, 165].

The mechanical properties of the process zone have traditionally been investigated using tensile tests. When testing the entire process zone, an overall decrease in yield strength ($R_{p0.2}$), ultimate tensile strength ($R_m$) and tensile elongation (A) compared to the base material has been reported [40, 168, 171]. Even though still below base material values, a tendency of increasing strength with increasing processing pitch has been observed [161, 162, 164, 167].

While the decrease in $R_{p0.2}$ has been attributed to the incompatibility boundary between the FSP inherent metallurgical zones, leading to fracture within the interface between the thermo mechanically affected zone and stir zone [39, 161, 163, 173, 174], the tensile elongation appears to be strongly dependent on the direction the material is tested in. Testing the process zone orthogonal to processing direction (PD) [164, 173–176, 176] yields a decrease in tensile elongation, whereas testing the process zone into processing direction yields an increase in tensile elongation. These differences can be accredited to the different volume fractions of unequal microstructures as well as their location within one specimen in dependence of the loading direction [39, 40, 168]. Generally, the evolution of the tensile tests of the various investigations are highly comparable as the material exhibits a higher strain hardening exponent and strain hardening capability compared to the base material [161, 166, 168, 177].

When regarding tensile results obtained by testing the entire process zone, it should be kept in mind that the tested material is not homogeneous due to the various microstructural zones within the specimen as previously investigated by Rao et al. [178] for Al 5083. Thus, the obtained results reflect an integration of tensile values over all participating microstructural zones, mainly incorporating the encountered stresses / strains of the metallurgically weakest zone.

The resulting texture in the center of the stir zone has been reported to encounter a tilt of the {0001} basal planes towards the processing direction with increasing processing

pitch [39, 179–181]. The neighboring regions of the stir zone on the other hand encounter a continuous rotation of the basal planes towards the transverse direction until the basal planes are completely rotated when reaching the thermo mechanically affected zone. While the rotation detailed above is mainly driven by the probe, the shoulder has a significant influence on the textural evolution in the upper part of the process zone. This region develops a texture mainly characterized by basal slip as well as twinning and exhibits high amounts of low angle boundaries [169].

The topic of formability after FSW/FSP has scarcely been investigated. The available literature shows, that FSP material can exhibit superplastic forming capabilities once the additional slip systems are thermally activated by conducting the experiments at temperatures between 350°C and 400°C [182]. At ambient temperature, the limited improvements in formability have been attributed to the microstructural and textural homogenization of the base material [170]. While most authors recognize the microstructural and textural changes imposed by FSP [183], a systematic investigation on how to control and use these changes with the aim of improving the formability of Mg-alloys is yet to be made. The present study thus focuses on demonstrating how said changes can be implemented and controlled. A detailed discussion of the resulting formability as well as a correlation to previous investigations will be given in section 5.3.3.

## 3.2 Magnesium and Magnesium Alloys

In this section, an overview over the general properties as well as the advantages and challenges of Mg in general and the Mg-alloy AZ31 in particular, will be given. Additionally this section will cover a detailed description of the deformation mechanisms present in Mg.

### 3.2.1 General Properties

Due to its low density of $\approx 1.74$ g/cm$^{-3}$ (at 20°C) Mg-alloys are not only lighter than aluminum alloys but also have a higher specific strength [23].

From a physical and chemical standpoint, Mg is an alkaline metal with the atomic number 12. At ambient temperatures, the lattice parameters of pure Mg are a = 0.32092 nm and c = 0.52105 nm, resulting in an c/a ratio of 1.6236 which is very close to the theoretically perfect hexagonally closed packed (HCP) structure with a ratio of c/a = 1.633 [184]. The most important physical properties of pure Mg are listed in Tab. 8.1 in the appendix.

### 3.2.2 Deformation Modes and Formability Characteristics

In the following an overview over the deformation behavior and formability characteristics of conventional Mg and Mg-alloys such as AZ31 will be given.
One of the main obstacles preventing the widespread use of Mg is its limited formability at ambient temperatures. From an industrial standpoint, these limitations lead to higher production costs in combination with lower outputs. While for commercial aluminum sheet material the final reduction step to the desired thickness can be carried out at ambient temperature, for Mg-alloys a temperature regime between 300°C and 450°C is required [185].

#### Work Hardening in Mg-Alloys

The macroscopically observable effect of work hardening can be rationalized by microstructural effects, namely the storage of dislocations which are introduced into the material during plastic deformation. With increasing plastic deformation, dislocations can build up at grain boundaries and obstacles like particles, forming dislocation forests which leads to an increase in necessary stress to further deform a pre-deformed crystal [186].
While a dislocation can be annihilated by another dislocation of the opposite sign, or cross slip of screw dislocations (the amount is a function of temperature), they seldom advance to the surface to be annihilated thus reducing the total amount of dislocations in the crystal [187]. Increasing temperature leads to increased dislocation mobility, responsible for higher cross slip activity as well as dislocation climb processes and for diffusion resulting in a decrease in strain hardening rate as well as the overall amount of dislocations [188].
Another hardening mechanism that must be considered is twinning. Even though twinning is mainly observed at ambient temperatures and low strains, the resulting reorientation of basal planes can block additional slip activity and thus, increase the necessary stress for further deformation [189].

#### Slip

The origin of the limited formability of Mg can be found in its crystal structure. Mg possesses a HCP crystal structure which limits possible plastic deformations. At ambient temperatures (below 225°C) the two primary active deformation mechanisms are the closed packed $\{0001\}$ basal slip into the closed packed $[11\bar{2}0]$ ($\langle a \rangle$ - slip) directions as well as $\{10\bar{1}2\}$ twinning along the $\langle 10\bar{1}1 \rangle$ direction [190]. The main deformation mechanisms of

Mg are thus $\{0001\}$ basal slip in all three permutations of the $\langle 11\bar{2}0\rangle$ direction resulting in three geometrical slip systems of which only two are independent. However, to satisfy the von Mises criterion for uniform deformation of a polycrystal, five independed slip systems are necessary [29].

Even though Mg can also deform by $\{10\bar{1}0\}-\langle a\rangle$ prismatic slip and $\{10\bar{1}1\}-\langle a\rangle$ pyramidal slip, the activation of these systems requires a higher resolved shear stresses (RSS) than what would be necessary for basal slip [191] (the $\tau_{CRSS}$ for basal slip in pure Mg is $\approx 0.5$ MPa [192]). An overview over the directions and slip planes in Mg is given in Figs. 3.6 and 3.7 respectively.

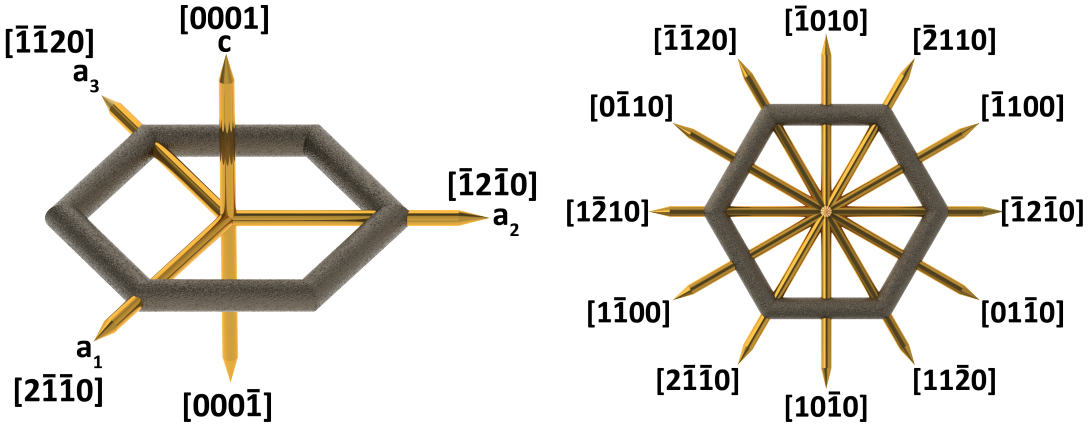


(a) (b)

Figure 3.6: Summary of the various directions of the Mg unit cell [193].

Generally, slip can occur when the resolved shear stress along a given slip plane (e.g. basal plane) and into the direction of slip has reached a critical value, $\tau_{CRSS}$. In order to compensate for the angle between the loading axis (uniaxial deformation) and the slip direction, the angle $\lambda$ is introduced. Thus, $\tau_{CRSS}$ can be written as $\tau_{CRSS} = P \cdot cos\lambda$ in which P is the critical stress acting on the slip plane into the direction of the axis. In order to compensate for possible slip plane rotation, its effective area must be taken into account which can be written as $A/cos\phi$. Finally, $\tau_{CRSS} = \sigma_y \cdot cos\phi \cdot cos\lambda$ in which the term $cos\phi \cdot cos\lambda$ is known as the Schmid factor $m$ [194]. Thus, the resolved shear stress reaches a maximum at a 45° inclination of the basal planes to the axis of deformation which can hence be regarded as most favorable for deformation. The textural modifications in the present study are thus aimed at imposing a rotation of the $\{0001\}$ basal planes within a range between 40° to 50° into processing direction in order increase the ease of basal slip

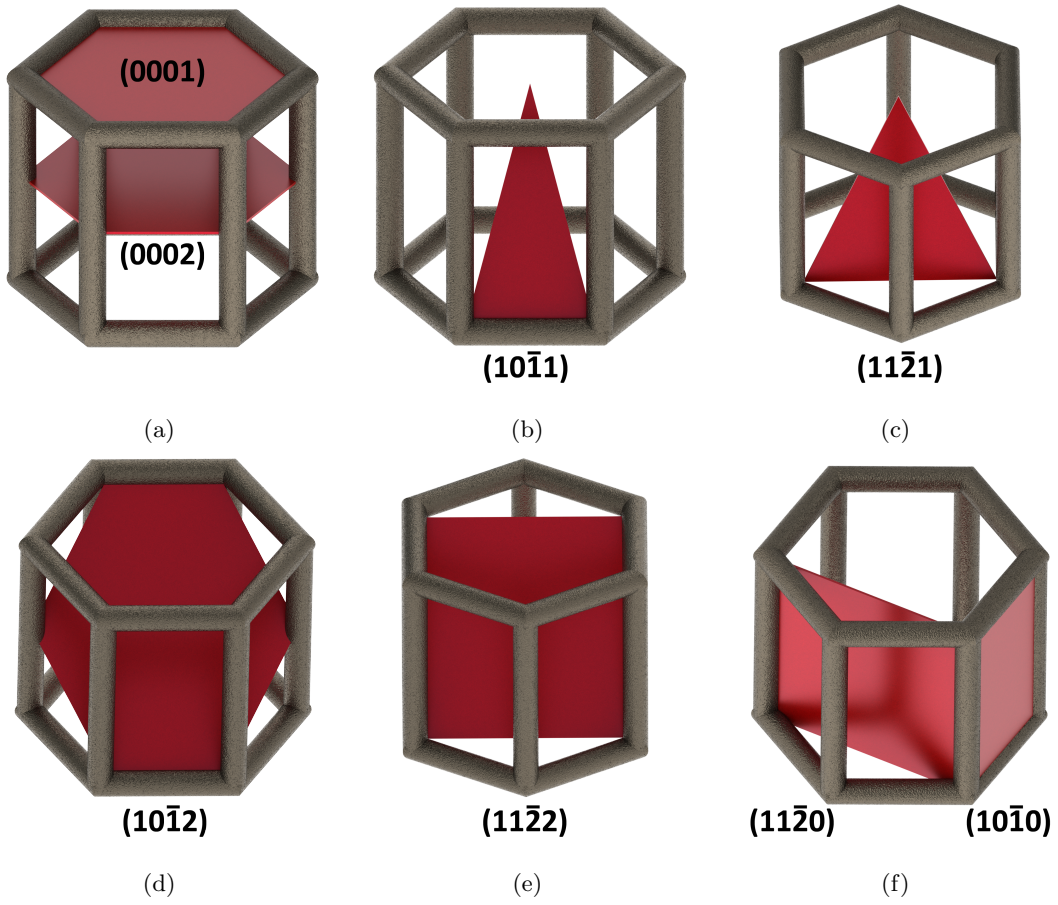


Figure 3.7: Slip planes of Mg: (a) Basal planes. (b) Pyramidal planes of the first order type 1 - $\{10\bar{1}1\}$. (c) Pyramidal planes of the first order type 2 - $\{11\bar{2}1\}$. (d) Pyramidal planes of the second order type 1 - $\{10\bar{1}2\}$. (e) Pyramidal planes of the second order type 2 - $\{11\bar{2}2\}$. (f) Prismatic planes type 1 $\{10\bar{1}0\}$ and type 2 $\{11\bar{2}0\}$ [193].

for in plane stretching.

The process of rolling Mg sheet material, which is the material investigated in this study, results in a predominantly basal type texture in which the $c$-axis (Fig. 3.6(a)) is parallel to the sheet normal. As basal, prismatic and pyramidal slip have all the same $\langle a \rangle$ - slip direction, they can not accommodate any deformation which is directed parallel to the $c$-axis [195]. A non zero shear plane for deformation perpendicular to the basal plane (parallel to the $c$-axis) is given by the $\{11\bar{2}2\} - \langle 11\bar{2}3 \rangle$ pyramidal slip plane, which is also called $\langle c + a \rangle$ - slip [196]. While this system does offer five independent slip systems and would therefore satisfy the von Mises criterion [29] it requires a significantly higher $\tau_{CRSS}$ than $\langle a \rangle$ - slip. Consequently, the activation of $\langle c + a \rangle$ - slip is usually only possible if aided by thermal activation.

### Twinning

Like most HCP crystals, strains imposed on a Mg crystal can be accommodated by twinning. In detail, mechanical twinning can occur on the $\{10\bar{1}2\}$ and $\{10\bar{1}1\}$ planes, which provide a shear component parallel to the $c$-axis, just as the previously discussed $\langle c+a \rangle$ - slip. These two twinning modes are called $\{10\bar{1}2\}$ extension and $\{10\bar{1}1\}$ contraction twinning as the resulting volumetric changes lead to an elongation or reduction along the $c$-axis, respectively [197–199]. While extension twinning is the most commonly observed twinning mode, it can only act along the $c$-axis. In a rolled sheet with its inherent basal texture ($c$-axis parallel to the normal direction (ND)), extension twins can not accommodate any tensile deformation within the sheet plane (along the transverse direction (TD) or rolling direction (RD)) as the applied stresses would lead to a compression along the $c$-axis.

Contraction twinning on the other hand can accommodate compression along the $c$-axis but are minute in extent as well as seldomly observed and have thus a limited contribution to the deformation properties [32, 200, 201].

The evolution of twins in a rolled sheet along the rolling direction can be described by two cases:

**Case I:** A compression perpendicular to the $c$-axis will result in activation of extension twins, due to a tensile strain component on the crystals $c$-axis . This activation results in a rotation of the basal planes by 86.3° around $\langle 11\bar{2}0 \rangle$ which rotates the $c$-axis into the compression direction resulting in a limitation for further deformation perpendicular to the $c$-axis.

**Case II:** On the other hand, a tensile load perpendicular to the $c$-axis can activate contraction twins but has limited textural influence. The majority of the imposed loads will thus be accommodated by prismatic $\langle a \rangle$ - slip which has a higher $\tau_{CRSS}$ compared to basal slip which in turn substantially limits the formability at ambient temperature [25].

It must additionally be taken into account that the magnitude of this behavior is strongly depended on the investigated alloy as increasing alloying content has been reported to decrease the $\tau_{CRSS}$ for prismatic slip (solution softening) [202, 203].

### 3.2.3 Modification Methods for Enhanced Formability

As alloying has not been part of the present study, the formability enhancements at ambient temperature using thermo-mechanical processing techniques will henceforth be described. Using FSP as the processing method of choice, two possible routes have been identified being textural modification and grain refinement.

#### Textural Modification of Mg AZ31

Modifying the particularly strong rolling inherent {0001} basal texture offers great opportunities to enhance the formability at ambient temperatures [204]. The field of textural modification can be subdivided into texture randomization and controlled textural alteration. While the former offers some ductility enhancement through an increase of work hardening capacity [43, 44, 205], controlled textural alterations can be applied to tailor the texture to a specific load case.

Huang et al. [34] used various rolling speeds to modify the basal texture and reported that a 15° tilt of the {0001} basal planes away from the normal direction already enhanced the ductility in tensile tests by activation of $\{10\bar{1}2\}$ extension twinning and the suppression of non basal slip. The authors attributed the higher ductility to an increase in work hardening capacity, with the most pronounced effect at the early stages of deformation. Using repeated unidirectional bending, Huang et al. [206] also reported that due to an increasing tilt of the $c$-axis away from the normal direction, the limit dome height, used to construct forming limit diagrams, increased compared to non-processed material.

Yuan et al. [42] used FSP as a texture modification technique and reported that depending on the measurement location within the process zone, $c$-axis tilts of an angular range between 37° - 86° could be achieved. Using tensile tests into processing direction and transverse direction, the authors describe basal slip to be the dominant deformation mechanism in the processing direction while pyramidal $\langle c+a \rangle$ slips dominates the deformation in transverse direction. In a later study Yuan et al. [41] reported that a fine grained microstructure in combination with a 35° - 55° $c$-axis tilt is responsible for the observed increase in tensile elongation of micro flat tensile tests. The authors attributed the ductility enhancements to basal slip and extension twinning accompanied by high amounts of strain hardening. All tested specimens fractured abruptly after a grain size dependent hardening regime, before developing noticeable necking.

### Grain Refinement

In addition to textural modifications, many authors reported enhanced formability of Mg-alloys by grain boundary sliding through grain refinement.

Choi et al. [207] tested ball milled Mg powders after hot extrusion by quasi isostatic compression in various grain size regimes. The authors found that the interaction of dislocations with grain and-or twin boundaries are the main driver for deformation at grain sizes above 1 $\mu$m. With decreasing grain size, the $R_{p0.2}$ increased in agreement with the Hall - Petch relationship. Within the intermediate regime between 1 $\mu$m to 100 nm, the observed dislocation pile-up mechanism becomes less significant as the effect of twining increasingly contributes to plastic deformation. Finally, at grain size below 100 nm, grain boundary sliding increasingly contributed to the rising formability resulting in an inverse Hall - Petch relationship as twinning becomes less pronounced.

Using equal channel angular pressing and rolling on Mg AZ31, Koike et al. [27,28] observed grain boundary sliding in tensile specimens with an average grain size of 6.5 $\mu$m to 8 $\mu$m. The authors describe the enhanced ductility to be related to dislocation cross slip to non basal planes resulting from grain boundary compatibility stresses present at ambient temperature. At 250°C, the authors found a similar effect which has been attributed to slip induced grain boundary sliding resulting from the previously detailed compatibility stresses at grain boundaries as well as the absorption and dissociation of lattice dislocations at grain boundaries.

Watanebe et al. [35] investigated the low temperature superplasticity of equal channel angular extruded Mg AZ31 using tensile tests at 200°C and low strain rates of $1 \cdot 10^{-5}$ to $1 \cdot 10^{-2}$ $s^{-1}$. The authors found that at an average grain size of 1.4 $\mu$m the encountered ductility enhancements are a result of equilibrium grain boundaries (low amounts of long range stresses), as no changes in grain boundary structure could be observed while the strain rate sensitivity remained constant.

Chai et al. [49] prepared fine grained (1.2 $\mu$m) Mg AZ91 by submerged FSP. Using tensile tests at 350°C and strain rates between $4 \cdot 10^{-4}$ to $2 \cdot 10^{-2}$ $s^{-1}$, the authors found that the main deformation mechanism is indeed grain boundary sliding which the authors attributed to the small grain size.

### 3.2.4 Magnesium Alloys

#### Denotation

Like many other alloying systems, Mg-alloys have their own denotational system. While the first letters denote the principal constituents, the following numbers denote their amount. The sophistication of the alloy, e.g. purity, is indicated by a letter after the constituent amounts. Finally, the applied temper is indicated after a dash. The alloys and temper denotations are listed in Tab. 8.2 and 8.4 in the appendix.

#### The Mg Aluminum - Zinc (AZ) Alloy Series

As with most metals, in order to be useful as an engineering material Mg has to be alloyed with other elements. While the alloy under investigation in the present study is of the Aluminum - Zinc (AZ) series, an overview over the most common alloying elements as well as their effect is listen in Tab. 8.5 in the appendix and a detailed description can be found in the literature [208, 209].

To this day, the Mg AZ series is one of the the most frequent commercially used alloying systems. Even though these systems have been developed over 50 years ago, the main constituents (Al, Zn and Mn) remain unaltered [210]. In contrast to rare earth containing alloys, the AZ series is independent of global trade regulations and relatively inexpensive to produce. The ease of producing Mg-alloys of the AZ series as well as their high solid solution strengthening can be attributed to the addition of aluminum. Corrosion is being limited by keeping the content of iron, copper and nickel below 50 ppm.

The drawback of using aluminum as an alloying element is the formation of the brittle intermetallic $Mg_{17}Al_{12}$ - $\gamma$ phase. While the solubility limit of aluminum at the eutectic temperature is $\approx$12 mass.%, it falls to below 1% at ambient temperatures. Consequently, the final amount of the $\gamma$ phase plays an important role in determining the mechanical properties of Mg-Al alloys [211].

Within the AZ series, the alloy AZ31 is currently used most frequently for sheet applications. Due to its limited cold rolling capabilities, it has to be rolled at elevated temperatures, increasing the production costs significantly. The avoidance of these limitations is therefore an ongoing challenge in which severe plastic deformation processes are playing a leading role [212].

### Magnesium AZ31B

Mg AZ31 is a wrought, solid solution strengthened alloy with 3Al, 1Zn and Mn (weight %) as its main constituents. It has the refinement grade B which allows for only limited amounts of iron, copper and nickel. The alloy can be obtained in three different tempers including as-fabricated (F), annealed (O) and hard-rolled (H24) [213]. The ASTM tolerated chemical composition is listed in Tab. 3.3.

Table 3.3: ASTM tolerated composition of Mg AZ31B (weight %) [213].

| Al | Mn | Zn | Cu | Si | Ni | Fe |
|---|---|---|---|---|---|---|
| 2.5 - 3.5 | 0.20 - 1.0 | 0.6 - 1.4 | max. 0.04 | max. 0.10 | max. 0.005 | max. 0.005 |

Even though it is not the strongest, most ductile or most corrosion resistant alloy in the AZ family, its relatively low cost and easy rollability has given AZ31 a leading role in the area of rolled Mg sheet material [214, 215]. The low aluminum contents yields only minor amount of the brittle $Mg_{17}Al_{12}$ - $\gamma$ phase, giving it reasonable strength and ductility [216]. In addition to FSW, several other welding techniques have been successfully applied to AZ31 such as arc welding [166], electron beam welding [217, 218], tungsten inert gas welding [219] and laser beam welding [220].

# 4 Experimental Approach, Equipment, Methods and Material

In the following sections the experimental approach, the equipment as well as the employed methods and materials of the present study will be elucidated.

## 4.1 Experimental Approach

Initially, process parameters and procedures leading to massive local deformation under consideration of high processing speeds for improved productivity in the Mg-alloy AZ31 have been developed.

- Process parameter study & preliminary evaluation of processing quality

Subsequently, the thermo-mechanical phenomena imposed by FSP on the microstructural and textural evolution have been investigated. Herein, the focus has been laid on the identification of microstructural zones with a high formability potential, the investigation of the resulting local mechanical properties as well as the definition of conditions for the transferability of the gained knowledge to larger scales.

- Prediction of the temperature evolution & selection of suitable process parameters
- Microstructural and textural analysis:
  - Optical microscopy
  - Scanning electron microscopy
  - Electron backscatter diffraction
- Mechanical testing for the determination of local properties:
  - Nanoindentation
  - Micro flat tensile testing

Finally, the formability of processed samples at ambient temperatures has been investigated and strategies addressing the applicability of the technology to industrial products have been establishment.

- Determination of a forming limit diagram

## 4.2 Processing Equipment

This section will give an overview over the FSP handling system, the utilized tool as well as the implementation of the various processing methods.

### 4.2.1 Handling System

FSP has been carried out using a five axis parallel kinematic robot, as shown in Fig. 4.1. The T805 robot has been built by Neos Robotics (now PKM) and is controlled by a Siemens Sinumerik 840D CNC control. Its center beam construction enhances the stiffness of the system and therefore enables the machine to withstand the acting processing forces at the desired processing speed. Depending on its position within the working envelope (2.4 m x 1,8 m x 0,8 m) the T805 can produce maximum forces of 45 kN in axial and 10 kN in processing direction (PD).

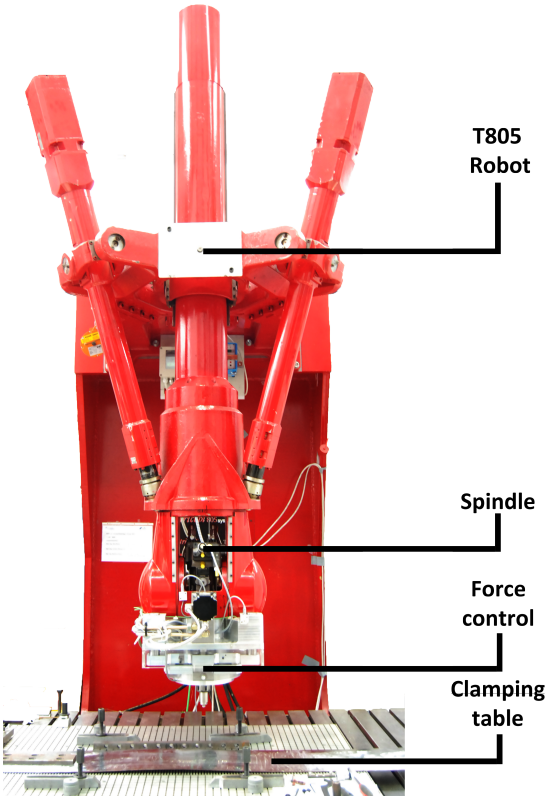


Figure 4.1: Handling system used for FSP.

The entire processing system is divided into two modules in which the first module is the robot itself, incorporating all elements to conduct the processing. The second module is the endeffector which is subdivided in a hydraulically driven spindle which is mounted inside the wrist of the robot as well as the force control unit which is operated by stepping motors in a master-slave configuration. Controlled by a code written in CoDeSys (Controller Development System), the force control system uses the information of four independent piezo force sensors to extend or retract a platform which in turn applies the desire axial force. Due to the residual elasticity within the handling system, the tool is positioned at a predefined angle into processing direction as well as into transverse direction. This way, the shoulder remains parallel to the sample sheet and a reproducible process qualities along the process line is ensured.

### 4.2.2 Endeffector Improvements

In order to achieve the required high rotational speeds as well as the increased response time of the force control unit necessary for high speed FSP, the preexisting endeffector underwent a significant redesign within this study. By upgrading the hydraulic system and replacing the hydraulic spindle motor with a unit which incorporates a variable volumetric flow rate, tool rotational speeds of up to 7000 rpm could be reached. Additionally, the actuators of the force control unit and the software controlling them have been upgraded to increase the response time of the system as well as to reach exercisable forces of up to 30 kN.

### 4.2.3 Tool

In the present study, a tool with variable probe length has been used and the appendant parts are shown in Fig. 4.2(a). It features a monolithic shoulder which is clamped by

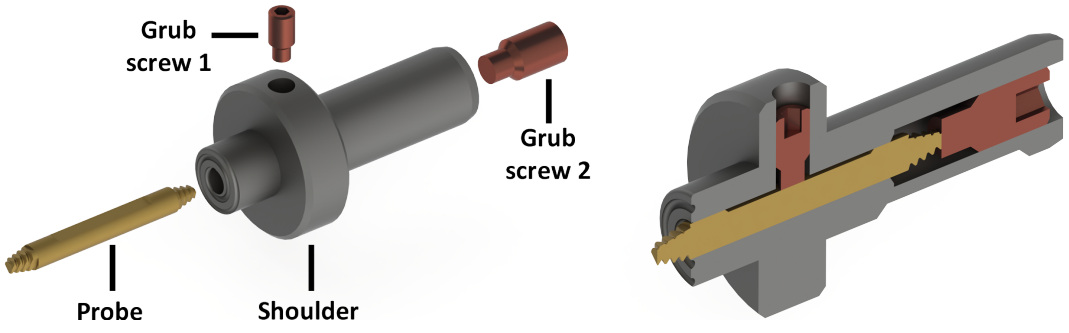


Figure 4.2: Exploded view (a) and assembly view (b) of the utilized tool.

a tool holder, fixed in the spindle. While the tool holder is made of standard tool steel, both shoulder and probe are manufactured from high performance Cr-Mo-V steel with a composition to 0.55%C, 1.0 Si, 0.75 Mn, 2.6 Cr, 2.25 Mo, 0.85 V and rest Fe [221]. The shoulder has a diameter of 13 mm and features a scroll in order to enhance material flow towards the stir zone. The probe geometry features a taper from ∅ 5 mm close to the shoulder to ∅ 2.5 mm. This geometry was chosen as a taper of the probe results in a taper of the resulting shear layer. The benefit of such taper will be discussed in section 5.2.2. The probe features a threaded triflat design, incorporating three flat surfaces to ensure material mixing and a spiral along its outside to ensure material transport from the top to the bottom of the stir zone. Detailed drawing of the shoulder as well as of the probe

can be found in Fig. 8.1 and 8.2 in the appendix.
The assembled tool is detailed in Fig. 4.2(b). While grub screw 1 has been used as a groove stone to prevent the probe from rotation within the shoulder, grub screw 2 has been used to set the probe to the desired length. In all experiments the probe length has been set to 1.9 mm.

### 4.2.4 Setup

For processing, the sheets have been fixed on a table which has been designed and manufactured specific for this purpose. The table incorporated the backing bar which is needed to accommodating the acting forces. To fix the sheets, all screw down clamps have been tightened to 25 Nm. As FSP has been conducted in a beed on plate configuration, fixing the sample sheet from the sides could be neglected.

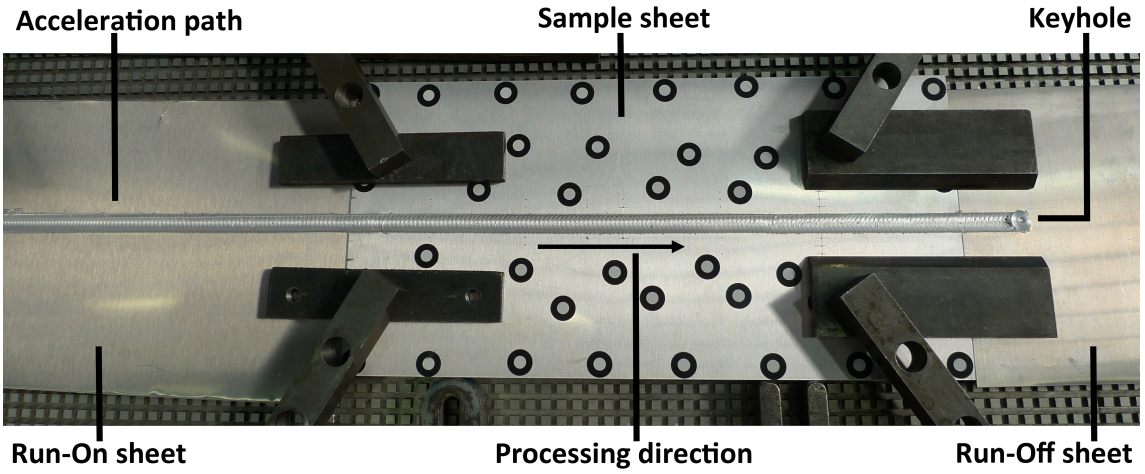


Figure 4.3: Clamping setup for FSP including the acceleration path on the run-on sheet, the sample sheet from which the specimen have been extracted and the run-off sheet with the keyhole.

As one of the aims of the present study has been to conduct processing at high speeds, the creation of a repeatable steady state required considerably more preparation than what is usually required for slower ($< 1$ m/min) FSW/FSP. The delayed appearance of a steady state has been accounted for by placing a run-on sheet before the sample sheet, effectively prolonging the length of the path in which the process can stabilize. The verification of the steady state will be presented in section 5.1.2. Similarly, the keyhole of the process, has been displaced to a run-off sheet which has been clamped behind the sample sheet as

shown in Fig. 4.3. After processing, the run-on and run-off sheets have been separated from the sample sheet.

### 4.2.5 Implementation

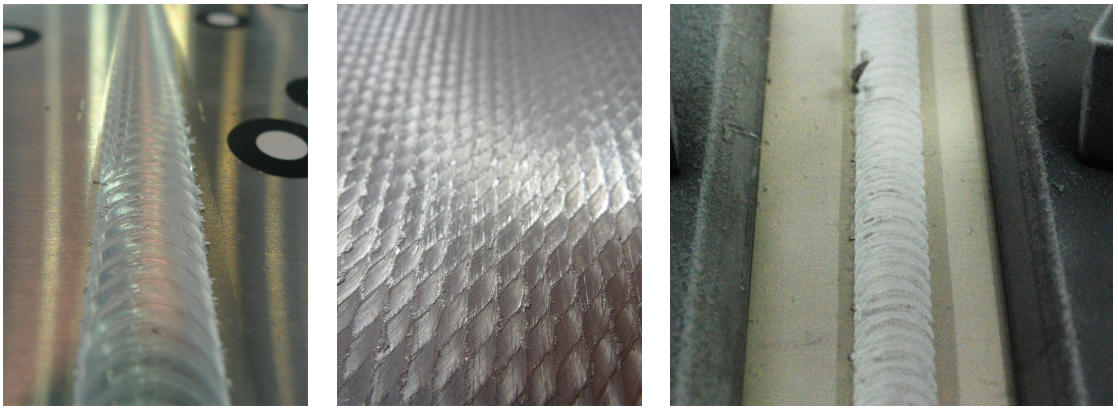

(a) (b) (c)

Figure 4.4: Surface appearance of (a) single line, (b) multi line and (c) externally cooled single line process zones.

FSP has been carried out in a single and multi line setup. Single line tests have been conducted as one pass over the entire sheet length (Fig. 4.4(a)) while multi line tests consisted of multiple passes over the entire sheet length (Fig. 4.4(b)). The setup for the multi line samples is essentially the same as for the single line samples with the difference that a broader backing bar has been used to account for the larger width of the sample. In the multi line samples, each path is displaced by 2 mm into the advancing side with respect to the prior one and orthogonal to the processing direction. The displacement towards the advancing side has been chosen as the retreating side offers a less pronounced metallurgical transition zone which usually experiences a higher strength [163, 173, 174]. After about 60 processing lines, an area of over 600 $cm^2$ has been created. Before each new processing step, the tool and sheet have been cooled down to ambient temperature.
In addition to the single and multi line samples produced at ambient temperature, an exploratory investigation has been conducted in an externally cooled state, in order to conserve the dynamic recrystallization texture and microstructure without alterations imposed by static recrystallization. This state has been created by submerging the sample sheet, the backing bar and the clamping equipment in a container filled with liquid nitrogen. Once the equipment reached a temperature of $\approx$ -196°C, the backing bar has been

mounted onto the thermally insulated machine table followed by the sample sheet and the clamping equipment. FSP has been conducted directly after the setup has been completed and the resulting process line is shown in Fig. 4.4(c).

## 4.3 Force and Temperature Measurements

In the following, an overview over the employed force and temperature measurements systems will be given.

### 4.3.1 Force Measurements

In addition to the axial force and rotational speed data acquired by the force control of the robot, the resulting reaction forces in horizontal and vertical direction have been measured with a force measuring table by Kistler AG. The table consists of two rigid plates, connected by four pre-stressed piezo force sensors. In order to minimize bending, and thus alterations of the measured values, a table which included the backing bar has been mounted on top of the force sensor table. Each force sensor consists of three pairs of quartz crystals one orientated into each of the three spacial dimensions. The horizontal force components in x-y direction are measured by shearing, whereas the vertical z component is measured by compression. The raw data is forwarded to a Kistler 5017B multichannel charge amplifier. The resulting amplified data is then passed as analogue values into a A/D converter and evaluated on a PC using Dynoware software. Using this setup, the resulting in plane force during processing have been measured. The evaluation of the data is detailed in section 5.1.2.

### 4.3.2 Temperature Measurements

The temperature measurements during processing have been conducted using 0.6 mm ⌀ - k type thermocouples from Thermocoax, incorporating a sealed shell tip to enhance the response time [222]. The thermocouples have been connected to a signal acquisition system (National Instruments - NI cDAQ-9172), consisting of a charge amplifier, an A/D converter and a data acquisition component. This system is capable of sampling 32 channels with a maximum frequency of 333 Hz. The output data has subsequently been evaluated using National Instruments' "LabView" control engineering environment. In order to position the thermocouples at a defined place, 1 mm ⌀ holes have been drilled at predefined

locations on the sample sheet. As the creation of a steady state heat flow condition during processing has been one aim of the process setup, two locations for the thermocouples have been chosen to verify a homogeneous temperature distribution through the sample sheet. The first set has been placed in the middle and the second at the end of the sample sheet.

The holes have been drilled at 10 mm, 15 mm and 20 mm to either side orthogonal to the anticipated center of the process zone as shown in Fig. 4.5. After filling up the holes with conductivity enhancing silver paste, the thermocouples have been put into place and additionally fixed with adhesive tape.

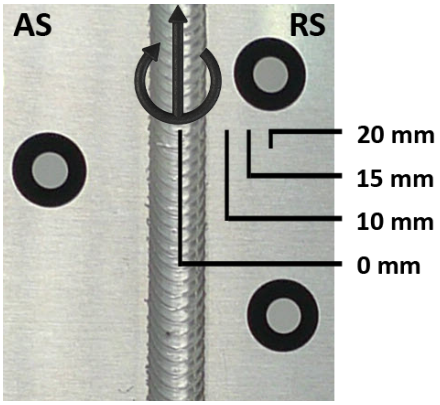


Figure 4.5: Position of the thermocouples on the sample sheet.

Due to the inherent elasticity of the machine, the actual process line, created by processing, is slightly misplaced towards the advancing side. As this disparity would lead to false input data for the thermal model, the correct thermocouple positions have been measured *post mortem* by preparing cross sections at the precise positions of the thermocouple holes and subsequently measuring the distance between the center of the process zone and the center of each drilled hole.

## 4.4 Mechanical Testing

The following sections will give an overview over the mechanical tests and analytical methods which have been employed in the present study. These include local and global mechanical testing such as nanoindentation, micro and macro flat tensile as well as formability tests.

### 4.4.1 Nanoindentation Tests

Nanoindentation tests have been conducted in order to obtain local mechanical properties of the base material and processed specimen. The tests have been performed on a Nanoindenter XP by Agilent offering a displacement resolution of 0.2 nm and a load resolution of 10 nN in accordance to DIN EN ISO 14577 [223]. A Berkovich indenter tip, which is a three faced pyramid with an opening angle of 65.3° from the center axis of the pyramid to

the center of one of the flats, has been used [224]. Even though the system is inherently load controlled, a displacement control method has been used to ensure a constant strain rate of 0.005 1/s during indentation.

All tests have been conduced on polished cross-sections of single line specimens. In order to investigate all metallurgical zones, indents have been evenly distributed at up to 200 positions across the entire process zone. At each position up to five indents have been placed, yielding an area of 5 x 200 indents per specimen. The vertical distance between each indent has been set to 50 $\mu$m and the horizontal distance between each position to 100 $\mu$m.

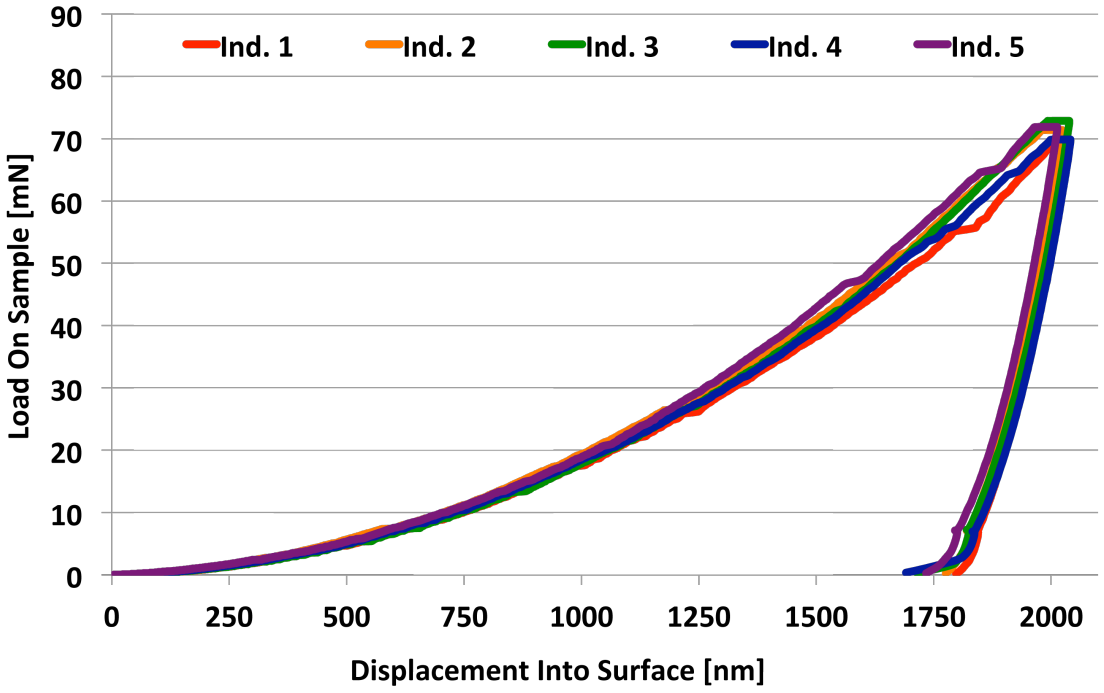


Figure 4.6: Typical loading and unloading curves of nanoindentation experiments.

Fig. 4.6 shows the typical loading and unloading curve for one set of five indents. For each curve, the surface contact point has been manually adjusted. For the evaluation of the data, hardness and modulus have been determined according to the Oliver & Pharr method [225] from the unloading curve as well as from continuous stiffness measurements during loading between 500 nm and 1500 nm of displacement into the specimen surface.

For the continuous stiffness measurement method, a small oscillation of 4 nm is superimposed on the indenter tip. From the resulting small unloading segments, the modulus, E

and the hardness, H have been derived. The hardness has been calculated as

$$H = \frac{P_{Spec}}{A_C(h)} \tag{4.1}$$

in which $P_{Spec}$ is the load on the specimen and $A_C(h)$ the projected contact area as a function of the displacement into surface. The modulus has been calculated as

$$E = \frac{\sqrt{\pi} S_C}{2\sqrt{A_C(h)}} \tag{4.2}$$

in which S is the contact stiffness. In addition to the Mg inherent ability to accommodate external stresses by twinning, the final results can also be affected by material pile-up or sink-in during indentation, yielding a larger, or respectively, smaller contact area than calculated from the tip area function. Hence, for selected specimens, three indents of each five indent row were imaged using SEM and the projected contact area ($A_{corr}$) has been measured manually. In order to calculate the corrected modulus $E_{corr}$ and hardness $H_{corr}$, the results were used to replace the area calculated from the indenter tip area function as a function of indentation depth using Eq. 4.3 and 4.4. The final results are presented in section 5.3.1.

$$E_{corr} = E\frac{\sqrt{A_C(h)}}{\sqrt{A_{Corr}}} \tag{4.3}$$

$$H_{corr} = H\frac{A_C(h)}{A_{Corr}} \tag{4.4}$$

### 4.4.2 Micro Flat Tensile Tests

Micro flat tensile tests have been conducted in order to determine the local mechanical properties of the stir zone. For each condition, five specimens have been extracted using electrical discharge machining (EDM). The specimens have been extracted at medium height from the center of the stir zone into processing direction to incorporated one texture and microstructure exclusively. A schematic of the extraction position is shown in Fig. 4.7. This

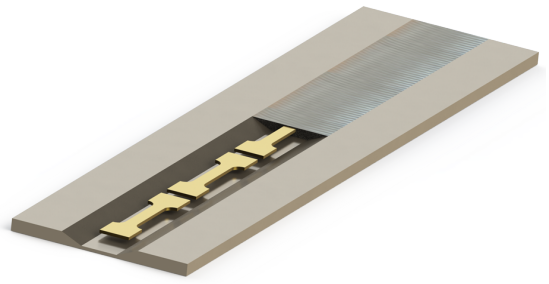

Figure 4.7: Schematic of the extraction position of the micro flat tensile specimen from the stir zone of single line samples.

approach has been chosen as previous investigations conducted by Suhuddin et al. [169] revealed a textural progression through the thickness of FSP samples.

As there is no particular standard describing the dimensioning of micro flat tensile specimens, the DIN EN 2002 001:2006 11 [226] and DIN EN ISO 6892 1:2009 12 [227] standards, which describe the dimensioning and testing conditions for macroscopic specimens, have been used as a basis for the dimensioning of the specimens used in the present study. The detailed drawings are shown in Fig. 8.4 in the appendix. All tests have been conducted on a Zwick Roell testing machine with a 2.5 kN load cell at a constant crosshead speed of 0.2 mm/min while using a Fiedler strain gauge. In order to correct for potential surface effects affecting the tensile results, the roughness of the micro flat tensile specimens has been measured using a Mitutoyo SJ 201 roughness measuring system in accordance to the DIN EN ISO 4288:1998 04 [228] standard. Using the roughness information, the effective load bearing cross section has been calculated using equation 4.5 in which $A_{eff}$ is the effective area, S the thickness of the specimens, W the width of the specimens and $R_z$ the average roughness depth [229].

$$A_{eff} = (S - 2R_z) \cdot (W - 2R_z) \tag{4.5}$$

### 4.4.3 Tensile Tests

In order to obtain standardized information about the mechanical properties of the base material, tensile tests in accordance with the DIN EN ISO 6892-1:2009-12 [227] standard have been conducted. For each rolling direction, five specimens have been tested, all tests have been carried out on a Zwick/Roell BZ1 tensile machine incorporating a 100 kN load cell and using a MTS 634.25F-24 strain gauge ($l_0 = 50$ mm). The maximum tensile traverse speed has been calculated using equations 4.6 and 4.7 with a value of 44 GPa for the elastic modulus [210] and a gauge length of $l_0$=50 mm. The dimensions of the specimens can be found in Fig. 8.3 in the appendix.

$$\dot{\sigma} \sim 10 \frac{N}{mm^2 \cdot s} \quad using \quad \dot{\epsilon} = \frac{\dot{\sigma}}{E} = \frac{10MPa}{44GPa} \tag{4.6}$$

$$with$$

$$\epsilon = \frac{l - l_0}{l_0} \quad gives \quad \dot{\epsilon} = \frac{v}{l_0} \quad yields \quad v_{max} = \frac{l_0 \cdot \dot{\sigma}}{E} = 0,68 \ \frac{mm}{min} \tag{4.7}$$

### 4.4.4 Formability Tests

The forming of sheet material into a predefined shape is extensively used in many different industrial branches [230] and extensive analytical, mathematical and numerical investigations have previously been conducted in this field [231–234]. All of which deal with the problem of predicting the forming capabilities of a given material in a given condition before fracture occurs. In the present study, information about the formability of the processed material has been gained by the widely used approach of creating forming limit diagrams (FLD) [235]. Developed by Keller et al. forming limit diagrams show in a minor - major strain diagram the materials ability for plastic deformation before local necking occurs.

#### Forming Limit Diagrams & Forming Limit Curves

The forming limit diagram illustrates the deformation state of a defined area on a specimen to a certain point throughout the test, represented by its major strain $\varphi_1$ and minor strain $\varphi_2$. The obtained information is transformed to calculate a forming limit curve (FLC), which is displayed in the forming limit diagram. This curve represents the boundary until which point a given material can be deformed before fracture occurs.

In the past, several methods such as the use of circular patterns on the specimen surface which will change to an ellipsis upon deformation [236], as well as numerical methods [237], have been used to obtain a forming limit diagram. Today, experimental investigations are usually conducted using a digital image correlation system. A detailed description of the digital image correlation system employed in the present study will be given in section 4.5.1 and can also be found in [238].

As shown in Fig. 4.8, a complete forming limit diagram consists of multiple measurements in different strain regions ranging from deep drawing to stretch forming and hereby reflecting the range of possible strains in real components. In order to construct a complete forming limit diagram, different testing methods with varying specimen geometries are needed. The specimen geometry for the present study has been chosen in accordance to the setup introduced by Hasek et al. [239–242]. A schematic of the different geometries is presented in Fig. 4.9(a) in which geometry I represents a deep drawing stress state while geometry VII represents stretch forming, respectively. All tests have been carried out concurrent to the test method introduced by Nakajima et al. [243] in which a hemispherical punch is used to deform flat specimen and in accordance with the sheet metal

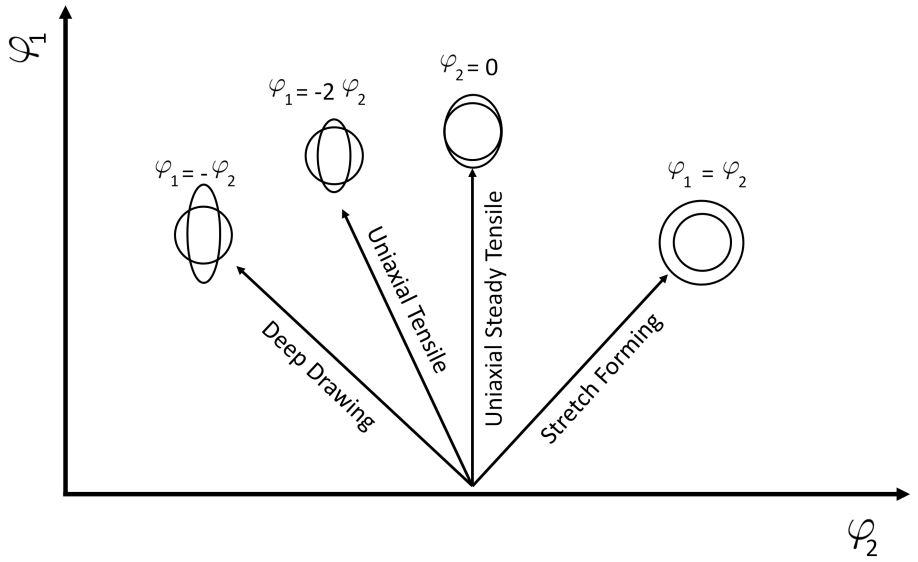


Figure 4.8: Different strain conditions for the construction of a forming limit diagram.

forming standards ISO 12004 [244,245]. Due to geometric constraints, the geometry of the Hasek specimens have been scaled by 1/2 resulting in a diameter of 100 mm with cutouts scaled respectively. The final dimensions of the specimens are detailed in Fig. 8.5 in the appendix.

For each geometry, three specimens have been cut from multi line samples in such ways that the cutouts point into processing direction (Fig. 4.9(b)), and machined to a thickness of 1 mm from both top and bottom. All tests have been conducted on an Erichsen hydraulically driven testing machine with a stainless steel punch sporting a ∅ 50 mm dome. Machine parameters have been set to 200 kN clamping force and 60 mm/min punch speed. The

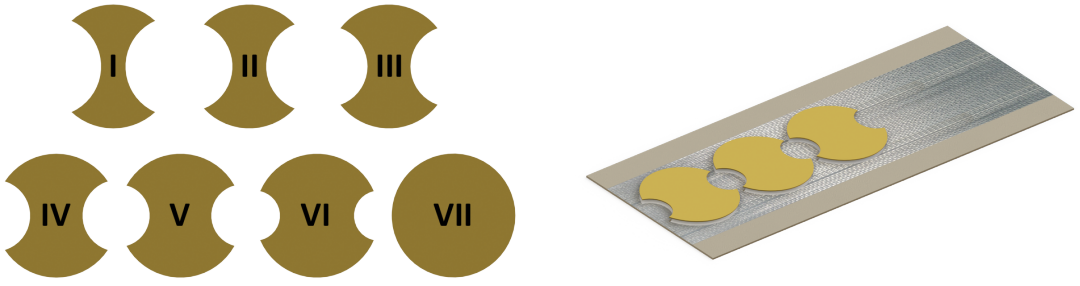


(a) (b)

Figure 4.9: Schematic of the sheet forming specimens (a) and their extraction position on multi line processed samples (b).

tribological system, which is necessary to minimize friction between specimens and punch, has been investigated beforehand on test specimens. Best results have been achieved using oil in combination with poly-ethylene foil of 0,05 mm thickness and a diameter of ∅ 33 mm.

While generally, the location of the resulting forming limit curve is strongly dependent on properties like sheet thickness, data acquisition, deformation history, friction etc. the comparison between different forming limit curves acquired under the same conditions is generally accepted [246–248].

## 4.5 Optical Analysis and Microscopy

### 4.5.1 Optical Strain Analysis

In order to obtain information about the local strain evolution during sheet forming tests, *in situ* digital image correlation analyses have been conducted. A commercially available digital image correlation system (GOM GmbH) has been used and the basic setup for sheet forming tests can be seen in Fig. 4.10(a).

The system uses two digital cameras, with a focal length of 63 mm - 66 mm, to continuously capture images during testing. In order to establish a geometrically defined condition, the cameras are positioned at a defined angle and distance to each other as well as to the specimen. The system divides the acquired images into sections (facets) and tracks them on the specimen surface as the deformation occurs. The system relies on the hypothesis, that the distribution of a gray scale value in one confined location (facet) does not change significantly from one frame to the next. Thus each facet in a deformed specimen e.g. after testing, can be matched to its counterpart in the undeformed state. In order for the system to be able to find the facets and trace them throughout the displacement, a contrast intensive pattern needs to be applied on the specimen surface [249]. In the case of sheet forming specimen, it is a stochastic gray scale pattern which is sprayed on the specimen by creating a white bottom and a black top layer. This way, the digital image correlation system can localize the facets and match their location between the deformed and undeformed state.

The testing itself is divided into the following subsequent steps: First, the digital image correlation system needs to be calibrated, positioned and equipped with sufficient lighting. Consequently, the specimen sporting the stochastic pattern is positioned in the testing

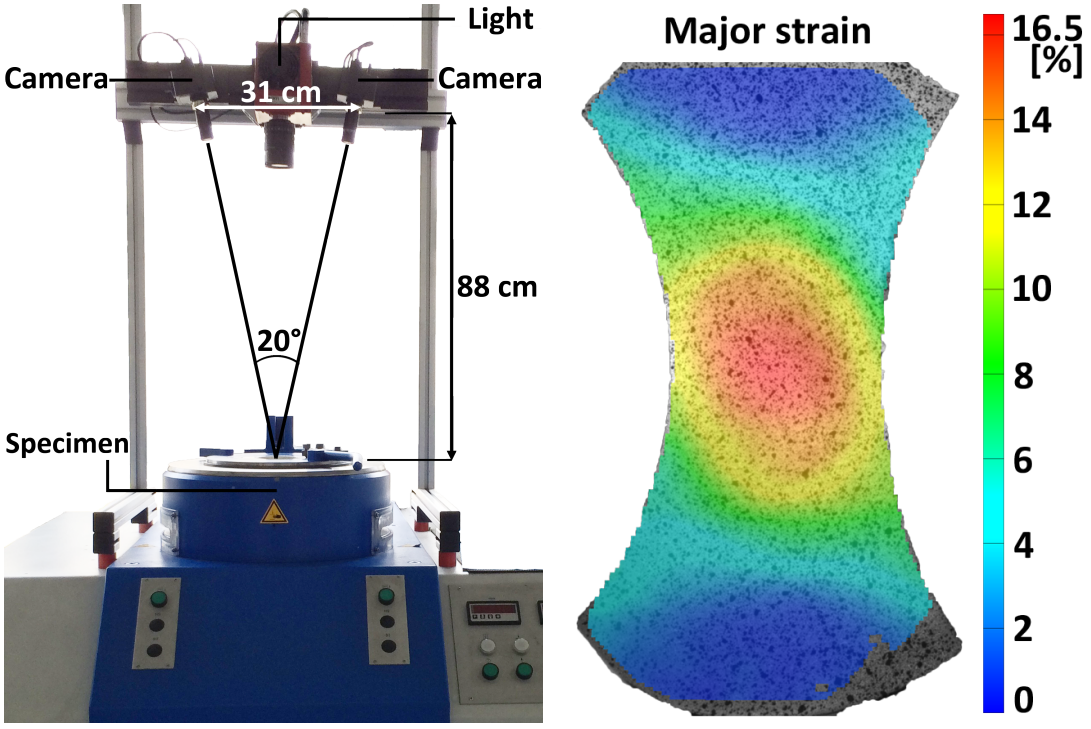


(a) (b)

Figure 4.10: Setup of the digital image correlation system for the sheet forming tests (a) and local strain overlay of a sheet forming specimen (b).

machine and a reference picture of the undeformed specimen is taken. During the course of the test, pictures are taken in a frequency that suffices the need for desired time resolution. As the position for each facets is known at all times, the spacial coordinates of these squared elements can be re-calculated to the reference picture. From the movement of the spacial coordinates on the surface of the specimen, the local strains can be calculated, giving an insight into the local strain distribution within the specimen. An example of a strain overlay in a sheet forming specimen is given in Fig. 4.10(b).

### 4.5.2 Microscopy

Within the present study, two different resolution levels of microstructure investigation have been conducted. The character of a process zone including the overall morphology, grain shape and size, as well as potential discontinuities have been investigated using optical microscopy (OM). In-depth investigations of the texture have been conducted using electron backscatter diffraction (EBSD) techniques. The various specimen preparation routes required for the different analytical techniques will be discussed below.

### Optical Microscopy

For optical microscopy, the specimens have been cut and embedded in the cold curing resign Demotec 30. Consequently the specimens have been ground using SiC paper of grit sizes between 1200 to 4000 on a Struers TegraPol31 automatic polishing machine with individual specimen holders. Final chemical polishing has been conducted using Struers - OPS solution with ethanol to avoid premature oxidation. Diluted picric acid has been utilized to further reveal the microstructure by submerging and etching the specimens for 30 s. Finally, the specimens have been cleaned with ethanol and dried under a hot air blower. All optical microscopy analysis have been conduced on a Leica DM IRM.

### Scanning Electron Microscopy / Electron Backscatter Diffraction

Due to the required electrical conductivity of the specimens, the preparation for scanning electron microscopy (SEM) and EBSD analysis has been conducted without an embedding resin. Instead, the specimens have been ground and polished inside an conductive holder. While the primary grinding steps are the same as for the optical microscopy preparation, the etching step has been replaced by electro polishing with a heavily diluted picric acid solution. If needed, the specimens have been detached from the holder and mounted on a SEM stub using conductive silver paste.

EBSD analyses have been conducted on a dual beam FEI Nova Nanolab 200 SEM equipped with a field emission gun. An EDAX TSL PEGASUS system sporting a Hikari camera has been used with acceleration voltages in the range between 15 kV and 20 kV, a working distance of 10 mm and a current of 2.2 nA. Orientation mapping using automatic beam scanning has been carried out with a step size of 0.5 - 2 $\mu$m. The obtained results have been analyzed using the TSL OIM Analysis V6 software. The average confident index for all investigated specimens has been within the order of $\approx 0.8$ as comparison measurements performed by EDAX Inc. [250] showed a 95% probability of correctly indexed patterns at confident index $> 0.1$. Grains comprising of $\leq$ three pixels have been removed from the acquired maps using the TSL software inherent grain-dilatation method to ensure the highest reliability of the obtained microstructural pictures. Perturbing boundaries, which are often caused by orientation noise have been removed by a 2° lower limit boundary disorientation cut off. Low angle boundaries have been separated from high angle boundaries by using a 15° criterion. Grain size measurements have been performed using the software inherent line intercept method.

## 4.6 Numerical Thermal Model

In thermo-mechanical processes, the imposed thermal cycle represents an important tool for liking the processing parameters to the resulting microstructure and texture and ultimately the mechanical properties. As the temperature inside of the process zone can not by measured directly using thermocouples, a numerical thermal model has been adapted in order to predict three temperature dependent properties, namely the location and magnitude of the maximum temperature as well as the dwell time. While the location gives insight as to where to expect a formability enhancing microstructure, the maximum temperatures are used to predict the potential for recrystallization within the respective areas. The dwell time on the other hand allows for a prediction of the recrystallization and/or annealing processes which might have taken place during high speed FSP.

The model chosen for this work is based on a thermal-pseudo-mechanical heat source model first described by Schmidt et al. [251]. The temperature evolution is predicted by using the energy input based on the temperature dependent flow stress of the material. The flow stress data is derived from yield stress data compiled by Baker et al. [213] according to equation 4.8 in which $\tau$ is the shear yield stress and $\sigma_y$ the tensile yield stress.

$$\tau = \frac{\sigma_y \ (T[^\circ C] + 273,3)}{\sqrt{3}} \tag{4.8}$$

To ensure that the predicted values mirror the actual thermal state during processing, the model has been calibrated using thermo-couple measurement data as detailed in section 4.3.2. The calibration of the model has been conducted in the following steps:

First, the distance between the drilled thermo-couple holes and the center of the stir zone has been measured in cross-sections cut from the processed samples. Next the thermal data at the given points has been aligned programmatically with the predicted thermal data. Finally the thermal model has been adapted to the newly acquired reference points.

The model itself has been implemented in Comsol Multiphysics and represents the 3D geometry of the experiment featuring the sample sheet, the tool and the backing bar as shown in Fig. 4.11(a). Herein the backing bar is made out of standard construction steel, the sample sheet of Mg and the tool out of hot working steel.

The model is meshed with $\approx$ 110000 quadratic tetrahedral elements as seen in Fig. 4.11(b). The mesh density is highest in the vicinity of the tool to sample sheet interface where heat is generated. Different processing speeds are implemented into the model by changing the

material feed velocity from the input to the output side of the sample sheet domain. An example of the predicted thermal trail behind the tool is shown in Fig. 4.11(c).

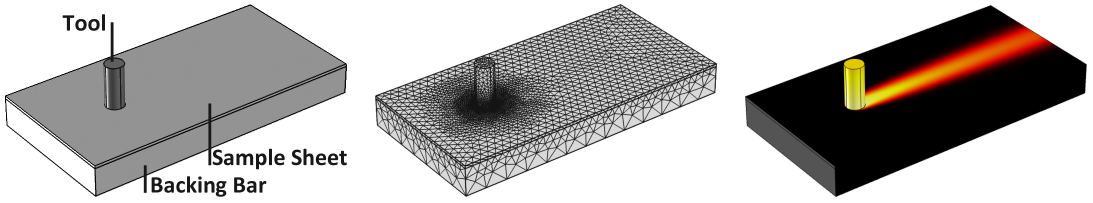


(a) (b) (c)

Figure 4.11: Sections of the modeled domains (a), the mesh for the utilized model (b) and an example of the thermal prediction (c).

The heat generation at the interface between the tool surface and the sample sheet material is determined according to the thermal-pseudo-mechanical heat source equation 4.9 ( [251]).

$$q = \omega \cdot \tau(T) \cdot r \tag{4.9}$$

Herein $q$ is the surface energy source, $\omega = 2 \cdot \pi \cdot n$ is the angular velocity of the tool and $r$ is the distance of a surface element to the axis of rotation. Heat generation created by the probe is not considered as it accounts for only a negligible part of the total heat generation. The governing equation of the model is the heat transfer equation 4.10

$$\nabla(-k\nabla T) = Q - \rho c_p \mathbf{u} \nabla T \tag{4.10}$$

with the boundary conditions including convective cooling to the tool, the backing and the surrounding air changes to equation 4.11.

$$-\mathbf{n}(-k\nabla T + \rho c_p \mathbf{u} T) = q + h(T_{inf} - T) \tag{4.11}$$

Herein $\mathbf{n}$ is the surface normal vector, $k$ is the thermal conductivity (156 [W/mK]), $T$ is the temperature, $Q$ is the total heat input, $\rho$ is the density, $c_p$ is the specific heat capacity, $u$ is the convection term in the heat transfer equation, $h$ is heat transfer coefficient to the tool (1500 [W/m$^2$K]) , backing (1500 [W/m$^2$K]) or air (10 [W/m$^2$K]), respectively, $q$ is the prescribed inward surface heat flux and $T_{inf}$ is the external temperature.

The convective energy transport term $\mathbf{u}$ in equation 4.10 is constructed as a superposition of the processing speed which is implemented in the sample sheet, the rotation of the tool which is implemented in the tool, and the analytical shear layer velocity within the region

of the shear layer in the sample sheet and under the tool. Within the sample sheet / shear layer region, $\mathbf{u}$ is constructed of the tangential velocity $\mathbf{u}_x = V_p - y/r \cdot v_{tan}(r)$ and $\mathbf{u}_y = x/r \cdot v_{tan}(r)$. In the tool $\mathbf{u}$ it is constructed of $\mathbf{u}_x = -\omega x$ and $\mathbf{u}_y = \omega y$.
Due to the extrusion of hot material around the tool as it is moving through the sample sheet, energy is not only transported by conduction but also by convection. In order to model the asymmetric temperature field common in FSP, the convective part needs to be taken into account as well. Therefore an analytical shear layer expression, previously introduced by Hilgert et at. [252, 253], has been adapted to the present geometry and used to prescribe the convective energy transport around the tool as detailed in the set of equations 4.12.

$$\begin{aligned} dz &= t_{sample\ sheet}/2 - z \\ \zeta &= dz/t_{sample\ sheet} \\ r_0 &= r_{probe} - dz \cdot tan(\alpha_p) \\ dr &= r - r_0 \\ r^* &= (1 - \zeta^{m_{shape}}) \cdot (r_{shoulder} - r_0) + r_0 \\ r_{fade} &= max((r - r^*), 0) \\ \rho &= max(dr/r^*, 0) \\ v_{tan} &= max(\omega \cdot r \cdot (1 - (\zeta^{m_z} \cdot \rho^{m_r}) - (r_{fade}/r_{sl})^{m_{fade}}), 0) \end{aligned} \tag{4.12}$$

Herein $dz$ is the normal distance from the tool shoulder surface, $t_{sample\ sheet}$ the sample sheet thickness and $z$ the z-coordinate (into tool axis). $\zeta$ is the normalized $dz$ and $\rho$ the normalized $dr$. $r_0$ is the corrected probe radius which is a function of the cylindrical part $r_{probe}$ and the tapered cone with the angle $\alpha_p$. $dr$ is the distance from the probe surface and $r$ the radius from the center of the rotational axis. $r^*$ is the shear layer outer boundary radius and $m_{shape}$ is the shear layer shape control variable. $r_{fade}$, $m_z$, $m_r$ and $r_{sl}$ are shape parameters calibrated from macrographs.
In addition to the prediction of the thermal field, the model has also been used to predict the energy input during processing. The energy input per unit length has been calculated by integrating the total heat generation over the interface area between the tool and the sample sheet and putting this value into perspective to the processing speed. In the following, the energy input per unit length is used to describe the correlation between processing parameters and the thermal energy introduced during processing.

## 4.7 Base Material

FSP has been performed on commercial Mg AZ31B - O sheet material obtained from Salzgitter Magnesium - Technologie GmbH. The O temper includes an annealing step at 345°C in order to homogenize the microstructure after rolling [213]. An overview over the literature values of the physical and processing properties is given in Tab. 4.1.

Table 4.1: Physical and processing properties of Mg AZ31B - O at ambient temperatures if not declared otherwise [213].

| **Physical** | **Processing** |
|---|---|
| Density: 1.78 g/cm$^3$ | Recrystallization Temperature (1h): 205°C |
| Liquidus Temperature: 632°C | Annealing Temperature: 345°C |
| Solidus Temperature: 566°C | Hot - Working Temperature: 230 - 425°C |
| Thermal Conductivity: 76.9 W/mK | |

The as-delivered sheets had dimensions of 2 mm x 1500 mm x 500 mm. Depending on rolling direction the samples have been cut into the following dimensions: rolling direction: 2 mm x 500 mm x 200; transverse direction: 2 mm x 400 mm x 200; 45° to rolling direction: 2 mm x 350 mm x 200. The chemical analysis showed a composition of 2.9wt.% Al, 0.74wt.% Zn, 0.29wt.% Mn with minor impurities of Si, Ni and Cu which is well within the composition limits for AZ31 [254].

#### Microstructure and Texture

A composition of the various textural features of the base material is presented in Fig. 4.12. The $\{0001\}$ and $\{10\bar{1}0\}$ pole figures (PF) (Fig. 4.12(a)) depict the texture distribution within the geometrical constraints of the sheet material.

The stereographic triangle or inverse pole figure (IPF) (Fig. 4.12(c)) depicts the intensity distribution between the $\langle 0001\rangle$, $\langle 10\bar{1}0\rangle$ and $\langle 2\bar{1}\bar{1}0\rangle$ poles. Due to the rolling process, the base material exhibits a distinct $\{0001\}$ basal texture in which the basal planes lie parallel and the $\{10\bar{1}0\}$ prismatic planes orthogonal to the processing direction. The texture intensity is $\approx$ 10 multiple time random (m.rd.) and the average grain size has been measured to be 5.8 $\mu$m.

The grain morphology can be seen in the inverse pole figure map (IPFM) depicted in Fig.

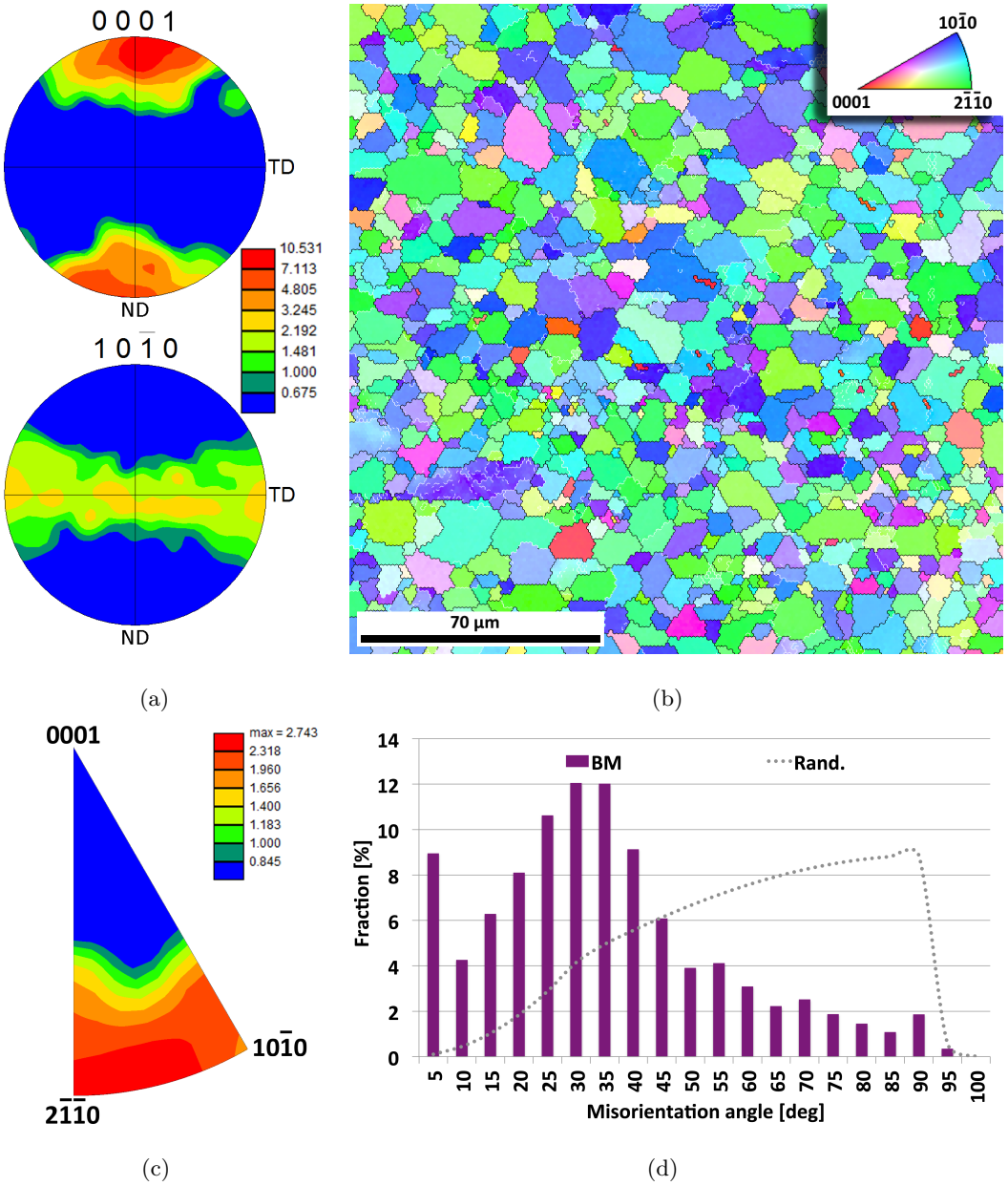


Figure 4.12: {0001} and {10$\bar{1}$0} pole figures (a), inverse pole figure map (b), [001] inverse pole figures (c) and misorientation angle chart (d) of the base material.

4.12(b). Grain boundary calculation of the base material reveals that most of the low angle boundaries are located within larger grains. The misorientation angle ratio (high angle boundary / low angle boundary) has been calculated to be 4.8 (82.9% to 17.1%). It should be noted that almost no twin boundaries have been found as only 0.8% of observed grain boundaries could be correlated to 86.3° {10$\bar{1}$2} ⟨11$\bar{2}$0⟩ extension twins.

The overall misorientation distribution is depicted in Fig. 4.12(d) in which two major

peak fractions can be made out. The low angle boundary peak can be accounted to the deformation effects of rolling which have not been entirely compensated by the subsequent annealing process. The peak buildup around 30° corresponds to an arbitrary rotation of the grains around the *c*-axis ⟨0001⟩ as the HCP crystal structure limits the possible rotations around the *c*-axis axis to 30° (rotations higher than 30° are symmetrically equivalent to rotations of less than 30°) which has previously been described by Beausir et al. [255].

### Mechanical Properties

In order to verify the quality of the provided base material, standard mechanical tests have been conducted including tensile and hardness. While the tensile tests have been conducted using five specimens for each of the three investigated directions (RD = L-T, TD = T-L and 45°), the hardness of the base material showed a constant value of 62 HV0.5 independent of rolling direction and the detailed tensile results are listed in Tab. 4.2.

Table 4.2: Tensile test results of the base material in full scale specimen including standard deviations. Reference values in parentheses [213].

| **Direction** | **$R_m$ [MPa]** | **$R_{p0.2}$ [MPa]** | **A [%]** | **E [GPa]** | **HV0.5** |
|---|---|---|---|---|---|
| RD (L-T) | 268 ± 1 (255) | 131 ± 1 (150) | 18 ± 3 (21) | 46 ± 2 (45) | 62 ± 5 (67) |
| TD (T-L) | 257 ± 7 (270) | 180 ± 4 (170) | 6 ± 1 (19) | 46 ± 1 (45) | 62 ± 5 (67) |
| 45° | 261 ± 1 (-) | 161 ± 1 (-) | 12 ± 1 (-) | 46 ± 1 (-) | 62 ± 5 (-) |

It can be seen that the base material exhibits an inverse correlation between tensile elongation and $R_{p0.2}$. While the rolling direction exhibits the lowest $R_{p0.2}$ of 131 MPa, it exhibits the highest $R_m$ of 268 MPa and a tensile elongation of 18%. On the other hand, the specimens tested in transverse direction exhibits the highest $R_{p0.2}$ of 180 MPa but experiences the lowest $R_m$ of 257 MPa as well as the lowest tensile elongation of 6%. It should be noted that the specimen tested in transverse direction exhibit substacially lower values than what has been reported in the literature. Even though this decrease might be rationalized by the differenced production environments, all samples for the present study have been tested in rolling direction in order to err on the side of caution.

# 5 Results and Discussion

The following section is divided into three main subjects to allow for a logical and comprehensive presentation and discussion of the obtained results. In section 5.1 the developed process parameters, the verification of the creation of a steady state as well as the prediction of the thermal evolution during processing will be presented and discussed. Section 5.2 will give an in-depth description of the present metallurgical and textural features of the processed material and will lay the foundation for the understanding of the macroscopic mechanical properties which will be presented in section 5.3. In detail, the mechanical investigations range from small scale nanoindentation analysis over micro flat tensile to full scale forming limit tests.

## 5.1 Process Parameters and Thermal Investigations

In FSP three basic parameters, tool rotational speed (RPM), axial force (FA) and processing speed (PS), are used to tailor the material properties to fulfill design needs such as strength or ductility. The respective process parameters and their contribution to FSP are listed in Tab. 5.1 while the various directions and rotations of the FSP process are shown in Fig. 5.1.

Table 5.1: Summary of the main process parameters and their contributions.

| **Parameter** | **Contribution / Definition** |
|---|---|
| Rotational speed | Introduces thermal energy into the system and defines the mixing of material. |
| Axial force | Consolidates the process zone. |
| Processing speed | Defines the process speed. |
| Processing direction | Defines the direction of the process. |
| Tool pitch around x axis ($\varphi_x$) | Defines the angle of the tool in respect to the workpiece orthogonal to processing direction. |
| Tool pitch around y axis ($\varphi_y$) | Defines the angle of the tool in respect to the workpiece into processing direction. |
| Process zone | Represents all zones influenced by processing. |

As the necessary thermal energy for the process is introduced via friction, the rotational speed has a significant influence on how much heat is introduced into the system [256]. The higher the rotational speed, the more frictional heat is generated, leading to a temperature increase in the process zone. It should be noted that the heat input through an increase in rotational speed experiences an upper limit once the viscosity of the plasticized material reaches a critical lower limit, reducing the friction between tool and material. Additionally the rotational speed contributes directly to the strain imposed onto the material as rising tool rotational speed increases the amount of strain introduced during processing [179]. Even though the axial force also participates in the generation of heat, as it defines the force with which the shoulder is pressed onto the sheet surface, its main contribution lies in the consolidation of the plasticized material to avoid material discontinuities at the bottom of the process zone [257].

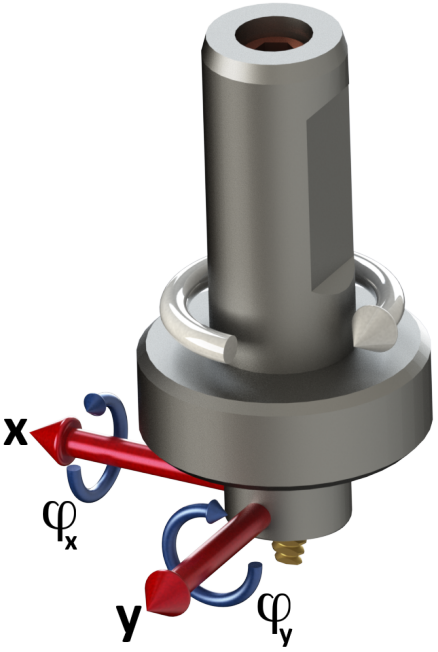


Figure 5.1: Schematic of the FSP tool with all directions and rotations indicated. X indicates the processing direction.

The processing speed, on the other hand, counteracts the heat generation of the rotational speed and axial force. At processing speeds below the thermal conductivity of the base material, the thermal field extends ahead of the tool resulting in the processing of preheated material. With increasing processing speed, the extend of the thermal field ahead of the tool decrease until it reaches no further than the tool itself and thus cold material is continuously fed into the process zone [253]. This results in an overall decrease in processing temperature and can even lead to the expulsion of the tool or to probe fracture. Depending on the intrinsic elasticity of the utilized handling system, the tilt angles $\varphi_y$ (into processing direction) and $\varphi_x$ (orthogonal to processing direction) become essential process parameters for the creation of sound process zones [258].

### 5.1.1 Process Parameter Development

The development of process parameters is scarcely described in the literature. While some authors explicitly use experimental [259] or numerical [260] approaches for a process parameter development, the vast majority of process parameters found in the literature are not described to have been derived with an underlaying preset.

As detailed in section 4.1 the process parameters for the present study, have been developed with the underlying presets of imposing massive deformation onto the material in order to enhance the ease of basal slip by reducing the size of the shear layer at speeds which are of industrial relevance. As industrially relevant processing speeds have not jet been reported in the literature, little comparative process parameters have been available. Thus, preliminary experiments have been conducted in which the processing speeds have been preset according to the following method.

The slowest processing speed (Condition A) has been chosen based on the upper end of what is commonly reported in the literature in order to be able to correlate the obtained results of this study to previous studies. The highest processing speeds (Conditions E and F) have been chosen according to previous experiments conducted internally at HZG [261]. The intermediate values have been chosen following a linear progression from the lowest to the highest processing speeds.

Using the fixed processing speeds, the second preset, imposing massive deformation in order to reduce the shear layer size, has been accounted for by using the following approach. As detailed above, the rotational speed significantly influences the thermal energy introduced into the material which in turn changes the geometry of the shear layer. In order to reduce the shear layer size the thermal input must be kept at a minimum. The tool rotational speed was thus systematically adjusted until sound process zones have been created, ascertaining that a minimum in thermal energy has been introduced into the process.

Finally, the overall soundness of the process zone has been evaluated by macrographical analysis using optical microscopy. If an insufficient bonding has been found within the process zone, the axial force has been adjusted accordingly. Using this methodology, a process windows has been created in which bounds, sound process zones can be obtained while leaving the shear layer size at a minimum. The obtained parameter window is shown in Fig. 5.2. For the final analysis, condition B and D have not been used as the gain in additional knowledge has been superimposed by the results of condition C and E, respectively. The finally chosen processing parameters, including the tilt angles $\varphi_y$ (into

processing direction) and $\varphi_x$ (orthogonal to processing direction) which have been used to account for the handling systems elasticity, are listed in Tab. 5.2.

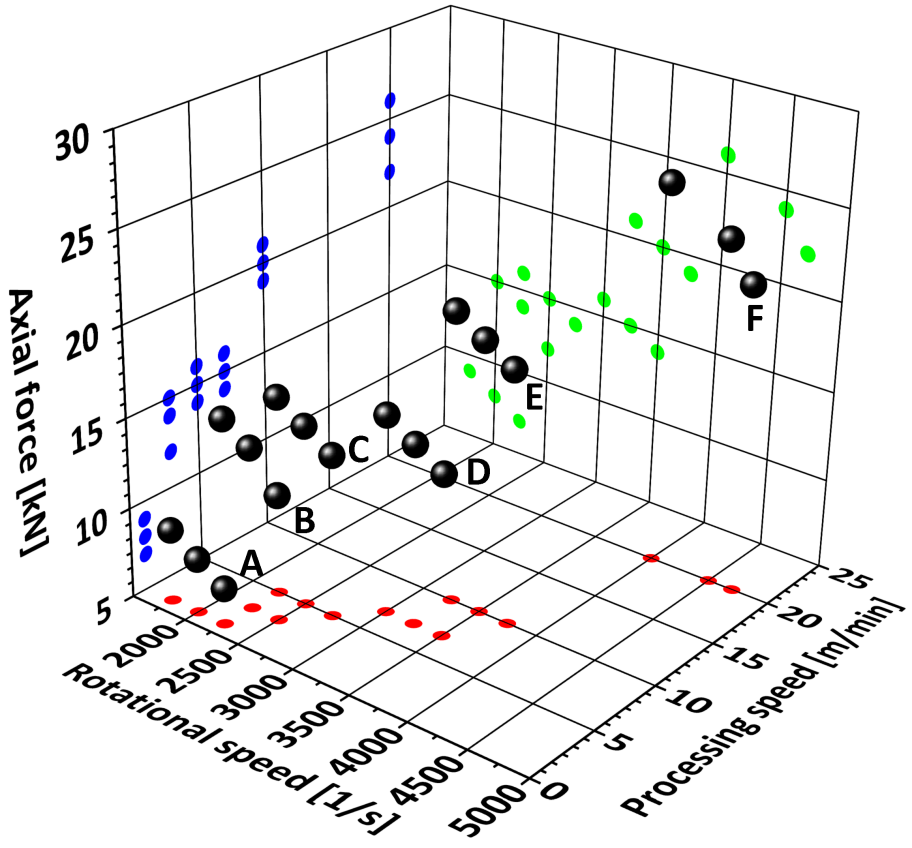


Figure 5.2: Complete parameter window obtained during the preliminary experiments.

Table 5.2: Summary of the final FSP parameters for single line (Cond. A - F), multi line (Cond. C & E) and externally cooled (Cond. E) samples.

| **Condition** | **Processing Speed** | **Axial Force** | **Rotational Speed** | $\varphi_x$ | $\varphi_x$ |
|---|---|---|---|---|---|
| A | 1 [m/min] | 8 [kN] | 2000 [1/min] | 0 [°] | -1 [°] |
| C | 5 [m/min] | 15 [kN] | 2500 [1/min] | 1 [°] | -1 [°] |
| E | 10 [m/min] | 20 [kN] | 3500 [1/min] | 1.5 [°] | -1 [°] |
| F | 20 [m/min] | 24 [kN] | 4500 [1/min] | 1.5 [°] | -1 [°] |

### 5.1.2 Steady State Verification

As detailed in section 4.2.4, an extended setup has been used in order to ensure that a steady state is brought to pass during processing. In order to verify that a steady state is indeed reached, force and tool rotational speed measurements have been conducted. While the tool rotational speeds and the axial forces could be obtained from the force control system itself, the forces into processing direction, which give the most detailed insight into the creation of a steady state, have been measured using the previously introduced independent force measuring platform. The axial forces for condition A, C and E are shown in Fig. 5.3.

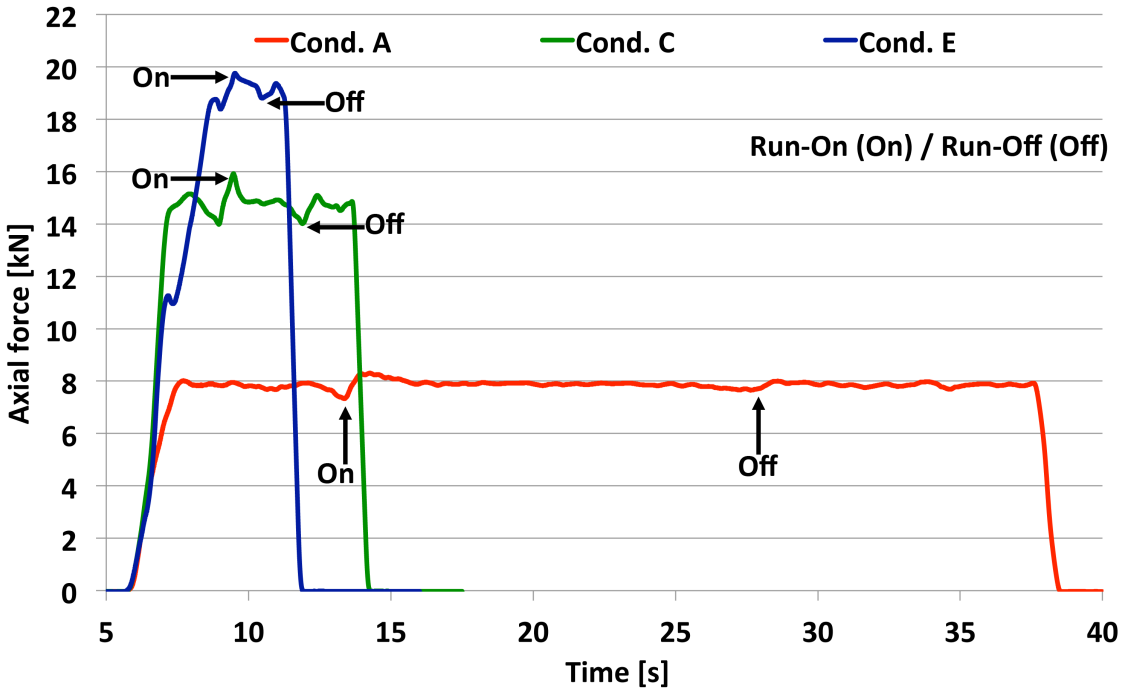


Figure 5.3: Axial forces during processing for conditions A, C and E.

With a sample length of 200 mm, the processing times are 12 s, 2.4 s and 1.2 s for condition A, C and E, respectively and the transition between the run-on sheet (On) and the run-off sheet (Off) is indicated for each curve. In detail it can be seen that while the set value of 8 kN (Cond. A) and 15 kN (Cond. C) have been reached in just under 1,7 s, it takes ≈ 3,6 s to reach the set value of 20 kN for condition E. This translates into ≈ 60 cm of traveled distance, which is less than the 1 m run-on sheet used for condition E.

The evolution of the rotational speeds with the respective transition locations is shown in

Fig. 5.4. In addition to visible run-on and run-off peaks, the plunge, the moment in which the tool is intruding into the material, has been indicated. As the material underneath the tool becomes increasingly plasticized, the rotational speed is briefly decreasing before the preset value is reached once again. Overall, the rotational speed remains constant during processing, which is of particular importance for the creation of a steady state.

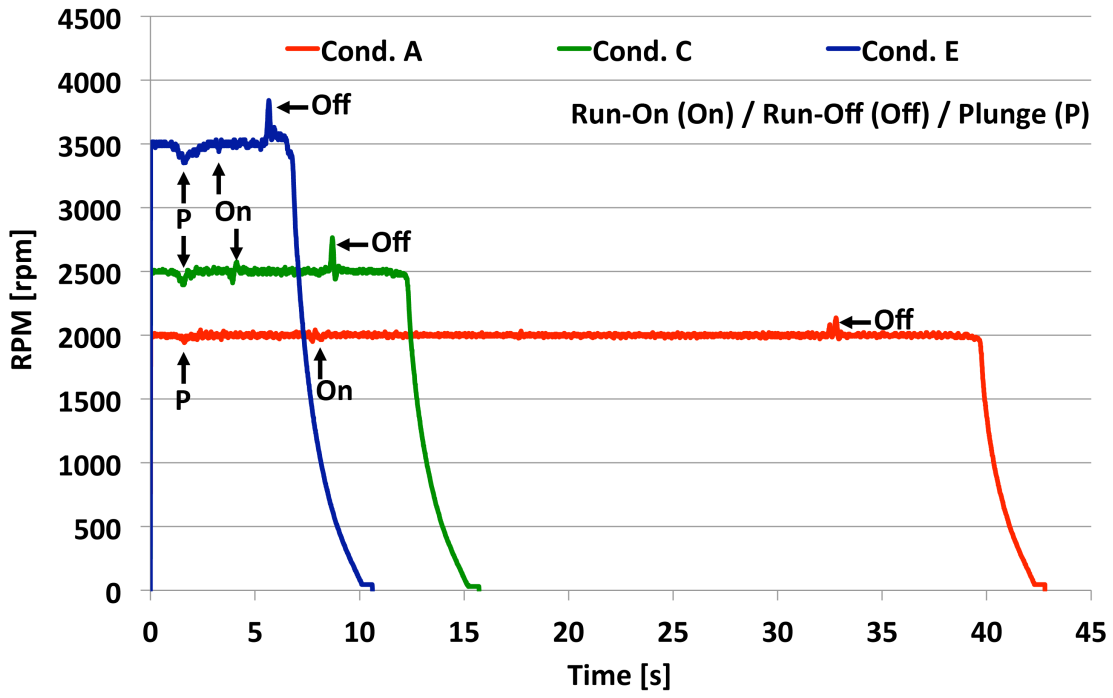


Figure 5.4: Rotational speeds during processing for conditions A, C and E.

The forces into processing direction are detailed in Fig. 5.5. For condition A, a peak at the beginning of the process (denoted Init.) can be seen which is typical for the the initiation of the translational movement. As the plasticized zone is confined to an area underneath the tool, the initiation of the translational movement results in a push of cold material into the process zone, resulting in a rapid increase of the counteracting forces. After the initiation of the process, the counteracting forces decrease to values between 0.2 kN and 0.25 kN and a steady state is reached after the run-on sheet has passed. The location from which the specimen for metallurgical and mechanical investigations have finally been taken from has been chosen to be the second half of the sample as indicated in Fig. 5.5.

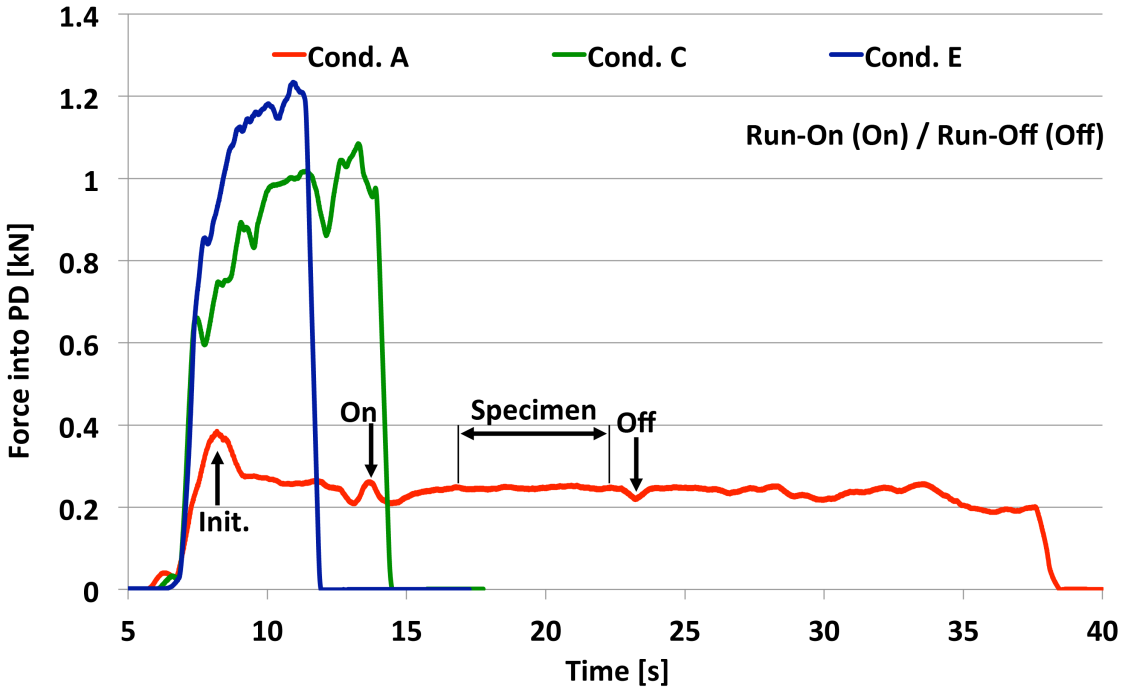


Figure 5.5: Overview over the forces into processing direction during processing for conditions A, C and E.

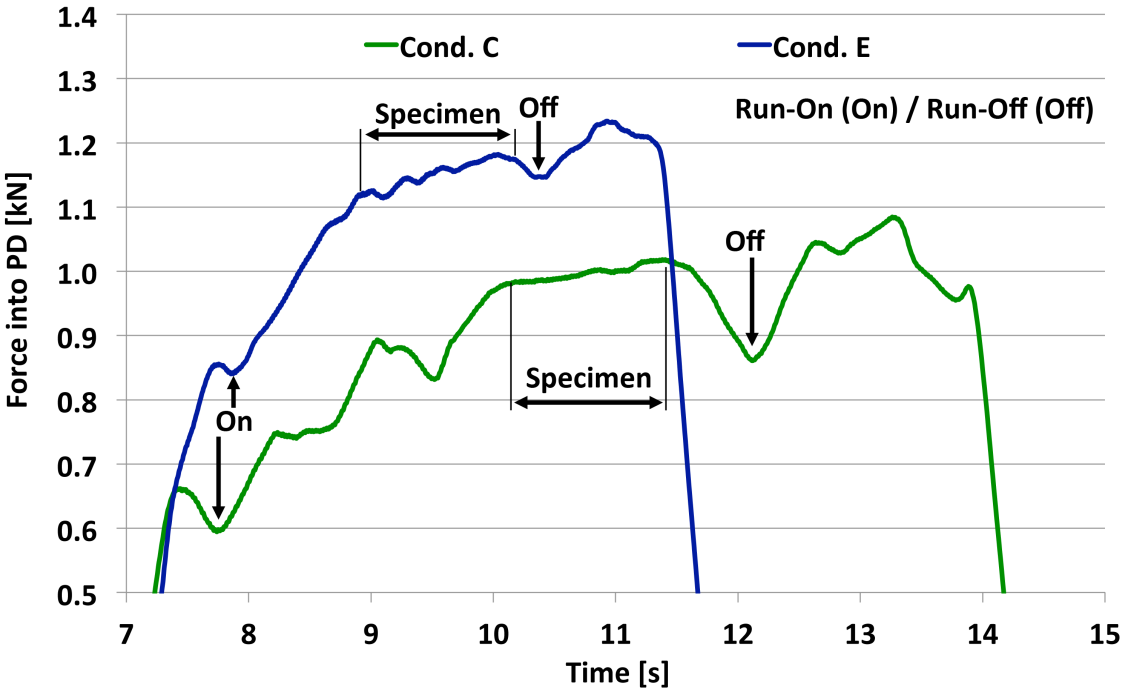


Figure 5.6: Detail of the forces into processing direction during processing for conditions C and E.

For condition C and E, the previously described overshoot at the beginning of the process is replaced by a continuous increase in counteracting forces as shown in detail in Fig. 5.6. This difference in the observed counteracting forces is a result of the way high speed FSP is initiated. Conventionally, the plunging of the tool and the initiation of the translational movement is conducted in two subsequent steps. In high speed FSP on the other hand, these two steps are executed as one, yielding a smoother intrusion of the tool and resulting in a homogeneous buildup in counteracting forces, which in turn is increasing the longevity of the tool.

In both conditions (C and E), the transition between the run-on sheet and the sample is clearly visible as reflected by a sudden drop in counteracting forces due to the gap between the two sheets. Following the run-on, the processing on the sample comes to pass in which a continuous force buildup occurs over a period of 4.2 s and 2.1 s for condition C and E, respectively (sample length: 350 mm). The gradient of this buildup is higher within the first half of the sample, and stabilized within the second half, indicating the appearance of a steady state. Even though the second half of the sample still exhibits a slight increase in counteracting forces (40N for condition C and 60N for condition E), the variation have been deemed acceptable as they represent $\approx 5$ % of the total acting forces.

In conclusion it can be noted that a steady state, yielding reproducible results, is indeed reached in high speed FSP towards the second half of the sample. All specimens for metallurgical and mechanical investigations have thus been taken from that area.

### 5.1.3 Thermal Field Predictions

In thermo-mechanical processes, the thermal cycle which the material has been exposed to, is one of the essential parameters to link the processing parameters to the resulting microstructure, texture and the mechanical properties. Thus, temperature investigations have been undertaken with the aim of predicting the location and the magnitude of the maximum temperatures as well as the dwell time for a given temperature. A thermal field surrounding the tool has been predicted by using the thermal model introduced in section 4.6 which has been calibrated by thermocouple measurements (section 4.3.2).

Typical temperature curves recorded with thermocouples placed 10 mm from the center of the programmed processing pass are presented in Fig. 5.7 in which each condition features two peaks which represent the advancing and retreating side, respectively. The observed difference in maximum temperature between the advancing and retreating side for a given

condition can be correlated to the previously described elasticity of the handling system (section 5.1) which is a result of the FSP inherent asymmetry [154].

Due to the unidirectional rotation of the tool, the handling system is slight displaced towards the advancing side during processing, yielding higher recorded temperatures in that area. As detailed in section 4.6, the accrued displacement has been taken into account when calibrating and applying the thermal model to predict the maximum temperatures as a function of processing condition.

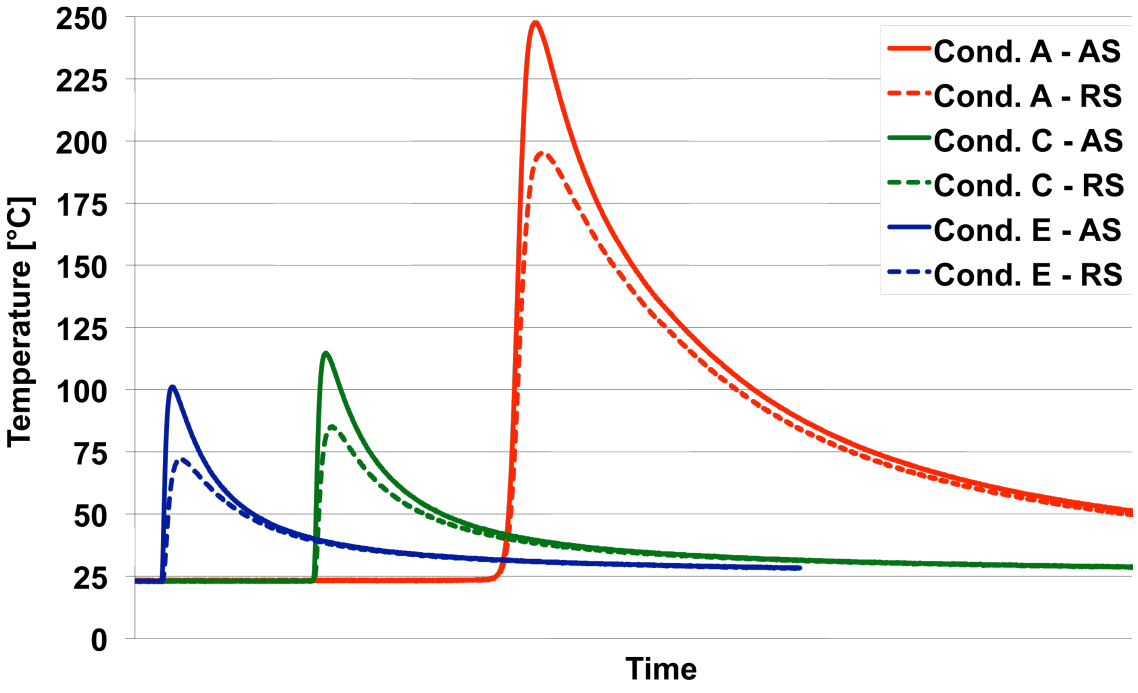


Figure 5.7: Typical temperature curves measured 10 mm from the center of the stir zone.

As shown in Fig. 5.8 the model predicts the maximum temperatures to be located around the probe and shows an overall decrease in maximum temperatures with increasing processing speed. In detail the stir zone reaches a maximum temperature of $\approx 470°C$ in condition A, which is comparable to results obtained by Darras et al. [155]. For condition E on the other hand, the maximum stir zone temperature decreases to $\approx 300°C$. It should be noted that due to a lack of calibration data for condition F, only the maximum temperature (270°C) in the stir zone is displayed.

The above results show, that the maximum stir zone temperatures of condition A to F are high enough for recrystallization processes ($> 205°C$) to take place [262]. This is essential for the understanding of the microstructural and textural evolution which will be

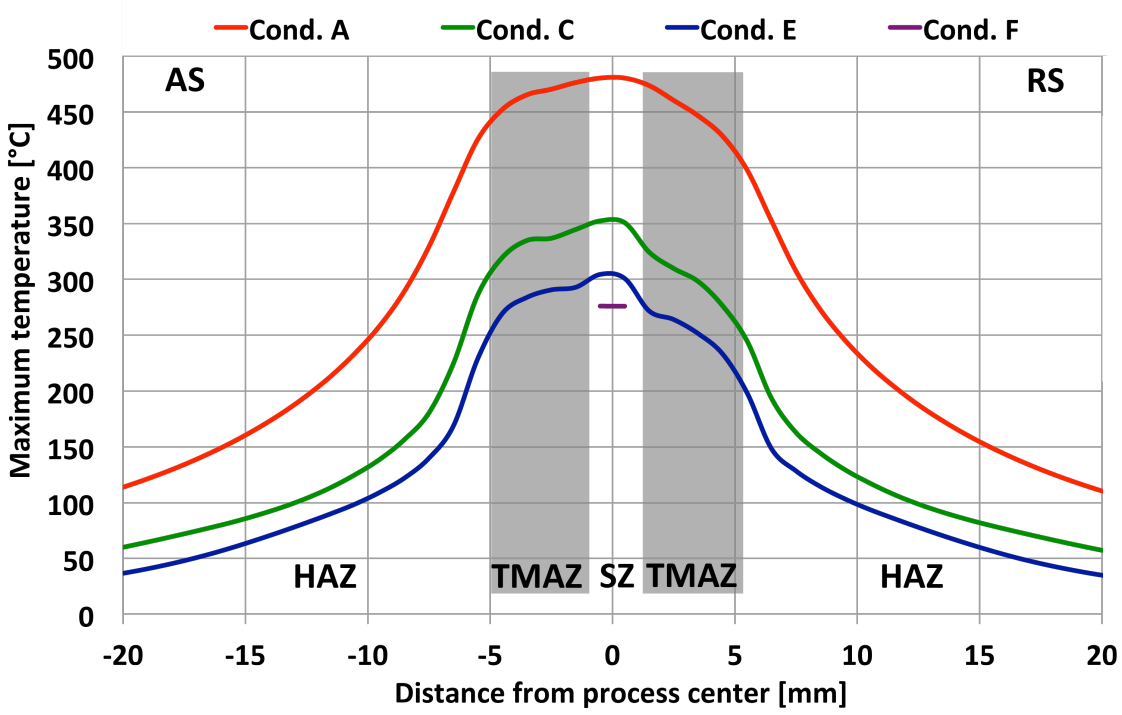


Figure 5.8: Predicted maximum temperatures and temperature distribution to the side of the tool for processing conditions A to F.

discussed in section 5.2. It should be pointed out, that in general, recrystallization is a function of process temperature as well as of the encountered strain and strain rate. Even though it has previously been tried to predict the strain rates occurring during FSW/FSP using analytical and numerical methods [165, 179, 263–266], the direct measurements of torque as well as imposed strains have proven difficult to obtain within the processing speed regime of the present study. The following analysis thus focuses on the effect of the process temperature when regarding the occurring recrystallization phenomena.

In addition to the maximum temperature, the model allows for the comparison of the thermal asymmetry between the advancing and retreating side as a function of processing speed. With rising processing speed the asymmetry in the stir zone increases slightly from 2°C for condition A to 20°C for condition E. This effect is related to the differences in convection and material flow as a function of processing speed. In condition A, the resulting maximum temperature and temperature distribution are strongly affected by the material transport around the tool. In detail, the tool travels 0.5 mm/rot which results in

material being picked up in front of the tool, heated up by friction, transported around the probe and redeposited behind the tool [266], yielding a more homogeneous temperature distribution. In the higher processing speed conditions on the other hand, the magnitude of this redistribution mechanism continuously decreases as the tool travels 2 mm/rot an 2.9 mm/rot for condition C and E, respectively.

For condition A, this low ratio results not only in an increased amount of frictional heat, mirrored by a higher maximum temperature, but also in an increased stirring of the material, leading to a more uniform contribution of thermal conduction and convection, resulting in a homogenization of the temperature in the stir zone. In the high processing speed regime (Cond. C to E), the contribution of the conductive part lessens as linear extrusion phenomena emerge. As the tool represents the only heat source, the relatively low thermal conductivity of Mg (156 W / (m·K)) [267] results in almost no heating of the material in front of the tool, such that cold material is continuously fed into the process zone, leading to further cooling and limited heat flux to the sides which finally yields a slightly inhomogeneous temperature field. This effect can most explicitly been seen when regarding the isothermal distribution for condition A, C and E as shown in Fig. 5.9 and 5.10.

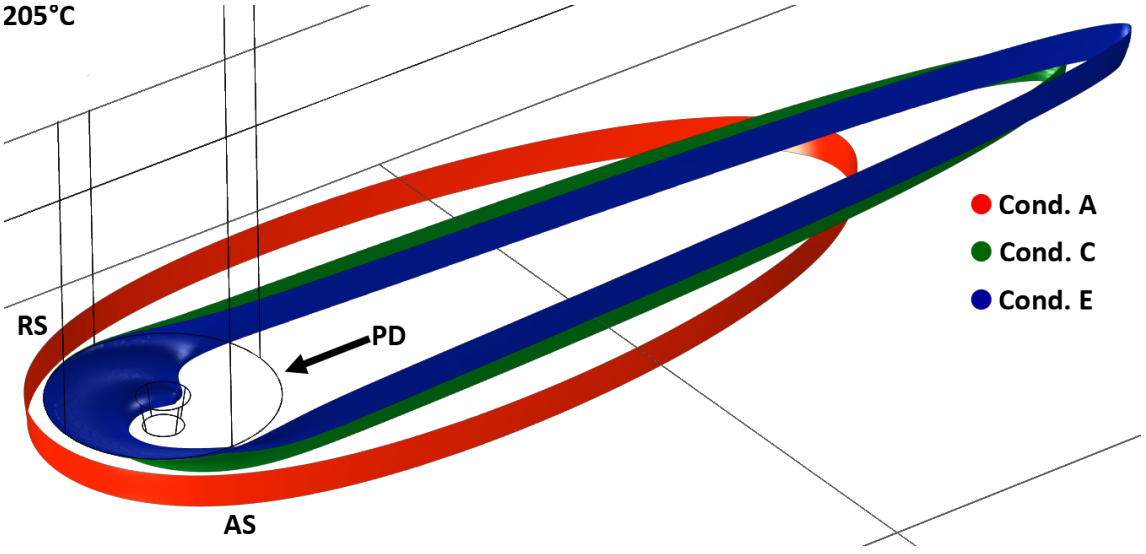


Figure 5.9: Isothermal distribution of conditions A, C and E for 205°C.

As shown in Fig. 5.9, the 205°C isotherms (recrystallization temperature) of all conditions completely surround the tool. In detail, the isotherm of condition A still exceeds the shoulder radius in front as well as to the sides of the tool. The isotherms of condition C

and E on the other hand exhibit a reduction in size and no longer exceed the shoulder radius neither in front nor to the sides of the tool. This trend continues when regarding the isotherms at 320°C as shown in Fig. 5.10. While the isotherm of condition A still completely surrounds the tool, it extends no longer to the front and experiences a reduction in extend to the sides of the tool. This reduction continues for the isotherms of condition C and E.

For condition C, the 320°C isotherm no longer covers the entire shoulder area while it sill extends slightly behind the tool. Finally, the isotherm of condition E experiences a further reduction in size remaining solely beneath the advancing side of the shoulder. As previously described, this effect can be correlated to the continuous feeding of cold material into the process zone. Both isothermal representations of Fig. 5.9 and 5.10 thus illustrate, that the stirring motion of conventional FSP is increasingly superimposed by extrusion phenomena within the investigated processing speed regime. This phenomenon will again be discussed in section 5.2.2 by taking the microstructural and textural results into account.

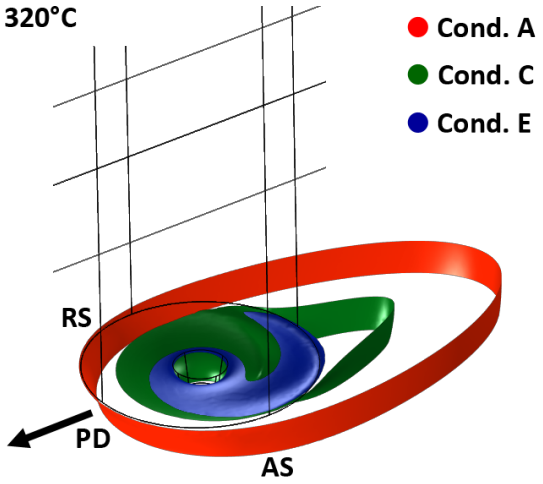


Figure 5.10: Isothermal distribution of conditions A, C and E for 320°C.

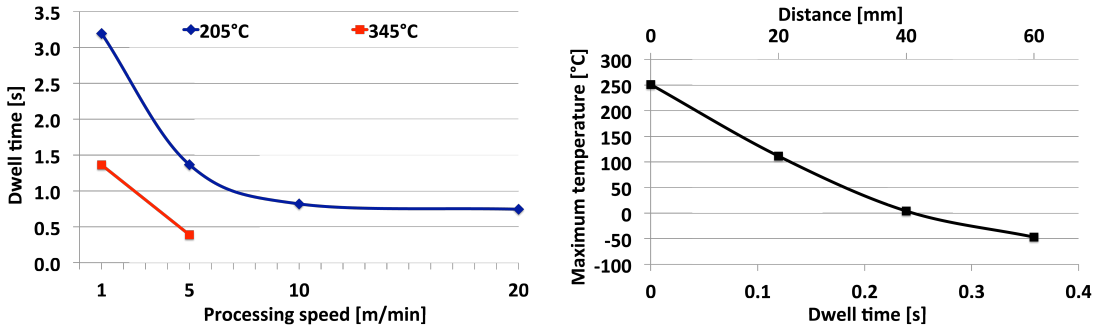


(a) (b)

Figure 5.11: Dwell time for the recrystallization (205°C) and annealing (345°C) temperatures as a function of processing speed (a). Dwell time for externally cooled samples (b).

In order to put the obtained results in relation to the resulting microstructure, the dwell time (the amount of time at which a certain temperature is maintained) of the stir zone has been calculated for the recrystallization and annealing temperature of 205°C and 345°C [262], respectively. The results are shown in Fig. 5.11(a) as a function of processing speed.

Overall, the dwell time within the recrystallization regime of 205°C is brief, reaching a maximum of 3.3 s for condition A (1 m/min) and only 0.8 s and 0.7 s for conditions E and F (10 m/min and 20 m/min), respectively. For the annealing temperature of 345°C on the other hand, the previously described decrease can only be observed for conditions A and C while conditions E and F are processed below the annealing temperature.

These results can directly be correlated to the recrystallization behavior at hand. As previously shown by Suhuddin et al. [169], dynamic recrystallization takes place as the tool passes, and can be regarded as a function of imposed strain, strain rate and temperature [33], which in turn are all functions of the processing parameters.

Dynamic recovery and static recrystallization on the other hand, take place once the tool has passed [27]. As annealing (345°C) as well as recrystallization (205°C) usually need multiple minutes to take place, it can safely be assumed, that both effects have only minute contributions to the resulting microstructure. Thus, dynamic recrystallization, with its thermal and strain component, can be considered to be the primary mechanism driving the microstructural and textural alterations which are detailed in section 5.2.2. For the present study, this result is highly desirable as the microstructural evolution of the process zone can thus be adjusted by selecting processing parameters which can impose the desired microstructural and textural changes without the need of taking extended effects of annealing or static recrystallization processes into account.

In order to fully suppress any residual occurrence of recovery processes, the detailed analysis of the evolving microstructure and texture in high speed FSP has been conducted using an externally cooled environment (section 4.2.4). The dwell time of these tests is shown in Fig. 5.11(b). While temperatures of about 250°C are reached right beneath the tool, it takes only 0,12 s to cool the specimen to about 100°C and another 0,24 s until -50°C is reached, 60 mm after the tool has passed. This ensures that only dynamic recrystallization is responsible for the resulting microstructure and texture. It should be mentioned, that due to the quick assembly necessary to maintain the low temperatures within the processing setup, only touch sensory equipment has been used. The employed sensors recorded

a surface temperature of -20°C directly after the tool has passed supporting the obtained numerical results.

The numerical thermal investigations have shown that the maximum temperature in the stir zone ranges from 450°C to 270°C depending on the chosen processing parameters. With rising processing speed, an increasing thermal asymmetry between the advancing and retreating side of the stir zone has been observed which has been attributed to the differences in convection and material flow as a function of processing speed. Investigations on the isothermal distribution have shown an increasing participation of extrusion phenomena with rising processing speed constituted by a continuous areal reduction of the respective isotherms in front of the tool. While the critical temperature for recrystallization (205°C) has been reached in all samples, the corresponding dwell time is too brief to consider dynamic recovery to be a microstructure influencing parameter. It can thus be concluded that dynamic recrystallization is mainly responsible for the microstructural and textural evolution of the samples.

## 5.2 Microstructure and Texture Investigations

In the following section, the microstructural and textural developments induced by FSP will be presented and discussed. After giving an overview over the various metallurgical zones created by FSP, the results of the single and multi line experiments will be presented and discussed in detail.

### 5.2.1 Externally Cooled Single Line Experiments

In order to identify microstructural zones with a texture suitable for enhanced formability, the process zone of the externally cooled samples (Cond. E see Tab. 5.2) has been thoroughly investigated using EBSD analysis techniques. The externally cooled samples have been chosen for these investigations as they offer a clear view into the microstructure and texture of the process zone, undiluted by potential post weld recrystallization processes. Herein the analysis has been focused on the stir zone and thermo mechanically affected zone, as only these zones undergo mechanical deformation during FSP. The advancing side has been chosen as previous investigations by Park et al. [268] and Woo et al. [40] have shown that while both sides are comparable in microstructure and texture, the different textural zone are more clearly distinguishable in the advancing side. The resulting large area inverse pole figure map can be seen in Fig. 5.12.

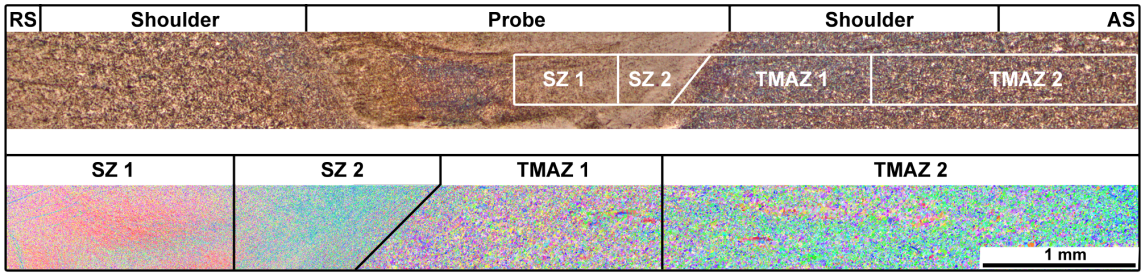


Figure 5.12: Macrograph depicting the area in which the texture evolution has been investigated and the respective inverse pole figure maps from the center of the stir zone to the thermo mechanically affected zone of the advancing side.

This overview stretches from the center of the stir zone (probe region) over the shoulder radius (shoulder region) into a transition region between the thermo mechanically affected and the heat affected zone. Within these different regions, four zones with distinct textural features can be observed, ranging from homogenized equiaxed and recrystallized grains in

the stir zone to deformed, highly twinned and mostly unrecrystallized grains in the thermo mechanically affected zone. Due to the different textures observed within each of the two microstructural zones, the stir zone as well as the thermo mechanically affected zone have additionally been subdivided into two individual zones denoted stir zone 1 and 2 and thermo mechanically affected zone 1 and 2, respectively.

In the following, the microstructural and textural features of the thermo mechanically affected zone as well as the stir zone will be discussed in detail. Additionally, an inverse pole figure map and a misorientation angle (MA) chart, a $\{0001\}$ and $\{10\bar{1}0\}$ pole figure and an inverse pole figure of the respective zones will be given.

#### 5.2.1.1 Thermo Mechanically Affected Zone

The thermo mechanically affected zone is the zone between the highly strained stir zone and the heat affected zone which is only thermally influenced. While the thermo mechanically affected zone is not exposed to the same material stirring by the probe as the stir zone, it does exhibit local material stirring at the top of the process zone induced by the shoulder. Additionally, the shoulder and probe induces compressive loads as well as a thermal cycle. Due to the limited amount of string the introduced strains are lower than in the stir zone, resulting in limited amounts of recrystallization which results in a highly twinned microstructure.

##### Thermo Mechanically Affected Zone 2

In Fig. 5.13 the textural features of the thermo mechanically affected zone 2, which is closest to the heat affected zone but still experiences mechanical loads mostly originating from the shoulder, are presented. The grain shape, which is similar to that of the base material (Fig. 4.12(b)), indicates that no significant recrystallization has taken place as shown in Fig. 5.13(a). Nevertheless, the grain size experiences a reduction to below 4 $\mu$m, which can be attributed to the large amount of twinning. The investigations reveal that 25% of the grain boundary fraction can be accounted to the 86° rotation, typical for the $\{10\bar{1}2\}$ extension twin system. As the axial forces originating from the shoulder act along to the *c*-axis, the observed extension twins can not be accredited to the former. It must thus be assumed that the advancement of the probe imposes compressive stresses orthogonal to the *c*-axis, which in turn activates extension twinning. This high amount of extension twins can already be seen in the inverse pole figure map, but it is most prominent

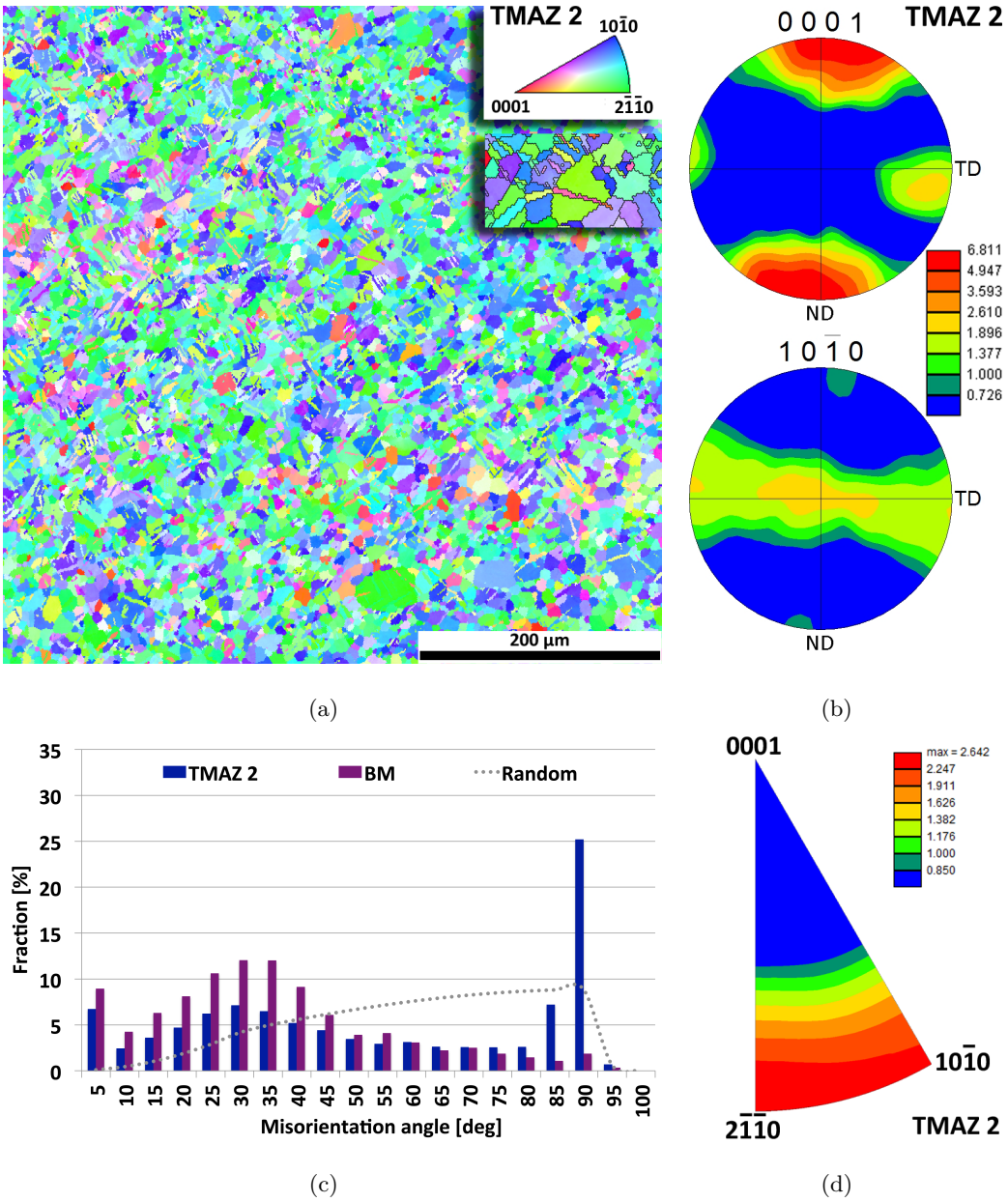


Figure 5.13: Inverse pole figure maps (a), {0001} and {10$\bar{1}$0} pole figures (b), misorientation angle chart (c) and [001] inverse pole figure (d) of the thermo mechanically affected zone 2.

in the misorientation angle distribution chart comparing the thermo mechanically affected zone 2 to the base material, as shown in Fig. 5.13(c). While the base material and thermo mechanically affected zone 2 both feature a small peak in the low angle boundary fraction between 5° and 10°, and an accumulation around the low end of the high angle boundaries at 30°, a distinct difference in the orientation regime between 85° and 90° is

visible. While the 5° to 10° peak is not associated with a particular axis and can thus be related to be deformation induced low angle boundaries, the peak buildup around 30° corresponds to the arbitrary rotation of the grains around the ⟨0001⟩ pole as previously detailed in section 4.7. The large peak at 86° on the other hand, shows a preference for the $\langle 11\bar{2}0 \rangle$ rotation axis and can therefore be attributed to high amounts of extension $\{10\bar{1}2\}$ twinning [269]. An example for a set of typical cross-grain twins can be seen in the insert of Fig. 5.13(a). The resulting misorientation angle ratio (high angle boundary / low angle boundary) reaches ≈ 8 at the outer circumference of the area influenced by the shoulder, showing an overall increase of high angle boundaries over low angle boundaries compared to the base material which has a misorientation angle ratio of only ≈ 5.

The pole figures shown in Fig. 5.13(b) (schematic of the orientation of the unit cell is shown in Fig. 5.14) confirm the assumption that the investigated zone underwent a thermo mechanical cycle. The small peak that is appearing in the transverse direction of the {0001} pole figure has not been seen in the base material and thus indicates a mechanical influence, while the intensity decrease from 10 to 6 m.rd. indicates the presence of a thermal component. Though the inverse pole figure shown in Fig. 5.13(d) closely resembles the textural distribution of the base material (Fig. 4.12(c)), a slight shift towards the ⟨0001⟩ pole can be observed.

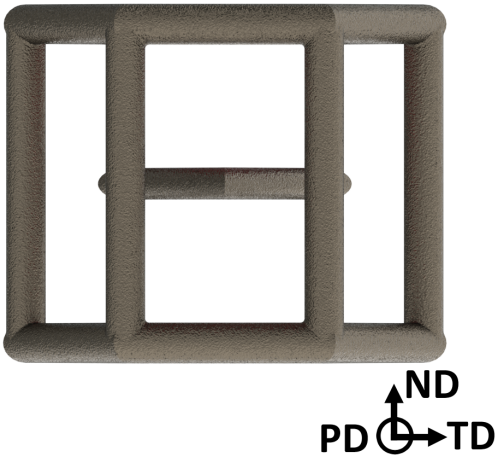


Figure 5.14: Schematic of the textural orientation in the thermo mechanically affected zone 2.

#### Thermo Mechanically Affected Zone 1

The thermo mechanically affected zone 1 is the intermediate region between the outer circumference of the shear layer, which is surrounding the probe and the thermo mechanically affected zone 2. It is therefore closer to the stir zone and thus exhibits stresses originating from the shoulder as well as from the probe. While the stresses originating from the shoulder should in principle be comparable to those which have been transmitted

to the thermo mechanically affected zone 2, the stresses transmitted from the shear layer surrounding the probe are further influencing the material. The effect of the additional stress on the microstructural and textural development are shown in Fig. 5.15.

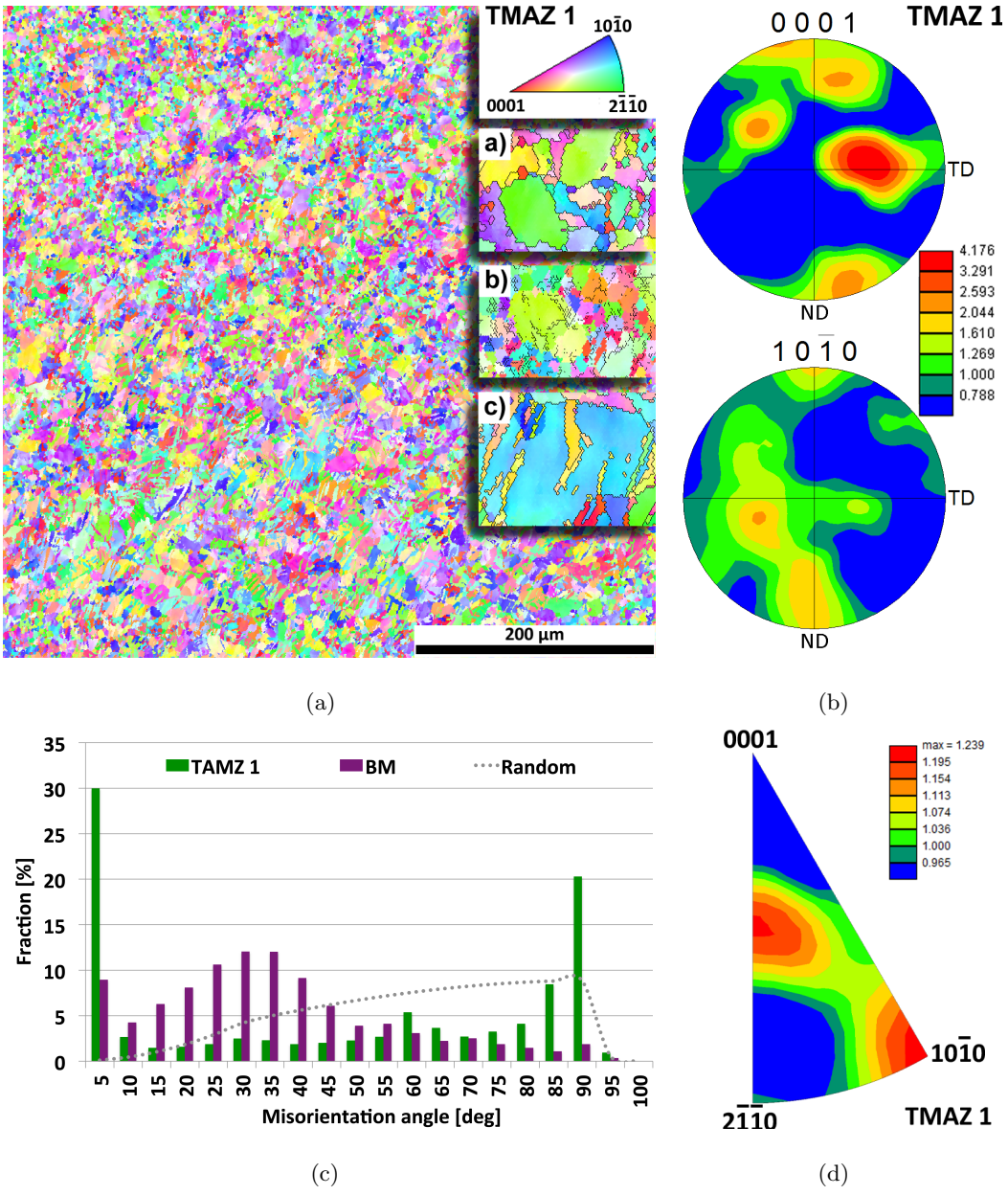


Figure 5.15: Inverse pole figure maps (a), {0001} and {$10\bar{1}0$} pole figures (b), misorientation angle chart (c) and [001] inverse pole figure (d) of the thermo mechanically affected zone 1.

The previously observed sharp grain and twin boundaries become less pronounced as the grain boundaries become rippled and the grain morphology becomes serrated. Small,

equiaxed grains are formed between larger grains with new, random orientations. These new grains have no low angle boundaries and are usually surrounded by grains of high angle boundaries as shown by insert a) in Fig. 5.15(a). This formation is mirrored by the misorientation angle distribution chart (Fig. 5.15(c)), as the {0001} $c-$axis rotational peak appears to have transformed into a single low angle boundary peak located between 5° and 10° which can be accounted to the increase in total strain. Similar observations have previously been made by Galiyev et al. for Mg ZK60 [270] and by Beer et al. for Mg AZ31 [271] and have been associated with the initial stages of discontinuous recrystallization.

In the thermo mechanically affected zone 1, the average grain size decreased to $\approx 2.2$ $\mu$m, which can be attributed to a strain induced size reduction of the original grain structure, as well as to the occurrence of fine, newly formed grains. Assuming a sufficiently high amount of thermal energy, this should have led to an increase in the high angle boundary fraction. Interestingly, this is not the case, as the high angle boundary values between 15° and 90° in the misorientation angle chart of Fig. 5.15(c) exhibit a slight decrease, while a strong low angle boundary peak located between 5° and 10° emerges. While some of the newly developed low angle boundaries stretch into and across larger grains, the majority congregates close to large grains with high angle boundaries as shown by insert b) in Fig. 5.15(a). The low angle boundary accumulation within larger grains indicates that the process of stress induced grain subdivision is incomplete within this area, due to the lack of sufficient thermal energy and the lack of easily activated slip systems. Similar effects have been observed by Al-Samman et al. [33] in Mg AZ31 during uniaxial compression tests at various temperatures and strain rates. Overall, the resulting misorientation angle ratio further decreases to $\approx 1.5$, which is not only substantially lower than the base material value but also the lowest value in all of the investigated zones, reflecting the stern increase in low angle boundaries.

While some $\{10\bar{1}2\}$ extension twins are still present in the material, their fraction is reduced to $\approx 9\%$ which can mainly be attributed to the formation of new, small grains. Additionally, the previously observed grain crossing morphology of extension twins is partly transformed into irregular shaped grains as shown by insert c) in Fig. 5.15(a), adding to the high amount of newly formed, serrated grains as well as to the increased low angle boundary fraction. Such transformation has also been observed by Al-Samman et al. [195] in Mg AZ31 during uniaxial compression tests at ambient temperature.

The corresponding pole figures (Fig. 5.15(b)) show an increasingly randomized texture with a single peak development in the transverse direction, a precursor of which has previously been observed in the thermo mechanically affected zone 2. The schematic of the unit cell can be seen in Fig. 5.16. The randomization is accompanied by a further decrease in textural intensity to ≈ 4 m.rd. as mirrored by the inverse pole figure (Fig. 5.15(d)), showing no preferable textural direction. It can thus be concluded, that the microstructural and textural evolution in the thermo mechanically affected zone 2 is primarily driven by the imposed strain and accompanied by discontinuous recrystallization.

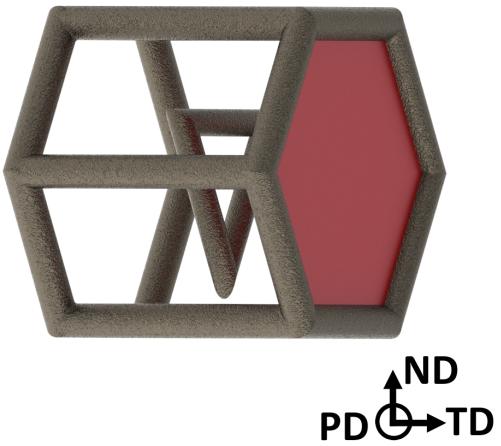


Figure 5.16: Schematic of the textural orientation in the thermo mechanically affected zone 1.

#### 5.2.1.2 Stir Zone

The stir zone (1 and 2) is the microstructural zone which is influenced the most by the rotation of the probe and the resulting shear layer surrounding it. The microstructure in the stir zone is homogenized and features small and recystallized grains which are equiaxed in shape. The stir zone also features two dominant textures as illustrated by the the two inverse pole figure maps in Fig. 5.17(a) and 5.19(a). Previous investigations by Park et al. [268,272] described the reorientation of the basal planes in the vicinity of the probe. In their research, the authors found that the shear deformation, introduced by the rotation of the probe, leads to an alignment of the {0001} basal planes with the macroscopic shear plane (shear layer), created by the tool and surrounding the probe surface.

Woo et al. [39, 40] reported on a superimposing effect of the shear layer created by the shoulder in the top surface of the process zone, resulting in a more randomized texture in this area.

As the texture investigations in the present study have systematically been taken from the center of the process zone, a superimposition of material flow originating from the shoulder is expected to be minimal, leaving the probe to be the main driver for material flow and

thus the reorientation of the basal planes. In the following it will be shown, that for high speed FSP, the magnitude of the $c$-axis tilt is a function of the shear layer geometry which in turn is a function of the processing parameters.

### Stir Zone 2

The microstructural evolution of the stir zone 2 is depicted in Fig. 5.17(a). Overall, the grain size is noticeably reduced to 1.5 $\mu$m and the grain morphology appears homogenized with equiaxed, recrystallized grains and no specific directional preference in either the probe or shoulder surface direction. The formation of new grains of similar size has been reported by Rhodes et al. [273] on Al 7050. The authors used friction stir spot welding on cooled and non-cooled samples in order to investigate the extend of recrystalliztion on the final microstructure. While the cooled samples reached grain sizes in the 10 - 100 nm range, a subsequent annealing of these cooled samples for 1 - 4 min at 350°C - 450°C led to grain growth and a final grain size in the same range as the non-cooled samples.

When comparing these results to the present study, it must be considered that the lattice diffusion rate ($1.8 \cdot 10^{-17}$) and grain boundary diffusion rate $1.1 \cdot 10^{-21} \cdot \delta$ (with $\delta$ being the grain boundary width) at $\approx$ 300°C for the Al-alloy used by Rhodes et al. is lower than the comparable values for Mg-alloys ($4.7 \cdot 10^{-17}$ and $2.0 \cdot 10^{-20} \cdot \delta$) [274]. These differences in lattice and grain boundary diffusion rate suggest that higher amounts of dynamic recovery processes are active in Mg as long as temperature is sufficiently high ($\geqslant$ 205°C for recrystallization [262]). As shown in section 5.1.3, these temperatures are indeed reached in the stir zone for all processing conditions. As these temperatures are only reached for a short amount of time, it must be assumed that the material in the stir zone undergoes a form of dynamic recrystallization which in turn results in the observed homogenized fine grained microstructure.

Similar grain morphologies in the stir zone have previously been reported by Chang et al. [45, 165] on FSP of externally cooled Mg AZ31. While the authors haven been able to further decrease the grain size below 1 $\mu$m by continuous cooling (in comparison, the stir zone grain size in the present study reaches a minimum at 1.5 $\mu$m), the dynamics behind the observed recrystallization mechanisms are comparable. The stresses which are induced by the process result in a highly strained material including a buildup of dislocation walls. Aided by the imposed thermal cycle, these dislocation walls transform into new, recrystallized grains. It should be noted, that the authors did not observe low

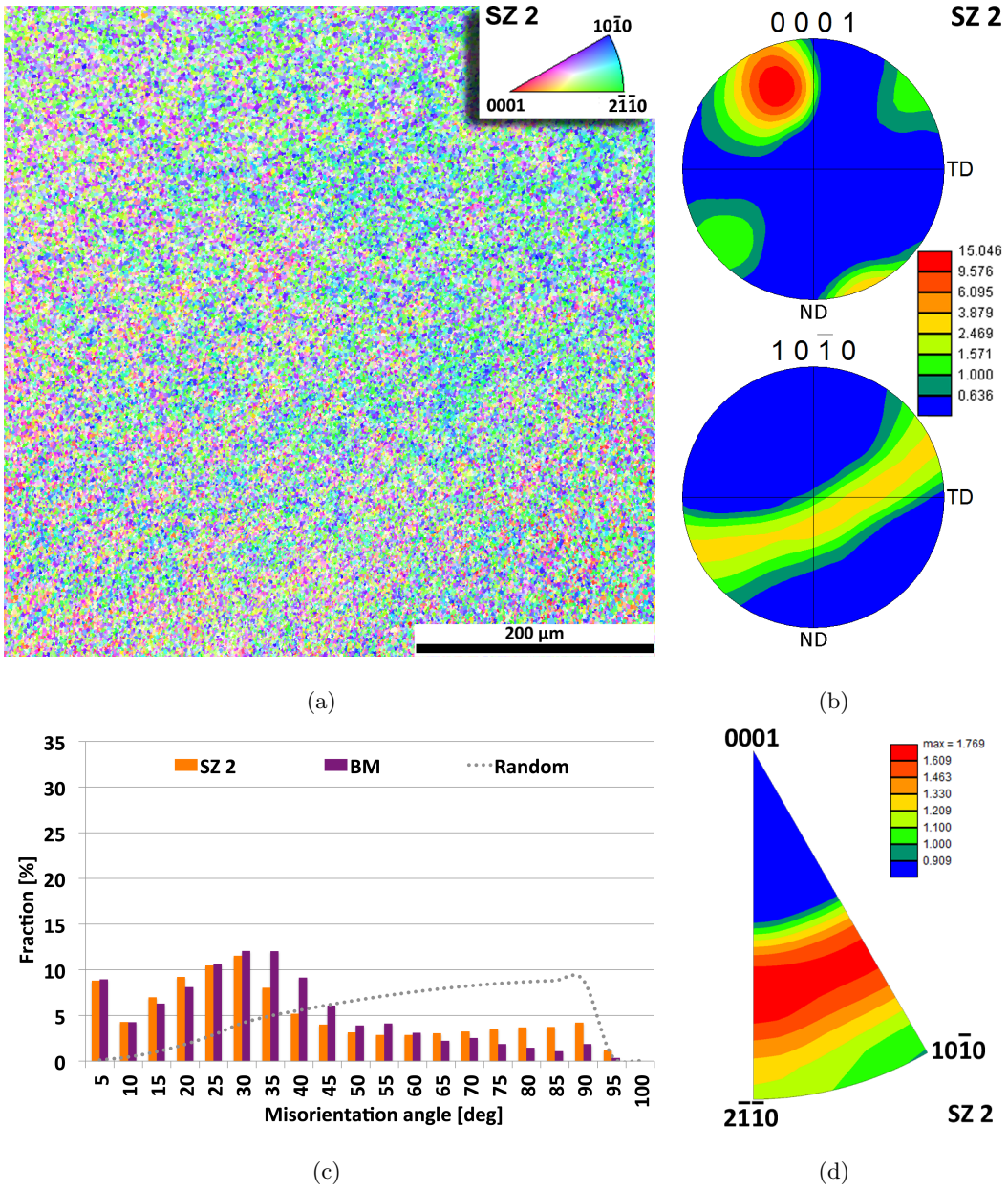


Figure 5.17: Inverse pole figure maps (a), {0001} and {10$\bar{1}$0} pole figures (b), misorientation angle chart (c) and [001] inverse pole figure (d) of the stir zone 2.

angle boundaries (sub grain domains) within newly formed grains suggesting that the onset of polygonization did not yet occur.

The misorientation angle distribution chart shown in Fig. 5.17(c) is very comparable to that of the base material. The previously observed low angle boundary and high angle boundary peak between 5° to 10° seen in the thermo mechanically affected zone 1 is replaced by a buildup around 30°. In addition, the lack of {10$\bar{1}$2} extension twins is

mirrored by the decrease in high angle boundaries around 86°. The misorientation angle ratio experiences a stark increase to ≈ 5 which is in the same regime as what has been observed in the base material, reinforcing the assumption of a recrystallized grain structure in the stir zone.

The pole figures shown in Fig. 5.17(b) (a schematic of the orientation of the unit cell is shown in Fig. 5.18) depict a consolidation of the basal planes and an initial shift of the former towards the processing direction, while the prismatic planes exhibit the rotational fibre texture previously observed in the base material. The 27° tilt of the *c*-axis towards the processing direction indicates an initial alignment of the {0001} basal planes with the macroscopic shear plane of the probe. Compared to the texture of stir zone 1, which will be shown in the pole figure in Fig. 5.19(b), the tilt of the *c*-axis is less pronounced. This further supports the argument that the texture in the stir zone exhibits a continuous alignment of the basal planes around the macroscopic shear layer from a stir zone - thermo mechanically affected zone interface up to the apex in the center of the stir zone.

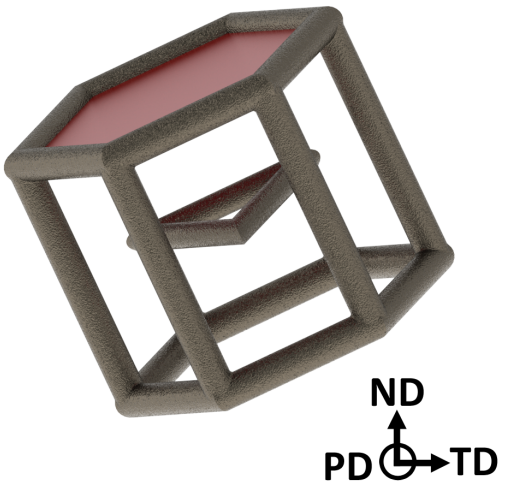


Figure 5.18: Schematic of the textural orientation in the stir zone 2.

Accompanied by the recrystallization and the consolidated tilt of the *c*-axis, the textural intensity of the stir zone 2 is rising to ≈ 15 m.rd. This is closely mirrored by the consolidation within the center of the inverse pole figure as depicted in Fig. 5.17(d).

### Stir Zone 1

The texture in the center of the process zone is depicted in Fig. 5.19(a).

Just as previously described for the stir zone 2, the center of the stir zone features small equiaxed grains, which appear recrystallized and to have no directional preference. The average grain size is ≈ 1.6 $\mu$m. The center oft the stir zone features virtually no twin boundaries, with $\{10\bar{1}2\}$ extension twin boundaries accounting for less than 0.2% of all grain boundaries.

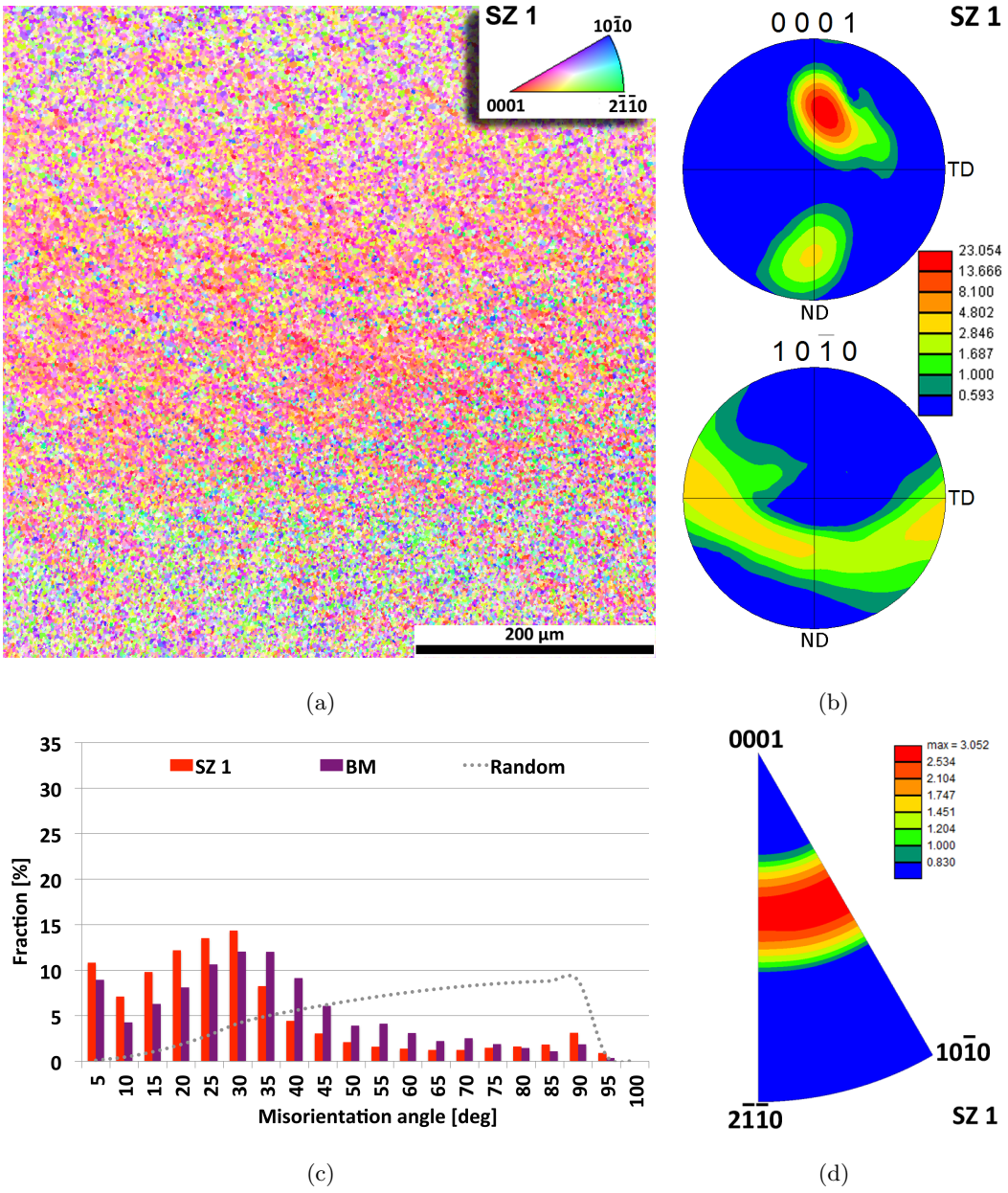


Figure 5.19: Inverse pole figure maps (a), {0001} and {10$\bar{1}$0} pole figures (b), misorientation angle chart (c) and [001] inverse pole figure (d) of the stir zone 1.

The textural differences between the two areas of the stir zone are mirrored more closely in the misorientation angle chart shown in Fig. 5.19(c). While the overall trend still broadly resembles that of the stir zone 2, the following differences can been observed: The low angle boundary fraction is increased, predominantly in the area between 10° and 15°. Additionally the low end of the high angle boundaries (25° to 35°) exhibits a further increase, indicating a consolidated rotation of the grains around the ⟨0001⟩

direction. The misorientation angle decreases in the angular range between 35° and 90°, which finally results in a misorientation angle ratio of over 3 compared to a stir zone 2 misorientation angle ratio of over 5. This decrease in misorientation angle ratio strongly mirrors the differences in textural developments induced by the varying strain imposed onto the material by the rotating tool.

The textural changes are most pronounced in the pole figures shown in Fig. 5.19(b) (schematic of the unit cell in Fig. 5.20). The previously observed consolidation and tilt of the *c*-axis towards the processing direction continues. The occurrence of a weak second peak at the opposite side of the pole figure can be associated with an additional rotation of some of the grains with a $\langle 0001 \rangle$ texture around the $\langle 11\bar{2}0 \rangle$ direction. The prismatic planes on the other hand exhibit a less homogeneous distribution and the intensity distribution within the developed band is slightly interrupted.

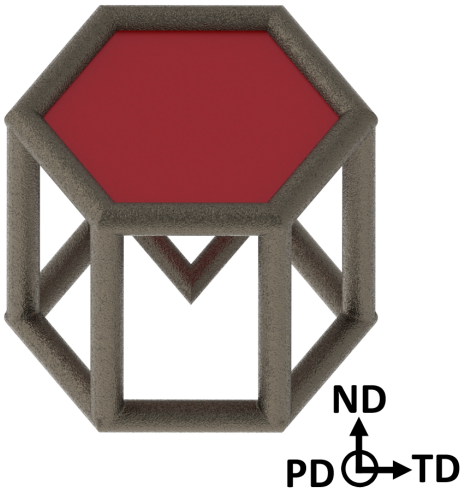


Figure 5.20: Schematic of the textural orientation in the stir zone 1.

The overall intensity further increases to 23 m.rd., which is the highest value measured throughout all regions as reflected by the 30° peak.

As previously mentioned, the ideal orientations of HCP crystals in simple shear has previously been investigated by Beausir et al. [255]. The authors have shown that the {0001} basal planes align themselves parallel to the macroscopic shear plane and termed it simple shear B-fibre texture. Within this texture, the grains are rotated around the $\langle 0001 \rangle$ direction. As previously discussed for the base material, the symmetry of the HCP crystal limits the maximum rotation which can be measured around $\langle 0001 \rangle$ to 30°. While the emergence of the B-fibre texture is correlated to basal slip, the rotation around $\langle 0001 \rangle$ arises from $\{10\bar{1}0\}$ $\langle 11\bar{2}0 \rangle$ prismatic slip [200, 275], as basal slip can not accommodate a rotation around the *c*-axis. The development of the simple shear B-fibre texture, extended by prismatic slip, therefore explains the broad maximum up to 30° in the misorientation angle chart (Fig. 5.19(c)), as well as the consolidation towards the $\langle 0001 \rangle$ pole in the inverse pole figure shown in Fig. 5.19(d).

In Figs. 5.21 and 5.22, various key figures are jointly presented in order to identify microstructural areas with textures suitable for enhanced formability.

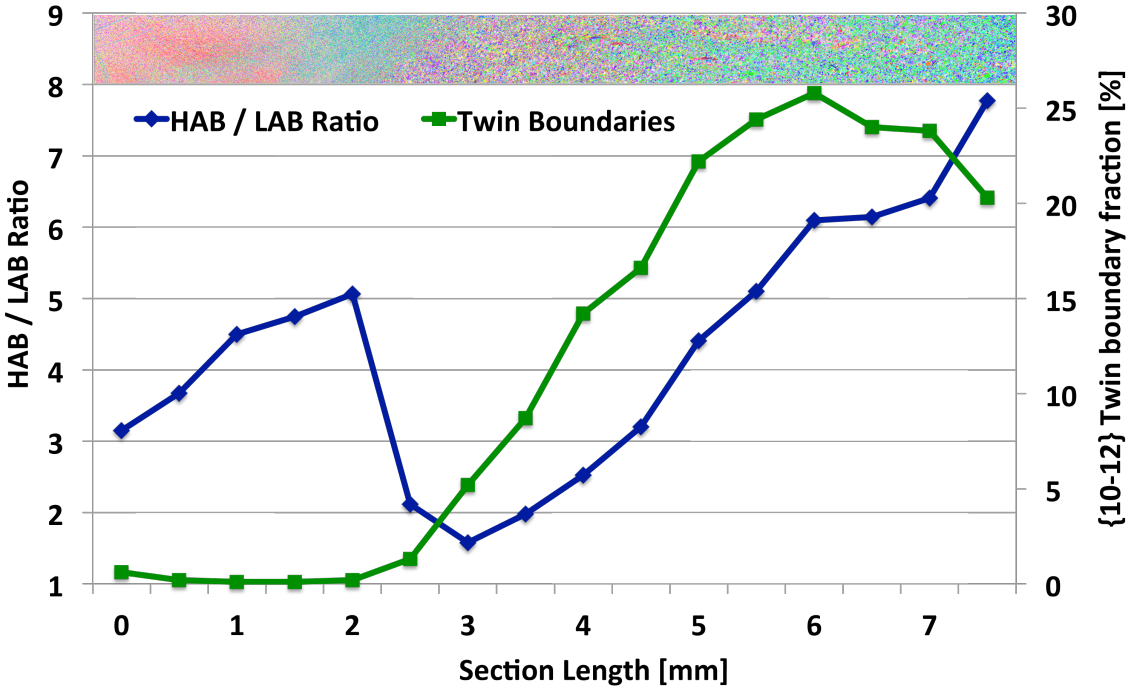


Figure 5.21: Misorientation angle ratio and area fraction of $\{10\bar{1}2\}$ extension twins throughout the investigated textural zones of an externally cooled sample (Cond. E).

In Fig. 5.21 the development of the twin boundaries and the misorientation angle ratio is presented. While both, the $\{10\bar{1}2\}$ extension twin boundaries as well as the misorientation angle ratio appear to experience a decrease throughout the thermo mechanically affected zone, some distinct differences have been observed.

Starting at the thermo mechanically affected zone and moving towards the stir zone, an initial increase in the amount of twin boundaries can be noted in the section length between 8 mm to 6.5 mm. While it can be assumed that the in-plane stresses arising from the probe are still acting as a driving force in activating extension twins, the stress contribution from the shoulder must also be considered. As the shoulder radius ($\varnothing$ = 13 mm) ends at 6.5 mm, the resulting stresses in the regime between 8 mm and 6.5 mm are no longer exclusively directed along the *c*-axis. This directional change can lead to an additional compressive stress along the $\langle 11\bar{2}0\rangle$ direction. As the twin boundary fraction of $\approx$ 20% at a section length of 8 mm (1.5 mm away from the outer circumference of the shoulder)

is still significantly higher than what has been observed for the base material (0.8%), it can be concluded that the stresses originating from the shoulder are still sufficiently high in the transition area to induce high amounts of twins, but are continuously diminishing towards the heat affected zone.

Within the area below the shoulder (section length 6.5 mm to 2.5 mm), the twin boundary fraction is continuously decreasing until it reaches a global minimum within the stir zone in which it stays beneath 1%. While the decrease of twin boundaries in the thermo mechanically affected zone might be attributed to twin induced development of new grains, the absence of twins in the stir zone points to dynamic recrystallization as described above and previously reported by Ponge et al. [276].

The misorientation angle ratio on the other hand experiences a continuous decrease from $\approx 7.8$ (section length 8 mm) to $\approx 1.6$ (section length 3 mm) and reaches the base material value of $\approx 4.8$ at a section length of $\approx 5.5$ mm. This continuous decrease can be attributed to two different, but converging effects. Firstly, the decreasing fraction of twin boundaries decreases the high angle boundary ratio, and secondly, dynamic recrystallization generates new, fine grains which can increase the low angle boundary fraction. Both effects result in an almost balanced misorientation angle ratio at the interface between stir zone 2 and thermo mechanically affected zone 1 at a section length of 3 mm. Within the stir zone, a steep increase followed by a continuous decay can be observed. While the initial soaring of the misorientation angle ratio in the interface region between the stir zone 2 and the thermo mechanically affected zone 1 can be attributed to an increase in incompatibility boundaries at the textural interface, the decay towards stir zone 1 can be accredited to the increase of the 30° $\langle 0001 \rangle$ rotation, which in turn is induced by the differences in strain conditions.

The development of the grain size and the intensity is presented in Fig. 5.22. While the grain size experiences a continuous decrease from $\approx 4$ $\mu$m to $\approx 2$ $\mu$m within the thermo mechanically affected zone, it reaches a threshold in the stir zone at an average value of $\approx 1.6$ $\mu$m. In the transition area at the previously discussed edge of the shoulder (section length of 6.5 mm), a steep drop can be observed which can be attributed to the increased amounts of extension twins, creating new grain boundaries.

The intensity, on the other hand, experiences an almost constant evolution within the thermo mechanically affected zone at an average value of $\approx 6$ m.rd. before it increases strongly within the stir zone, reaching an intermediate plateau in the interface between

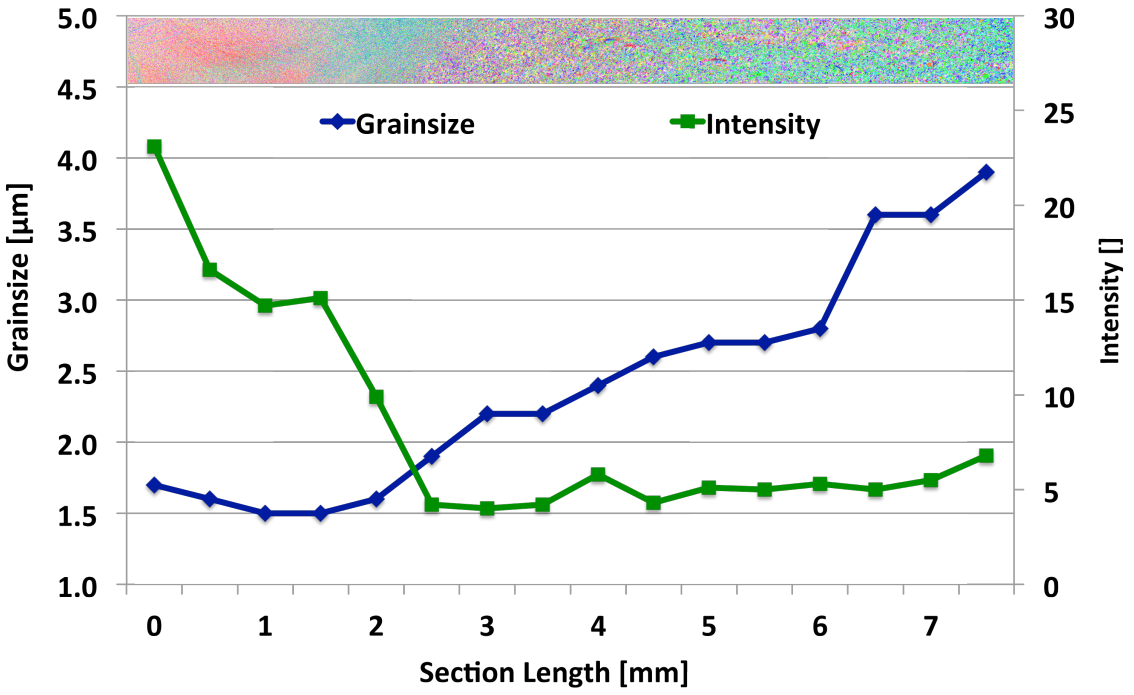


Figure 5.22: Grain size distribution and textural intensity throughout the investigated textural zones of an externally cooled sample (Cond. E).

stir zone 1 and 2. The intensity increase within the stir zone can be attributed to the occurrence of recrystallization, which incorporates a directed reorientation of the grains.

#### 5.2.1.3 Texture Analysis

As detailed in the literature review (section 3.1.2), the research previously conducted on the textural evolution throughout the metallographic regions from base material to the stir zone is limited. The authors which have conducted such investigations argue that the texture undergoes a continuous rotation from the base material over the thermo mechanically affected zone towards the center of the stir zone, in which the basal planes align with the macroscopic shear planes [39, 169, 181]. In the present study, a similar shift has been observed, which fits well with the results obtained by Beausir et al. [255,277], even though the trend itself appears more discrete in nature. In order to identify microstructural areas with potentially higher formability, the information of the deformation mechanisms compiled in section 3.2.2 have been used. Conclusively, two main drivers for enhanced formability at ambient temperature have been identified. Primarily, controlled textural modifications are reported to enhance {0001} basal slip as well as to improve the activation

of extension twins. Secondly, but reported mainly for higher temperatures, grain boundary sliding through grain refinement also bears the promise of enhancing formability. Tab. 5.3 lists the deformation modes of Mg as a function of the location within the inverse pole figure, as shown in Fig. 5.23.

Due to its low CRSS, basal slip is the most thought after deformation mode. As shown in Fig. 5.23, single and double basal slip occurs predominantly in the intermediate region between the $\langle 0001 \rangle$, $\langle 10\bar{1}0 \rangle$ and $\langle 2\bar{1}\bar{1}0 \rangle$ poles. From all identified zones within the externally cooled experiments, the center of the stir zone (SZ 1) offers the highest tilt of the $c$-axis, which in turn yields the highest Schmid factor on the basal planes, as compiled by Nan et al. [278]. In addition to the small grain size and a low amount of preexisting twin boundaries, the inverse pole figure of stir zone 1 (Fig. 5.19(d)) shows a textural tendency towards the $\langle 0001 \rangle$ pole without entering into region II of Fig. 5.23. The above results thus point to the stir zone 1 to be of particular interest for investigations aiming at enhanced formability.

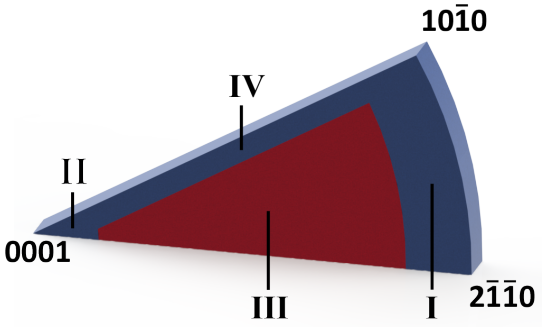


Figure 5.23: Inverse pole figure of orientation dependent active deformation mechanisms in Mg [200].

Table 5.3: Description of the deformation modes corresponding to Fig. 5.23 [200].

| **Region** | **Compression** | **Tension** |
|---|---|---|
| I | $\{10\bar{1}2\}$ twinning, prismatic slip, $\langle a \rangle$ pyramidal slip | prismatic slip, $\langle a \rangle$ pyramidal slip |
| II | $\langle c+a \rangle$ pyramidal slip | $\{10\bar{1}2\}$ twinning, $\langle a \rangle$ pyramidal slip |
| III | single basal slip | single basal slip |
| IV | double basal slip | double basal slip |

### 5.2.2 Single Line Experiments

The effect of different processing conditions (developed in section 5.1) onto the microstructural and textural evolution has been investigated for the single line samples. All single

line samples have been processed without external cooling. Particular investigative focus has been laid on the development of the shape of the macroscopic shear plane (shear layer) which in turn influences the resulting texture and in such the tilt of the *c*-axis. The mechanical response to the developed processing conditions has been investigated by small scale mechanical testing, namely nanoindentation and micro flat tensile test (sections 5.3.1 and 5.3.2).

The knowledge gained by the textural investigations and mechanical tests of the single line samples, has been transferred to create larger processed areas from which formability specimens have been prepared. The resulting microstructures and textures will be detailed in section 5.2.3 while the results of the formability tests will be presented in section 5.3.3.

The results of the investigations on externally cooled samples revealed not only that the microstructure and texture of the stir zone is most suitable for enhanced formability, but also that apart from a tilt towards the processing direction, the *c*-axis exhibits an additional tilt towards the normal direction which is schematically depicted in Fig. 5.24. This result is distinguished from investigations conducted by Wang et al. [181] as the authors found a continuous rotation of the *c*-axis from the transverse direction towards the processing direction with increasing proximity to the center of the stir zone. Thus, the rotation occurred solely within the transverse direction - processing direction plane.

In order to limit the additional rotation found in the present study, which is representing an additional degree of freedom, all texture investigations on the single line samples (section 5.2.2) have been conducted in the center of the stir zone. Additionally, all investigations have been conducted at mid-thickness of the stir zone, as previous investigations by

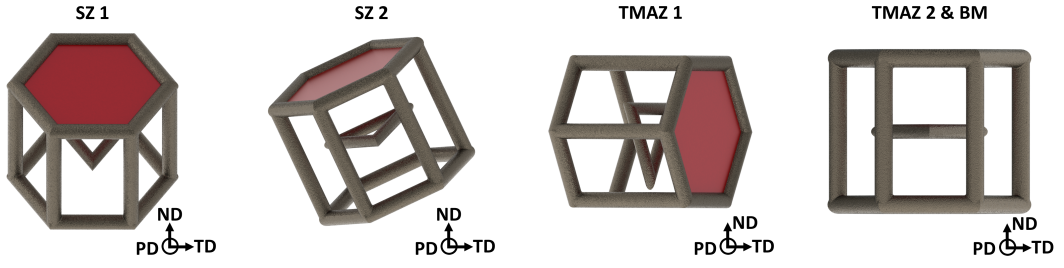


Figure 5.24: The evolution of the texture from the center of the stir zone to the base material. The {0001} basal planes are indicated by red areas.

Suhuddin et al. [169] have suggested a texture variations throughout the sample thickness. The texture results for the single line experiments are shown in Fig. 5.25.

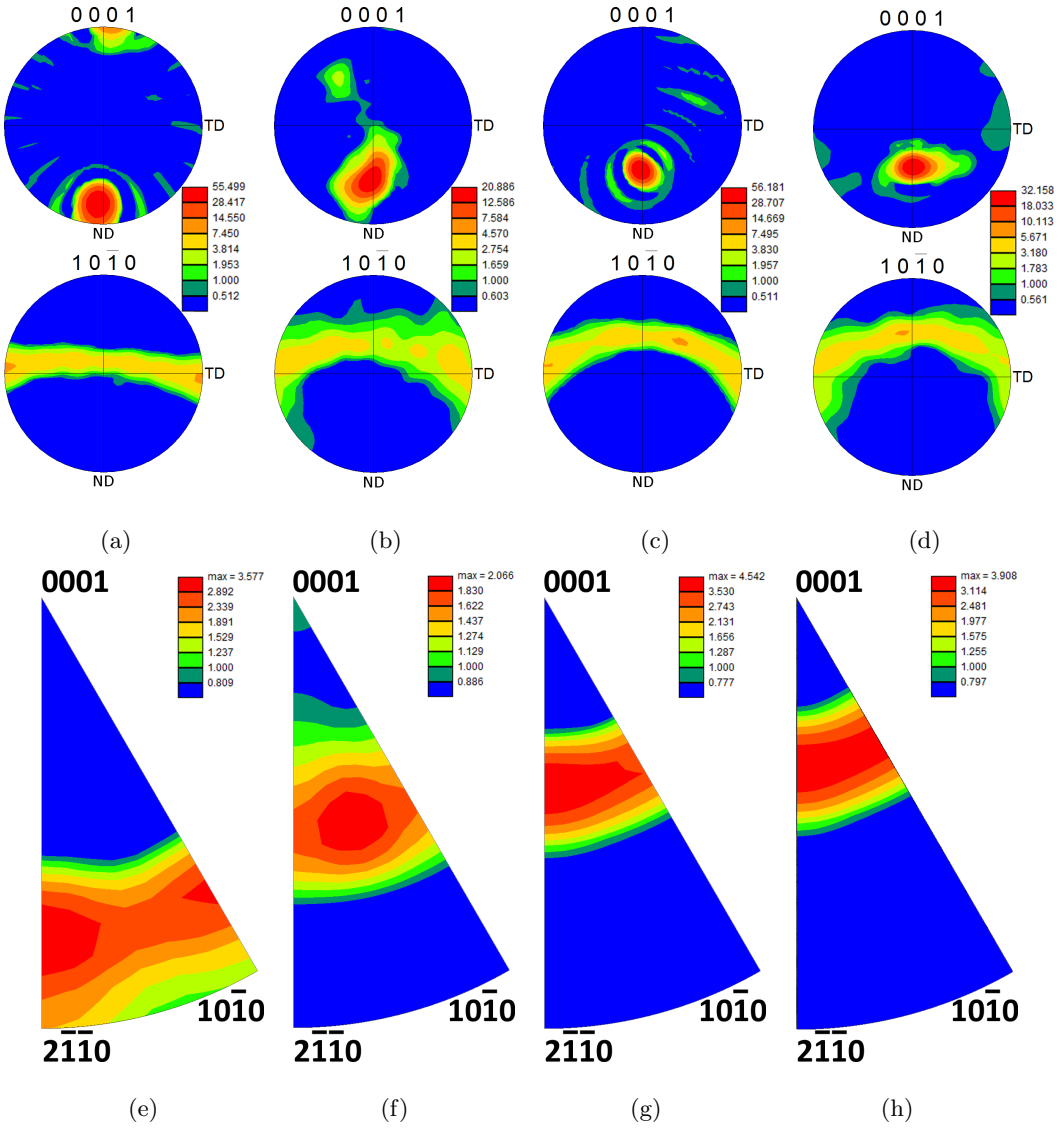


Figure 5.25: {0001} and $\{10\bar{1}0\}$ pole figures and [001] inverse pole figures from the center of the stir zone of condition A (a and e), condition C (b and f), condition E (c and g) and condition F (d and h).

For processing condition A (Fig. 5.25(a)), the *c*-axis exhibits a minor tilt of 14° out of the normal direction and into processing direction, as previously seen for the externally cooled samples. Additionally, some minor reflections at the outer circumference of the pole figures hemisphere are visible. The homogeneously distributed rotation of the prismatic planes along the transverse direction of the $\{10\bar{1}0\}$ pole figure is still intact. The inverse pole

figure mirrors this minor tilt of the $c$-axis as the textural distribution is slightly shifted from the $\langle 10\bar{1}0\rangle$ and $\langle 2\bar{1}\bar{1}0\rangle$ pole to the $\langle 0001\rangle$ pole.

Fig. 5.25(b) depicts the pole figures of the samples processed in condition C. While the basal planes within the main peak are less consolidated compared to condition A, a second, minor peak is evolving at the opposite end of the hemisphere, which has previously been observed in Fig. 5.19(b). In addition, the homogeneous distribution of the prismatic planes appears broader and somewhat serrated with a first occurrence of an arching around the processing direction. The $c$-axis exhibits a further tilt to $\approx 33°$ into processing direction. The inverse pole figure (Fig. 5.25(f)) clearly mirrors this trend, as the texture is moving away from the $\langle 10\bar{1}0\rangle$ and $\langle 2\bar{1}\bar{1}0\rangle$ poles into the direction of the $\langle 0001\rangle$ pole.

This trend continues with increasing processing speed, as shown in Fig. 5.25(c), depicting the pole figures for the samples processed in condition E. The previously observed small secondary peak in the $\{0001\}$ pole figure softens to a longer and broader tail which has previously been observed for the samples processed in condition A (Fig. 5.25(a)). Due to the $c$-axis tilt, this tail is now no longer surrounding the pole figure but crossing it towards the normal direction. The prismatic planes in the $\{10\bar{1}0\}$ pole figure reconsolidate and continue to arch around the processing direction. The tilt of the $c$-axis reaches 42°, which can also be seen in the inverse pole figure in Fig. 5.25(g) as the texture tends to move towards the $\langle 0001\rangle$ pole.

Finally the material processed in condition F (Fig. 5.25(d)) experiences a similar textural consolidation with only some minor incidents at the outer circumference of the hemisphere. The tilt of the $c$-axis reaches its highest values at 47°, while the arching of the prismatic planes intensifies. The corresponding IFP (Fig. 5.25(h)) outlines the consolidation towards the $\langle 0001\rangle$ pole, even though a small distribution can be noticed around the $\langle 2\bar{1}\bar{1}0\rangle$ pole.

The evolution of the basal tilt as a function of processing speed is depicted in Fig. 5.26 and can be subdivided into two slopes. The first slope S1 ranges from the base material to condition C with an increase of $\approx 7°/(\mathrm{m/min})$. The second slope S2 shows a significantly less sharp increase of $\approx 0.5°/(\mathrm{m/min})$. Following this trend, it could thus be argued, that with the current probe geometry, the increase will cease completely within an angular range between 50° to 60° which will be further discussed in the following.

While various earlier studies [42, 169, 268, 272] suggested a tilt of the $c$-axis of up to 90° in the center of the stir zone ($c$-axis ∥ processing direction), they have not been observed in the present study. This can be explained by the formation mechanism of the shear layer

itself.

As previously described for the stir zone in section 5.2.1, the basal planes tend to reorient themselves parallel to the macroscopic shear plane. As all previous studies have been conducted at considerably lower processing speeds, the resulting shear layer surrounding the probe has been reported to be substantially larger. In high speed FSP on the other hand, the shear layer is limited to the close vicinity of the probe. Due to this close vicinity, the physical geometry of the probe gains in importance in the shear layer geometry development and the corresponding geometry of the stir zone. In this context, Fig. 5.27 displays examples of two cross-sections of material processed in condition A and E respectively with and overlay of the probe and the shoulder. Additionally an indication of the interface angle of the shear layer is shown.

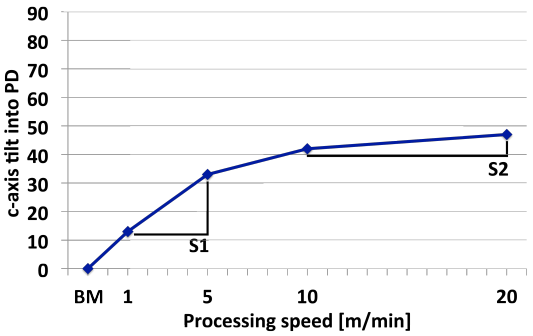


Figure 5.26: Rotation of the basal planes into processing direction as a function of processing speed.

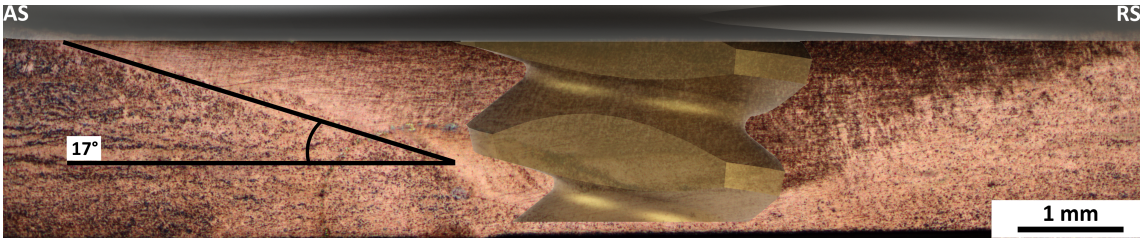


(a)

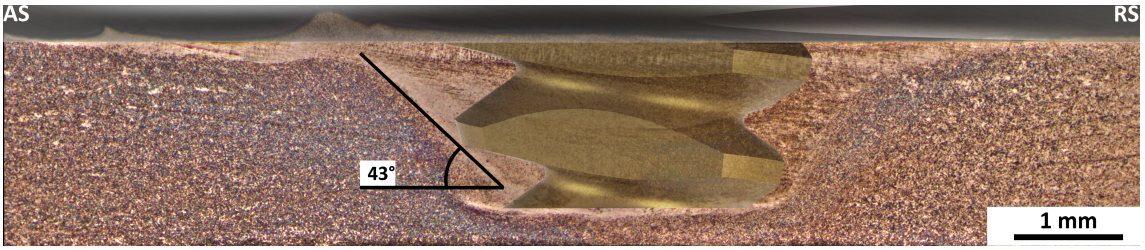


(b)

Figure 5.27: Macrographs of material processed in condition A (a) and E (b) with an overlay of the probe geometry as well as the shear layer interface angles.

Due to the slower processing speed and therefore higher heat input of condition A (Fig.

5.27(a)), the stir zone extends over almost the entire shoulder radius, resulting in a small shear layer interface angle of $\approx 17°$. In contrast, the stir zone of condition E (Fig. 5.27(b)), is significantly reduced in size and results in a shear layer interface angle of $\approx 43°$, which is close to the actual probe geometry. Both interface angles correspond reasonably well to the tilt of the *c*-axis measured from the pole figures being 14° for condition A and 42° for condition E, respectively.

It can thus be argued that the *c*-axis tilt is indeed mainly driven by the geometry of the macroscopic shear plane as the basal planes reorient themselves parallel to the interface angle of the shear layer. As detailed in section 3.2.2, a *c*-axis tilt of 45° is most thought after in regards to enhancing basal slip. For the present study the obtained results show that this desired tilt can indeed be reached (condition E $\approx 42°$ - condition F $\approx 47°$) with the developed processing parameters in combination with the chosen tool geometry.

As the geometry of the shear layer can be regarded a function of the processing parameters and probe geometry, it can be assumed that the tilt of the *c*-axis comes to an end once the geometry of the shear layer is identical to the geometry of the probe. Due to the remaining influence of the shoulder, this extreme case remains theoretical in nature as shown by the minute increases in *c*-axis tilt between condition E and F.

In addition, the evolution of the misorientation angle has also been investigated and is presented in Fig. 5.28. The misorientation angle angle distribution for condition A (Fig. 5.28(a)) experiences three angular regions of interest. A low angle boundary peak between 2° and 15°, a high angle boundary agglomeration between 15° and 30°, and a small high angle boundary peak between 85° and 95°.

The low angle boundary peak can be attributed to the imposed plastic deformation resulting in low angle boundaries between recrystallized grains, while the agglomeration between 15° and 30° can be accredited to the previously discussed rotation around the *c*-axis. The high angle boundary peak between 85° and 95° on the other hand is shifted slightly towards higher misorientation angles and can therefore not be attributed to 86° $\{10\bar{1}2\}$ extension twins as the twin boundary fraction lies below 1%. It can however be attributed to a transformation of previous twin boundaries to high angle boundaries. Mironov et al. [279] explained this to be a deformation induced rotation of the twins and matrix away from their initial orientations which is shown in the high magnification detail of Fig. 5.28(e), in which high angle boundaries and low angle boundaries are marked in black and white, respectively.

With increasing processing speed (Cond. C in Fig. 5.28(b)), the high angle boundary peak vanishes as the misorientation angle distribution closely resembles that of the base material, with the exception of the remaining low angle boundary peak.

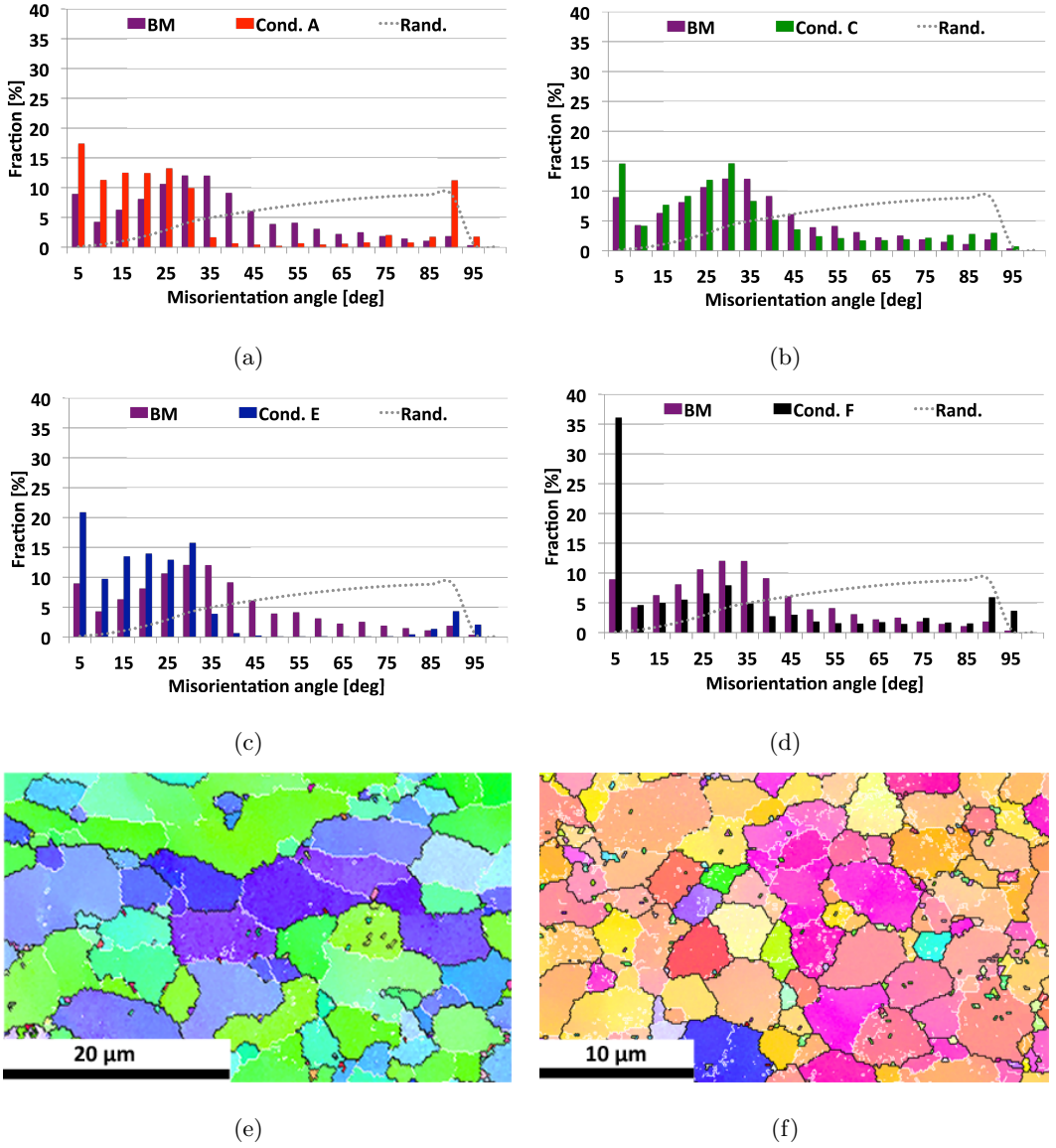


Figure 5.28: Misorientation angle charts from the stir zone of condition A (a), C (b), E (c) and F (d) including details of a deformation induced matrix rotation of condition A (e) and increasing low angle boundaries within larger recrystallized grains of condition F (f).

Further increasing the processing speed results in a continuous increase of the low angle boundary fraction, as most prominently visible by the high low angle boundary peak for condition F shown in Fig. 5.28(d). The highest fraction of low angle boundaries is located within the larger recrystallized grains, as shown by the high magnification detail of Fig.

5.28(f). The mechanisms behind this increase will be discussed on page 89.

### Probe Geometry Verification Experiments

From the above results it can be concluded that the *c*-axis tilt, and thus the ease of basal slip, can be tailored by a knowledge based implementation of processing parameters and probe geometry. In order to substantiate the assumption that the geometry of the shear layer can indeed be controlled by varying probe geometries, verification experiments have been conducted. Within these experiments, three probe geometries with varying taper angles between 0° and 50° (Fig. 5.29) have been used. Each geometry has been used

(a) (b) (c)

Figure 5.29: Probe geometries for the shear layer modification experiments. Probe geometry 1 with 0° taper (a), probe geometry 2 with 25° taper (b) and probe geometry 3 with 50° taper (c).

to create single line samples by processing the material in condition E, using the same shoulder and handling system as in the previous single line experiments. The resulting textures are shown in Fig. 5.30. As expected, the *c*-axis tilt continuously decreases with increasing taper angle, best shown by the {0001} pole figures. While for probe geometry 1 (0° taper) a *c*-axis tilt of ≈ 55° into processing direction can be observed, probe geometry 2 (25° taper) shows a decreases to ≈ 44°. For probe geometry 3 (50° taper), the *c*-axis tilt continues and decreases to ≈ 30°. The same observations can be made from the inverse pole figures which show a continuous movement of the textural distribution away from the ⟨0001⟩ pole towards the $\langle 10\bar{1}0\rangle$ and $\langle 2\bar{1}\bar{1}0\rangle$ poles. It can thus be concluded that the shear layer geometry, and with it the texture of the processed material, can indeed be controlled by the probe geometry if FSP is conducted at high speeds.

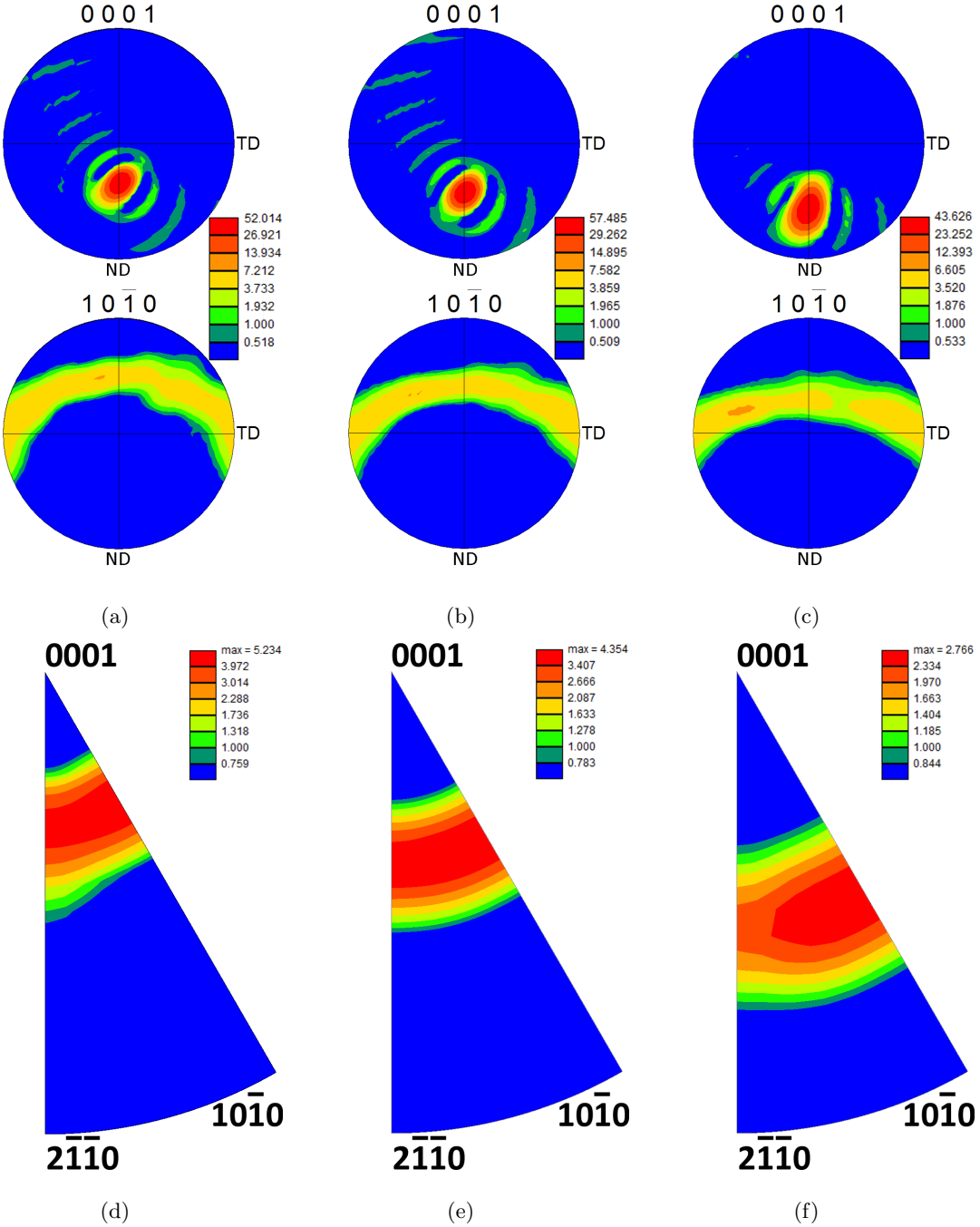


Figure 5.30: {0001} and {$10\bar{1}0$} pole figures and [001] inverse pole figures from the center of the stir zone of probe geometry 1 with 0° taper (a and d), probe geometry 2 with 25° taper (b and e) and probe geometry 3 with 50° taper (c and f).

### Recrystallization Considerations

The observed continuous increase in the low angle boundary fraction have not been observed in the externally cooled samples. Traditional recrystallization theories assume that dislocations which are introduced during cold working form dislocation walls within existing grains, which in turn form dislocation arrangements and pile-ups until the prior grain structure is abolished. By adding thermal energy, these dislocations will eventually give rise to a new, recrystallized grain structure [280].

As shown by the thermal investigations in section 5.1.3, the maximum time available for recrystallization at 205°C is limited to under 4 s and for annealing at 345°C the dwell time is under 1.5 s which is significantly lower than what is reported to be necessary for recrystallization or annealing processes to take place [262, 281, 282]. It must therefore be considered that the material experiences the shorter and more complex process of dynamic recrystallization during FSP. The formation of dynamically recrystallized zones has previously been investigated by Galiyev et al. [270]. The authors describe that with increasing imposed strain, the original grain structure is progressively deformed and subsequently consumed by new dynamically recrystallized regions, which are known as necklace structures. As the initial necklace grains are formed by bulging, they naturally have a similar orientation as their parent grains, thus represent low angle boundaries. With increasing dynamic recrystallization, which requires additional thermal energy, the misorientation can increase to values between 5° to 20° [276].

Generally dynamic recrystallization can be subdivided into continuous (CDRX) and discontinuous dynamic recrystallization (DDRX). While it is assumed that for continuous dynamic recrystallization sufficiently large continuous thermal inputs transform preexisting dislocation arrangements into newly formed grains, discontinuous dynamic recrystallization initiates recrystallization but halts the process once the thermal input is interrupted. Due to this interruption, the newly formed grains still include randomly oriented dislocations. With rising temperatures, the randomly oriented dislocations can arrange themselves to dislocation lines. These lines transform (polygonize) into low angle boundaries, located within grains which are usually surrounded by high angle boundaries [283].

Within the present study, this effect can be noticed most prominently when comparing the externally cooled samples, which are processed in condition E, to the corresponding samples processed at ambient temperature as well as to the samples processed in condition F. While it is assumed that continuous dynamic recrystallization and discontinuous dynamic

recrystallization occurs in all samples, their extend differs greatly. The externally cooled samples exhibit a grain size of ≈ 1.8 $\mu$m and a misorientation angle ratio of ≈ 3. On the other hand, the grain size of the samples processed at ambient temperature increases to 2.5 $\mu$m with a misorientation angle ratio of below 1.5. A comparison between the grain size and misorientation angle ratio as well as the maximum temperatures as a function of processing speeds is given in Fig. 5.31.

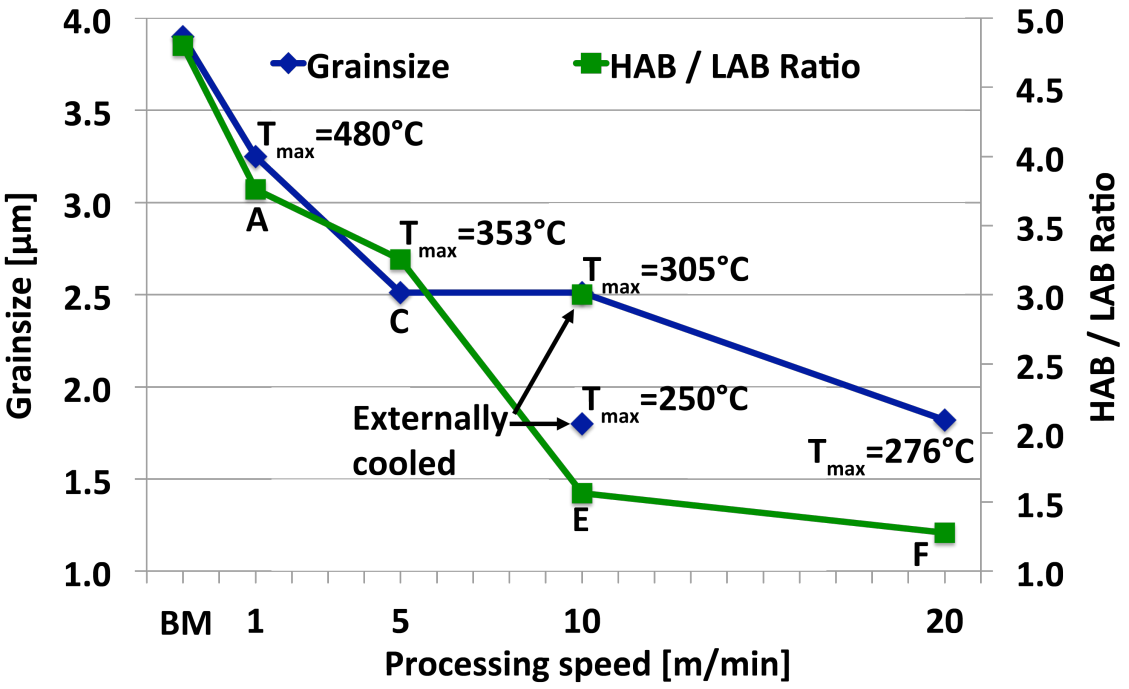


Figure 5.31: Grain size, misorientation angle ratio and maximum temperature as a function of processing speed including the externally cooled sample.

Interestingly, the externally cooled samples (Cond. E) as well as the samples processed in condition F have the same dynamically recrystallized grain size of ≈ 1.8 $\mu$m. This indicates, that in the temperature regime between ≈ 250°C to ≈ 280°C the sensitivity of the dynamically recrystallized grain size to the applied strain rate decreases. In the temperature regime between ≈ 300°C to ≈ 350°C (Cond. C and E), similar observations can be made as the dynamically recrystallized grain size (2.5 $\mu$m) remains constant. At the significantly higher temperatures of condition A (480°C), the dynamically recrystallized grain size reaches values above 3.3 $\mu$m. Similar results have been obtained by Al-Samman et al. [33] showing a decreasing dynamically recrystallized grain size sensitivity to the applied strain rate at decreasing temperatures by applying uniaxial compression to extruded

Mg AZ31 in the temperature regime between 200°C to 400°C.

Interestingly this relation does not hold true in the transition between condition E to F. While the difference in maximum temperature between the two conditions remains at ≈ 30°C the grain size decreases from 2.5 $\mu$m to 1.8 $\mu$m. This difference can be explained by the effect of varying strain. In their experiments, Al-Samman et al. [33] preset the applied strain to a constant value but varied the strain rate. In FSP, the primary driver for the strain rate is thought to be the rotational speed of the tool [165,179]. This might hold true as long as the processing speed is kept low enough to be superimposed by the rotational speed. In high speed FSP on the other hand, the contribution of the processing speed to the total endured strain increases.

This effect can best be explained by calculating the travel of the probe before it performs one full rotation: In condition A, the center of the probe travels 0.5 mm before performing one full rotation. In conditions C, E and F, the probe travels 2 mm/rot, 2.9 mm/rot and 4.4 mm/rot respectively. Due to this additional translational movement, the consolidation mechanism in high speed FSP should in principle be divided into a stirring and an extrusion component. In the extrusion of Mg, the level of dynamic recovery is sufficiently low to allow dynamic recrystallization above a temperature of 240°C [284]. Thus, after deformation, fine grains are formed at original grain boundaries, leading to material strengthening by the substructures formed during dynamic recrystallization. It can therefore be argued that the two severe plastic deformation processes, stirring and extrusion, are contributing to the formation of the process zone in which the thermal input is mainly governed by the stirring component whereas plastic deformation stems from stirring as well as extrusion. In the case at hand, the extrusion motion between condition E to F increases by 1.5 mm/rot and it can thus be argued that the observed decrease in grain sizes (Fig. 5.31) stems from this increase in extrusion motion. As previously described in section 5.1.3, recrystallization phenomena are a function of process temperature as well as strain rate. Due to the difficulty of obtaining suitable modeling input data at the present processing speeds, the present study focuses on the effect of the process temperature when describing the occurring recrystallization phenomena.

Concerning the misorientation angle ratio, the results depicted in Fig. 5.31 show that grain growth in the externally cooled samples initiates during the passing of the tool but is interrupted due to the cooling effect of the surroundings. This results in small recrystallized grains which still contain high amounts of deformation energy in the form of dislocations,

which are randomly oriented and not yet polygonized. The samples processed at ambient temperature, on the other hand, experience a less forceful cooling which results in larger grain sizes. Additionally, the randomly oriented dislocations within the grains polygonize and form low angle boundaries, which in turn results in the decrease in misorientation angle ratio as previously seen in Figs. 5.19(c) and 5.28(d). This effect of increasing polygonization becomes even more pronounced when additional thermal energy is added through an external process as shown for the micro flat tensile tests in section 5.3.2.

### 5.2.3 Multi Line Experiments

Fig. 5.32 depicts a sketch illustrating the process zone superpositions during multi line processing. The first pass creates a conventional single line process zone (Z.1), with the previously observed grain refinement originating from dynamic recrystallization. Once the second pass is made, zone Z.1 is partly consumed by zone Z.2, which extends into already processed material of zone Z.1.


Figure 5.32: Sketch of the overlying process zones of the multi line process.

Due to the additional strains imposed by the shoulder and probe, as well as the additional thermal cycle during the second pass, the remaining Z.1 zone exhibits a slightly different texture than the single line material. Once the third pass is made, a third zone is superimposed in which zone Z.3 is processed over a majority of zone Z.2, resulting in a final grain size between 0.9 $\mu$m and 1.3 $\mu$m. The pattern is then repeated multiple times until the full sample width is reached.

As previously stated in section 4.4.4, the specimens for formability tests, which have been created from multi line processed material, have been machined to a thickness of 1 mm by removing 0.5 mm from top and bottom of the processed sample. This way it could be ensured that the tested material underwent a repetitive pattern of two overlaying single line process zones, without the influence of the shoulder and the bottom layer of semi-processed material.

The resulting textures of the multi line samples are shown in the pole figures and inverse pole figures of Fig. 5.33. The pole figures of condition C (Fig. 5.33(a)) closely resemble the ones previously observed for the single line processed material (Fig. 5.25(b)), including a high intensity singular basal peak with a secondary peak at the opposite side of the

hemisphere. In addition, the more distributed texture of the single line experiments, (Fig. 5.25(f)) gives way to a more consolidated texture which moves towards the ⟨0001⟩ pole, as shown in Fig. 5.33(b). While the *c*-axis tilt into processing direction is with ≈ 42° higher than the single line experiments (≈ 33°), a rotation from the normal direction of ≈ 45° around the processing direction can also be seen.

This rotation towards the transverse direction can be associated with the superimposing nature of the multi line process. As one single line is placed at 2 mm distance to the next, multiple macroscopic shear planes, including the probe of the second pass as well as the stresses introduced by the shoulder, are acting on the material. The textural investigations thus picture a region besides a respective stir zone center and can thus be compared to the stir zone 2 (Fig. 5.17(b)), in which the macroscopic shear plane is less intense, resulting in additional tilt towards the transverse direction.

This effect becomes even more pronounced for the sample processed in condition E. As shown in the pole figures 5.33(c), a rotation of ≈ 90° from the normal direction around the processing direction can be noted.

In addition to the rotation, the tilt of the *c*-axis spreads out, creating a protracted area in the angular range between ≈ 38° to ≈ 64° which is highly desirable for enhanced multi axial formability. Both, the rotation of the high intensity peak away from the normal

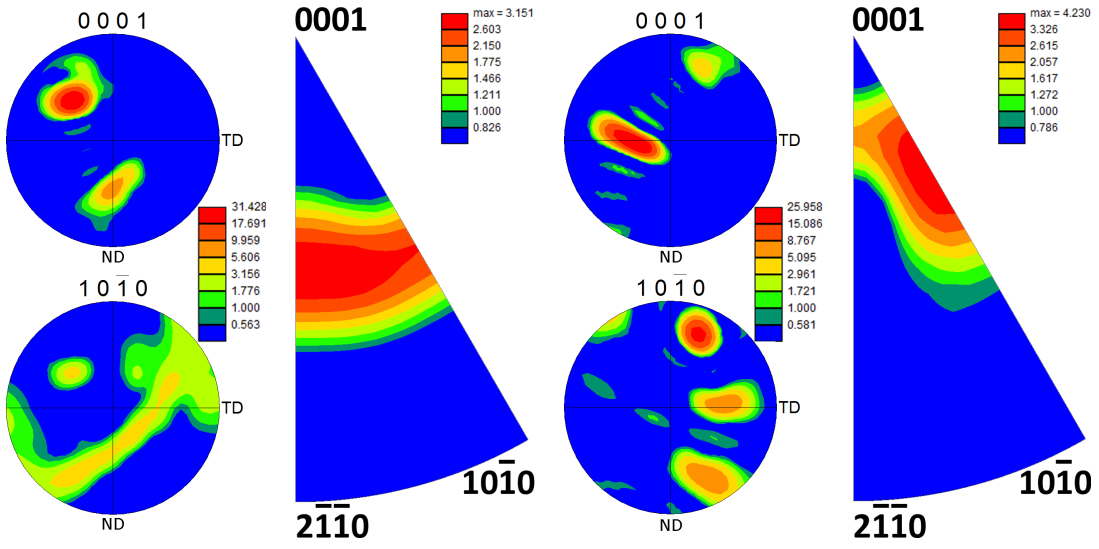


(a) (b) (c) (d)

Figure 5.33: {0001} and {10$\bar{1}$0} pole figures and [001] inverse pole figures of the multi line samples processed in condition C (a, b) and condition E (c, d).

direction and the rotation of the $c$-axis towards the transverse direction, can be attributed to the multiple passes of the tool. The difference between condition C and E results of the decreasing shear layer size with increasing processing speed and increasing axial force. While the {0001} pole figure (Fig. 5.33(c)) of condition E still closely resembles what has been observed for the single line experiments, the $\{10\bar{1}0\}$ pole figure depicts a completely new textural evolution. The previously observed low intensity band structure (Fig. 5.25(c)) experiences break down and gives way to multiple singular peaks with higher intensities. These peaks represent discrete rotations of the $\{10\bar{1}0\}$ prismatic planes around the $c$-axis. This observation is supported by angular measurements between the peaks, showing rotations of $\approx 60°$ which is in agreement with the rotation of one $\{10\bar{1}0\}$ prismatic plane to the next. This effect is mirrored in more detail in the inverse pole figure shown in Fig. 5.33(d). In comparison to the inverse pole figure for condition C, a clear shift away from the $\langle 2\bar{1}\bar{1}0\rangle$ pole towards the $\langle 0001\rangle$ pole can be noted. As this effect has not been observed in the single line experiments, it can be concluded that the multiple processing instances are responsible for the shift away from the $\langle 2\bar{1}\bar{1}0\rangle$ pole while simultaneously pronouncing the $\{10\bar{1}0\}$ prismatic planes. Al-Samman et al. [200] investigated orientation dependent slip and twinning during compression and tension of strongly textured Mg AZ31. In their research, the authors found similar textural shifts as observed in Fig. 5.33(d) and attributed them to the activation of double basal slip.

The misorientation angle distribution for conditions C and E is shown in Fig. 5.34. As observed in the single line experiments, a large, deformation-induced low angle boundary peak emerges and increases with increasing processing speed.

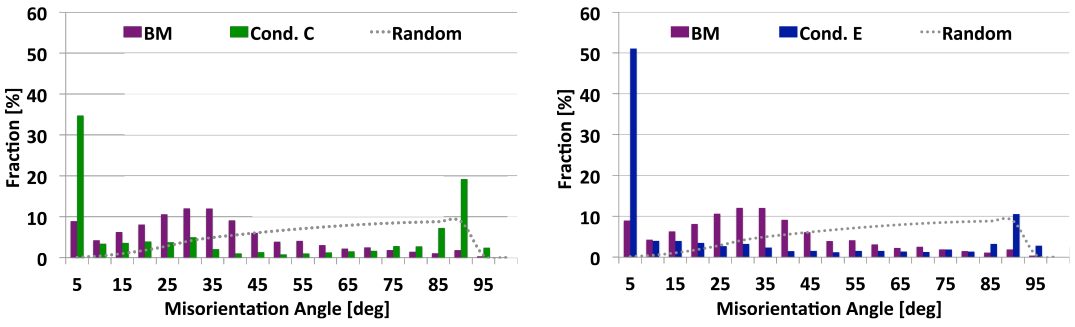


(a) (b)

Figure 5.34: Misorientation angle charts of multi line samples processed in condition C (a) and E (b).

In both conditions, the low angle boundaries are dominantly located as subdomains within new, recrystallized grains and seldom create a new grain boundary. The misorientation angle ratio further decreases with respect to the single line material values resulting in a ratio of 1.47 and 0.73 for condition C and E, respectively, making them the lowest values of all investigated conditions. The corresponding increase of low angle boundaries can be explained by the additional processing step, adding further strain to already processed material.

In both conditions, the regime between 10° and 85° shows only minor fractions. The buildup between 15° and 30°, on the other hand, is muted and closely resembles the ideal random orientation. As previously detailed for the single line material, the high angle boundary peak between 85° and 95° can not be attributed to 86° $\{10\bar{1}2\}$ extension twinning as their overall fraction remains below 3%. The high angle boundary peak, which is decreasing with increasing PS, can thus also be attributed to deformation induced crystallographic rotation of twins and matrix from their initial orientations.

#### Interface Zones

As previously shown in Fig. 5.32, the multi line process produces overlapping zones in which an interface between the respective stir zones is created. This interface features a distinct microstructural and textural evolution which is detailed in the inverse pole figure maps, pole figures and inverse pole figures shown in Fig. 5.35.

In detail, Fig. 5.35 depicts the transition zone in a sequence of three pictures in which transition zone 1 is adjacent to the first homogenized stir zone. Transition zone 2 is an intermediate region between the stir zone and the final interface region of transition zone 3. Beyond transition zone 3 a stir zone reemerges and the pattern repeats itself.

A more detailed understanding of the textural evolution can be gained from the pole figures and inverse pole figures of Fig. 5.35. In the pole figures from transition zone 1 to transition zone 3, the *c*-axis tilt as well as the intensity peak close to the center of the pole figure is continuously decreasing from one transition zone to the next.

While the *c*-axis tilt of transition zone 1 still closely resembles the stir zone texture of the multi line material depicted in Fig. 5.33(a), transition zone 3 experiences a *c*-axis tilt away from the center of the pole figure while the rotation around the processing direction remains. This shift is to be expected, as the second pass in multi line processing will create a new stir zone center (previously denoted stir zone 1) and a transition zone (previously

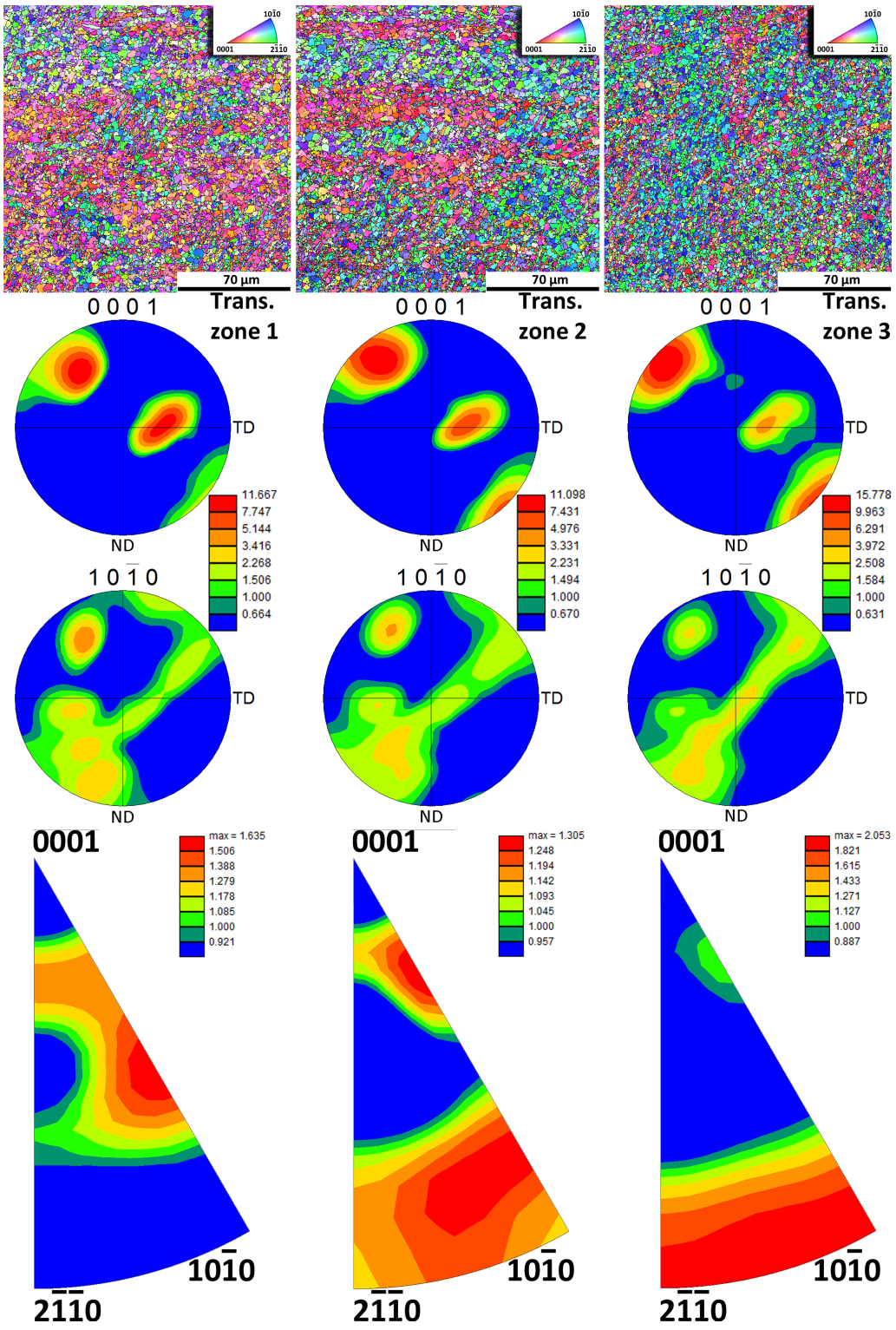


Figure 5.35: Inverse pole figure maps, {0001} and {10$\bar{1}$0} pole figures and [001] inverse pole figures of the transition zone of the multi line samples processed in condition C.

denoted stir zone 2) onto already processed material.

As shown in the inverse pole figures of transition zone 1 to transition zone 3, the $\langle 0001 \rangle$ pole oriented texture continuously changes to a texture in which the $\langle 10\bar{1}0 \rangle$ and $\langle 2\bar{1}\bar{1}0 \rangle$ poles experience evenly distributed textural components. This shift can be attributed to the re-processing of already textured material. While the shift towards the $\langle 10\bar{1}0 \rangle$ and $\langle 2\bar{1}\bar{1}0 \rangle$ pole would generally promote other deformation mechanisms besides basal slip, Kang et al. [44] showed that increased textural randomization can result in higher deformation capabilities. The misorientation angle distribution for all three transition zones is given in Fig. 5.36.

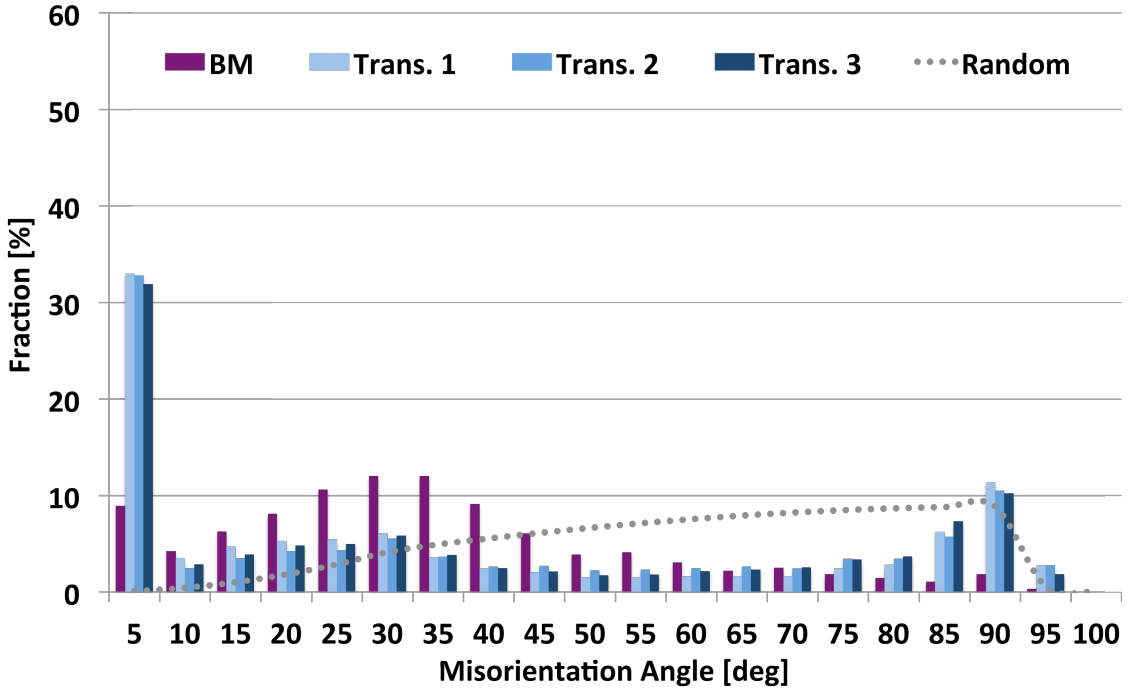


Figure 5.36: Misorientation angle chart for the transition zone of a multi line sample (Cond. C).

While no significant differences can be made out within the three transition zones, a distinct decrease in the high angle boundary peak between 85° and 95° compared to the stir zone material (Fig. 5.34(a)) can be observed. As previously discussed, this decrease can be attributed to a deformation induced reorientation of matrix grains accompanied by dynamic recrystallization. The textural intensity in the interface decreases to 11 - 15 m.rd., which is close to the base material values and much lower than values measured in the stir zone. While this decrease can be explained by the randomization of the texture, it is

interesting to note that the misorientation angle ratio increases slightly to values between 1.5 and 2 while the grain size remains within the previously measured regime between 0.9 $\mu$m and 1.3 $\mu$m. It can thus be argued that a further reduction of the grain size might be accomplished by additional passes over already processed material as previously investigated by Ramesh-Babu et al. [182] and Chang et al. [45].

### 5.2.4 Summary of the Microstructure and Texture Investigations

The textural understanding gained from the externally cooled samples has been utilized to fabricate material with a basal slip enhancing textures in single and multi line samples by using high speed FSP.

In the results from the single line processed material, a pronounced texture could be observed. This texture mainly features a tilt of the *c*-axis into processing direction. This tilt is a function of the macroscopic shear plane, which is mainly governed by the geometry of the shear layer. The shear layer geometry on the other hand is governed by the processing pitch and tool geometry. The tilt of the *c*-axis can thus be tailored using high speed FSP in combination with appropriate processing parameters and tool geometries. With increasing processing speed, the overall textural distribution additionally moves towards the $\langle 0001 \rangle$ pole, which is desired for enhanced formability, as illustrated in Fig. 5.23. The increasing amount of low angle boundaries appears to be correlated to dynamic recrystallization, promoting poligonization of randomly oriented dislocations within newly formed grains.

The multi line experiments revealed a persistent decrease in grain size and a rotation of the *c*-axis. While the texture in the center of the stir zone of the single line samples revealed a tilt towards the processing direction, the multi line experiments exhibit an additional tilt towards the transverse direction, which can be correlated to the superposition of a second and possibly a third macroscopic shear layer onto already processed material. In condition E, the $\{10\bar{1}0\}$ prismatic planes additionally exhibit a discrete rotation. While the overall textural tendency towards the $\langle 0001 \rangle$ pole is still present, a pronounced textural intensity between the $\langle 0001 \rangle$ and the $\langle 10\bar{1}0 \rangle$, should promote double basal slip, which is highly desired for enhanced formability. The amount of low angle boundaries increases with the main fraction located within newly formed grains, supporting the above statement of rising poligonization with increasing strain and temperature. The interface region between the stir zones shows a reorientation of the $\{0001\}$ basal planes away from the processing direction towards the normal direction.

## 5.3 Mechanical Testing

In the following, the mechanical testing results will be presented and discussed. In detail, the nanoindentation tests have been aimed at investigating the correlation of the resulting texture to the materials ability to form extension twins. Micro flat tensile tests have been carried out to investigate the mechanical response of a single microstructure and texture in larger specimen and to facilitate the transferability of the obtained knowledge to full scale specimen. Finally, the formability of fully processed specimen has been investigated by forming limit tests.

### 5.3.1 Nanoindentation Tests

In general, the pastic volume introduced by a nanoindenter can be considered to have the shape of a sphere which results in a complex stress state. The deformation response of the tested material must thus be regarded as a function of this complex stress state [285]. As detailed in section 3.2.2, the deformation response of Mg is primarily driven by twinning and basal slip. For the present study, this is of particular importance as it allows to correlate the texture resulting from high speed FSP to the materials ability to form extension twins at a high spatial resolution.

The formation of twins has been detailed in section 3.2.2. It has been shown, that $\{10\bar{1}2\}$ extension twins are most commonly observed in Mg. They are formed once a tensile load is applied along the $c$-axis or a compressive load onto the prismatic planes and in turn do not form under compressive loading along the $c$-axis.

Once an extension twin has formed, it rotates the $c$-axis by 86.3° around the $\langle 11\bar{2}0\rangle$ direction, which consequently limits further deformation along the $c$-axis as schematically depicted in Fig. 5.37. Basal slip, on the other hand, occurs as soon as a load is applied at any other angle than 0° or 90° to the $c$-axis. The possible activation of slip is frequently analyzed with help of the Schmid factor $m$, which is defined as the ratio between the critical resolved shear stress $\tau_{CRSS}$ and the yield stress

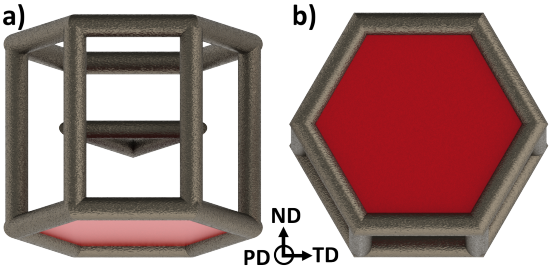


Figure 5.37: Schematic of the rotation of the unit cell due to extension twinning. (a) before and (b) after twinning.

$\sigma_Y$ ($m = \tau_{CRSS}/\sigma_Y$). The Schmid factor can be described by a double *cos* relationship of $m = cos\phi\ cos\lambda$ in which $\phi$ and $\lambda$ are the angles between the loading direction and the slip/twinning plane normal and the slip/twinning direction, respectively [286]. With a high Schmid factor only small $\sigma_Y$ are required to achieve a certain $\tau_{CRSS}$. Plotting the Schmid factor as a function of the angle between the *c*-axis and the loading direction creates a parabola between $m = 0$ and $m = 0.5$ with the maximum at 45° [278]. A tilt of the *c*-axis by 45° into the loading direction can thus be considered most favorable for basal slip. It should be noted at this point that the gathering of reliable information on the $\tau_{CRSS}$ for the different deformation modes in Mg is an ongoing challenge.

For the interpretation of the following results, the order at which twinning and basal slip occurs must be considered. Shin et al. [287] describe the formation of twins, and in particular extension twins, to be the initial deformation mechanism in nanoindentation of Mg. This is of particular importance as the textural alterations found in the processed specimen of the present study can either promote or demote twinning.

All measurements have been conducted on cross-sections, such that the indenter is pointing into processing direction. Hardness and modulus were both determined during loading via continuous stiffness measurement and unloading using the standard Olilver & Pharr [225] method. Both values agreed reasonably well, hence only hardness and modulus from unloading are plotted in the following. A complete overview over all acquired data can be found in Fig. 8.6 and 8.7 in the appendix.

#### Base Material

The resulting hardness and modulus values of the base material are presented in Fig. 5.38. An overall homogeneous distribution can be observed in which the hardness shows an average value of ≈ 0.78 GPa and the Young's modulus reaches an average value of ≈ 45.9 GPa. These results are in good agreement with values previously reported in the literature [213]. For the following investigations of the single line experiments, the same hardness and modulus scale as for the base material will be used to enhance the comparability.

#### Single Line Experiments

The hardness and modulus results for single line experiments in condition A are shown in Fig. 5.39. The thermo mechanically affected zone 1 (-7 mm to -1.5 mm) displays an

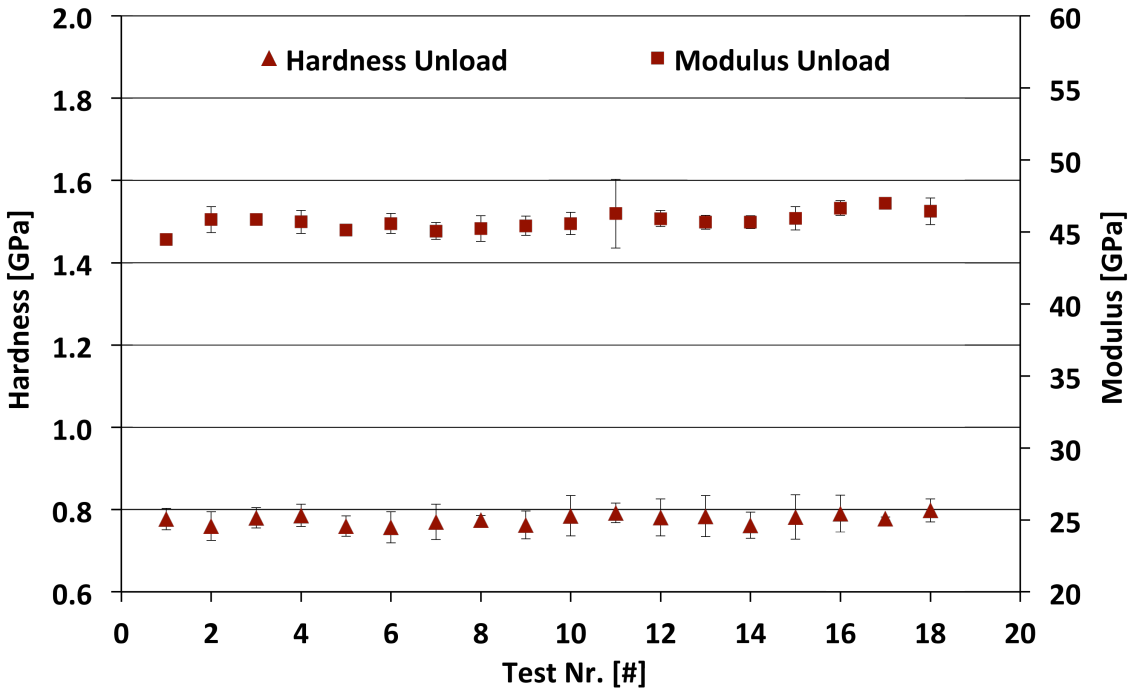


Figure 5.38: Hardness and modulus results from nanoindentation tests of the base material.

average hardness distribution of ≈ 0.8 GPa, which is close to what has been observed for the base material. Towards the center of the stir zone, the hardness continuously decreases until an average value of ≈ 0.72 GPa is reached. This decrease can be explained by the microstructural and textural conditions of the process zone:

In the base material, the *c*-axis (Fig. 5.24(d) on page 81) is oriented orthogonal to the loading direction as shown in section 4.7. This results in extension twinning directly underneath the indenter tip where the loading direction is parallel to the indentation direction. Once the material underneath the indenter has been twinned by extension twinning, the rotation of the basal planes by 86.3° around $\langle 11\bar{2}0 \rangle$ results in a decreasing ease of subsequent basal slip.

In the stir zone of condition A, on the other hand, the observed decrease in hardness can be related to the ability of limited basal slip after the formation of extension twins. As the *c*-axis of the stir zone is tilted by only ≈ 14° (Fig. 5.25), extension twins can still easily be formed. The following rotation by 86.3° will retain the materials ability for limited basal slip resulting in the observed decrease in hardness.

The nanoindentation results for the single line material processed in condition C are shown in Fig. 5.40. Due to the higher volatility of the results and in order to compensate

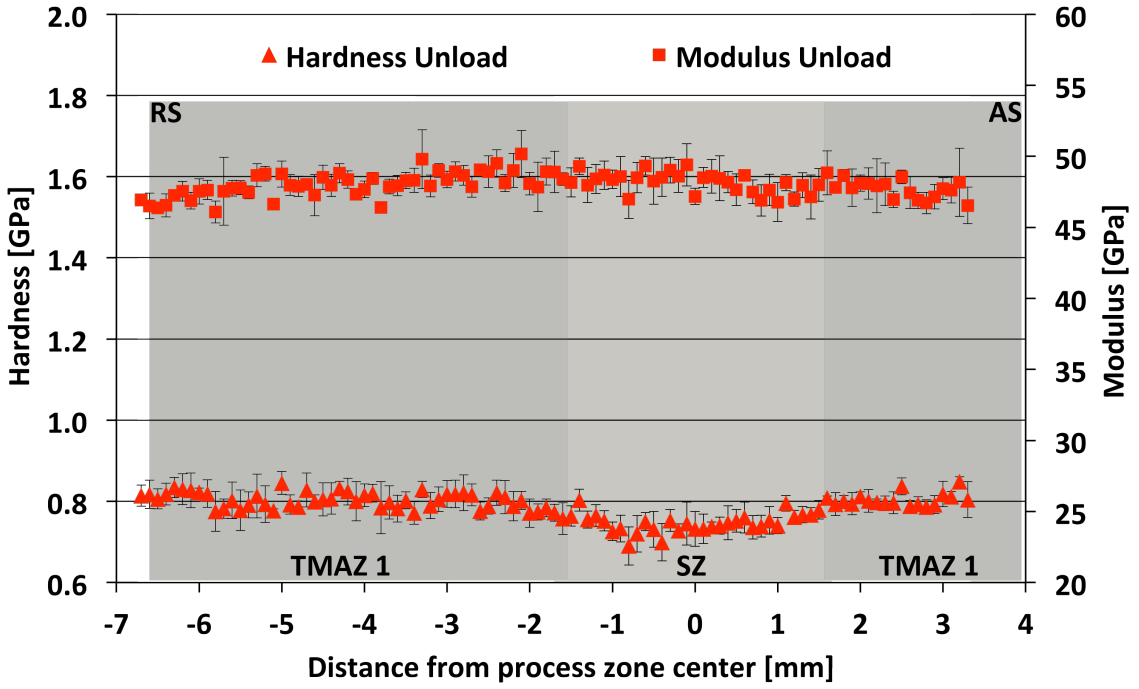


Figure 5.39: Hardness and modulus results from single line nanoindentation tests of condition A.

for potential material pile-up or sink-in during indentation (see section 4.4.1), correction measurements have been conducted. Within these measurements, the contact area has been measured manually and the newly obtained value used to recalculate a corrected modulus and hardness value. The corrected modulus and hardness values are shown as an overlay for condition C and E in Fig. 5.40 and Fig. 5.42, respectively. The following discussion will be focused on the corrected values.

Condition C exhibits a more diverse hardness evolution compared to condition A. The thermo mechanically affected zone 2 (-12 mm to - 7 mm) features a significant increase in hardness reaching values of up to 1 GPa. The hardness increase in the thermo mechanically affected zone 2 can be correlated to the existence of twin boundaries after processing as described in section 5.2.1 and shown in detail in Fig. 5.21. Due to the high ratio between the translational and rotational motion in high speed FSP, the material to the side of the tool experiences a compressive loading onto the prismatic planes which results in the formation of extension twins. Thus, pre-twined material is tested during nanoindentation effectively hindering further twinning and decreasing the ease of subsequent basal slip.

Within the thermo mechanically affected zone 1 (-7 mm to - 1.5 mm), the hardness is

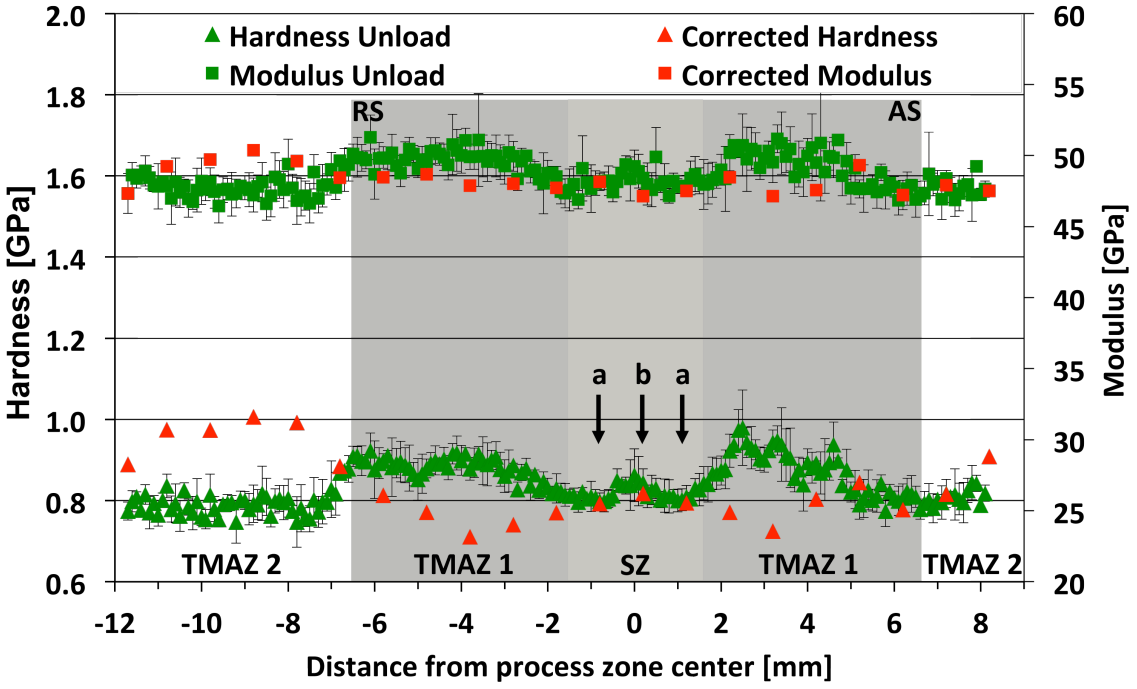


Figure 5.40: Hardness and modulus results from single line nanoindentation tests of condition C.

decreasing below base material values. This can be correlated to the reduction of pre-existing twin boundaries (Fig. 5.21) and the increasing randomization of the texture (Fig. 5.15(b)). While the reduction of pre-existing twin boundaries aids the formation of new twins, the increased textural randomization eases basal slip in the present multiaxial stress state which is surrounding the indenter.

Within the area of the stir zone, the hardness increases (Fig. 5.40 - a), until reaching base material values in the center (Fig. 5.40 - b). As the amount of twin boundaries in the stir zone falls below 1% (Fig. 5.21), the observed increase in hardness can be correlated to the effect of *c*-axis tilt on the ease of the creating extension twins. In regions a, the hardness reaches the level of the base material as a balance between the formation of extension twins and basal slip is reached. Due to the rotation of the basal planes around the shear layer, the *c*-axis is slightly tilted away from the axis of compression (Fig. 5.41 - a)). This results in a decrease in the formation of extension twins coupled with an increase in basal slip reaching in total the same amount of compliance as the base material. In region b (the center of the stir zone), on the other hand, the *c*-axis is further aligned with the axis of compression (Fig. 5.41 - b)) resulting in an increase in hardness as the ease of activating

extension twinning is reduced.

The resulting hardness distribution for condition E is shown in Fig. 5.42. While the thermo mechanically affected zone 2 (7 mm to 12 mm) and the thermo mechanically affected zone 1 (-7 mm to -2.5 mm) still feature the previously observed hardness increase and decrease, respectively, the stir zone experiences a continuous hardness decrease towards its center. This decrease can be attributed to the continued tilt of the $c$-axis into compression direction. While this tilt of $\approx 42°$ hinders the activation of extension twinning, it further promotes basal slip, which in the case of condition E results in a decrease in hardness compared to the base material.

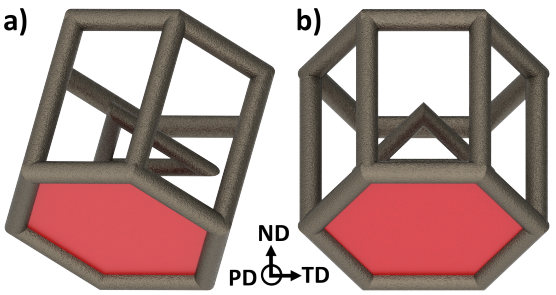


Figure 5.41: Representation of the rotation of the unit cell in the two regions of the stir zone as indicated in Fig. 5.40.

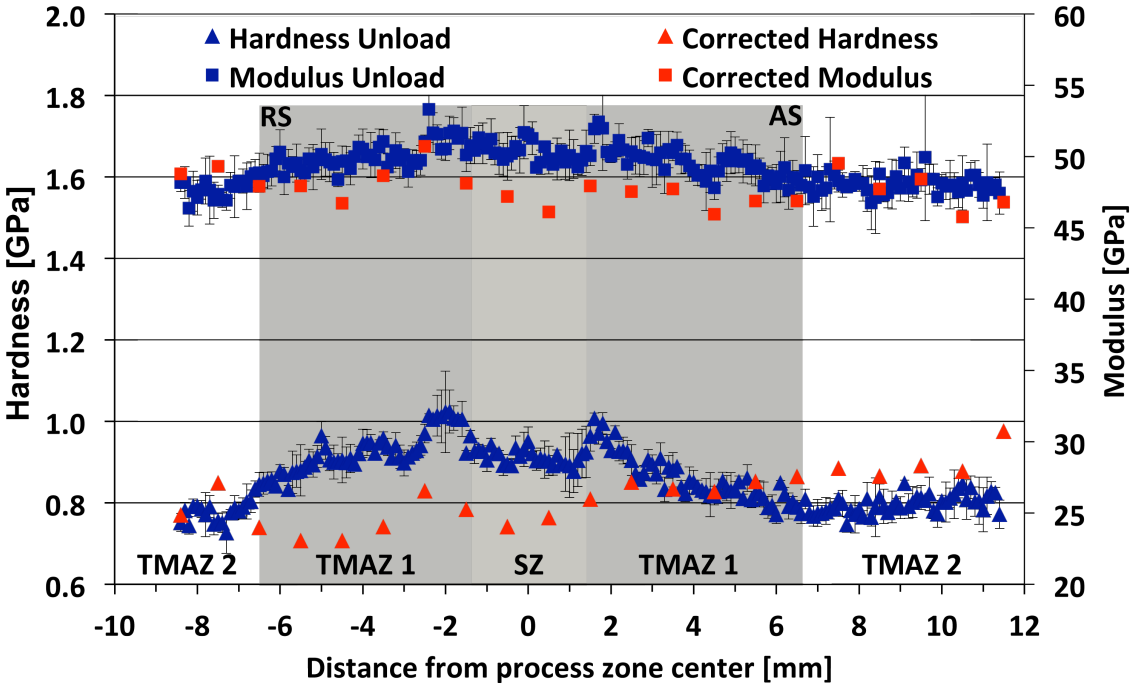


Figure 5.42: Hardness and modulus results from single line nanoindentation tests of condition E.

Interestingly, the grain size appears to have no discernible effect on the resulting hardness. While the material processed in condition C and E exhibit similar grain sizes in the stir

zone, the resulting hardness values differ greatly. It can thus be concluded that the crystal reorientation and thus the resulting change in Schmid factor are mainly responsible for the observed differences in hardness.

In conclusion, the nanoindentation results reflect the materials ability or inability to deform via $\{10\bar{1}2\}$ extension twins and via $\{0001\}$ $\langle 11\bar{2}0\rangle$ basal slip. The results thus mirror the observed texture evolution in the single line specimen and confirm the assumptions for the respective metallurgical zones. In detail, the formation of extension twins results in an initial decrease in hardness while the resulting rotation of the *c*-axis by 86.3° $\langle 11\bar{2}0\rangle$ is likely to hinder subsequent deformation such as basal slip. The grain size appears to have only minor effects on the resulting mechanical properties. The controlled rotation of the *c*-axis into a basal slip favorable position can thus allow for large scale formability as will be presented in the following sections 5.3.2 and 5.3.3.

### 5.3.2 Micro Flat Tensile Tests

Micro flat tensile tests have been conducted in order to determine the local properties of the stir zone. Base material specimens have been tested into rolling direction, transverse direction and at 45° to the rolling direction and the summary of the tensile results is given in Tab. 5.4.

Table 5.4: Tensile test results of the base material in micro flat tensile specimen.

| Direction | $R_m$ [MPa] | $R_{p0.2}$ [MPa] | A [%] |
|---|---|---|---|
| RD | 259 ± 4 | 149 ± 22 | 11 ± 4 |
| TD | 223 ± 27 | 141 ± 24 | 7 ± 4 |
| 45° | 241± 15 | 157 ± 11 | 8 ± 5 |

Processed specimens of conditions A, C, E and F have been tested into processing direction. Fig. 5.43 depicts representative stress - strain curves of the base material (tested in rolling direction), as well as specimens processed in conditions A, C, E and F. Due to the low average surface roughness of 6,45 $\mu$m, micro notch effects did not significantly alter the stress state.

### Mechanical Properties

The base material stress - strain response as shown in Fig. 5.43 is consistent with what has previously been seen for the macroscopic specimens (section 4.7). After an initial elastic regime, the increasing plastic deformation leads an area of work hardening and finally fracture with limited necking. While the $R_m$ of the base material reaches values of almost 260 MPa, which is well within the regime observed for the macroscopic specimens, the tensile elongation exhibits mean values between 7% and 11% (Tab. 5.4), which is below of what has previously been observed for the macroscopic specimen.

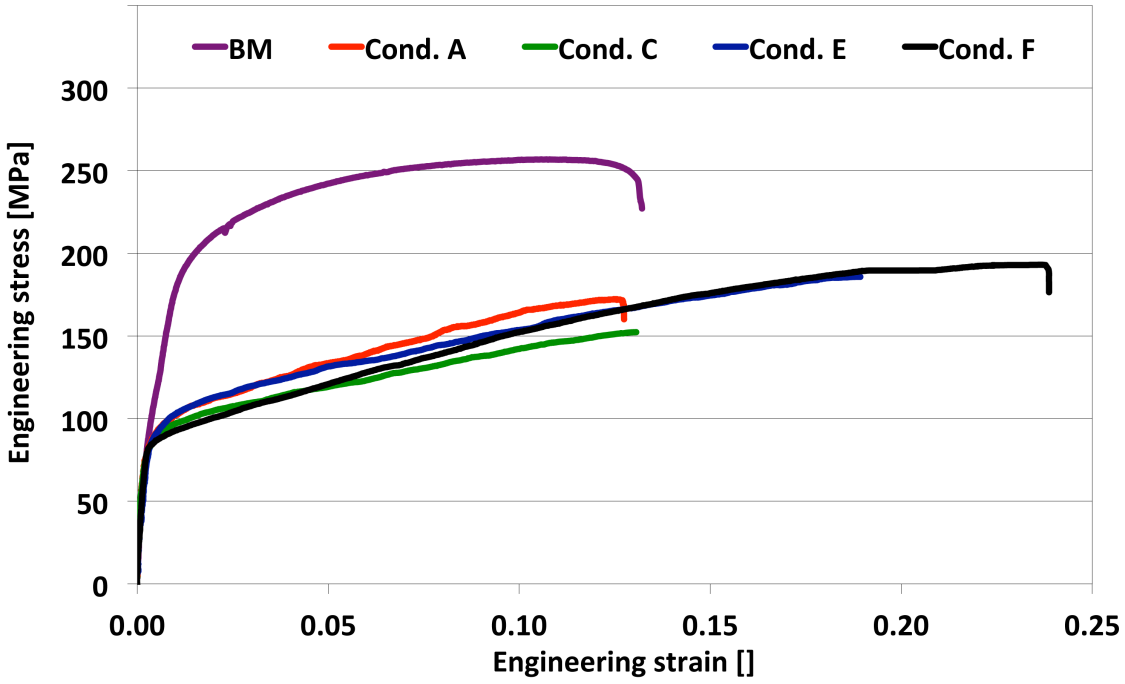


Figure 5.43: Representative engineering stress - strain curves for micro flat tensile tests.

The stress - strain response of the processed material differs greatly from that of the base material. While all processed specimens exhibit a decrease in $R_{p0.2}$ and $R_m$, the most noticeable change can be seen in the increased tensile elongation, with increasing processing speed. In detail, the $R_{p0.2}$ and $R_m$ show a reduction from 122 MPa and 255 MPa (base material) to 85 MPa and 175 MPa, respectively. This reduction rules out grain boundary strengthening with decreasing grain size as the primary deformation controlling mechanism in Mg AZ31, as proposed by Yuan et al. [41].

The three step strain hardening and necking regime observed for the base material is replaced by a long and continuous increase in work hardening, initiating at an earlier

yield point for all processed specimens. Similar stress strain curve evolutions for FSP Mg AZ31 have previously been observed by Woo et al. [39]. While cross-sectional tensile tests (‖ transverse direction) revealed a decrease in tensile elongation, specimen tested into processing direction and taken from the stir zone revealed an increase over the base material of up to 28% accompanied by a reduction in $R_{p0.2}$. The authors correlate, the increase in elongation and decrease in tensile strength to the textural changes in the stir zone, namely the variation in the Schmid factor value for basal slip, which is in accordance to the textural results of the present study as summarized in section 5.2.1.3.

While the specimen processed in condition A fracture at approximately the same strain level as observed for the base material, the specimen in condition E increase their straining capability by up to 40%. The specimen processed in condition F even surpass those values with a tensile elongation of 24%, resulting in an increase of 85% compared to the base material. Almost no necking has been observed as the specimen fracture abruptly. Fig. 5.44 depicts the tensile results of the base and processed material and a list of all tensile results of the processed material is given in Tab. 8.3 in the appendix.

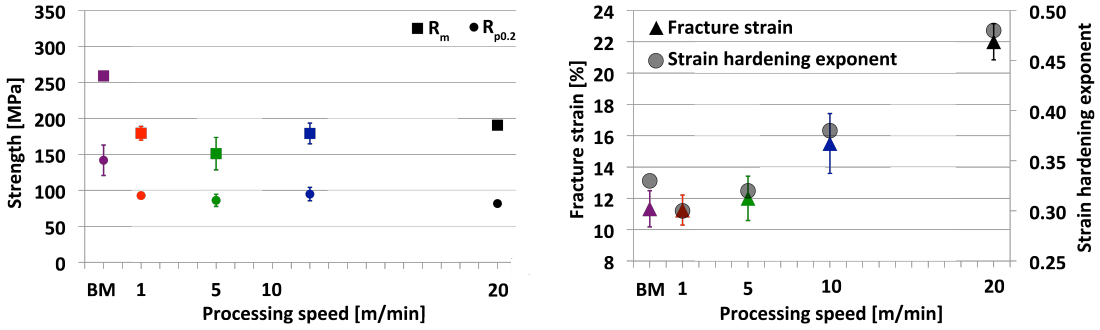


(a) (b)

Figure 5.44: Ultimate tensile and yield strength (a) and fracture strain and strain hardening exponent (b) of micro flat tensile specimens including the standard deviations.

While the mean $R_{p0.2}$ values for the processed specimens are confined to a narrow band between 82 MPa and 95 MPa, the $R_m$ experiences a greater variation ranging from 151 MPa to 191 MPa. The strain hardening exponent n, which has been derived from $n = dlog(\sigma)/dlog(\epsilon)$ evaluated from the slope of the $log(\sigma), log(\epsilon)$ plot of the true stress strain curves, experiences a similar increasing trend. Comparable results have been reported by Kang et al. [44], stating an increase in strain hardening exponent with an increase in grain size, as well as softening of the sharp rolling texture. Even though the results of

the present study suggest a much smaller influence of the grain size, the positive effect of texture modification can be confirmed.

One possible explanation for the uniform reduction in $R_{p0.2}$ and $R_m$, observed in all processed specimens might be found in the $\tau_{CRSS}$ relationship formulated by Hutchinson et al. [203]. The authors propose that an increase in dislocation density, as induced by FSP [288], could dampen the strong anisotropic properties usually observed in HCP alloys which is described to be one of the limiting factors for low temperature formability. This decrease in anisotropy is ascribed to a decrease in $\tau_{CRSS}$ ratio between prismatic and basal slip with increasing dislocation density which in turn results in a reduction of $R_{p0.2}$.

A more texture based explanation for the reduction in $R_{p0.2}$ and the observed increase in tensile elongation can be found by the promotion of basal slip and extension twinning [289] by the tilt of the *c*-axis towards the processing direction. Results supporting this statement have been obtained by Chen et al. [204], reporting an increase in tensile ductility due to the weakening of the rolling inherent basal texture.

A reduction in $R_{p0.2}$ accompanied by improved ductility has also been observed by Yang et al. [290]. The authors have investigated ultra fine grained Mg AZ31, which after annealing treatment underwent grain growth, resulting in a reduction of residual stresses and higher n values. Similar effects have been observed in the present study as the n values increase with increasing processing speed as shown in Fig. 5.44(b). Additionally, microstructural investigations on the machined specimens revealed an increase in grain size for condition E and F compared to the pre-machined condition. This increase can be attributed to the thermal cycle occurring during specimen preparation by electrical discharge machining. In order to quantify this change for conditions E and F, grain size measurements have been undertaken in three heights (close to the top surface, the middle and the bottom surface), showing a homogeneous increase in grain size. While the as processed samples showed a grain size range between 2.5 $\mu$m (Cond. E) and 1.8 $\mu$m (Cond. F), the machined specimens experienced an increase to 3.1 $\mu$m and 4.1 $\mu$m for condition E and F, respectively.

This processing condition dependent grain growth indicates different levels of remaining residual strains within the processed material, as higher processing speeds result in higher levels of grain growth. The influence of electrical discharge machining on the texture, on the other hand, is negligible as shown in Fig. 5.45(a) and 5.45(c). Compared to the as-processed material (Fig. 5.25), the same consolidation of the basal planes, paired with a slight fanning out has been observed. Additionally, a limited rotation around

the processing direction can be noted, which can be related to a minimal rotation of the specimen in the mounting process. Similar effects have been investigated by Yang et al. [281], showing only minor textural changes of initially hot deformation and consequently annealed Mg AZ31. Additionally Wang et al. [181] investigated the dependence of grain size (6.1 $\mu$m to 2.6 $\mu$m) on the tensile behavior of FSP Mg AZ31 and concluded that the

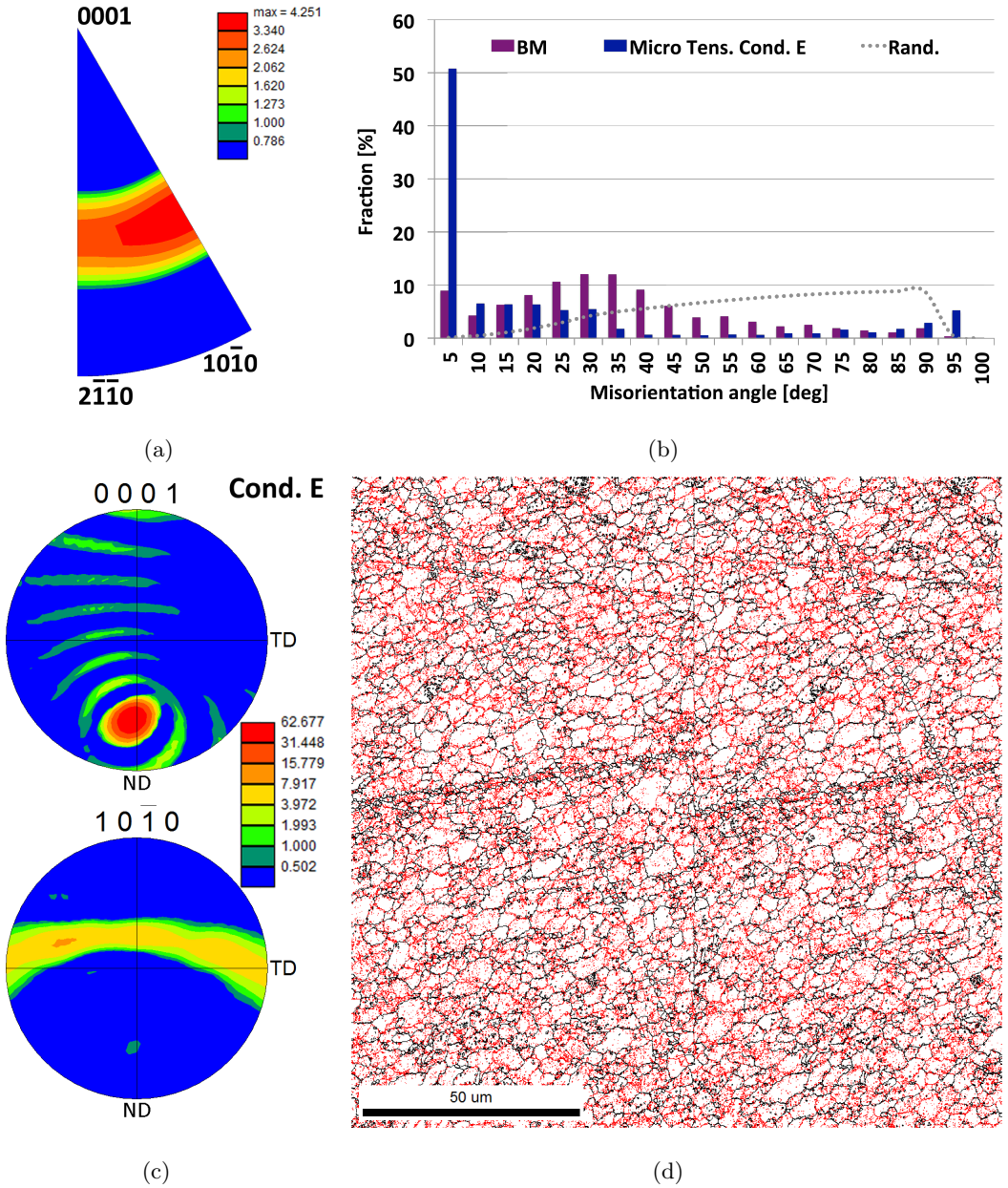


Figure 5.45: Exemplary [001] inverse pole figure (a), pole figure (b), misorientation angle chart (c) and grain boundary map (d) of a condition E specimen prepared by electrical discharge machining.

textural changes in the stir zone superimpose the variations in grain size.

In addition to the consistent tilt of the basal planes, the misorientation angle distribution (Fig. 5.45(b)) shows a further increase in low angle boundaries compared to the as-processed material shown in Fig. 5.28(c). As previously detailed in section 5.2.2, the additional thermal energy introduced via electrical discharge machining is thought to lead to further polygonisation of the remaining randomly oriented dislocations, which in turn form low angle boundaries. The increase in low angle boundaries is shown in Fig. 5.45(d), in which low angle boundaries and high angle boundaries are marked in red and black, respectively. Large amounts of low angle boundaries can be found within grains surrounded by high angle boundaries. Previous investigations by Edalati et al. [75] conducted on high pressure torsion of pure Mg showed, that high amounts of high angle boundaries are an important factor for strengthening the material. It can thus be inversely argued that a low amount of high angle boundaries, as observed in the present study, might be one factor to increase the materials formability.

It can therefore be argued that the increased tensile elongation for condition E and F is primarily driven by the textural modifications, giving rise to easily activated twinning and basal slip, while the contribution of grain size appears to have only a minor, if not negligible, effect.

#### Microstructure and Deformation Mechanisms

An overview over the post test microstructures of the base material and the specimens processed in condition A, E and F can be seen in Fig. 5.46. For each condition, regions of interest are marked and will be discussed in the following.

The post test microstructure of the base material is given in Fig. 5.46(e). In detail, the original grain size and shape is conserved, including the previously described agglomeration of small grains, forming clusters close to larger grains (I). The presence of occasional twins can be observed. These are located inside a grain without reaching both grain boundaries (II) or extending from one grain boundary to the next (III). The presence of extension twins within the base material under tensile load has been expected to be rather small, as the base material texture would only allow for compression twins. As compression twins are not only contributing very little to the overall deformation but are also difficult to visualize in an optical microscope [199] it can be concluded that the twins visible in Fig. 5.46(e) are indeed $\{10\bar{1}2\}$ extension twins.

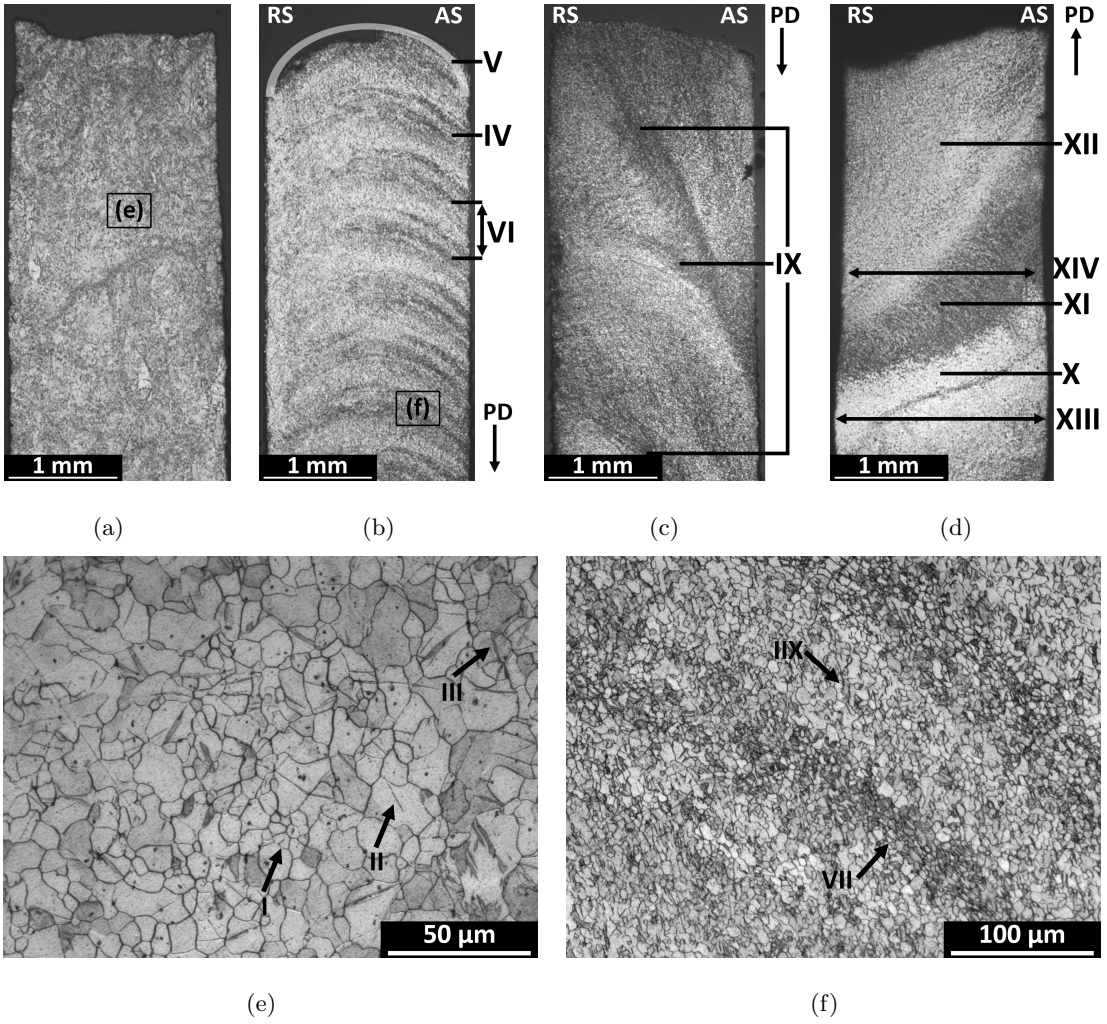


Figure 5.46: Overview over a fractured micro flat tensile specimens of the base material (a), condition A (b), condition E (c) and condition F (d). Macrograph of the deformation zone of a fractured micro flat tensile specimens. Base material (e) and condition A (f).

The effect of $\{10\bar{1}2\}$ extension twinning on the deformation behavior of Mg has already been discussed in section 3.2.4. Investigations conducted by Huang et al. [34] have shown that $\{10\bar{1}2\}$ extension twins are primarily activated during the initial stage of tensile deformation. In combination with basal slip, which is also occurring primarily during the first deformation stages, the strain incompatibility at grain boundaries rises. In turn, non-basal slip systems become active as soon as the stress concentration due to strain incompatibility is sufficiently high [27,28]. Considering the orientation of the basal planes within the base material, which are unfavorably oriented for extension twinning and basal slip, it becomes clear that non-basal slip mechanisms are likely to contribute to the deformation of the

base material as previously reported in the literature [39, 286]

In comparison to the base material, the processed specimen show a repetitive pattern in which the rotation of the tool is mirrored. The effect is most prominent in the material processed in condition A, as shown in the overview of Fig. 5.46(b). The repetitive rounded pattern (IV) has a spacing of ≈ 0.5 mm (VI), corresponding well to the 2 rotations / mm advancement of condition A. It can thus be argued that the repetitive pattern originates from the processing itself. In detail, the pattern consists of highly twinned (VII) and non twinned (IIX) areas as shown in Fig. 5.46(f).

As described above, the occurrence of extension twins within the processed material is not only expected due to the *c*-axis tilt towards the processing direction, but sought after as it enhances the formability of the material. In contrast to condition E and F, the occurrence of extension twins in condition A is limited to a thin layer. Even though this layer can accommodate a certain amount of deformation, its limited size helps to explain why the total tensile elongation of condition A is only within the range of the base material. The specimen of condition A fracture by closely following the rounded layers pattern as shown in Fig. 5.46(b) (V).

Due to the faster processing speed, the obvious repetitive pattern visible in condition A (Fig. 5.46(b)) is less pronounced in for condition E and F, as seen in Figs. 5.46(c) and 5.46(d), respectively.

While the size of the deformation zones for condition E (IX) already exhibit a noticeable increase over condition A, the most prominent regions are developing in condition F, which will be further discussed. As shown in Fig. 5.46(d), three different deformation areas have developed, denoted X, XI and XII, and the respective detailed micrographs to these region can be seen in Figs. 5.47 and 5.48.

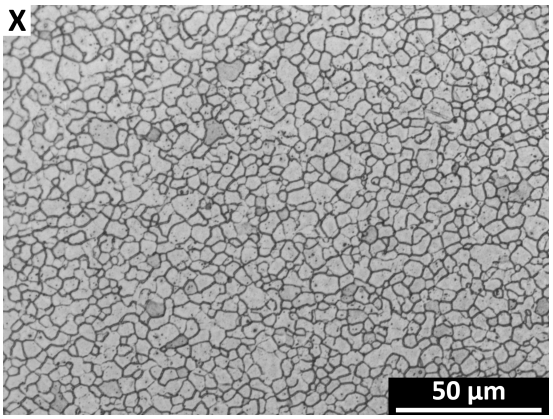


Figure 5.47: Post tests microstructure of area X of condition F.

In addition to the obvious microstructural changes, a macroscopic change in specimen thickness can be noted, as indicated in Fig. 5.46(d) in which the wider region is denoted XIII and the thinned region XIV. In detail, Fig. 5.47 depicts the area of the specimen in

which no thinning has taken place and which is located next to the highly twinned region XI. Not only does region X experience almost no twinning at all, but its grain morphology closely resembles that of the as processed samples.

This is in stark contrast to the microstructure of region XI, as shown in Fig. 5.48(a). While the grain morphology is still intact, high amounts of twinning throughout the entire area can be seen. From Fig. 5.46(d) it is also evident that the region encountering the highest amount of thinning is located between the highly twinned region stretching from one side of the specimen to the other.

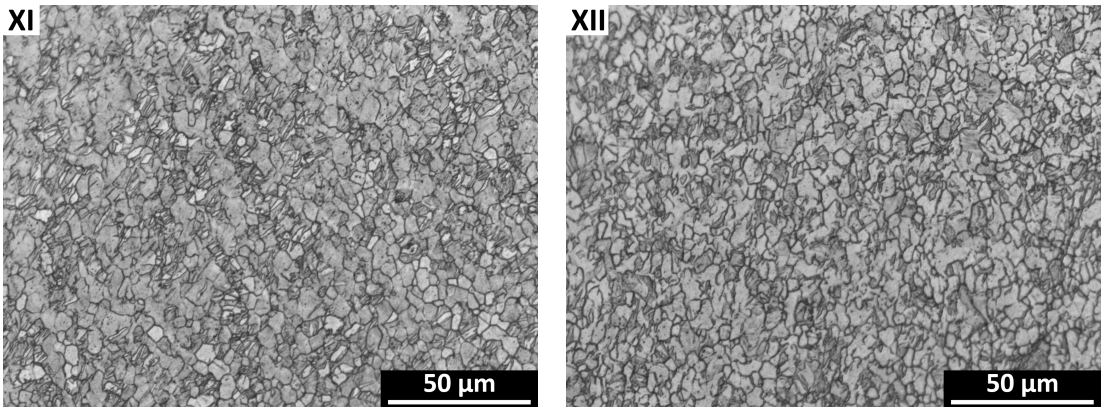


(a) (b)

Figure 5.48: Post tests microstructure of the deformation areas XI and XII of condition F.

Fig. 5.48(b) depicts the region XII, which is located close to the highly twinned area. Region XII also exhibits a thinning of the specimen as well as considerable amounts of twinning which indicates plastic deformation through slip in addition to twinning. Keeping the texture of condition F in mind (section 5.2.2), it can be assumed that mainly basal slip will have contributed to the deformation of area XII.

From the results above, the following conclusions can be drawn: The increased ductility of condition E and F is primarily driven by enhanced basal slip capabilities, due to a reduced $\tau_{CRSS}$ resulting from an increased inclination of the $c$-axis into tensile direction, as detailed in section 5.2. In contrast to what has been reported by Yang et al. [290], the tensile deformation of fine grained material is still mainly governed by extension twinning. Interestingly the grain size appears to have no discernible effect on the deformation behavior.

### 5.3.3 Forming Limit Tests

Formability tests have been conducted on multi line specimens in order to gain further insight into the deformation capabilities of the processed material. Using the results from the micro flat tensile tests and under the consideration of process stability (in condition F, the durability of the tool was not sufficiently high for multi line processing), conditions C and E have been chosen for multi line experiments. In the following, geometries I and VII (compare to Fig. 4.9(a)) have been chosen for a more detailed discussion, as they represent the most distinct differences in strain states between uniaxial tension (Geometry I) and stretch forming (Geometry VII). This way, the occurring changes in strain evolution can best be illustrated. For the final forming limit curve and anisotropy calculations, all specimen geometries have been considered. Fig. 5.49 and 5.50 show the major and minor strains exactly one frame before fracture occurs for the respective geometries. Iso-strain lines have been included in order to achieve a direct comparability. An overview over the major and minor strain evolution for geometry I is given in Fig. 5.49.

In detail, the major strain of the base material (Fig. 5.49(a)) increases homogeneously towards the center of the specimen along the major axis (Y axis), reaching a maximum local strain of $\approx 8\%$. For a better comparability to the other conditions, the 6% iso strain line has been indicated (I).

While condition C (Fig. 5.49(b)) experiences a similar strain distribution towards the center of the specimen, a single spot of high strain can be made out in the outer circumference of the center region, which constitutes the initiation site for fracture. Even though this highly strained region attires most of the local deformation, the 6% iso strain line indicates significant growth of the strained region while the center region of the specimen exhibits major strains between 9% and 11%.

Compared to condition C, condition E (Fig. 5.49(c)), experiences a more centralized strain build-up reaching values of up to 16% in the center of the specimen. In contrast to the previously observed circular shape in the center, condition E exhibits a more elliptical strain build-up, which spreads onto the outer regions. In addition, this region appears much more homogenized compared to the base material, indicating a more isotropic strain distribution. The 6% iso strain line has moved further from the center approaching the outer circumference of the specimen (III).

In summary, the major strains of the processed material in geometry I exhibit a gradual increase of endured strains up to 100% the base material values without significant changes

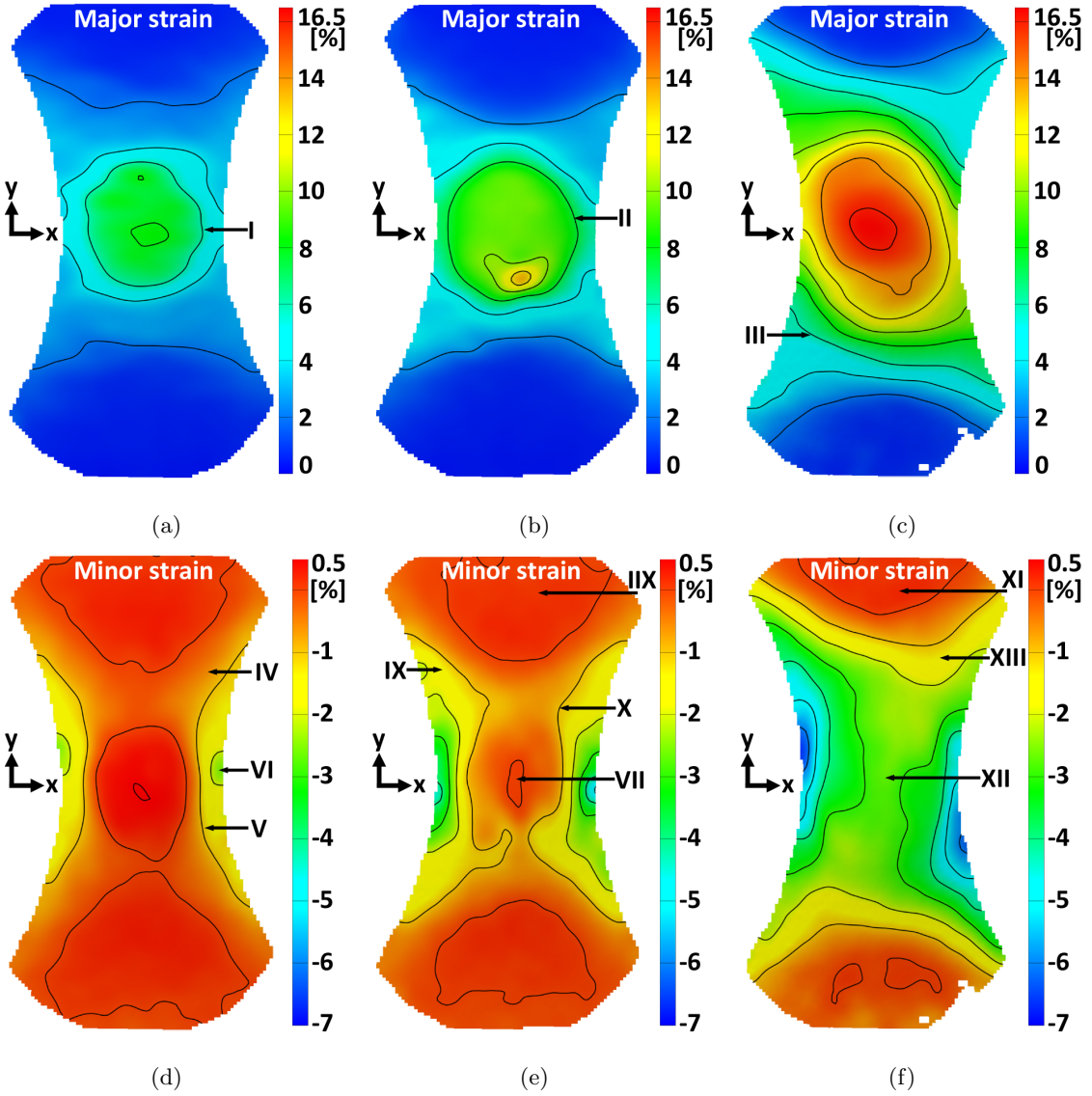


Figure 5.49: Major and minor strains of specimen geometry I, one frame before fracture of the base material (a & d), condition C (b & e) and condition E (c & f).

in strain geometry.

The minor strains on the other hand exhibit a more diverse evolution. Fig. 5.49(d) depicts the minor strain build-up of the base material. While negative minor strains and 45° shear bands (IV) can be noted along the major axis of the specimen, the center shows a positive minor strain build-up, gradually decreasing to $\approx 0\%$ along the major axis and rapidly entering negative minor strain regimes along the minor axis (X - direction). For comparison the -1% minor strain iso lines have been indicated (V). Edge effects (VI) are not considered in this discussion, as rapid transitions e.g. along the edges of the specimen

are to be handled with care if received from a digital image correlation system.

Condition C (Fig. 5.49(e)) experiences a more diffuse positive minor strain build-up in the center (VII). When moving along the major axis, this positive strain briefly changes into negative minor strains before positive minor strains are again visible at the sides of the specimen (IIX). The angle of the previously observed shear bands is decreasing to $\approx 30°$ (IX) indicating a more diffuse strain build-up. Finally the -1% minor strain iso lines (X) show enhanced straining capabilities, as this region exhibits a significant growth compared to the base material.

The most drastic change can be observed for the specimen processed in condition E (Fig. 5.49(f)). The previously observed positive minor strain build-up in the center of the specimen has completely shifted to the ends of the major axis (XI), resulting in a fully negative strain regime in the center (XII). The previously observed shear bands are further diffused and become eccentric in nature. An increased formability can be noticed by an enlarged area, enclosed by the -1% to -2% minor strain iso lines (XIII).

The major and minor strain evolution for geometry VII is shown in Fig. 5.50. Compared to specimen geometry I, the overall diversity becomes less pronounced. This is expected, as the geometry of this specimen is representing the stretch forming regime. In detail, the major strain of the base material (Fig. 5.50(a)) exhibits a centralized strain build-up, with the 6% iso strain line indicated with (I) and the point of fracture located slightly off centered (II). From the center, the strain distribution along the major and minor axis experiences a steady decrease. From the overall shapes of the iso lines, a somewhat serrated distribution can be made out.

Condition C (Fig. 5.50(b)) experiences a similar evolution in which the area encircled by the 6% iso strain line (III) becomes larger. The point of the highest major strain is shifted towards the center of the specimen (IV), indicating a more homogeneous strain distribution.

The major strain distribution for condition E can be seen in Fig. 5.50(c). While the area enclosed by the 6% iso strain line (V) remains comparable in size to condition C, the overall evolution appears much less serrated as the iso strain lines become increasingly circular in shape, indicating a reduction of anisotropy.

The evolution of the minor strains, shown in Figs. 5.50(d) to 5.50(f) is very comparable to the previously shown major strain evolution. Due to the larger specimen geometry,

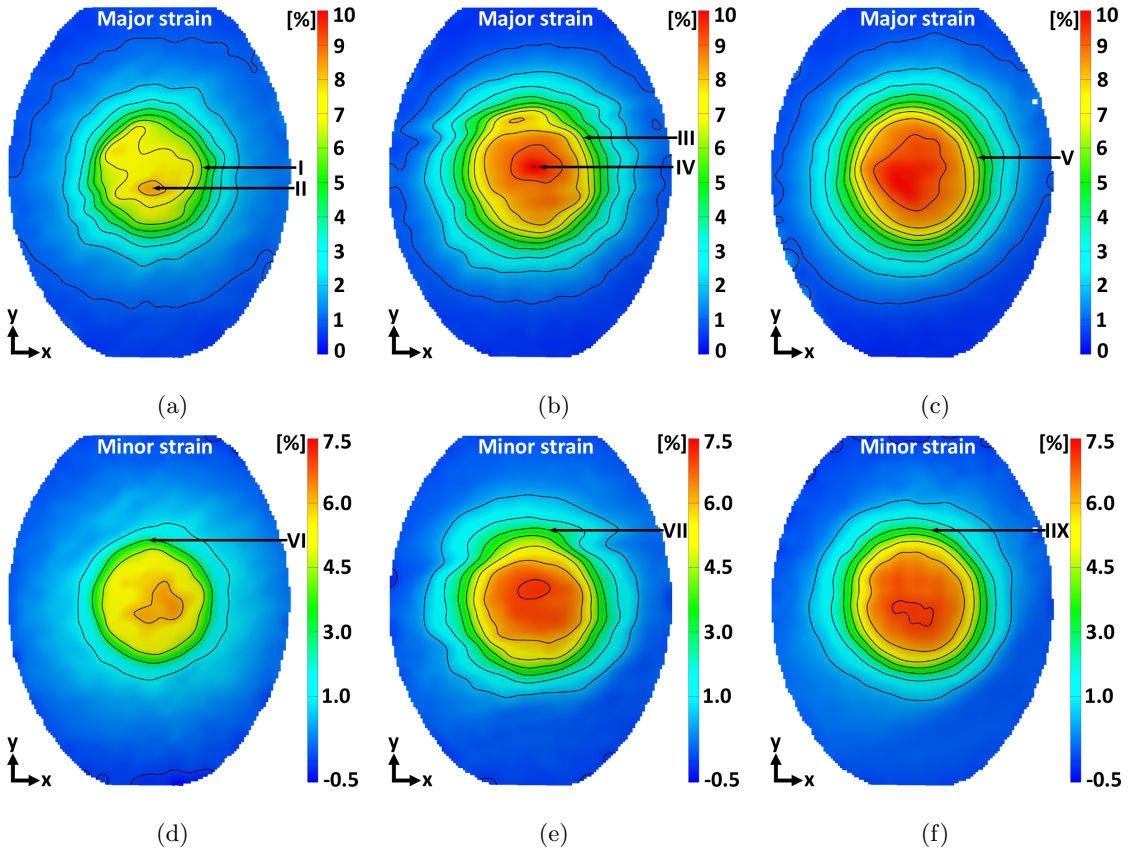


Figure 5.50: Major and minor strains of specimen geometry VII, one frame before fracture of the base material (a & d), condition C (b & e) and condition E (c & f).

the magnitude of negative minor strains is drastically reduced, resulting in a primary major strain build-up with values between 6% and 7% for the base material and processed material, respectively. While the 3% iso strain lines show some growth for the processed material (VI - IIX), the most noticeable effect is the strain homogenization with increasing processing speed, also indicating a reduction in anisotropy.

Conclusively, it can be noted that high speed FSP has not only resulted in higher major and minor strains in both extremes of possible specimen geometries and thus strain conditions, but also homogenized the strain distribution within the respective specimen, which indicates a reduction in anisotropy. The effect of the differences in applied strain on the forming limit curve will be discussed in the following.

In order to quantify the formability of a given material, it is necessary to obtain the strain limits in addition to the minor and major strain ratios. The forming limit curve describes this limit by ascribing a critical major strain to every minor strain and can thus be considered a property of the respective material. The forming limit curve is constructed

by applying parallel crosssections orthogonal to the crack and over the entire specimen length as shown in Fig. 5.51(a). In a next step, the curves (Fig. 5.51(b)) of the obtained strains are fitted using an inverse parabola (Eq. 5.1) within the bounds of the maximum of the second derivative of the curves to each side of the crack:

$$f(x) = 1/(ax^2 + bx + c) \tag{5.1}$$

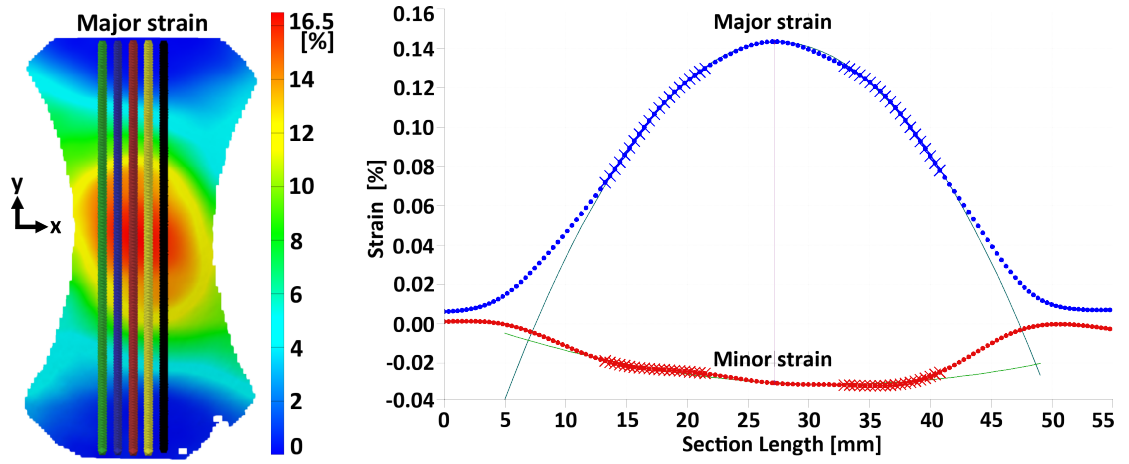


(a) (b)

Figure 5.51: Example of cross-sections on a geometry I specimen for minor and major strain calculations (a). Major and minor strain with fitting parabolas as a function of section length obtained from the specimen shown in Fig. 5.51(a) - (b).

Finally, the maximum of the parabola marks the highest forming limit strain which is plotted as a point of the forming limit curve in a forming limit diagram, as shown in Fig. 5.52. Within the forming limit diagram, every geometry has been tested by three specimens with each five sections thus resulting in 15 strain couples per geometry. In order to compare the different processing conditions to one another, the mean value of the 15 strain points per geometry have been compiled to a single point and interconnected by linear interpolations.

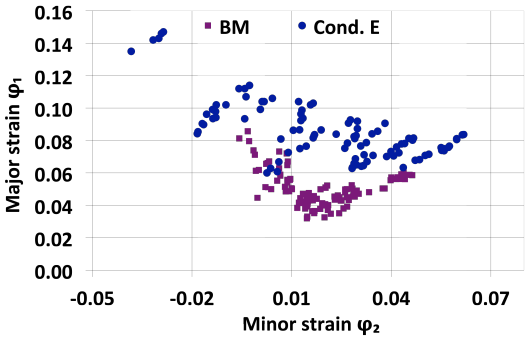


Figure 5.52: Forming limit diagram with resulting data points for the base material and condition E.

The resulting forming limit curves are presented in Fig. 5.53. In theory, every strain pair below the respective forming limit curve can be considered a region of safe deformation. It should be noted, that due to the calculation of the mean value for each specimen geometry, the resulting forming limit curve (Fig. 5.53) represents an interpolation. Due to the fact

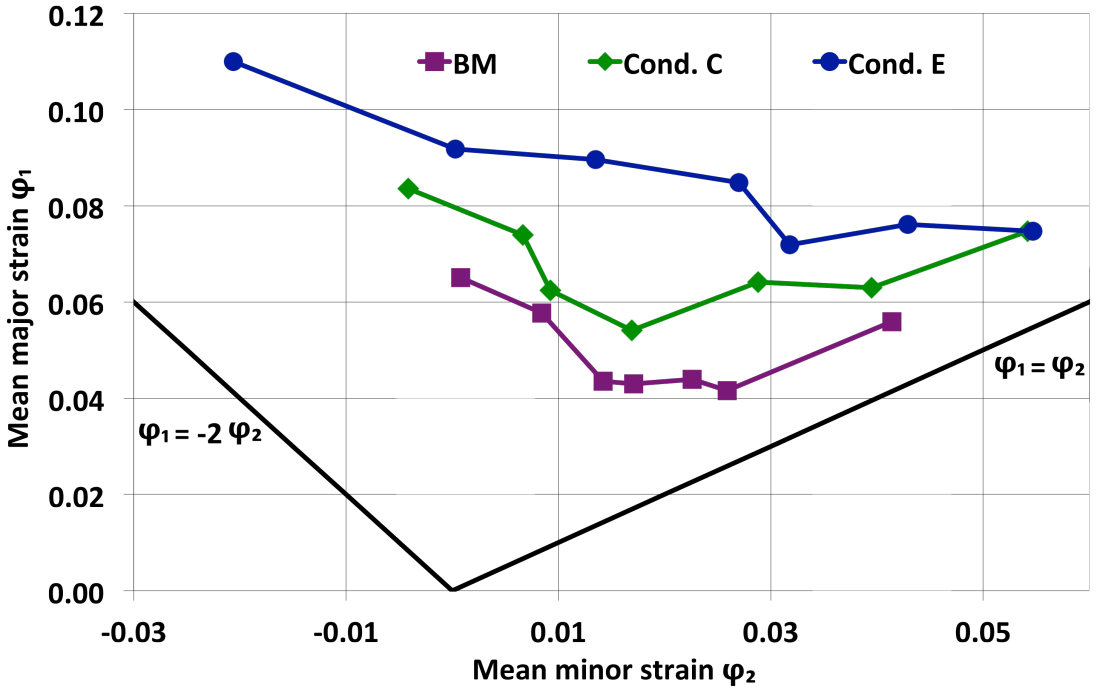


Figure 5.53: Resulting forming limit diagram with forming limit curves for the base material, condition C and condition E.

that this holds true for all tested conditions, a comparison within the tested forming limit curve regime is valid. For a more coherent presentation of the forming limit curve in Fig. 5.53, the boundaries for stretch forming $\varphi_1 = \varphi_2$ and for uniaxial tension $\varphi_1 = -2 \cdot \varphi_2$ are included, as all investigated forming limit curves are confined within these bounds. The overall shift of all forming limit curves towards positive minor strains can be ascribed to the combination of the flat sheet and the small radius punch, resulting in a limited amount of stretch forming at the initial stages of the test.

In detail, a continuous increase in formability with increasing processing speed can be noted. While this increase is most prominent in the major strain regime, resulting in an upwards shift of the forming limit curve, a distinct broadening within the minor strain regime can also be made out. A detailed comparison of the formability increase for each specimen geometry of the processed material with the base material is presented in Fig.

5.54. The graphs are constructed as such that the calculated mean points of the respective geometry are compared to one another.

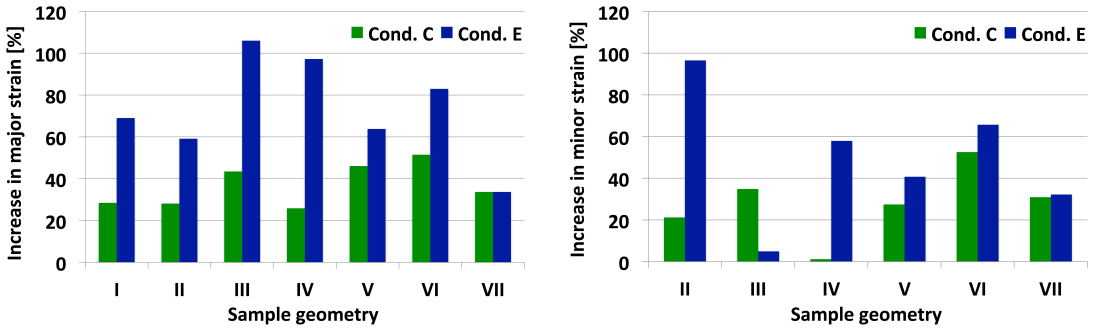


(a) (b)

Figure 5.54: Percentage increases in major (a) and minor strain (b) for condition C and E over the base material. Specimen geometry I for the minor strains has not been plotted as the base materials proximity to zero would lead to disproportional increases for the processed material.

For the major strains (Fig. 5.54(a)), the uniaxial tensile and plane strain regime (specimen geometry I and II) reach increases of almost 30% for condition C and around 60% for condition E. Between the plane strain and stretch forming regime (specimen geometry III to VI), this trend is intensified as increases of up to 50% for condition C and over 100% for condition E can be achieved. Close to the stretch forming regime (specimen geometry VII), the two conditions are very similar, with a formability increase of over 30%. Within the minor strains (Fig. 5.54(b)) the plane strain regime for condition E exhibits increases of up to 100%, while both conditions exhibit similar values towards the stretch forming regime.

In order to put the obtained results into perspective, a comparison to the available literature will be given in the following. Beforehand it should be noted that comparisons between different formability experiments must be interpreted with care. As compiled by Altan et al. [291], the forming limit curves can be significantly influenced by the specimen thickness and geometry, the test conditions such as lubrication, punch geometry, clamping forces as well as test speed. Due to the various evaluation methods incorporating different strain paths, the comparison between the various test methods such as the Nakajima, Marciniak or limited dome height experiments is limited.

Formability studies on unprocessed Mg AZ31 at elevated temperatures between 200°C

and 300°C have previously been conducted by Bruni et al. [292]. The authors found an increase in formability and a decrease in flow stress with rising temperature. Additionally, the strain hardening exponent shows a decrease with decreasing strain rate and rising temperature. As a result, the forming limit curve increases with temperature and decreases with strain rate. In contrast to the present study, the forming limit curve experiences the highest increases in the stretch forming regime. The authors attribute this behavior to the activation of additional slip systems at elevated temperatures, the occurrence of grain boundary sliding, dynamic recrystallization and grain growth.

Limited dome height experiments on FSP Mg AZ31 at elevated temperatures have recently been conducted by Bruni et al. [293] and Ramesh-Babu et al. [182]. Bruni et al. investigated the temperature regime between 250°C and 350°C. While the authors noted a decrease in flow stress with increasing temperature, the resulting forming limit curve did not reach the formability of the base material, which is attributed to the unfavorable orientation of the specimen with respect to the processing direction, resulting in an undesired microstructure and texture. Ramesh-Babu et al. investigated the formability at even higher temperatures of 350°C to 450°C. The authors report that FSP material can indeed exhibit superplastic forming capabilities at these temperatures if low strain rates are employed.

Venkateswarlu et al. [294] also used limited dome height measurements on friction stir processed Mg AZ31 to construct a forming limit diagram. While the authors found formability enhancements for the processed material, they did not to comment on the testing temperature as well as the specimen thickness. The authors have attributed the enhancements to a reduction in grain size and homogenization of the base material, but failed to comment on the initial or post processing grain size. EBSD investigations of the base and processed material have revealed similar textures, showing no tilt of the basal planes, which does indeed support the authors statement that the observed enhancements have primarily been driven by a homogenization of the corse base material microstructure.

In summary the available literature shows that the formability of FSP Mg AZ31 can indeed be increased if tested at elevated temperatures. The present study on the other hand shows that significant increases in formability can been obtained in thin Mg AZ31 at ambient temperatures using high speed FSP. Additionally it can be assumed that the materials formability can be increase even further if tested in higher temperature regimes.

### Anisotropy

In order to investigate the effect of FSP on the anisotropy of the material, the plastic strain ratio r has been evaluated using the digital image correlation system. Due to the inherent basal texture of Mg-alloys, the deformation is usually inhomogeneous in nature, which in turn has a substantial influence on the mechanical properties. The r-value can thus give an insight into the resulting anisotropic differences between the processed and base material. For tensile tests, the r-value is frequently calculated using Eq. 5.2 in which $\epsilon_w$ and $\epsilon_l$ are the width and longitudinal strains, respectively [295]:

$$r = -\epsilon_w/(\epsilon_l + \epsilon_w) \tag{5.2}$$

The measurement of the thickness strains is already challenging in conventional tensile tests, where the specimen width is usually measured manually at a given axial strain [191]. In forming limit tests, this approach is not applicable as it would imply complete unloading and dismounting of the specimen with a precise repositioning of the specimen in the testing machine after the thickness has been measured. The r-value has thus been calculated using the true strain values $r = ln(w_1/w_0)\ /\ ln(t_1/t_0)$ in which $w$ and $t$ are the width and thickness direction, respectively [296]. By using volume consistency ($l_0 \cdot w_0 \cdot t_0 - l_1 \cdot w_1 \cdot t_1 = 0$) the following substitution can be made: $r = ln(w_1/w_0)\ /\ ln(w_0 \cdot l_0/w_1 \cdot l_1)$ [297]. Finally, the widths (x) and lengths (y) as well as strains are substituted by $ln(l_1/l_0) = ln(1+\epsilon_l)$ and $ln(w_1/w_0) = ln(1+\epsilon_w)$ yielding Eq. 5.3.

$$r = ln\ (1+\epsilon_x)\ /\ ln\ (1\ /\ ((1+\epsilon_y) \cdot (1+\epsilon_x))) \tag{5.3}$$

It should be noted that due to the $ln$ in the denominator of this equation, most of the results have a negative sign. In order to present the results in a more common fashion, the absolute values have been used for further discussion. While for most materials the r-values are usually constant once a relatively large strain is reached (>15% and above) [295], Lou et al. [191] reported increasing r-values with increasing global strain on Mg AZ31. In order to capture such behavior, the r-value has been calculated over the entire specimen surface and for the entire length of the test. The calculations have been conducted on specimen geometries I, IV and VII in order to investigate the effect of different strain states as described above.

Previous investigations by Kang et al. [298], using tensile tests with digital image correlation, show that Mg-alloys exhibit a high sensitivity to the width and thickness strain measurement method. The authors argue that due to the nonlinear evolution of strain distribution on the sheet surface, strains should be measured at certain points rather than over the entire specimen length. The evaluation of the readily calculated specimen has thus been focused upon point (I), as shown in Fig. 5.55. The resulting r-values paired with their major and minor strain counterparts are shown in Fig. 5.56.

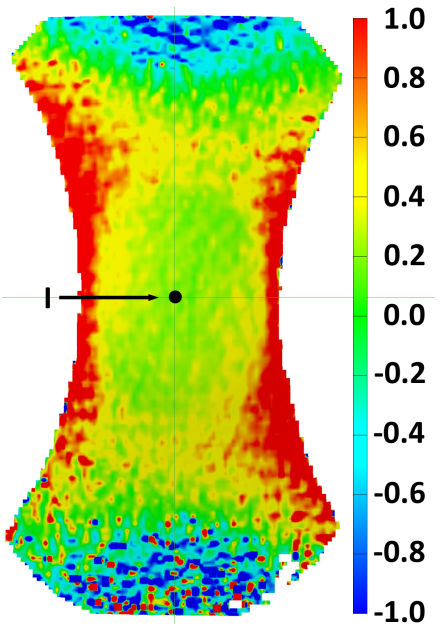


Figure 5.55: Exemplary formability specimen with r-value distribution.

While the strain values are plotted over the entire course of the test, the r-values are plotted beginning at 60% (of the entire test length) into the test (initial stages showed increased levels of noise) until the last frame before fracture. For geometry I ( Fig. 5.56(a) - uniaxial tension) the increase in major and minor strain for the processed material is most prominent, as two strain regimes develop. In the beginning of the test the minor and major strains of all conditions increase homogeneously until a major strain of $\approx$ 4% and corresponding minor strain of $\approx$ 2% is reached. After the slope reaches this turning point the minor strains for all specimen exhibit a change in sign, thus decreasing, while the major strains are continuously increasing. In the following, the base material and condition C fracture at $\approx$ 0.5% and 0% minor strain, respectively while condition E sustains minor strains up to $\approx$ -2.8% at a respective major strain of over 16%. The corresponding anisotropy curves (Fig. 5.56(b)) mirror this behavior as the base material and condition C experience a continuous decrease in r-values as the test progresses. As the base material does not reach negative minor strain values, its r-value does not decrease to zero. While condition C experiences a similar progression, without crossing into negative minor strains, condition E experiences a turn around in r-values after equalizing the previous positive minor strain build-up.

With rising specimen size and the corresponding change in strain state to a zone between plane strain and stretch forming (geometry IV), the strain - strain evolution becomes less distinct as shown in Fig. 5.56(c). While the initial increase of minor strains up to a major

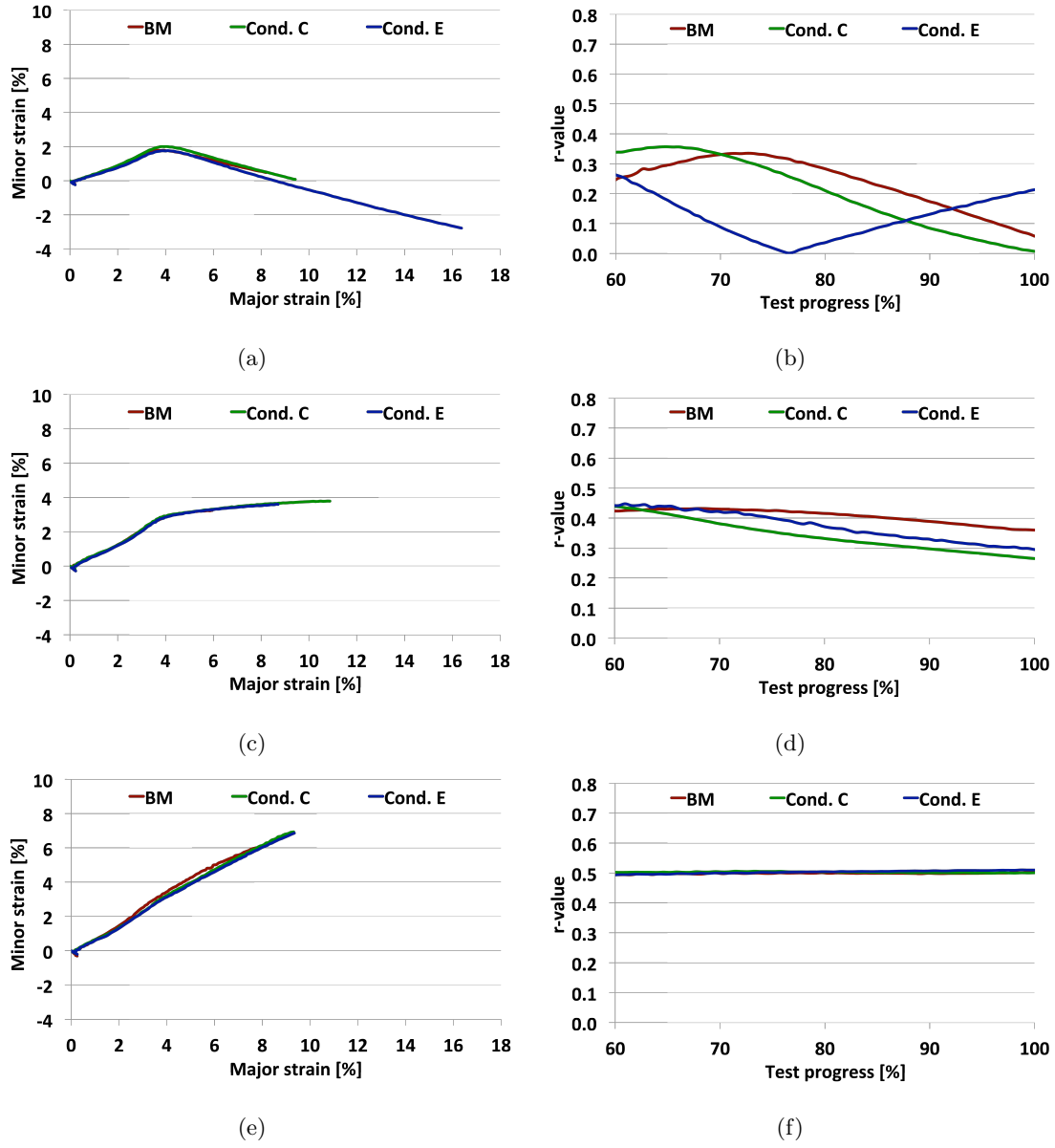


Figure 5.56: Major and minor strain evolution as well as the r-value evolution over the length of the tests for geometry I (a, b), IV (c, d) and VII (e, f).

strain value of $\approx 4\%$ is comparable to the one previously observed for geometry I, the following change in slope is less pronounced and remains positive until fracture occurs. Throughout the test, all specimens follow a similar path and differ only in the amount of sustained minor and major strain. While both conditions of processed material clearly exceed the sustainable strain of the base material, condition C exhibits the highest amount of major strains while sustaining comparable levels of minor strains. The corresponding r-values are shown in Fig. 5.56(d). Even though a slight fanning out is experienced by

all specimens as the test progresses, a similar trend is followed, resulting in final r-values ranging between 0.28 and 0.35.

With increasing specimen size, the consolidating trend intensifies, as shown for the stretch forming geometry VII. As depicted in Fig. 5.56(d), all conditions follow a similar path until the specimen fractures at minor strains of $\approx 6\%$ and $\approx 7\%$ for the base material and the processed material, respectively. The effect of this constant strain ratio is mirrored by the emergence of a plateau for r-values of all conditions at 0.5, as shown in Fig. 5.56(f).

Overall, a trend of decreasing anisotropy can be made out within the investigated material, as the strain condition moves from uniaxial tensile (geometry I) to stretch forming (geometry VII). The most noticeable differences in r-value can be seen for geometry I, as the material processed in condition E experiences a continuous increase in sustained negative minor strains. Similar results have been reported by Kang et al. [298] on FSP tensile specimen. The authors attribute the increased forming limit for the in-plane strain path to the modified (tilted) *c*-axis texture.

While this characteristic is still present in the larger specimen geometries, it is less pronounced, resulting in the observed consolidation of the r-value. The results indicate that the r-value is not only depending on the processing condition but also on the specimen size and must thus be regarded individually for the respective geometries. The increase in r-value with increasing specimen size, which in turn results in higher stresses, might by attributed to the activation of non-basal $\langle a \rangle$ slip, as reported by Koike et al. [299] and Lou et at. [191]. The authors associated the increasing r-value with a gradual shift from thickness strains to width strains. The activation of non-basal $\langle a \rangle$ slip near grain boundaries has also been reported by Yang et al. [290]. The authors argue that grain refinement below 3 $\mu$m results in an increased r-value, resulting in improved formability.

Such an assumption might be supported by the approximation and final coinciding of the forming limit curves for condition C and E (Fig. 5.53). Even though the textures for condition C and E both promote extension twinning and basal slip as their primary deformation mechanism, the resulting formability differs greatly for geometries I to IV, which represents the area between uniaxial tension ($\varphi_1 = -2 \cdot \varphi_2$) and uniaxial steady tension ($\varphi_2 = 0$). Within this regime, condition E appears to have the ability to sustain high major strains, consequently leading to high negative minor strains.

For geometry IV - VII, the $\varphi_1/\varphi_2$ ratio moves from uniaxial steady tension ($\varphi_2 = 0$) to stretch forming ($\varphi_1 = \varphi_2$). In this region, the amount of basal slip appears to be super-

imposed by other deformation mechanisms, such as non-basal $\langle a \rangle$ slip modes. It can thus be argued that the transition regime of uniaxial steady tension and deep drawing might be less affected by the previously described texture and microstructural modifications.

Conclusively the forming limit tests have shown that increased formability at ambient temperature can be obtained by controlled texture modification. While the effect of increased formability in the tension regime can mainly be attributed to the tilt of the $c$-axis into processing direction and transverse direction, resulting in an extension twinning and basal slip favoring texture, the endured strain consolidation within the stretch forming regime indicate the additional activation of non-basal $\langle a \rangle$ slip modes. The major to minor strain ratios and the resulting r-values have shown that FSP decreases the anisotropy inherent to Mg which additionally appears to be specimen size and processing condition dependent.

# 6 Summary

In the following, the results of the present study will be summarized.

### Processing Parameters

As detailed in section 5.1, high speed FSP has been successfully conducted over a wide range of processing parameters, including the highest processing speeds reported in the literature today. It has been shown that an increase in processing speed, which is necessary to obtain a small shear layer, can provide defect free process zones while increasing formability. The development of a steady state has been verified by determining the reaction forces of the material to high speed FSP (section 5.1.2).

### Thermal Model and Temperature Predictions

A numerical thermal model, introduced in section 4.6, has been used to predict the thermal evolution in the center of the stir zone as well as the geometry of the isotherms for selected temperatures as presented in section 5.1.3. The results have shown that the maximum temperatures in the stir zone experience a continuous decrease from 470°C to 270°C with increasing processing speed. Furthermore, the maximum temperature appears to be reaching a lower limit as the externally cooled samples still experience maximum temperatures of 250°C. By investigating the isothermal distribution around the tool for 205°C and 320°C, the increasing influence of extrusion phenomena within high speed FSP could be visualized.

Additionally, the dwell times, the time at which the material will retain a given temperature, have been calculated. The results have shown that the time available for recrystallization (205°C) is $\approx$ 3 s for the highest temperature condition (condition A). For the annealing temperature of 345°C, the available time is reduced to $\approx$1.3 s.

### Microstructure and Texture

The aim of texture modifications has been to enhance the formability of the processed material at ambient temperature. This has primarily been achieved by adjusting the tilt of the *c*-axis to an angular range between 40° and 50° into processing direction, which in turn yields a higher Schmid factor at a given $\tau_{CRSS}$. The tilt of the basal planes has been controlled by the geometry of the macroscopic shear plane which in turn is defined by the geometry of the shear layer. It has been shown that in high speed FSP, the geometry of the shear layer is a function of the processing parameters and chosen tool geometry as detailed in section 5.2.2.

From the textural investigations on externally cooled samples, four different zones have been made out. Among these four zones, the stir zone has been chosen for further investigations due to its microstructural and textural advantages such as fine grain size, high $c$-axis tilt angle, low amounts of twin boundaries and comparably low misorientation angle ratio as shown in section 5.2.

**Single Line** experiments have revealed, that an increase in processing speed results in a continuous textural shift towards the $\langle 0001 \rangle$ pole ($c$-axis tilt into processing direction) and a decrease in grain size. Additionally, an increasing amount of low angle boundaries has been observed which appears to be correlated to discontinuous dynamic recrystallization, which promotes poligonization of randomly oriented dislocations within newly formed grains, as detailed in section 5.2.2.

**Multi Line** experiments, as shown in section 5.2.3, have revealed a persistent decrease in grain size and a additional rotation of the $c$-axis. While the single line experiments have revealed a tilt of the $c$-axis into processing direction, the multi line experiments experienced an additional tilt towards the transverse direction. This has been correlated to the superpositioning effect of a second and third macroscopic shear layer on already processed material. It has been shown, that the $\{\bar{1}2\bar{1}0\}$ prismatic planes of condition E experience a discrete rotation compared to the homogeneous rotation observed for the other specimen. The previously observed textural shift towards the $\langle 0001 \rangle$ pole base been maintained. The region of highest intensity has been enlarged to the basal slip favorable range between $\approx 38°$ to $\approx 64°$ while the material processed in condition E additionally exhibits a pronounced textural intensity between the $\langle 0001 \rangle$ and the $\langle 10\bar{1}0 \rangle$ pole, which has been shown to promote double basal slip, desired for enhanced formability.

As seen for the single line experiments, the amount of low angle boundaries has increased further with the main fraction located within newly formed grains, supporting the above statement of rising poligonization with increasing strain and temperature. The interface region between two stir zones has experienced a reorientation of the $c$-axis away from the processing direction towards the normal direction, resulting in a higher textural randomization which has proven valuable in multi axial stress states.

#### Nanoindentation

As detailed in section 5.3.1 an overall trend of decreasing hardness with rising processing speed has been observed. In detail, the base material exhibits a texture induced preference

for $\{10\bar{1}2\}$ extension twinning. Due to the slight textural modification of condition A, the material exhibits a hardness decrease in the stir zone, which has been correlated to a combination of $\{10\bar{1}2\}$ extension twinning and $\{0001\}\ \langle 11\bar{2}0\rangle$ basal slip.

With increasing processing speed, the hardness increases mainly in the thermo mechanically affected zone 2. This has been correlated to the pre-twinned condition of the material, which inhibits further twinning (section 5.2.1). In the thermo mechanically affected zone 1, a decrease in hardness has been observed which has been correlated to the decreasing amount of pre-existing twins within this area as well as an increasing randomization of the texture. In the stir zone of the material processed in condition C, a slight increases in hardness has been observed, which has been attributed to the tilt of the *c*-axis into compression direction, decreasing the materials ability to form extension twins. Within the stir zone of the material processed in condition E on the other hand, the tilt of the *c*-axis is advanced far enough to activate basal slip more easily resulting in the observed decrease in hardness.

#### Micro Flat Tensile Tests

The effects of texture modification on the local tensile properties of the stir zone has been evaluated by micro flat tensile tests on single line material, as presented in section 5.3.2. The results have shown a tendency of increasing ductility with increasing tilt of the *c*-axis into tensile direction, which in turn is a function of processing speed. With high amounts of strain hardening, an increase in tensile elongation of up to 85% compared to the base material has been reached. The enhanced ductility appears to be mainly driven by basal slip and extension twinning, while the grain size appears to have no noticeable effect on the deformation behavior.

#### Formability Tests

The formability of multi line processed material has been tested by employing Hasek specimens in a Nakajima type test. As detailed in section 5.3.3, the employed textural modification has substantially increased the formability partly over 100% of the base material, which has mainly been attributed to the previously described tilt of the *c*-axis into processing direction and transverse direction, resulting in a texture favoring basal slip. The observed consolidation of endured strain within the stretch forming regime indicates an additional activation of basal and non basal $\langle a\rangle$ slip modes.

The most striking differences have been detailed in a comparison between the smallest and the largest sample geometry, in which the most significant variation could be noted in the amount of minor strain endured by the processed material. In addition, FSP led to a substantial homogenization of the strain distribution across the sample. The compiled forming limit diagram has shown a continuous increase in formability in all strain conditions with increasing processing speed.

Anisotropy investigations have shown that controlled texture modification using FSP can decrease the anisotropy, inherent to magnesium, while the magnitude of the effect is dependent on the specimen size and processing condition.

# 7 Conclusions

With respect to the main objectives of this work (section 4.1), the conclusions have been subdivided into the following sections:

### Processing

Within the present study, high speed FSP has successfully been used to enhance to formability of Mg AZ31. Particularly in respect to the introduction of the process in an industrial environment, the obtained processing speeds are a necessity.

Numerical thermal investigations predicted the maximum temperature in the stir zone, while continuously decreasing with increasing processing speed, to be high enough for recrystallization processes to take place. The dwell time at elevated temperatures has been predicted to be too short for annealing or static recrystallization processes to have a significant influence on the resulting microstructure. Consequently dynamic recrystallization is regarded to be mainly responsible for the microstructural and textural evolution of the process zone. In the scope of the present study this is highly desirable as dynamic recrystallization is a function of the total amount of strain, strain rate and temperature which in turn are all functions of the processing parameters. It has therefore been shown, that the extend of recrystallization, and with it the microstructural and textural evolution, can be adjusted by selecting suitable processing parameters.

Within the processed material, the recrystallization mechanisms and particularly the evolution of the grain size in the stir zone suggests that the total amount of strain imposed onto the material by high speed FSP is also influenced by the translational movement of the tool. Due to the tools rapid translational movement, the consolidation mechanism in high speed FSP are to be divided into a stirring and an extrusion component in which the thermal input is mainly governed by the stirring component whereas plastic deformation stems from stirring as well as extrusion.

### Microstructure and Texture

Microstructural investigations of the process zone have shown that the geometry (size and shape) of the shear layer surrounding the probe is a function of the processing parameters and tool geometry. It has been shown that with increasing processing speed, the tilt of the $c$-axis, which is a necessary precursor for enhanced basal slip, is reaching a threshold between 40° and 50° (with 0° being the rolling texture) as the shear layer is evermore resembling the probe geometry. As the shear layer represents the macroscopic shear plane

along which the basal planes are oriented, this result yields the ability of tailoring the tilt of the basal planes by using a knowledge based approach of selecting processing parameters and tool geometry.
The knowledge gained from single line samples has been transferred to create multi line samples featuring a tailored microstructure and texture. The results show a broadening of the reoriented *c*-axis to a protracted area in the angular range between $\approx 38°$ to $\approx 64°$ which is favorable for enhanced formability.

**Mechanical Testing**

Nanoindentaion experiments conducted on the processed specimen revealed a strong dependency between texture and resulting hardness. Particularly the materials ability to form extension twins has been observed to be primarily influencing the hardness evolution which had its most notable effect in the pre-twinned thermo mechanically affected zone 2 in which the highest hardness results have been observed. The hardness evolution in the stir zone has been described as a function of *c*-axis tilt angle in which an increasing tilt angle promotes basal slip and thus decreases the resulting hardness.
Micro flat tensile tests of the stir zone of single line samples have shown, that while the formation of extension twins can still be observed in the tested specimen, the occurrence of basal slip is superimposing the twinning effect when tested in larger scale specimen. The assumption of an increasing ease of basal slip with an increasing tilt of the *c*-axis towards to processing direction has been confirmed as the samples processed in condition E (10 m/min) and condition F (20 m/min) exhibited substantial increases in ductility over the base material.
Transferring the obtained knowledge to large scale formability tests conducted on multi line samples have supported the above statement as an increase in processing speed resulted in a substantial increase in the formability at ambient temperature. Additionally it has been shown, that high speed FSP decreases the Mg inherent anisotropy.
In summary, the mechanical tests confirmed the textural results on every tested scale.

The obtained results show that knowledge based texture alterations using high speed FSP is a suitable tool for tailoring material properties to the desired needs and can substantially increase the formability of Mg AZ31 at ambient temperatures.

# 8 Appendix

## Drawings

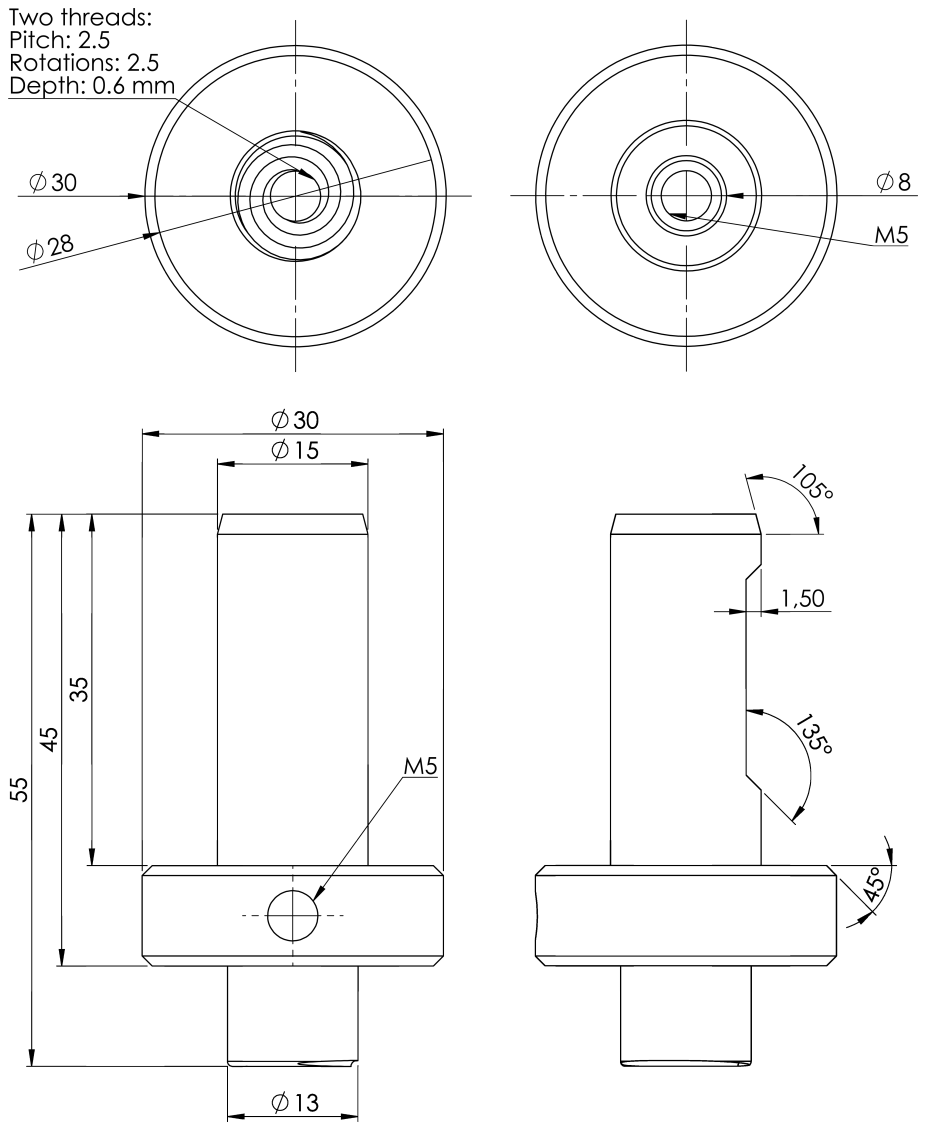


Figure 8.1: Drawing including detailed dimensions of the shoulder utilized in the present study. All values in mm.

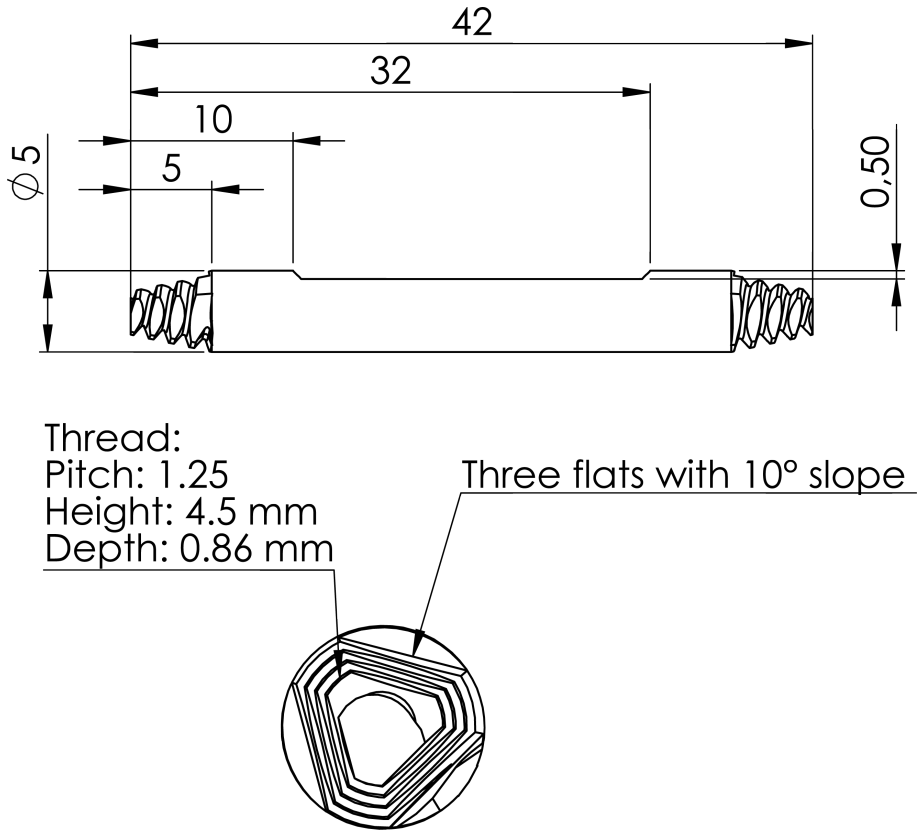


Figure 8.2: Drawing including detailed dimensions of the probe utilized in the present study. All values in mm.

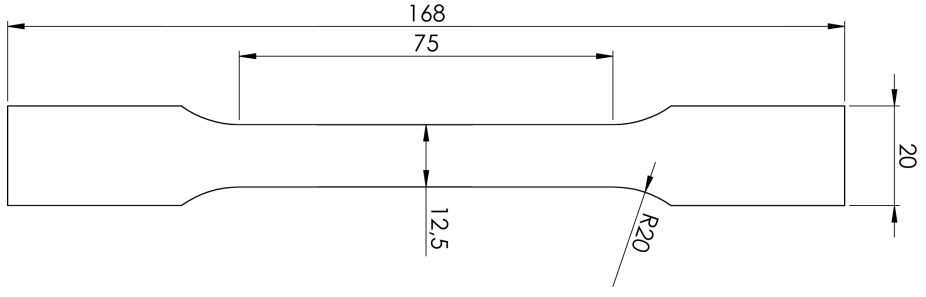


Figure 8.3: Drawing including detailed dimensions of the full scale tensile specimen. All values in mm.

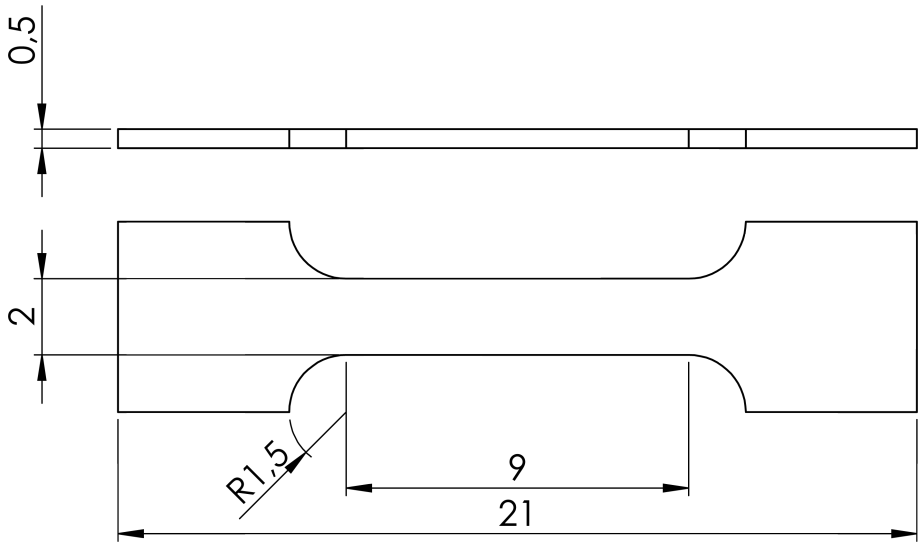


Figure 8.4: Drawing including detailed dimensions of the micro flat tensile specimen. All values in mm.

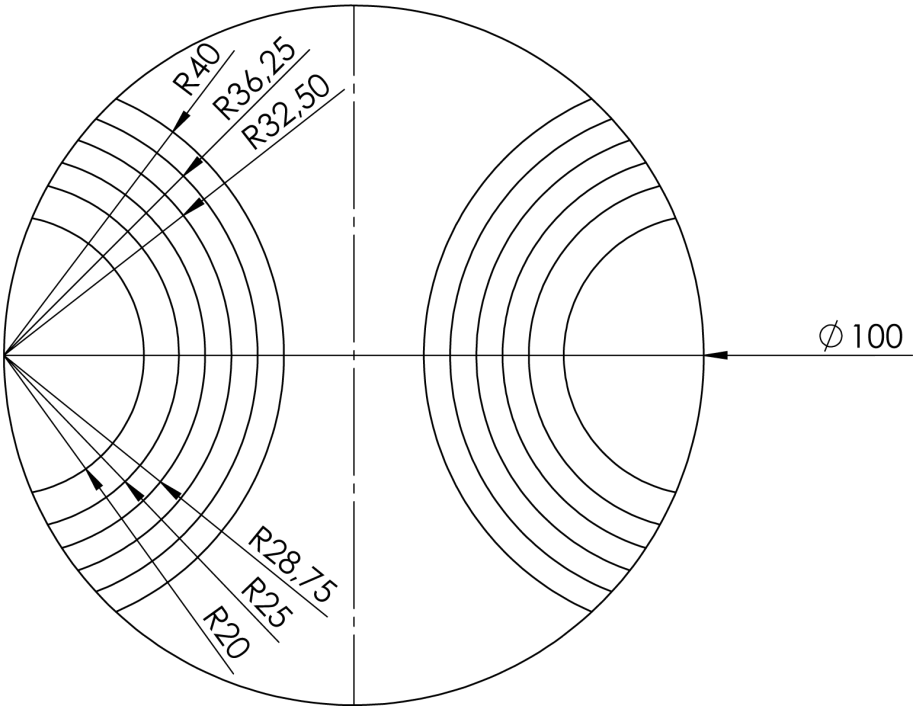


Figure 8.5: Drawing including detailed dimensions of the forming limit specimens. All values in mm.

## Tables

Table 8.1: Physical properties of pure Mg at ambient temperatures if not declared otherwise [267].

| **Name** | **Property** | **Name** | **Property** |
|---|---|---|---|
| Atomic number: | 12 | Atomic weight: | 24.30 |
| Density: | 1.738 g/cm$^3$ | Youngs modulus: | 45 GPa |
| $R_m$: | 80 - 180 MPa | Fracture strain: | 1% - 12% |
| Melting point: | 650°C | Boiling point: | 1090°C |
| Heat capacity: | 1.05 kJ/kg | Heat of fusion: | 195 kJ/kg |
| Heat conductivity: | 156 W/mK | Linear expansion: | $26 \cdot 10^{-6}$ K$^{-1}$ |
| Degree of shrinkage: | 4.2% - 5% | Normal potential: | -2.37 V |
| Elektronegativity: | 1.31 | El. conductivity: | 22.4 W/Ω mm$^{-2}$ |

Table 8.2: Denotation of the various alloying elements used for Mg [209]

| | | | | | | | |
|---|---|---|---|---|---|---|---|
| A | Aluminum | F | Iron | M | Manganese | S | Silicon |
| B | Bismuth | G | - | N | Nickel | T | Tin |
| C | Copper | H | Thorium | P | Lead | W | Yttrium |
| D | Cadmium | K | Zirconium | Q | Silver | Y | Antimony |
| E | Rare Earth | L | Lithium | R | Chromium | Z | Zink |

Table 8.3: Tensile results of micro flat tensile specimen for condition A to F.

| Condition | $R_m$ [MPa] | $R_{p0.2}$ [MPa] | A [%] |
|---|---|---|---|
| A | 179.3 ± 9.6 | 92.7 ± 2.3 | 11.3 ± 1.0 |
| C | 151.0 ± 22.6 | 86.1 ± 8.6 | 12.0 ± 1.4 |
| E | 179.0 ± 14.4 | 94.8 ± 9.3 | 15.5 ± 1.9 |
| F | 190.5 ± 3.8 | 81.6 ± 3.1 | 22.0 ± 1.2 |

Table 8.4: Temper denotation for Mg-alloys [209, 300]

| | |
|---|---|
| F | as fabricated |
| O | annealed recrystallized |
| H | strain hardened |
| T | thermally treated to reduce stable tempers |
| W | solution heat treated (unstable temper) |
| H1 | strain hardened only |
| H2 | strain hardened and partially annealed |
| H3 | strain hardened and stabilized |
| T1 | cooled and naturally aged |
| T2 | annealed |
| T3 | solution heat treated and cold worked |
| T4 | solution heat treated |
| T5 | cooled and artificially aged |
| T6 | solution heat treated and artificially aged |
| T7 | solution heat treated and stabilized |
| T8 | solution heat treated, cold worked and artificially aged |
| T9 | solution heat treated, artificially aged and cold worked |
| T10 | cooled, artificially aged and cold worked |

Table 8.5: Most common alloys and their effects [208, 209]

| **Element** | **Result** |
|---|---|
| Aluminum | Most commonly used alloying material. Maximum solubility of 12.7 wt.% reaching a peak increase in strength and ductility at about 6 wt.%. Constitutes the basis of most die casting alloys. The intermetallic $Mg_{17}Al_{12}$ phase is persistent. |
| Zinc | One of the most commonly used alloying elements especially in combination with Al in e.g. AZ31, AZ91. |
| Calcium | Used to increase the creep resistance essentially replacing the thermally unstable $Mg_{17}Al_{12}$ phase with the $Al_{12}Ca$ phase. Additionally it improves the rolling ability. |
| Lithium | Lighter than Mg thus further decreasing weight with a max. solubility of 5.5 wt.%. Decreases strength while increasing ductility. The bcc secondary phase capacitates the production of wrought products in the $\alpha + \beta$ or $\beta$ phase. |
| Manganese | Used with max. 2 wt.% as an addition to other alloys to form now compounds, reduce the solubility of iron or improve the corrosion resistance. |
| Rare Earths | Improves the high temperature strength as well as the creep resistance and ductility. Usually added as Mischmetal. |
| Yttrium | Used together with RE to increase high temperature creep resistance. |
| Silicon | Decreases the viscosity of molten Mg but is seldom used. |
| Silver | Positive effects on age hardening as well as high temperature properties of Mg-alloys containing Re. |
| Zirkonium | Refines the grain size in a dissolved state but can not be used in combination with Al or Mn as stable secondary phases are formed. |

## Nanoindentation Data

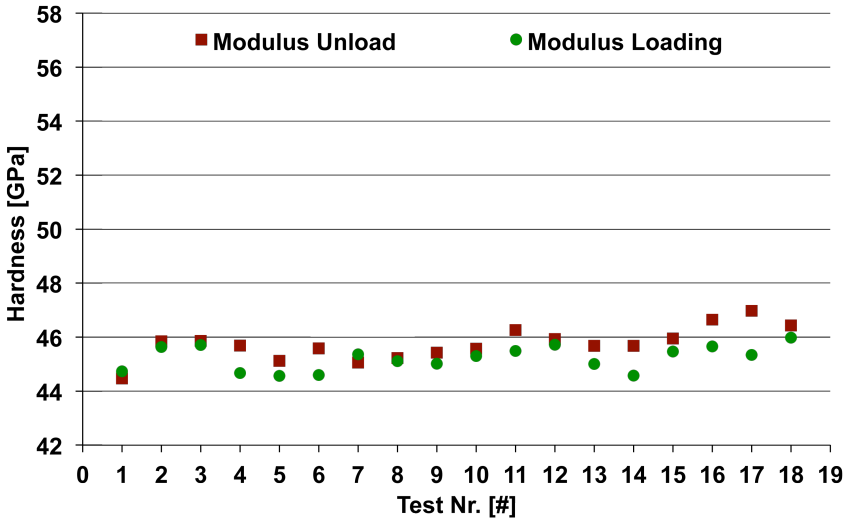


(a)

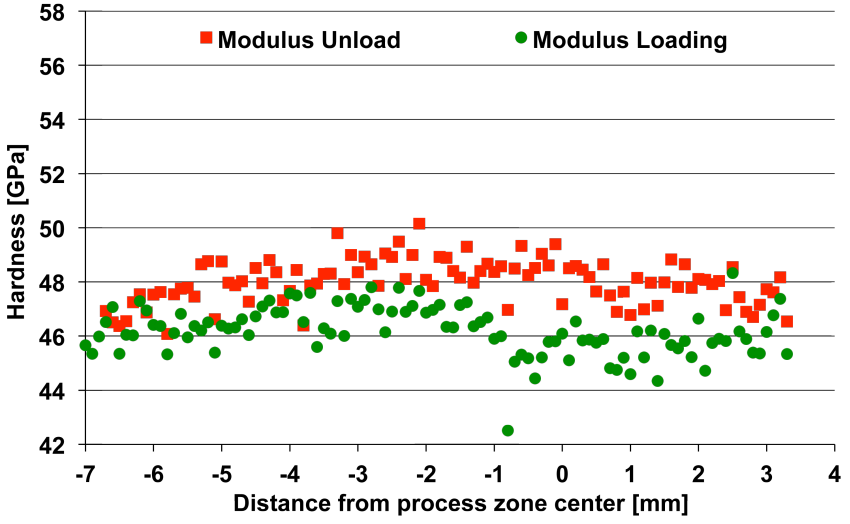


(b)

Figure 8.6: All modulus values of the nanoindentation experiments for the base material and single line condition A.

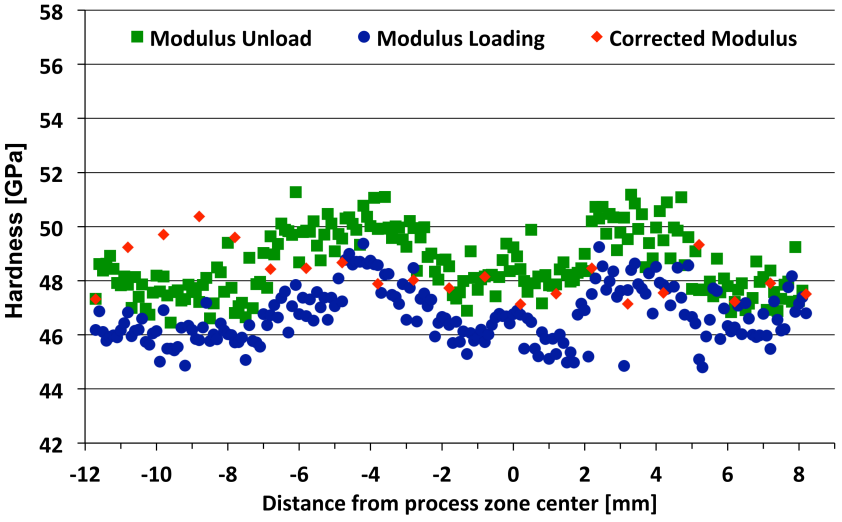


(a)

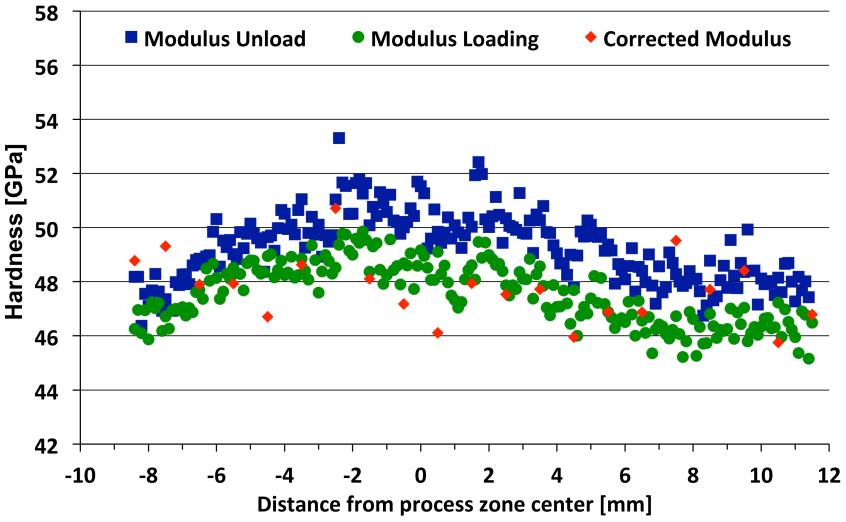


(b)

Figure 8.7: All modulus values of the nanoindentation experiments for single line condition C and E.

# 9 List of Publications, Awards and Patents

### Journal Papers

- L. L. Hütsch, J. Hilgert, and K. Herzberg, J. F. Santos, and N. Huber. Temperature and texture development during high speed friction stir processing of magnesium AZ31. *Adv. Eng. Mat.*, 14(9):762 – 771, 09 2012.
- L. L. Hütsch, K. Herzberg, J. F. Santos, and N. Huber. A study on local thermal and strain phenomena of high-speed friction stir-processed mg AZ31. *Weld. in the World*, 57(4):515 – 521, 07 2013.
- L. L. Hütsch, J. Hütsch, K. Herzberg, J. F. dos Santos, and N. Huber. Increased room temperature formability of Mg AZ31 by high speed friction stir processing. *Mat. and Des.*, 54(0):980 – 988, 02 2014.

### International Conferences

- 63rd Annual Assembly of the International Institute of Welding (IIW) / 11 to 16.07.2010, Istanbul, Turkey.
- 140th Annual Meeting & Exhibition TMS 2011 / 27.02 to 03.03.2011, San Diego, USA.
- 9th International Conference on Magnesium Alloys and their Applications / 08 to 12.07.2012, Vancouver, Canada.
- 1st International Joint Symposium on Joining and Welding (IJS-JW2013) / 06 to 08.11.2013, Osaka, Japan.

### Awards

- Best paper award at the 1st International Joint Symposium on Joining and Welding (IJS-JW2013) / 06 to 08.11.2013, Osaka, Japan.

## Patents

- Filed european patent (EP 14184329.2) concerning a *Hybrid multi-shoulder friction stir welding tool with semi-stationary intermediate shoulder for the joining of thin double-walled hollow profiles.* (As of November 2014).
- Filed european patent (EP 14184331.8) european patent concerning a *Semi-stationary friction stir welding tool including a shoulder with a friction based torque adjustment.* (As of November 2014).

# List of Figures

# List of Tables

# Bibliography


[1] P. Blain. Steel perspective for the automotive industry. *http://www.oecd.org/sti/ind/50498824.pdf*, 09 2013.

[2] H. Friedrich and S. Schumann. Research for a new age of magnesium in the automotive industry. *J. of Mat. Proc. Tech.*, 117(3):276 – 281, 11 2001.

[3] National highway trafic savety administration. Baseline scenarios for the clean air for europe (CAFE) programme. *http://www.nhtsa.gov/cars/rules/CAFE/CAFEData.htm*, 09 2013.

[4] A. Taub, P. Krajewski, A. Luo, and J. Owens. The evolution of technology for materials processing over the last 50 years: The automotive example. *JOM*, 59(2):48 – 57, 02 2007.

[5] W. S. Miller, L. Zhuang, J. Bottema, A. J. Wittebrood, P. De Smet, A. Haszler, and A. Vieregge. Recent development in aluminium alloys for the automotive industry. *Mat. Sci. and Eng. A*, 280(1):37 – 49, 03 2000.

[6] F. Ostermann. *Anwendungstechnologie Aluminium*, volume 1. Springer, 2 edition, 2007.

[7] K.U. Kainer. *Megnesium alloys and Technology*, volume 1. Wiley-VCH, 2003.

[8] S. Das. Magnesium for automotive applications: Primary production cost assessment. *JOM*, 55(11):22 – 26, 11 2003.

[9] K. Hono, C. L. Mendis, T. T. Sasaki, and K. Oh-ishi. Towards the development of heat-treatable high-strength wrought Mg alloys. *Scr. Mater.*, 63(7):710 – 715, 10 2010.

[10] K.U. Kainer. *Megnesium alloys and Technology*, volume 1, pages 304 – 305. Wiley-VCH, 2003.

[11] F. Klocke and W. König. *Fertigungsverfahren*, volume 1, pages 321 – 325. Springer, 8 edition, 2008.

[12] E. Aghion, B. Bronfin, and D. Eliezer. The role of the magnesium industry in protecting the environment. *J. of Mat. Proc. Tech.*, 117(3):381 – 385, 11 2001.

[13] D. Eliezer, E. Aghion, and F. H. Froes. Magnesium science, technology and applications. *Adv. Eng. Mat.*, 5(3):201 – 212, 12 1998.

[14] D. Fechner, N. Hort, and K.U. Kainer, editors. *Magnesium Recycling System Prepared by Permanent Mould- and High Pressure Die Casting*, Magnesium Technology Series. TMS, 2009.

[15] D. Fechner, C. Blawert, N. Hort, H. Dieringa, and K. U. Kainer. Development of a magnesium secondary alloy system for mixed magnesium post-consumer scrap. *Mat. Sci. and Eng. A*, 576(0):222 – 230, 08 2013.

[16] M. Kulekci. Magnesium and its alloys applications in automotive industry. *Int. J. of Adv. Manuf. Tech.*, 39(9):851 – 865, 11 2008.

[17] G. S. Cole and A. M. Sherman. Light weight materials for automotive applications. *Mater. Charact.*, 35(1):3 – 9, 07 1995.

[18] E. Aghion, B. Bronfín, F. Von Buch, S. Schumann, and H. Friedrich. Newly developed magnesium alloys for powertrain applications. *JOM*, 55(11):30 – 33, 11 2003.

[19] D. S. Mehta, S. H. Masood, and W. Q. Song. Investigation of wear properties of magnesium and aluminum alloys for automotive applications. *J. of Mat. Proc. Tech.*, 155 - 156:1526 – 1531, 11 2004.

[20] A. K. Mondal, D. Fechner, S. Kumar, H. Dieringa, P. Maier, and K. U. Kainer. Interrupted creep behaviour of mg alloys developed for powertrain applications. *Mat. Sci. and Eng. A*, 527(9):2289 – 2296, 04 2010.

[21] B. L. Mordike and T. Ebert. Magnesium: Properties - applications - potential. *Mat. Sci. and Eng. A*, 302(1):37 – 45, 04 2001.

[22] K.U. Kainer. *Megnesium alloys and Technology*, volume 1, page 108. Wiley-VCH, 2003.

[23] B. L. Mordike and F. Hehmann. *Magnesium Alloys and Their Applications*, volume 1. DGM Informationsgesellschaft, 1992.

[24] V. I. Ryazantsev, V. A. Fedoseev, and V. N. Matsnev. Construction of the welded body of vehicles from aluminium alloys. *Weld. Int.*, 14(5):407 – 412, 09 2000.

[25] J. Hirsch and T. Al-Samman. Superior light metals by texture engineering: Optimized aluminum and magnesium alloys for automotive applications. *Acta Mater.*, 61(3):818 – 843, 02 2013.

[26] E. Doege and K. Dröder. Sheet metal forming of magnesium wrought alloys - formability and process technology. *J. of Mat. Proc. Tech.*, 115(1):14 – 19, 08 2001.

[27] J. Koike, T. Kobayashi, T. Mukai, H. Watanabe, M. Suzuki, K. Maruyama, and K. Higashi. The activity of non-basal slip systems and dynamic recovery at room temperature in fine-grained AZ31B magnesium alloys. *Acta Mater.*, 51(7):2055 – 2065, 04 2003.

[28] J. Koike, R. Ohyama, T. Kobayashi, M. Suzuki, and K. Maruyama. Grain-boundary sliding in AZ31 magnesium alloys at room temperature to 523 K. *Mater. Trans.*, 44(4):445–451, 03 2003.

[29] R. V. Mises. Mechanik der plastischen Formänderung von Kristallen. *ZAMM*, 8(3):161 – 185, 06 1928.

[30] L. W. F. Mackenzie and M. O. Pekguleryuz. The recrystallization and texture of magnesium zinc cerium alloys. *Scr. Mater.*, 59(6):665 – 668, 08 2008.

[31] D. Hardie and R. N. Parkins. Lattice spacing relationships in magnesium solid solutions. *Phil. Mag.*, 4(43):815 – 825, 01 1959.

[32] T. Al-Samman. Comparative study of the deformation behavior of hexagonal magnesium–lithium alloys and a conventional magnesium AZ31 alloy. *Acta Mater.*, 57(7):2229 – 2242, 04 2009.

[33] T. Al-Samman and G. Gottstein. Dynamic recrystallization during high temperature deformation of magnesium. *Mat. Sci. and Eng. A*, 490(1-2):411 – 420, 08 2008.

[34] X. Huang, K. Suzuki, A. Watazu, I. Shigematsu, and N. Saito. Mechanical properties of Mg Al Zn alloy with a tilted basal texture obtained by differential speed rolling. *Mat. Sci. and Eng. A*, 488(12):214 – 220, 08 2008.

[35] H. Watanabe, T. Mukai, K. Ishikawa, and K. Higashi. Low temperature superplasticity of a fine-grained ZK60 magnesium alloy processed by equal-channel-angular extrusion. *Scr. Mater.*, 46(12):851 – 856, 06 2002.

[36] R. Gehrmann, M. M. Frommert, and G. Gottstein. Texture effects on plastic deformation of magnesium. *Mat. Sci. and Eng. A*, 395(1-2):338 – 349, 03 2005.

[37] R. S. Mishra, Z. Y. Ma, and I. Charit. Friction stir processing: a novel technique for fabrication of surface composite. *Mat. Sci. and Eng. A*, 341(1-2):307 – 310, 01 2003.

[38] R. S. Mishra and Z. Y. Ma. Friction stir welding and processing. *Mat. Sci. and Eng. R*, 50(1-2):1 – 78, 05 2005.

[39] W. Woo, H. Choo, D. W. Brown, P. K. Liaw, and Z. Feng. Texture variation and its influence on the tensile behavior of a friction-stir processed magnesium alloy. *Scr. Mater.*, 54(11):1859 – 1864, 06 2006.

[40] W. Woo, H. Choo, M. B. Prime, Z. Feng, and B. Clausen. Microstructure, texture and residual stress in a friction-stir-processed AZ31B magnesium alloy. *Acta Mater.*, 56(8):1701 – 1711, 04 2008.

[41] W. Yuan and R. S. Mishra. Grain size and texture effects on deformation behavior of AZ31 magnesium alloy. *Mat. Sci. and Eng. A*, 558:716 – 724, 12 2012.

[42] W. Yuan, R. S. Mishra, B. Carlson, R. K. Mishra, R. Verma, and R. Kubic. Effect of texture on the mechanical behavior of ultrafine grained magnesium alloy. *Scr. Mater.*, 64(6):580 – 583, 03 2011.

[43] J. Chen, H. Fujii, Y. Sun, Y. Morisada, and R. Ueji. Fine grained Mg-3Al-1Zn alloy with randomized texture in the double-sided friction stir welded joints. *Mat. Sci. and Eng. A*, 580:83 – 91, 08 2013.

[44] D. H. Kang, D. W. Kim, S. Kim, G. T. Bae, K. H. Kim, and Nack J. Kim. Relationship between stretch formability and work-hardening capacity of twin-roll cast Mg alloys at room temperature. *Scr. Mater.*, 61(7):768 – 771, 10 2009.

[45] C.I. Chang, X.H. Du, and J.C. Huang. Producing nanograined microstructure in Mg-Al-Zn alloy by two-step friction stir processing. *Scr. Mater.*, 59(3):356 – 359, 08 2008.

[46] R. S. Mishra, M. W. Mahoney, S. X. McFadden, N. A. Mara, and A. K. Mukherjee. High strain rate superplasticity in a friction stir processed 7075 Al alloy. *Scr. Mater.*, 42(2):163 – 168, 12 1999.

[47] S. H. Kang, Y. S. Lee, and J. H. Lee. Effect of grain refinement of magnesium alloy AZ31 by severe plastic deformation on material characteristics. *J. of Mat. Proc. Tech.*, 201(1 - 3):436 – 440, 05 2008.

[48] A. Yamashita, Z. Horita, and T. G. Langdon. Improving the mechanical properties of magnesium and a magnesium alloy through severe plastic deformation. *Mat. Sci. and Eng. A*, 300(1-2):142 – 147, 02 2001.

[49] F. Chai, D. Zhang, Y. Li, and W. Zhang. High strain rate superplasticity of a fine-grained AZ91 magnesium alloy prepared by submerged friction stir processing. *Mat. Sci. and Eng. A*, 568(0):40 – 48, 04 2013.

[50] R. J. Groza and J. F. Shackelford. *Materials Processing Handbook*, pages IX–X. CRC Press, 03 2007.

[51] A. F. Harding. *European societies in the Bronze Age*, pages XV – XVIII. Cambridge University Press, Cambridge, 2000.

[52] H. J. Bargel and G. Schulze. *Werkstoffkunde*, volume 10, pages 143 – FF. Springer, 2008.

[53] P. Höller, V. Hauk, G. Dobmann, C. O. Ruud, R. E. Green, C. O. Ruud Jr., and D. J. Snoha. *Characterization of Crystallographic Texture in Aluminium Can Stock by X-Ray Diffraction*, pages 267 – 272. Springer, 1989.

[54] R. J. Groza and J. F. Shackelford. *Materials Processing Handbook*, pages 3.11 – 3.12. CRC Press, 03 2007.

[55] R. J. Groza and J. F. Shackelford. *Materials Processing Handbook*, page 12.4. CRC Press, 03 2007.

[56] R. J. Groza and J. F. Shackelford. *Materials Processing Handbook*, page 12.5. CRC Press, 03 2007.

[57] A. Kolahi, A. Akbarzadeh, and M. R. Barnett. Electron back scattered diffraction (EBSD) characterization of warm rolled and accumulative roll bonding (ARB) processed ferrite. *J. of Mat. Proc. Tech.*, 209(3):1436 – 1444, 02 2009.

[58] M. Eizadjou, H. Danesh Manesh, and K. Janghorban. Microstructure and mechanical properties of ultra-fine grains (UFGs) aluminum strips produced by ARB process. *J. Alloys Compd.*, 474(1–2):406 – 415, 04 2009.

[59] A. K. Talachi, M. Eizadjou, H. D. Manesh, and K. Janghorban. Wear characteristics of severely deformed aluminum sheets by accumulative roll bonding (ARB) process. *Mater. Charact.*, 62(1):12 – 21, 01 2011.

[60] L. Ghalandari and M. M. Moshksar. High-strength and high-conductive Cu/Ag multilayer produced by ARB. *J. Alloys Compd.*, 506(1):172 – 178, 09 2010.

[61] A. P. Zhilyaev and T. G. Langdon. Using high-pressure torsion for metal processing: Fundamentals and applications. *Prog. Mat. Sci.*, 53(6):893 – 979, 08 2008.

[62] T. Hebesberger, H. P. Stüwe, A. Vorhauer, F. Wetscher, and R. Pippan. Structure of Cu deformed by high pressure torsion. *Acta Mater.*, 53(2):393 – 402, 01 2005.

[63] K. Edalati, Z. Horita, S. Yagi, and E. Matsubara. Allotropic phase transformation of pure zirconium by high-pressure torsion. *Mat. Sci. and Eng. A*, 523(1-2):277 – 281, 10 2009.

[64] K. Edalati and Z. Horita. Significance of homologous temperature in softening behavior and grain size of pure metals processed by high-pressure torsion. *Mat. Sci. and Eng. A*, 528(25-26):7514 – 7523, 09 2011.

[65] M. W. Fu, Y. W. Tham, H. H. Hng, and K. B. Lim. The grain refinement of Al-6061 via ECAE processing: Deformation behavior, microstructure and property. *Mat. Sci. and Eng. A*, 526(1-2):84 – 92, 11 2009.

[66] W. N. Tang, R. S. Chen, J. Zhou, and E. H. Han. Effects of ECAE temperature and billet orientation on the microstructure, texture evolution and mechanical properties of a Mg-Zn-Y-Zr alloy. *Mat. Sci. and Eng. A*, 499(1-2):404 – 410, 01 2009.

[67] B. Huarte, C. J. Luis, I. Puertas, J. León, and R. Luri. Optical and mechanical properties of an Al-Mg alloy processed by ECAE. *J. of Mat. Proc. Tech.*, 162-163:317 – 326, 05 2005.

[68] C. J. Luis, R. Luri, and J. León. Strain and temperature analysis of AA-1370 processed by ECAE at different temperatures. *J. of Mat. Proc. Tech.*, 164-165:1530 – 1536, 05 2005.

[69] H. Chang, M. Y. Zheng, K. Wu, W. M. Gan, L. B. Tong, and H. G. Brokmeier. Microstructure and mechanical properties of the accumulative roll bonded (ARBed) pure magnesium sheet. *Mat. Sci. and Eng. A*, 527(27 - 28):7176 – 7183, 10 2010.

[70] M. Y. Zhan, W. W. Zhang, and D. T. Zhang. Production of Mg-Al-Zn magnesium alloy sheets with ultrafine-grain microstructure by accumulative roll-bonding. *Trans. Nonf. Met. Soc. China*, 21(5):991 – 997, 05 2011.

[71] Q.F. Wang, X.P. Xiao, J. Hu, W.W. Xu, X.Q. Zhao, and S.J. Zhao. An ultrafine-grained AZ31 magnesium alloy sheet with enhanced superplasticity prepared by accumulative roll bonding. *Int. J. of Iron and Steel Res.*, 14(5, Supplement 1):167 – 172, 08 2007.

[72] Tien-Chan Chang, Jian-Yi Wang, Chia-Ming O, and Shyong Lee. Grain refining of magnesium alloy AZ31 by rolling. *J. of Mat. Proc. Tech.*, 140(1-3):588 – 591, 08 2003. Proceedings of the 6th Asia Pacific Conference on materials Processing.

[73] P. Serre, R. B. Figueiredo, N. Gao, and T. G. Langdon. Influence of strain rate on the characteristics of a magnesium alloy processed by high-pressure torsion. *Mat. Sci. and Eng. A*, 528(10-11):3601 – 3608, 04 2011.

[74] R. B. Figueiredo and T. G. Langdon. Development of structural heterogeneities in a magnesium alloy processed by high-pressure torsion. *Mat. Sci. and Eng. A*, 528(13-14):4500 – 4506, 05 2011.

[75] K. Edalati and Z. Horita. High-pressure torsion of pure metals: Influence of atomic bond parameters and stacking fault energy on grain size and correlation with hardness. *Acta Mater.*, 59(17):6831 – 6836, 10 2011.

[76] M. Kai, Z. Horita, and T. G. Langdon. Developing grain refinement and superplasticity in a magnesium alloy processed by high-pressure torsion. *Mat. Sci. and Eng. A*, 488(1-2):117 – 124, 08 2008.

[77] A. Ma, J. Jiang, N. Saito, I. Shigematsu, Y. Yuan, D. Yang, and Y. Nishida. Improving both strength and ductility of a mg alloy through a large number of ECAP passes. *Mat. Sci. and Eng. A*, 513 - 514(0):122 – 127, 07 2009.

[78] R. B. Figueiredo, I. J. Beyerlein, A. P. Zhilyaev, and T. G. Langdon. Evolution of texture in a magnesium alloy processed by ECAP through dies with different angles. *Mat. Sci. and Eng. A*, 527(7 - 8):1709 – 1718, 03 2010.

[79] S. Suwas, G. Gottstein, and R. Kumar. Evolution of crystallographic texture during equal channel angular extrusion (ECAE) and its effects on secondary processing of magnesium. *Mat. Sci. and Eng. A*, 471(1 - 2):1 – 14, 12 2007.

[80] H. K. Lin, J. C. Huang, and T. G. Langdon. Relationship between texture and low temperature superplasticity in an extruded AZ31 Mg alloy processed by ECAP. *Mat. Sci. and Eng. A*, 402(12):250 – 257, 08 2005.

[81] T. Mukai, M. Yamanoi, H. Watanabe, and K. Higashi. Ductility enhancement in AZ31 magnesium alloy by controlling its grain structure. *Scr. Mater.*, 45(1):89 – 94, 07 2001.

[82] Y. T. Zhu, T. C. Lowe, R. Z. Valiev, V. V. Stolyarov, V. V. Latysh, and G. J. Raab. Ultrafine-grained titanium for medical implants. *Patent Office of the United States*, US Patent 6399215, 06 2002.

[83] W. M. Thomas, E. D. Nicholas, J. C. Needham, M. G. Murch, P. Templesmith, and C. J. Dawe. Improvements to friction welding, twi ltd. *Patent Office of GB*, GB Patent Nr. 0615480, 12 1992.

[84] W. M. Thomas, K. I. Johnson, and C. S. Wiesner. Friction stir welding - recent developments in tool and process technologies. *Adv. Eng. Mat.*, 5(7):485 – 490, 07 2003.

[85] W. M. Thomas, D. J. Staines, E. R. Watts, and I. M. Norris. The simultaneous use of two or more friction stir welding tools. *Int. J. for the Join. of Mat.*, 17(1):1 – 6, 01 2005.

[86] W. M. Thomas, E. D. Nicholas, J. C. Needham, M. G. Murch, P. Templesmith, and C. J. Dawes. Friction stir welding. *Patent Office of GB*, GB Patent Nr. 2306366, 05 1997.

[87] R. W. Carter. Auto-adjustable tool for self-reacting and conventional friction stir welding. *Patent Office of the United States*, US Patent Nr. 6758382, 07 2004.

[88] D. M. Potter and R. K. Hansen. Friction stir welding apparatus, system and method. *Patent Office of the United States*, US Patent Nr. 7866532, 01 2011.

[89] I. Stol and J. W. Cobes. Multi-shouldered fixed bobbin tools for simultaneous friction stir welding of multiple parallel walls between parts. *Patent Office of the United States*, US Patent Nr. 7198189, 04 2007.

[90] S. H. C. Park, S. Hirano, S. Kaga, M. Onose, N. Tominaga, and Y. Yoshimura. *Development of Tatsumaki Friction Stir Welding*, pages 139 – 146. John Wiley & Sons, Inc., 2011.

[91] W. M. Thomas, C. S. Wiesner, D. J. Marks, and D. G. Staines. Conventional and bobbin friction stir welding of 12% chromium alloy steel using composite refractory tool materials. *Sci. and Tech. of Weld. and Join.*, 14(3):247 – 253, 04 2009.

[92] R. Uyyuru and S. Kailas. Numerical analysis of friction stir welding process. *J. of Mat. Eng. Perform.*, 15(5):505 – 518, 10 2006.

[93] N. Kamp, A. Sullivan, and J.D. Robson. Modelling of friction stir welding of 7XXX aluminium alloys. *Mat. Sci. and Eng. A*, 466(1-2):246 – 255, 09 2007.

[94] I. Tansel, M. Demetgul, H. Okuyucu, and A. Yapici. Optimizations of friction stir welding of aluminum alloy by using genetically optimized neural network. *Int. J. of Adv. Manuf. Tech.*, 48(1):95 – 101, 04 2010.

[95] Begriffe: Metallschweißprozesse - Teil: 100 / Vocabulary: Metal welding processes - Part: 100. *Beuth*, DIN 1910-100:2008-02, 02 2008.

[96] Schweißen von Kunststoffen, Verfahren / Welding of Plastics, Processes. *Beuth*, DIN 1910-3:1977-09, 09 1977.

[97] G. E. Cook, R. Crawford, D. E. Clark, and A. M. Strauss. Robotic friction stir welding. *Ind. Robot: An Intern. J.*, 31(1):55 – 63, 2004.

[98] M. B. Prime, T. Gnäupel-Herold, J. A. Baumann, R. J. Lederich, D. M. Bowden, and R. J. Sebring. Residual stress measurements in a thick, dissimilar aluminum alloy friction stir weld. *Acta Mater.*, 54(15):4013 – 4021, 09 2006.

[99] L. Fratini, G. Macaluso, and S. Pasta. Residual stresses and FCP prediction in FSW through a continuous fe model. *J. of Mat. Proc. Tech.*, 209(15 - 16):5465 – 5474, 08 2009.

[100] J. Altenkirch, A. Steuwer, M. Peel, D.G. Richards, and P.J. Withers. The effect of tensioning and sectioning on residual stresses in aluminium AA7749 friction stir welds. *Mat. Sci. and Eng. A*, 488(1-2):16 – 24, 08 2008.

[101] M. Z. H. Khandkar, J. A. Khan, A. P. Reynolds, and M. A. Sutton. Predicting residual thermal stresses in friction stir welded metals. *J. of Mat. Proc. Tech.*, 174(1 - 3):195 – 203, 05 2006.

[102] A. Pirondi, L. Collini, and D. Fersini. Fracture and fatigue crack growth behaviour of PMMC friction stir welded butt joints. *Eng. Fracture Mech.*, 75(15):4333 – 4342, 10 2008.

[103] M. Ericsson and R. Sandström. Influence of welding speed on the fatigue of friction stir welds, and comparison with MIG and TIG. *Int. J. of Fatigue*, 25(12):1379 – 1387, 12 2003.

[104] C. Vidal, V. Infante, and P. Vilaça. Assessment of improvement techniques effect on fatigue behaviour of friction stir welded aerospace aluminium alloys. *Proc. Eng.*, 2(1):1605 – 1616, 04 2010.

[105] X. Cao and M. Jahazi. Effect of welding speed on butt joint quality of Ti-6Al-4V alloy welded using a high-power Nd:YAG laser. *Opt. and Las. in Eng.*, 47(11):1231 – 1241, 11 2009.

[106] P. A. Fleming, C. E. Hendricks, D. M. Wilkes, G. E. Cook, and A. M. Strauss. Automatic seam-tracking of friction stir welded T-joints. *Int. J. of Adv. Manuf. Tech.*, 45(5 - 6):490 – 495, 11 2009.

[107] S. Sheikhi, R. Zettler, and J. F. dos Santos. Fortschritte beim Rührreibschweißen von Aluminium, Magnesium und Stahl. *Mat.-wiss. u. Werkstofftech.*, 37(9):762 – 767, 09 2006.

[108] S. Mironov, Y. S. Sato, and H. Kokawa. Development of grain structure during friction stir welding of pure titanium. *Acta Mater.*, 57(15):4519 – 4528, 09 2009.

[109] S. Mironov, Y. Zhang, Y. S. Sato, and H. Kokawa. Development of grain structure in [beta]-phase field during friction stir welding of Ti-6Al-4V alloy. *Scr. Mater.*, 59(1):27 – 30, 07 2008.

[110] W.-B. Leeand C.-Y. Lee, W.-S. Chang, Y.-M. Yeon, and S.-B. Jung. Microstructural investigation of friction stir welded pure titanium. *Mater. Lett.*, 59(26):3315 – 3318, 11 2005.

[111] M. H. Mathon, V. Klosek, Y. de Carlan, and L. Forest. Study of PM2000 microstructure evolution following fsw process. *J. Nucl. Mater.*, 386 - 388:475 – 478, 04 2009.

[112] W.-B. Lee and S.-B. Jung. The joint properties of copper by friction stir welding. *Mater. Lett.*, 58(6):1041 – 1046, 02 2004.

[113] U. Dressler, G. Biallas, and U. A. Mercado. Friction stir welding of titanium alloy TiAl6V4 to aluminium alloy AA2024-T3. *Mat. Sci. and Eng. A*, 526(1-2):113 – 117, 11 2009.

[114] Y. C. Chen and K. Nakata. Microstructural characterization and mechanical properties in friction stir welding of aluminum and titanium dissimilar alloys. *Mat. and Des.*, 30(3):469 – 474, 03 2009.

[115] M. Aonuma and K. Nakata. Effect of alloying elements on interface microstructure of Mg-Al-Zn magnesium alloys and titanium joint by friction stir welding. *Mat. Sci. and Eng. B*, 161(1-3):46 – 49, 04 2009.

[116] W.-B. Lee, M. Schmuecker, U. A. Mercardo, G. B., and S.-B. Jung. Interfacial reaction in steel-aluminum joints made by friction stir welding. *Scr. Mater.*, 55(4):355 – 358, 08 2006.

[117] T. Yasui, Y. Shimoda, M. Tsubaki, and M. Fukumoto. Welding properties between 6063 aluminum and S45C steel by friction stir. In *Proceedings of the Fifteenth (2005) International Offshore and Polar Engineering Conference, Vol. 4*, pages 39 – 43, 2005.

[118] Y.C. Chen and K. Nakata. Friction stir lap joining aluminum and magnesium alloys. *Scr. Mater.*, 58(6):433 – 436, 03 2008.

[119] Y. S. Sato, S. H. C. Park, M Michiuchi, and H. Kokawa. Constitutional liquation during dissimilar friction stir welding of Al and Mg alloys. *Scr. Mater.*, 50(9):1233 – 1236, 05 2004.

[120] A. C. Somasekharan and L. E. Murr. Microstructures in friction-stir welded dissimilar magnesium alloys and magnesium alloys to 6061-T6 aluminum alloy. *Mater. Charact.*, 52(1):49 – 64, 03 2004.

[121] J. Yan, Z. Xu, Z. Li, L. Li, and S. Yang. Microstructure characteristics and performance of dissimilar welds between magnesium alloy and aluminum formed by friction stirring. *Scr. Mater.*, 53(5):585 – 589, 08 2005.

[122] P. Liu, Y. Li, J. Wang, H. Ma, G. Guo, and H. Geng. Microstructure and phase constituents in the interface zone of Mg/Al diffusion bonding. *Metal. and Mat. Trans. B*, 37(4):649 – 654, 08 2006.

[123] Y. J. Kwon, I. Shigematsu, and N. Saito. Dissimilar friction stir welding between magnesium and aluminum alloys. *Mater. Lett.*, 62(23):3827 – 3829, 08 2008.

[124] A. Kostka, R. S. Coelho, J. F. dos Santos, and A. R. Pyzalla. Microstructure of friction stir welding of aluminium alloy to magnesium alloy. *Scr. Mater.*, 60(11):953 – 956, 06 2009.

[125] R. S. Mishra and M. W. Mahoney. *Friction Stir Welding and Processing.* ASM International, 1 edition, March 2007.

[126] K. V. Jata, M. W. Mahoney, and R. S. Mishra. *Friction Stir Welding and Processing.* TMS, 2001.

[127] K. V. Jata, M. W. Mahoney, and R. S. Mishra. *Friction Stir Welding and Processing II.* TMS, 2003.

[128] K. V. Jata, M. W. Mahoney, and R. S. Mishra. *Friction Stir Welding and Processing III.* TMS, 2005.

[129] Z. Y. Ma, R. S. Mishra, and M. W. Mahoney. Superplastic deformation behaviour of friction stir processed 7075Al alloy. *Acta Mater.*, 50(17):4419 – 4430, 10 2002.

[130] Z. Y. Ma, S. R. Sharma, R. S. Mishra, and M. W. Mahoney. Microstructural modification of cast aluminum alloys via friction stir processing. *Mat. Sci. For.*, 426 - 432:2891 – 2896, 08 2003.

[131] Z. Y. Ma, R. S. Mishra, and M. W. Mahoney. Superplasticity in cast A356 induced via friction stir processing. *Scr. Mater.*, 50(7):931 – 935, 04 2004.

[132] Z. Y. Ma, S. R. Sharma, and R. S. Mishra. Effect of friction stir processing on the microstructure of cast A356 aluminum. *Mat. Sci. and Eng. A*, 433(1-2):269 – 278, 10 2006.

[133] Z. Y. Ma, R. S. Mishra, and F. C. Liu. Superplastic behavior of micro-regions in two-pass friction stir processed 7075Al alloy. *Mat. Sci. and Eng. A*, 505(1-2):70 – 78, 04 2009.

[134] Z. Y. Ma, A. L. Pilchak, M. C. Juhas, and J. C. Williams. Microstructural refinement and property enhancement of cast light alloys via friction stir processing. *Scr. Mater.*, 58(5):361 – 366, 03 2008.

[135] Y. J. Kwon, I. Shigematsu, and N. Saito. Mechanical properties of fine-grained aluminum alloy produced by friction stir process. *Scr. Mater.*, 49(8):785 – 789, 10 2003.

[136] D. C. Hofmann and K. S. Vecchio. Submerged friction stir processing (SFSP): An improved method for creating ultra-fine-grained bulk materials. *Mat. Sci. and Eng. A*, 402(1-2):234 – 241, 08 2005.

[137] C. J. Hsu, P. W. Kao, and N. J. Ho. Ultrafine-grained Al-Al2Cu composite produced in situ by friction stir processing. *Scr. Mater.*, 53(3):341 – 345, 08 2005.

[138] P. B. Berbon, W. H. Bingel, R. S. Mishra, C. C. Bampton, and M. W. Mahoney. Friction stir processing: a tool to homogenize nanocomposite aluminum alloys. *Scr. Mater.*, 44(1):61 – 66, 01 2001.

[139] I. S. Lee, P. W. Kao, and N. J. Ho. Microstructure and mechanical properties of Al-Fe in situ nanocomposite produced by friction stir processing. *Intermetallics*, 16(9):1104 – 1108, 09 2008.

[140] S. Mironov, Y. S. Sato, and H. Kokawa. Microstructural evolution during friction stir-processing of pure iron. *Acta Mater.*, 56(11):2602 – 2614, 06 2008.

[141] R. S. Mishra and M. W. Mahoney. Friction stir processing: A new grain refinement technique to achieve high strain rate superplasticity in commercial alloys. In *Superplasticity in advanced materials, ICSAM-2000*, volume 357 - 359, pages 507 – 512, 2001.

[142] D. G. Hattingh, C. Blignault, T. I. van Niekerk, and M. N. James. Characterization of the influences of fsw tool geometry on welding forces and weld tensile strength using an instrumented tool. *J. of Mat. Proc. Tech.*, 203(1-3):46 – 57, 07 2008.

[143] C. Bruni, G. Buffa, L. d'Apolito, A. Forcellese, and L. Fratini. Tool geometry in friction stir welding of magnesium alloy sheets. In *Sheet metal 2009*, volume 410 - 411, pages 555 – 562, 2009.

[144] Y.C. Chen and K. Nakata. Effect of tool geometry on microstructure and mechanical properties of friction stir lap welded magnesium alloy and steel. *Mat. and Des.*, 30(9):3913 – 3919, 10 2009.

[145] S. M. Chowdhury, D. L. Chen, S. D. Bhole, and X. Cao. Effect of pin tool thread orientation on fatigue strength of friction stir welded AZ31B-H24 Mg butt joints. *Proc. Eng.*, 2(1):825 – 833, 04 2010.

[146] G. Buffa, J. Hua, R. Shivpuri, and L. Fratini. Design of the friction stir welding tool using the continuum based FEM model. *Mat. Sci. and Eng. A*, 419(1-2):381 – 388, 03 2006.

[147] R.S. Mishra and M.W. Mahoney. *Friction Stir Welding and Processing*, pages 42–43. ASM International, 1 edition, March 2007.

[148] R. J. Heideman. Friction stir welding tool. *Patent Office of the United States*, US Patent Nr. 6053391, 04 2000.

[149] K. Kumar and Satish V. Kailas. The role of friction stir welding tool on material flow and weld formation. *Mat. Sci. and Eng. A*, 485(1-2):367 – 374, 06 2008.

[150] E. S Holt and L. J. Lang. Programmable friction stir welding process. *Patent Office of the United States*, US Patent Nr. 5713507, 03 1998.

[151] B. Han, Y. Huang, S. Lv, L. Wan, J. Feng, and G. Fu. AA7075 bit for repairing AA2219 keyhole by filling friction stir welding. *Mat. and Des.*, 51(0):25 – 33, 10 2013.

[152] L. Liming, W. Jifeng, and S. Gang. Hybrid laser-TIG welding, laser beam welding and gas tungsten arc welding of AZ31B magnesium alloy. *Mat. Sci. and Eng. A*, 381(1-2):129 – 133, 09 2004.

[153] S. M. Fatemi-Varzaneh, A. Zarei-Hanzaki, and H. Beladi. Dynamic recrystallization in AZ31 magnesium alloy. *Mat. Sci. and Eng. A*, 456(1 - 2):52 – 57, 05 2007.

[154] L. Commin, M. Dumont, J.-E. Masse, and L. Barrallier. Friction stir welding of AZ31 magnesium alloy rolled sheets: Influence of processing parameters. *Acta Mater.*, 57(2):326 – 334, 01 2009.

[155] B. M. Darras, M. K. Khraisheh, F. K. Abu-Farha, and M. A. Omar. Friction stir processing of commercial AZ31 magnesium alloy. *J. of Mat. Proc. Tech.*, 191(1-3):77 – 81, 08 2007.

[156] P. Cavaliere and P.P. de Marco. Superplastic behaviour of friction stir processed AZ91 magnesium alloy produced by high pressure die cast. *J. of Mat. Proc. Tech.*, 184(1-3):77 – 83, 04 2007.

[157] R.S. Mishra and M.W. Mahoney. *Friction Stir Welding and Processing*, page 2. ASM International, 1 edition, March 2007.

[158] T. Freeney and R. Mishra. Effect of friction stir processing on microstructure and mechanical properties of a cast-magnesium-rare earth alloy. *Metal. and Mat. Trans. A*, 41(1):73 – 84, 01 2010.

[159] M. M. Shtrikman. The current state and development of the friction stir welding process (review), part 1. *Weld. Int.*, 22(8):564 – 569, 09 2008.

[160] R.S. Mishra and M.W. Mahoney. *Friction Stir Welding and Processing*, page 1. ASM International, 1 edition, March 2007.

[161] N. Afrin, D. L. Chen, X. Cao, and M. Jahazi. Microstructure and tensile properties of friction stir welded AZ31B magnesium alloy. *Mat. Sci. and Eng. A*, 472(1 - 2):179 – 186, 01 2008.

[162] W. B. Lee, Y. M. Yeon, and S. B. Jung. Joint properties of friction stir welded AZ31B - H24 magnesium alloy. *Mater. Sci. Technol.*, 19(06):785 – 790, 06 2003.

[163] M. Pareek, A. Polar, F. Rumiche, and J. E. Indacochea. Metallurgical evaluation of AZ31B-H24 magnesium alloy friction stir welds. *J. of Mat. Eng. Perform.*, 16(5):655 – 662, 10 2007.

[164] X. Cao and M. Jahazi. Effect of welding speed on the quality of friction stir welded butt joints of a magnesium alloy. *Mat. and Des.*, 30(6):2033 – 2042, 06 2009.

[165] C.I. Chang, X.H. Du, and J.C. Huang. Achieving ultrafine grain size in Mg-Al-Zn alloy by friction stir processing. *Scr. Mater.*, 57(3):209 – 212, 08 2007.

[166] S. M. Chowdhury, D. L. Chen, S. D. Bhole, X. Cao, E. Powidajko, D. C. Weckman, and Y. Zhou. Tensile properties and strain-hardening behavior of double-sided arc welded and friction stir welded AZ31B magnesium alloy. *Mat. Sci. and Eng. A*, 527(12):2951 – 2961, 05 2010.

[167] S. M. Chowdhury, D. L. Chen, S. D. Bhole, and X. Cao. Tensile properties of a friction stir welded magnesium alloy: Effect of pin tool thread orientation and weld pitch. *Mat. Sci. and Eng. A*, 527(21 - 22):6064 – 6075, 08 2010.

[168] B. Darras and E. Kishta. Submerged friction stir processing of AZ31 magnesium alloy. *Mat. and Des.*, 47(0):133 – 137, 05 2013.

[169] U. F. H. R. Suhuddin, S. Mironov, Y. S. Sato, H. Kokawa, and C.-W. Lee. Grain structure evolution during friction-stir welding of AZ31 magnesium alloy. *Acta Mater.*, 57(18):5406 – 5418, 10 2009.

[170] G. Venkateswarlu, D. Devaraju, M. J. Davidson, B. Kotiveerachari, and G. R. N. Tagore. Effect of overlapping ratio on mechanical properties and formability of friction stir processed Mg AZ31B alloy. *Mat. and Des.*, 45(0):480 – 486, 03 2013.

[171] X. Wang and W. Kuaishe. Microstructure and properties of friction stir butt-welded AZ31 magnesium alloy. *Mat. Sci. and Eng. A*, 431(1-2):114 – 117, 09 2006.

[172] R. Johnson and P. Threadgill, editors. *Friction stir welding of magnesium alloys*, Magnesium Technology. TMS, 2003.

[173] S. Lim, S. Kim, C.-G. Lee, S. Kim, and C. Yim. Tensile behavior of friction-stir-welded AZ31-H24 Mg alloy. *Metal. and Mat. Trans. A*, 36(6):1609 – 1612, 06 2005.

[174] G. Padmanaban and V. Balasubramanian. An experimental investigation on friction stir welding of AZ31B magnesium alloy. *Int. J. of Adv. Manuf. Tech.*, 49(1 - 4):111 – 121, 10 2009.

[175] A. Alavi Nia, H. Omidvar, and S. H. Nourbakhsh. Investigation of the effects of thread pitch and water cooling action on the mechanical strength and microstructure of friction stir processed AZ31. *Mat. and Des.*, 52(0):615 – 620, 12 2013.

[176] M. A. Gharacheh, A.H. Kokabi, G.H. Daneshi, B. Shalchi, and R. Sarrafi. The influence of the ratio of rotational speed / traverse speed ([$\omega$]/v) on mechanical properties of AZ31 friction stir welds. *Int. J. of Mach. Tools and Man.*, 46(15):1983 – 1987, 12 2006.

[177] N. Afrin, D. L. Chen, X. Cao, and M. Jahazi. Strain hardening behavior of a friction stir welded magnesium alloy. *Scr. Mater.*, 57(11):1004 – 1007, 12 2007.

[178] D. Rao, K. Huber, J. Heerens, J. F. dos Santos, and N. Huber. Asymmetric mechanical properties and tensile behaviour prediction of aluminium alloy 5083 friction stir welding joints. *Mat. Sci. and Eng. A*, 565:44 – 50, 03 2013.

[179] C. I. Chang, C. J. Lee, and J. C. Huang. Relationship between grain size and Zener-Holloman parameter during friction stir processing in AZ31 Mg alloys. *Scr. Mater.*, 51(6):509 – 514, 08 2004.

[180] J. Yang, B.L. Xiao, D. Wang, and Z.Y. Ma. Effects of heat input on tensile properties and fracture behavior of friction stir welded Mg-3Al-1Zn alloy. *Mat. Sci. and Eng. A*, 527(3):708 – 714, 01 2010.

[181] Y. N. Wang, C. I. Chang, C. J. Lee, H. K. Lin, and J. C. Huang. Texture and weak grain size dependence in friction stir processed Mg-Al-Zn alloy. *Scr. Mater.*, 55(7):637 – 640, 10 2006.

[182] S. Ramesh Babu, V. S. Senthil Kumar, L. Karunamoorthy, and G. Madhusudhan Reddy. Investigation on the effect of friction stir processing on the superplastic forming of AZ31B alloy. *Mat. and Des.*, 53(0):338 – 348, 01 2014.

[183] Q. Yang, S. Mironov, Y. S. Sato, and K. Okamoto. Deformation behavior of friction stir processed magnesium alloys. In *TMS 2011*, 2011.

[184] H. E. Friedrich and B. L. Mordike. *Magnesium Technology*, page 64. Springer, 1 edition, 2006.

[185] H. E. Friedrich and B. L. Mordike. *Magnesium Technology*, pages 274 – 275. Springer, 1 edition, 2006.

[186] P. Lukáč and Z. Trojanová. Hardening and softening in selected magnesium alloys. *Mat. Sci. and Eng. A*, 462(1 - 2):23 – 28, 07 2007.

[187] K. Máthis, Z. Trojanová, and P. Lukáč. Hardening and softening in deformed magnesium alloys. *Mat. Sci. and Eng. A*, 324(1 - 2):141 – 144, 02 2002.

[188] W. Blum, P. Zhang, B. Watzinger, B. v. Grossmann, and H. G. Haldenwanger. Comparative study of creep of the die-cast Mg-alloys AZ91, AS21, AS41, AM60 and AE42. *Mat. Sci. and Eng. A*, 319 - 321:735 – 740, 12 2001.

[189] P. Zhang, B. Watzinger, Q. P. Kong, and W. Blum. Creep and fracture of engineering materials and structures. *Key Eng. Mat.*, 171 - 174:609 – 616, 2000.

[190] W. F. Hosford and R. M. Cadell. *Metal Forming Mechanics and Metallurgy*, volume 3. Cambridge University Press, 2007.

[191] X.Y. Lou, M. Li, R.K. Boger, S.R. Agnew, and R.H. Wagoner. Hardening evolution of AZ31B Mg sheet. *Int. J. of Plasticity*, 23(1):44 – 86, 01 2007.

[192] S. Kleiner and P. J. Uggowitzer. Mechanical anisotropy of extruded Mg–6% Al–1% Zn alloy. *Mat. Sci. and Eng. A*, 379(1 - 2):258 – 263, 08 2004.

[193] E. F. Emley. *Principles of magnesium technology*, pages 483 – 489. Pergamon Press, Oxford; New York, 1966.

[194] G.V. Raynor. *The physical metallurgy of magnesium and its alloys*, page 223. International Series of Monographs in the Science of the Solid State. Pergamon Press, 1959.

[195] T. Al-Samman and G. Gottstein. Room temperature formability of a magnesium AZ31 alloy: Examining the role of texture on the deformation mechanisms. *Mat. Sci. and Eng. A*, 488(1-2):406 – 414, 07 2008.

[196] T. Obara, H. Yoshinga, and S. Morozumi. $\{11\bar{2}2\}\ \langle 1123\rangle$ slip system in magnesium. *Acta Metall.*, 21(7):845 – 853, 07 1973.

[197] M.R. Barnett, Z. Keshavarz, A.G. Beer, and D. Atwell. Influence of grain size on the compressive deformation of wrought MgAl3Zn1. *Acta Mater.*, 52(17):5093 – 5103, 10 2004.

[198] M. R. Barnett. Twinning and the ductility of magnesium alloys: Part I: Tension twins. *Mat. Sci. and Eng. A*, 464(1-2):1 – 7, 08 2007.

[199] M. R. Barnett. Twinning and the ductility of magnesium alloys: Part II. Contraction twins. *Mat. Sci. and Eng. A*, 464(1-2):8 – 16, 08 2007.

[200] T. Al-Samman, X. Li, and S. Ghosh Chowdhury. Orientation dependent slip and twinning during compression and tension of strongly textured magnesium AZ31 alloy. *Mat. Sci. and Eng. A*, 527(15):3450 – 3463, 06 2010.

[201] H. Yoshinaga, T. Obara, and S. Morozumi. Twinning deformation in magnesium compressed along the C-axis. *Mat. Sci. and Eng.*, 12(5-6):255 – 264, 11 1973.

[202] A. Akhtar and E. Teghtsoonian. Solid solution strengthening of magnesium single crystals -I alloying behaviour in basal slip. *Acta Metall.*, 17(11):1339 – 1349, 11 1969.

[203] W. B. Hutchinson and M. R. Barnett. Effective values of critical resolved shear stress for slip in polycrystalline magnesium and other hcp metals. *Scr. Mater.*, 63(7):737 – 740, 10 2010.

[204] W.Z. Chen, X. Wang, E.D. Wang, Z.Y. Liu, and L.X. Hu. Texture dependence of uniform elongation for a magnesium alloy. *Scr. Mater.*, 67(10):858 – 861, 11 2012.

[205] C. H. Cáceres and A. H. Blake. On the strain hardening behaviour of magnesium at room temperature. *Mat. Sci. and Eng. A*, 462(1 - 2):193 – 196, 07 2007.

[206] G.-S. Huang, H. Zhang, X.-Y. Gao, B. Song, and L. Zhang. Forming limit of textured AZ31B magnesium alloy sheet at different temperatures. *Trans. Nonf. Met. Soc. China*, 21(4):836 – 843, 04 2011.

[207] H. J. Choi, Y. Kim, J. H. Shin, and D. H. Bae. Deformation behavior of magnesium in the grain size spectrum from nano- to micrometer. *Mat. Sci. and Eng. A*, 527(6):1565 – 1570, 03 2010.

[208] G. V. Raynor. *The physical metallurgy of magnesium and its alloys.* Pergamon Press, New York, 1959.

[209] H. E. Friedrich and B. L. Mordike. *Magnesium Technology*, pages 80 – 82. Springer, 1 edition, 2006.

[210] H. E. Friedrich and B. L. Mordike. *Magnesium Technology*, page 68. Springer, 1 edition, 2006.

[211] F. Czerwinski. *Magnesium Alloys - Design, Processing and Properties*, volume 1, pages 95 – 96. InTech, 2011.

[212] F. Czerwinski. *Magnesium Alloys - Design, Processing and Properties*, volume 1, page 43. InTech, 2011.

[213] H. Baker. *Magnesium and magnesium alloys*, page 258. ASM International, 1999.

[214] E. F. Emley. *Principles of magnesium technology*, page 453. Pergamon Press, Oxford; New York, 1966.

[215] B.-P. Zhang, Y.-F. Tu, J.-Y. Chen, H.-L. Zhang, Y.-L. Kang, and H. G. Suzuki. Preparation and characterization of as-rolled AZ31 magnesium alloy sheets. *J. of Mat. Proc. Tech.*, 184(1-3):102 – 107, 04 2007.

[216] M. Marya, L. G. Hector, R. Verma, and W. Tong. Microstructural effects of AZ31 magnesium alloy on its tensile deformation and failure behaviors. *Mat. Sci. and Eng. A*, 418(1-2):341 – 356, 02 2006.

[217] S. Su, H. Lin, J. Huang, and N. Ho. Electron-beam welding behavior in Mg-Al-based alloys. *Metal. and Mat. Trans. A*, 33(5):1461 – 1473, 05 2002.

[218] V. Ventzke, S. Riekehr, and M. Koçak. Mikrostrukturelle und mechanische Eigenschaften von laserstrahlgeschweißtem Magnesiumfeinblech AZ31-HP mit und ohne Zusatzwerkstoffe. *Mat.-wiss. u. Werkstofftech.*, 39(7):435 – 447, 07 2008.

[219] Z. Sun, D. Pan, and J. Wei. Comparative evaluation of tungsten inert gas and laser welding of AZ31 magnesium alloy. *Sci. and Tech. of Weld. and Join.*, 7(6):343 – 351, 12 2002.

[220] J. Zhu, L. Li, and Z. Liu. CO2 and diode laser welding of AZ31 magnesium alloy. *Appl. Surf. Sci.*, 247(1 - 4):300 – 306, 07 2005.

[221] Udehom GmbH. Hotvar - properties. *http://www.uddeholm.de - /german/files/downloads/hotvar-english_050103.pdf*, 09 2013.

[222] Thermocoax-GmbH. *Thermocoax Mantelthermoelements Auswahl und Anwendung*, 2002.

[223] Instrumentierte Eindringprüfung zur Bestimmung der Härte und anderer Werkstoffparameter - Teil 1: Prüfverfahren / Instrumented indentation test for hardness and materials parameters - Part 1: Test method. *Beuth*, DIN EN ISO 14577-1:2012-03, 03 2012.

[224] E.S. Berkovich and M.M. Khrushchov. Methods of determining the hardness of very hard materials: The hardness of diamond. *Ind. Diam. Rev.*, 11:42 – 49, 02 1951.

[225] W.C. Oliver and G.M. Pharr. An improved technique for determining hardness and elastic modulus using load and displacement sensing indentation experiments. *J. Mater. Res.*, 7(6):1564 – 1583, 06 1992.

[226] Zugversuch bei Raumtemperatur / Tensile testing at ambient temperature. *Beuth*, DIN EN 2002-001:2006-11, 11 2006.

[227] Zugversuch - Teil 1: Prüfverfahren bei Raumtemperatur / Tensile testing - Part 1: Method of test at room temperature. *Beuth*, DIN EN ISO 6892-1:2009-12, 12 2001.

[228] Regeln und Verfahren für die Beurteilung der Oberflächenbeschaffenheit / Rules and procedures for the assessment of surface texture. *Beuth*, DIN EN ISO 4288:1998-04, 04 1998.

[229] N. Kashaev, M. Horstmann, V. Ventzke, S. Riekehr, and N. Huber. Comparative study of mechanical properties using standard and micro-specimens of base materials Inconel 625, Inconel 718 and Ti-6Al-4V. *J. Mater. Res. Technol.*, 2(1):43 – 47, 01 2013.

[230] W. C. Emmens, G. Sebastiani, and A. H. van den Boogaard. The technology of incremental sheet forming - a brief review of the history. *J. of Mat. Proc. Tech.*, 210(8):981 – 997, 06 2010.

[231] J. Gronostajski, A. Matuszak, A. Niechajowicz, and Z. Zimniak. The system for sheet metal forming design of complex parts. *J. of Mat. Proc. Tech.*, 157 - 158(0):502 – 507, 07 2004.

[232] N. Alberti and L. Fratini. Innovative sheet metal forming processes: numerical simulations and experimental tests. *J. of Mat. Proc. Tech.*, 150(12):2 – 9, 12 2004.

[233] K. Jackson and J. Allwood. The mechanics of incremental sheet forming. *J. of Mat. Proc. Tech.*, 209(3):1158 – 1174, 02 2009.

[234] M. Nebebe Mekonen, D. Steglich, J. Bohlen, L. Stutz, D. Letzig, and J. Mosler. Experimental and numerical investigation of Mg alloy sheet formability. *Mat. Sci. and Eng. A*, 586(0):204 – 214, 12 2013.

[235] S. Keller and A. Backofen. *Pastic instability and fracture in sheets stretched over rigid punches.*, pages 25 – 48. MIT, 1963.

[236] E. Doege and B. Behrens. *Handbuch der Umformtechnik: Grundlagen, Technologien, Maschinen*, page 317. Springer, 2010.

[237] M. C. Butuc, A. B. da Rocha, J. J. Gracio, and J. F. Duarte. A more general model for forming limit diagrams prediction. *J. of Mat. Proc. Tech.*, 125 - 126(0):213 – 218, 09 2002.

[238] GOM GmbH. Material properties: Determination of process limitations in sheet metal forming - forming limit diagram. *http://www.gom.com/fileadmin/user_upload/industries/flc_fld_EN.pdf*, 09 2013.

[239] V. Hasek. Untersuchung und theoretische Beschreibung wichtiger Einflussgrößen auf das Grenzformänderungsschaubild. *Bleche Rohre Profile*, 5:213 – 220, 1978.

[240] V. Hasek. Untersuchung und theoretische Beschreibung wichtiger Einflussgrößen auf das Grenzformänderungsschaubild. *Bleche Rohre Profile*, 6:285 – 292, 1978.

[241] V. Hasek. Untersuchung und theoretische Beschreibung wichtiger Einflussgrößen auf das Grenzformänderungsschaubild. *Bleche Rohre Profile*, 10:493 – 499, 1978.

[242] V. Hasek. Untersuchung und theoretische Beschreibung wichtiger Einflussgrößen auf das Grenzformänderungsschaubild. *Bleche Rohre Profile*, 12:619 – 627, 1978.

[243] K. Nakajima, T. Kikuma, and K. Hasaku. Study of the fomarbility of steel sheets. *Yawata Technical Report No. 264*, 1:141 – 154, 1968.

[244] Messung und Anwendung von Grenzformänderungsdiagrammen in Stanzereien - Teil: 1 / Measurement and application of forming-limit diagrams in the press shop - Part: Measurement and application of forming-limit diagrams in the press shop - Part: 2. *Beuth*, ISO 12004-1:2009-02, 02 2009.

[245] Bestimmung von Grenzformänderungskurven in Laboratorie - Teil: 2 / Determination of forming-limit curves in the laboratory - Part: 2. *Beuth*, ISO 12004-2:2008-10, 10 2008.

[246] D. W. A. Rees. Factors influencing the fld of automotive sheet metal. *J. of Mat. Proc. Tech.*, 118(13):1 – 8, 12 2001.

[247] M. Geiger and M. Merklein. Determination of forming limit diagrams - a new analysis method for characterization of materials' formability. *CIRP Annals - Manufacturing Technology*, 52(1):213 – 216, 2003.

[248] S. Ahmadi, A.R. Eivani, and A. Akbarzadeh. Experimental and analytical studies on the prediction of forming limit diagrams. *Comp. Mat. Sci.*, 44(4):1252 – 1257, 02 2009.

[249] GOM GmbH. ARAMIS - Optical 3D Deformation Analysis. *http://www.gom.com/metrology-systems/digital-image-correlation.html*, 09 2013.

[250] D. P. Field. Recent advances in the application of orientation imaging. *Ultramic.*, 67(1-4):1–9, 1997.

[251] H. Schmidt and J. H. Hattel. Thermal modelling of friction stir welding. *Scr. Mater.*, 58(5):332 – 337, 03 2008.

[252] J. Hilgert, H. N. B. Schmidt, J. F. dos Santos, and N. Huber. Thermal models for bobbin tool friction stir welding. *J. of Mat. Proc. Tech.*, 211(2):197 – 204, 02 2011.

[253] L. L. Hütsch, J. Hilgert, K. Herzberg, J. F. Santos, and N. Huber. Temperature and texture development during high speed friction stir processing of magnesium AZ31. *Adv. Eng. Mat.*, 14(9):762 – 771, 09 2012.

[254] H. Baker. *Magnesium and magnesium alloys*, page 17. ASM International, 1999.

[255] B. Beausir, L. S. Tóth, and K. W. Neale. Ideal orientations and persistence characteristics of hexagonal close packed crystals in simple shear. *Acta Mater.*, 55(8):2695 – 2705, 05 2007.

[256] J. Q. Li and H. J. Liu. Effects of tool rotation speed on microstructures and mechanical properties of $aa2219-t6$ welded by the external non-rotational shoulder assisted friction stir welding. *Mat. and Des.*, 43:299 – 306, 01 2013.

[257] M. S. Shtrikman. Current state and development of friction stir welding (review). part 2. improvement of tools and welding method. *Weld. Int.*, 22(10):712 – 719, 10 2008.

[258] M. M. Shtrikman. Current state and development of friction stir welding part 3. industrial application of friction stir welding. *Weld. Int.*, 22(11):806 – 815, 11 2008.

[259] H. Lombard, D.G. Hattingh, A. Steuwer, and M.N. James. Optimising fsw process parameters to minimise defects and maximise fatigue life in 5083-H321 aluminium alloy. *Eng. Frac. Mech.*, 75(3-4):341 – 354, 02 - 03 2008.

[260] Z. Zhang and H. W. Zhang. Numerical studies on controlling of process parameters in friction stir welding. *J. of Mat. Proc. Tech.*, 209(1), 01 2009.

[261] R. Zettler, A. M. da Silva, and J. F. dos Santos. High speed friction stir welding of a wrought magnesium AZ31 alloy. In *Alusil*, 2007.

[262] H. Baker. *Magnesium and magnesium alloys*, page 259. ASM International, 1999.

[263] C. M. Sellars and W. J. McTegart. On the mechanism of hot deformation. *Acta Metall.*, 14(9):1136 – 1138, 09 1966.

[264] Y. S. Li, Y. Zhang, N. R. Tao, and K. Lu. Effect of the Zener-Hollomon parameter on the microstructures and mechanical properties of Cu subjected to plastic deformation. *Acta Mater.*, 57(3):761 – 772, 02 2009.

[265] K. E. Tello, A. P. Gerlich, and P. F. Mendez. Constants for hot deformation constitutive models for recent experimental data. *Sci. and Tech. of Weld. and Join.*, 15(3):260 – 266, 04 2010.

[266] R. Nandan, G. G. Roy, T. J. Lienert, and T. Debroy. Three-dimensional heat and material flow during friction stir welding of mild steel. *Acta Mater.*, 55(3):883 – 895, 02 2007.

[267] K.U. Kainer. *Megnesium alloys and Technology*, volume 1, page 2. Wiley-VCH, 2003.

[268] S. H. C. Park, Y. S. Sato, and H. Kokawa. Basal plane texture and flow pattern in friction stir weld of a magnesium alloy. *Metal. and Mat. Trans. A*, 34(4):987 – 994, 04 2003.

[269] M. D. Nave and M. R. Barnett. Microstructures and textures of pure magnesium deformed in plane-strain compression. *Scr. Mater.*, 51(9):881 – 885, 11 2004.

[270] A. Galiyev, R. Kaibyshev, and G. Gottstein. Correlation of plastic deformation and dynamic recrystallization in magnesium alloy ZK60. *Acta Mater.*, 49(7):1199 – 1207, 04 2001.

[271] A. G. Beer and M. R. Barnett. Microstructural development during hot working of Mg3Al1Zn. *Metall. and Mat. Transa. A*, 01(38):1856 – 1867, 01 2007.

[272] S. H. C. Park, Y. S. Sato, and H. Kokawa. Effect of micro-texture on fracture location in friction stir weld of Mg alloy AZ61 during tensile test. *Scr. Mater.*, 49(2):161 – 166, 07 2003.

[273] C. G. Rhodes, M. W. Mahoney, W. H. Bingel, and M. Calabrese. Fine-grain evolution in friction-stir processed 7050 aluminum. *Scr. Mater.*, 48(10):1451 – 1455, 05 2003.

[274] H. J. Forst and M. F. Ashby. *Deformation-Mechanism Maps*, pages 21, 44. Pergamon Press, Oxford, 1982.

[275] A. Staroselsky and L. Anand. A constitutive model for hcp materials deforming by slip and twinning: application to magnesium alloy AZ31B. *Int. J. of Plasticity*, 19(10):1843 – 1864, 10 2003.

[276] D. Ponge and G. Gottstein. Necklace formation during dynamic recrystallization: mechanisms and impact on flow behavior. *Acta Mater.*, 46(1):69 – 80, 12 1998.

[277] B. Beausir, S. Suwas, L. S. Tóth, K. W. Neale, and J. J. Fundenberger. Analysis of texture evolution in magnesium during equal channel angular extrusion. *Acta Mater.*, 56(2):200 – 214, 01 2008.

[278] X.-L. Nan, H.-Y. Wang, L. Zhang, J.-B. Li, and Q.-C. Jiang. Calculation of schmid factors in magnesium: Analysis of deformation behaviors. *Scr. Mater.*, 67(5):443 – 446, 09 2012.

[279] S. Yu. Mironov, G. A. Salishchev, M. M. Myshlyaev, and R. Pippan. Evolution of misorientation distribution during warm 'abc' forging of commercial-purity titanium. *Mat. Sci. and Eng. A*, 418(1 - 2):257 – 267, 02 2006.

[280] H. J. Bargel and G. Schulze. *Werkstoffkunde*, volume 10, page 29. Springer, 2008.

[281] X.-Y. Yang, Y.-K. Zhu, H. Miura, and T. Sakai. Static recrystallization behavior of hot-deformed magnesium alloy AZ31 during isothermal annealing. *Trans. Nonf. Met. Soc. China*, 20(7):1269 – 1274, 07 2010.

[282] Y. V. R. K. Prasad and K. P. Rao. Effect of homogenization on the hot deformation behavior of cast AZ31 magnesium alloy. *Mat. and Des.*, 30(9):3723 – 3730, 02 2009.

[283] H. J. Bargel and G. Schulze. *Werkstoffkunde*, volume 10, pages 30–32. Springer, 2008.

[284] H. E. Friedrich and B. L. Mordike. *Magnesium Technology*, page 300. Springer, 1 edition, 2006.

[285] S.P. Baker. *Nanoindentation Techniques*, pages 5908–5915. Elsevier, Oxford, 2001.

[286] S. R. Agnew and Ö. Duygulu. Plastic anisotropy and the role of non-basal slip in magnesium alloy AZ31B. *Int. J. of Plasticity*, 21(6):1161 – 1193, 06 2005.

[287] J. H. Shin, S. H. Kim, T. K. Ha, K. H. Oh, I. S. Choi, and H. N. Han. Nanoindentation study for deformation twinning of magnesium single crystal. *Scr. Mater.*, 68(7):483 – 486, 04 2013.

[288] M. Barmouz, K. Abrinia, and J. khosravi. Using hardness measurement for dislocation densities determination in fsped metal in order to evaluation of strain rate effect on the tensile behavior. *Mat. Sci. and Eng. A*, 559(0):917 – 919, 01 2013.

[289] A. Jain and S. R. Agnew. Modeling the temperature dependent effect of twinning on the behavior of magnesium alloy AZ31B sheet. *Mat. Sci. and Eng. A*, 462(12):29 – 36, 07 2007.

[290] Q. Yang and A.K. Ghosh. Deformation behavior of ultrafine-grain (UFG) AZ31B Mg alloy at room temperature. *Acta Mater.*, 54(19):5159 – 5170, 11 2006.

[291] T. Altan and A. E. Tekkaya. *Sheet Metal Forming Fundamentals*, pages 44 – 51. ASM International, 2012.

[292] C. Bruni, A. Forcellese, F. Gabrielli, and M. Simoncini. Effect of temperature, strain rate and fibre orientation on the plastic flow behaviour and formability of AZ31 magnesium alloy. *J. of Mat. Proc. Tech.*, 210(10):1354 – 1363, 07 2010.

[293] C. Bruni, A. Forcellese, F. Gabrielli, and M. Simoncini. Post-welding formability of AZ31 magnesium alloy. *Mat. and Des.*, 32(5):2988 – 2991, 05 2011.

[294] G. Venkateswarlu, M. J. Davidson, and G. R. N. Tagore. Modelling studies of sheet metal formability of friction stir processed Mg AZ31B alloy under stretch forming. *Mat. and Des.*, 40(0):1 – 6, 09 2012.

[295] A. S. Khan, A. Pandey, T. Gnäupel-Herold, and R. K. Mishra. Mechanical response and texture evolution of AZ31 alloy at large strains for different strain rates and temperatures. *Int. J. of Plasticity*, 27(5):688 – 706, 05 2011.

[296] K. Ohashi, H. Utsunomiya, and R. Matsumoto. Evaluation of r -value of steels using vickers hardness test. *Journ. of Physics: Conference Series*, 379(1):012045, 2012.

[297] S. Aleksandrovic, M. Stefanovic, D. Adamovic, and V. Lazib. Variation of normal anisotropy ratio r during plastic forming. *Journ. of Mech. Eng.*, 55(6):8, 07 2009.

[298] J. Kang, D. S. Wilkinson, R. K. Mishra, W. Yuan, and R. S. Mishra. Effect of inhomogeneous deformation on anisotropy of AZ31 magnesium sheet. *Mat. Sci. and Eng. A*, 567:101 – 109, 04 2013.

[299] J. Koike. Enhanced deformation mechanisms by anisotropic plasticity in polycrystalline Mg alloys at room temperature. *Metal. and Mat. Trans. A*, 36(7):1689 – 1696, 07 2005.

[300] A. Stevenson. *Heat Treating*, volume 4 of *ASM Handbook*. ASM International, 1991.